

Activity of novel ferronucleosides in pancreatic cancer cells

By

Marium Rana



UNIVERSITY OF
BIRMINGHAM

A thesis submitted to the
University of Birmingham
for the degree of
DOCTOR OF PHILOSOPHY

School of Chemistry

College of Engineering and Physical Science

University of Birmingham

February 2022

UNIVERSITY OF
BIRMINGHAM

University of Birmingham Research Archive

e-theses repository

This unpublished thesis/dissertation is copyright of the author and/or third parties. The intellectual property rights of the author or third parties in respect of this work are as defined by The Copyright Designs and Patents Act 1988 or as modified by any successor legislation.

Any use made of information contained in this thesis/dissertation must be in accordance with that legislation and must be properly acknowledged. Further distribution or reproduction in any format is prohibited without the permission of the copyright holder.

Abstract

Pancreatic ductal adenocarcinoma (PDAC) is an aggressive disease with an extremely poor prognosis attributed to late diagnosis and limited therapeutic options. Acquired chemoresistance to drugs such as gemcitabine, used to treat PDAC creates a clinical demand for novel anticancer agents that exhibit similar potency, evade cross resistance, and improve patient outcome. The clinical success of cisplatin has driven interest into metal complexes which has led to the proposal of organometallic compounds as anticancer agents. These compounds, particularly ferrocene-based complexes such as ferrocifen, have shown promising anticancer activity exhibiting different effects to those observed with existing anticancer drugs. As part of their drug discovery work, Tucker *et al.* synthesised a novel ferronucleoside called TUC-1 which showed promising anticancer activity. In this work, the anticancer activity of TUC-1 and derivatives is evaluated in a range of pancreatic cancer cell lines compared to established chemotherapeutics supported by TUC-1 evaluation in NCI-60 panel of cancer cell lines. This is followed by investigations into the mechanism of action with an emphasis on DNA replication fork stalling and downstream events. Pre-clinical data evaluating the drug metabolism and pharmacokinetic properties of TUC-1 is also presented. In addition to this, a synergistic relationship is established between TUC-1 and a Chk kinase inhibitor, AZD7762, that is shown to potentiate the effects of TUC-1.

Acknowledgements

First and foremost, I would like to extend my sincerest gratitude to my supervisors Professor James Tucker, Dr Nikolas Hodges, and Dr Isolda Romero-Canelón for always supporting and encouraging my work, gently guiding me through this endeavour and nurturing the scientist in me. Jim, thank you for trusting me with this project, always providing me with the tools to see this to completion and encouraging me to widen my horizons by presenting our work to the scientific community. I wouldn't have the confidence in my skills without your strong support. Isolda, without your advice and kind guidance I would not have been able to bridge the different disciplines, you were always the silent support I knew I could rely on when things didn't quite work out. Nik, I think it's safe to say I would not have reached this far without your supervision since my undergraduate. From every failed experiment to triumph you were always there guiding me through it all, turning the negatives into positives, never questioning my ability even when I had self-doubts and going above and beyond to help me. I will always be grateful for the safe space you created for me to learn, for your unwavering support and for giving a shy and timid undergraduate student this opportunity. Thank you for being the best teacher and mentor.

I would like to extend my thanks to the past and present members of the Hodges group for being my brainstormers when things didn't work out and creating a kind atmosphere to work in. Dr Alessio Perotti, thank you for training the little rookie who shadowed you and for sharing your Italian wisdom (I can still count to 10 in Italian!). Nic and Garret, thank you for being such good friends I will always remember the

many chats, giggles, and coffees in between all the science. Thanks to all the project students; Lucy Bisset, James Smith, and Emma Lamden for their contributions.

A big thank you to all the past and present members of the Tucker group. Ed, Francia, Jake, Jack, Liyao, Yifeng and Aldrich thank you for your friendship and humour, it made our social gatherings that much more enjoyable. Klaudia, Georgina and Charlotte, what started as casual coffee breaks has flourished into a beautiful lifelong friendship. Thank you, girls, for being there through the happy and not-so-happy moments and being my very own cheerleaders.

Thank you to Professor Jo Morris and her lab group for their invaluable help and contribution that made this story more complete. Special thanks to Katherine Ellis for her expertise and countless hours spent teaching me fibres, a breakthrough moment for me and this project. A huge thanks to Professor Rob De Bruin and Dr Cosetta Bertoli and members of the group at UCL for welcoming me in their lab for all the preliminary fibre studies. I would also like to extend my gratitude to the National Cancer Institute, particularly Dr Mark Kunkel for his expert advice on the NCI-60 data.

A special thanks to Dr Tim Knowles for always making time for a chat, for his kind and honest advice and for the unpaid therapy sessions! You guided me through unsuccessful interviews and tricky situations, encouraging me to have trust in myself and for that I will always be grateful.

To all my friends from school, college and university, you know who you are, thank you for being the strong support I can always fall back on, I love you guys.

To my family, Mum, Dad, Amna Api, Aisha and Ahad bhai, thank you for being the strength I needed to accomplish this and being my biggest supporters. Special thanks to my mum who is my greatest inspiration and absolute hero, without whom none of this would be possible. I would have given up long ago if it wasn't for the strong determination and fighter spirit you instilled in all of us. You are the wind beneath my wings, I hope you are proud.

Table of Contents

CHAPTER 1 – INTRODUCTION.....	1
1.1 Introduction.....	1
1.2 Cancer biology	1
1.2.1 The cell cycle and cancer	3
1.2.2 DNA Replication	8
1.2.3 DNA damage	12
1.2.4 Checkpoint proteins.....	15
1.2.5 Cell death	18
1.3 Pancreatic Cancer	24
1.3.1 Pancreatic ductal adenocarcinoma (PDAC)	25
1.4 Drug screening	27
1.4.1 National Cancer Institute (NCI).....	27
1.4.2 COMPARE algorithm.....	28
1.5 Chemotherapy	29
1.5.1 Nucleoside analogues	30
1.5.2 Metallodrugs	34
1.5.3 Organometallic complexes	35
1.6 TUC-1	42
1.7 Project Aims	44
1.8 References	48
CHAPTER 2 – MATERIALS AND METHODS	57
2.1 Compound synthesis	57
2.2 Cell culture	57
2.3 Cell viability	59

2.3.1 Cell seeding	59
2.3.2 Drug exposure	59
2.3.3 MTT assay	63
2.3.4 Statistical analysis	63
2.4 Cell cycle analysis	66
2.4.1 Cell preparation and drug exposure	66
2.4.2 Sample processing and detection	66
2.4.3 Statistical analysis	67
2.5 Quantitation of apoptosis by Annexin V binding	68
2.5.1 Cell preparation and drug exposure	68
2.5.2 Sample processing and detection	68
2.5.3 Statistical analysis	69
2.6 UV-vis spectroscopy for DNA binding	70
2.7 Detection of gamma-H2AX	70
2.7.1 Flow cytometry	70
2.7.2 Confocal microscopy	73
2.8 DNA fibre fluorography	75
2.8.1 Cell preparation and drug exposure	75
2.8.2 Spreading DNA fibres	76
2.8.3 Immunostaining	76
2.8.4 Statistical analysis	77
2.9 Western blot analysis	78
2.9.1 Preparation of cell lysates and drug exposure	78
2.9.2 Electrophoresis using SDS-PAGE	78
2.9.3 Protein detection	79
2.9.4 Statistical analysis	79
2.10 Gene expression analysis	80
2.10.1 Sample preparation and drug exposure	80
2.10.2 PCR Array	80
2.10.3 Targeted qPCR	80
2.10.4 p53 Sequencing	83
2.10.5 Statistical analysis	85
2.11 References	86
 CHAPTER 3 – <i>IN VITRO</i> DRUG METABOLISM AND PHARMACOKINETIC STUDIES (DMPK) WITH TUC-1	 87
3.1 Introduction	87

3.2 Results	93
3.2.1 Log D _{7.4} and kinetic aqueous solubility	93
3.2.2 Blood-plasma ratio and plasma protein binding	94
3.2.3 TUC-1 stability	98
3.2.4 Metabolite identification	104
3.3 Discussion	106
3.4 Future work	112
3.5 References	114
4.1 Introduction.....	118
4.2 Results	122
4.2.1 TUC-1 Cytotoxicity.....	122
4.2.2 NCI-60 screen	127
4.2.3 Cell cycle inhibition	139
4.2.4 Cell death	142
4.3 Discussion	146
4.4 Future work	154
4.5 References	155
CHAPTER 5 – DNA REPLICATION DYNAMICS AND TRANSCRIPTOMIC RESPONSE TO TUC-1	159
5.1 Introduction.....	159
5.2 Results	162
5.2.1 DNA binding	162
5.2.2 DNA strand breaks	163
5.2.3 DNA fibre fluorography	167
5.2.4 Checkpoint activation	170
5.2.5 Gene expression analysis	172
5.3 Discussion	180
5.4 Future work	187
5.5 References	188

CHAPTER 6 – THE CYTOTOXICITY OF TUC-1 IS ENHANCED BY CHK KINASE INHIBITION	192
6.1 Introduction.....	192
6.2 Results	196
6.2.1 Synergy	196
6.2.2 Cell cycle arrest.....	199
6.2.3 Replication fork dynamics.....	203
6.2.4 DNA double strand breaks	207
6.2.5 Transcriptomic profile	212
6.3 Discussion	214
6.4 Future work	220
6.5 References	221
CHAPTER 7 – GENERAL DISCUSSION	226
7.1 Background	226
7.2 Summary and significance	227
7.2 References	232
CHAPTER 8 – APPENDICES.....	235
8.1 Supporting Information for Chapter 2	235
Supporting Information for Chapter 3	237
8.2 Supporting Information for Chapter 4	251
8.3 Supporting Information for Chapter 5	252
8.4 References	254

List of illustrations

Figure 1.1. Growth factor signalling.

Figure 1.2. The mammalian cell cycle.

Figure 1.3. Eukaryotic DNA replication.

Figure 1.4. Chemical structure of DNA synthesis inhibitors aphidicolin.

Figure 1.5. DNA analogues used as probes to monitor DNA replication.

Figure 1.6. DNA damage is induced by a range of different exogenous and endogenous sources.

Figure 1.7. Cell cycle checkpoints regulate progression through the cycle.

Figure 1.8. Different modes of cell death with distinct morphological outcomes.

(Created in BioRender.com)

Figure 1.9. Initiation of apoptosis.

Figure 1.10. Mechanism of ferroptosis.

Figure 1.11. Disease progression of pancreatic ductal adenocarcinoma (PDAC) and accompanying genetic mutations.

Figure 1.12. Chemical structures of nucleoside analogues (A) Gemcitabine, (B) 5-fluorouracil and (C) Capecitabine.

Figure 1.13. (A) Incorporation of thymidine nucleotide and (B) Gemcitabine by DNA polymerase during DNA synthesis.

Figure 1.14. Chemical structure of metallodrug cisplatin.

Figure 1.15. Chemical structure of titanocene dichloride.

Figure 1.16. Ferrocene moiety undergoes a redox reaction yielding a ferrocenium cation.

Figure 1.17. Chemical structure of anticancer drug (A) Tamoxifen and (B) its ferrocene derivative Ferrocifen.

Figure 1.18. Chemical structures of ferrocenyl-nucleobases.

Figure 1.19. Nucleosides and ferronucleosides.

Figure 1.20. Chemical structures of TUC-1 and derivatives.

Figure 2.1. Example concentration response curves of single agent and fixed potency combination treatment.

Figure 3.1. Calculated log D (pH 7.4) of TUC-1 compared to control compounds.

Figure 3.2. Blood-plasma ratio of (A) TUC-1 and (B) control compounds in human (male), mouse (male) and rat (male) models.

Figure 3.3. Plasma protein binding of TUC-1.

Figure 3.4. Blood stability of TUC-1 and control compounds propantheline and imidapril in human, mouse, and rat blood.

Figure 3.5. Half-life of TUC-1 and control compounds as assessed in cryopreserved hepatocytes from human (mixed gender), mouse (male) and rat (male).

Figure 3.6. Intrinsic clearance of TUC-1 and control compounds as assessed in cryopreserved hepatocytes from human (mixed gender), mouse (male) and rat (male).

Figure 4.1. Chemical structure of (A) OMe TUC-1, (B) NMe TUC-1, (C) TUC-1* and (D) Regioisomer 2-(S).

Figure 4.2. Concentration response curves for TUC-1 and its derivatives in PDAC cell lines.

Figure 4.3. Concentration response curves for TUC-1 and its derivatives in human osteosarcoma cell lines.

Figure 4.4. Concentration response curves for TUC-1, cisplatin and gemcitabine in MRC5 fibroblasts.

Figure 4.5. Mean graphs for TUC-1 showing GI_{50} , TGI and LC_{50} endpoints for each cell line in the NCI-60 panel.

Figure 4.6. Box and whisker plot showing GI_{50} distribution of TUC-1 compared to cisplatin and gemcitabine as determined by the NCI-60 evaluation.

Figure 4.7. Scatter graph showing GI_{50} value for each cell line following treatment with TUC-1, Cisplatin and Gemcitabine.

Figure 4.8. COMPARE analysis of TUC-1 showing similarity of pattern of activity in NCI-60 panel against compounds in the NCI database with the GI_{50} endpoint.

Figure 4.9. PRISM analysis of TUC-1 GI_{50} data identified compounds with a similar pattern of activity in the NCI-60 panel of cell lines.

Figure 4.10. PILOT analysis of compounds with suitable rigid structures identified in PRISM showing similar pattern of activity in NCI-60 panel and high correlation coefficient with TUC-1.

Figure 4.11. STRING network analysis of the top 25 genes identified in the COMPARE analysis of TUC-1 GI₅₀ data against microarray dataset provided by NCI/DTP.

Figure 4.12. Cell cycle distribution of MIA PaCa-2 cells after treatment with TUC-1.

Figure 4.13. Cell cycle distribution of PDAC cell lines MIA PaCa-2, BxPC3 and CFPAC-1 following treatment with TUC-1 and TUC-1*.

Figure 4.14. Concentration response curves for TUC-1 and Erastin in the presence or absence of ferrostatin-1.

Figure 4.15. TUC-1 induces apoptosis in MIA PaCa-2 cells.

Figure 5.1. UV absorption spectra of TUC-1 in the presence of calf-thymus DNA.

Figure 5.2. TUC-1 induced DNA single strand breaks in newly synthesised DNA.

Figure 5.3. TUC-1 induces DNA double strand breaks in genomic DNA of PDAC cell lines.

Figure 5.4. Representative images of MIA PaCa-2 cells exposed to TUC-1 and Etoposide following γ H2AX labelling.

Figure 5.5. TUC-1 inhibits DNA replication assessed at single molecule resolution by DNA fibre fluorography.

Figure 5.6. Western blotting for DNA damage response proteins including phosphorylated Chk kinases, H2AX and RPA following TUC-1 treatment in MIA PaCa-2 cells.

Figure 5.7. List of 39 genes related to DNA-repair that are statistically significantly upregulated in MIAPaCa2 cells following treatment with TUC-1.

Figure 5.8. List of genes upregulated in the qPCR array in CFPAC-1 and BxPC3.

Figure 5.9. TUC-1 induces a conserved transcriptional response in PDAC cell lines MIA PaCa-2, BxPC3 and CFPAC-1.

Figure 5.10. Gene expression changes following treatment with TUC-1 are independent of p53 status.

Figure 5.11. Relative gene expression analysis of p53 homologs, p63 and p73 in MIA PaCa-2, BxPC3, CFPAC-1, HCT116 p53^{+/+} and HCT116 p53^{-/-} cell lines.

Figure 6.1. Concentration response curve for AZD7762 in MIA PaCa-2 cells.

Figure 6.2. AZD7762 potentiates the activity of TUC-1 in MIA PaCa-2 cells.

Figure 6.3. TUC-1 combined with AZD7762 has a greater effect on the cell cycle than single treatment.

Figure 6.4. TUC-1-induced replication fork inhibition is enhanced by AZD7762.

Figure 6.5. Representative images of DNA fibres from MIA PaCa-2 cells exposed to TUC-1, AZD7762, TUC-1 in combination with AZD7762.

Figure 6.6. AZD7762 enhances the effect of TUC-1 on DNA double strand breaks.

Figure 6.7. Representative images of MIA PaCa-2 cells exposed to AZD7762, TUC-1 and TUC-1 in combination with AZD7762.

Figure 6.8. Representative images of MIA PaCa-2 cells exposed to AZD7762, TUC-1 and TUC-1 in combination with AZD7762 after 24-hour recovery.

Figure 6.9. AZD7762 suppresses the DDR transcriptional response induced by TUC-1.

Figure 7.1. TUC-1 stalls DNA replication in pancreatic ductal adenocarcinoma leading to DNA strand breaks and Chk1 mediated intra-S checkpoint response.

Figure S1. Experimental 96-well plate setup used for MTT cytotoxicity studies of compounds with typical concentration range 0-200 μ M.

Figure S2. Experimental 96-well plate setup used to investigate ferroptosis by of TUC-1 or Erastin (0-200 μ M) in the presence and absence of Ferrostatin-1 10 μ M.

Figure S3. Experimental 96-well plate setup used for TUC-1 (0-200 μ M) cotreatment with fixed concentrations of AZD7762.

Figure S4. Experimental 96-well plate setup used for TUC-1 and AZD7762 cotreatment at fixed IC₅₀ ratios.

Figure S5. p53 genotyping by sequencing in PDAC cell lines MIA PaCa-2, CFPAC-1 and BxPC3.

List of Tables

Table 2.1. Sequences of primers used for qPCR analysis of STRING clusters.

Table 2.2. Standard qPCR reaction mixture for genes of interest.

Table 2.3. PCR cycling program used for Brilliant III SYBR Green Master Mix.

Table 2.4. Sequences of primers used for p53 sequencing in PDAC cell lines.

Table 2.5. Reaction mixture for p53 sequencing.

Table 3.1. Clearance categories for compounds based on species specific intrinsic clearance by hepatocytes.

Table 3.2. Kinetic aqueous solubility of TUC-1 compared to control compounds.

Table 3.3. Fraction unbound and percentage bound (%) values of TUC-1 and control compounds verapamil and warfarin in human, mouse, and rat models.

Table 3.4. Half-life of TUC-1 in human, mouse, and rat blood compared to control compounds.

Table 3.5. Summary of the top three metabolites with tentative structures assigned, quantification is based on the mass spectrometric (MS) response.

Table 4.1. IC₅₀ values of TUC-1 and its derivatives expressed in µM in MIA PaCa-2, BxPC3 and CFPAC-1 cell lines.

Table 4.2. IC₅₀ values of TUC-1 and non-phosphorylatable analogues of TUC-1 expressed in µM in TK positive (HOS1) and TK negative (143B) osteosarcoma cell lines.

Table 4.3. Selectivity index of TUC-1, cisplatin, and gemcitabine for PDAC cell lines.

Table 4.4. Mean GI₅₀, TGI and LC₅₀ values obtained for TUC-1 in the NCI-60 panel compared to metalloidrug cisplatin and nucleoside analogue gemcitabine.

Table 4.5. Mean GI₅₀, TGI and LC₅₀ values obtained for TUC-1 in different tumour subtypes of the NCI-60 panel.

Table 4.6. List of cell lines in the NCI-60 panel least sensitive to gemcitabine (GI₅₀ 100 µM).

Table 4.7. List of cell lines in the NCI-60 panel least sensitive to TUC-1 (GI₅₀ 100 µM).

Table 4.8. COMPARE analysis using the standard agents GI₅₀ and TGI endpoints.

Table 6.1. Combinatory index calculated for different IC₅₀ combinations of TUC-1 and AZD7762 (Synergy: CI <1).

Table S1: *TP53* mutational status of cell lines identified as most sensitive to TUC-1 in the NCI-60 panel.

Table S2: List of all 53 genes with more than a 2-fold increase in expression in MIAPaCa2 cells treated with TUC-1 (10 µM, 24 hours) compared to untreated controls.

Abbreviations

2D – Two-dimensional

3D – Three-dimensional

BSA – Bovine serum albumin

CDK – Cyclin-dependent kinase

Cp – Cyclopentadiene

dCD – Deoxycytidine deaminase

DNA – Deoxyribose nucleic acid

dNTP – Deoxynucleoside triphosphates

DTP – Developmental therapeutics program

ER – Estrogen receptor

GF – Growth factor

gH2AX – gamma H2AX

HPV – Human papillomavirus

LC/MS – Liquid chromatography-mass spectrometry

MoA – Mechanism of action

MS – Mass spectrometry

MTT – 3-(4,5-Dimethylthiazol-2-yl)-2,5-Diphenyltetrazolium Bromide

NCI – National cancer institute

PCC – Pearson's correlation coefficient

PCR – Polymerase chain reaction

PD – Pharmacodynamic

PK – Pharmacokinetic

PPB – Plasma protein binding

qPCR – Quantitative polymerase chain reaction

Rb – Retinoblastoma

ROS – Reactive Oxygen Species

SAR – Structure-activity relationship

TNFR1 – Type 1 TNF receptor

UV – Ultraviolet

Chapter 1 – Introduction

1.1 Introduction

An increase in cancer incidence coupled with growing resistance to established chemotherapeutics such as gemcitabine and cisplatin has created a demand for new drug candidates. This is made more important by the poor selectivity and severe side effects of existing drugs including hepatotoxicity¹, cardiotoxicity², nephropathy³ etc. reducing drug efficacy. Therefore, it is important that new alternatives or emerging synergistic candidates, have comparable or better efficacy, minimise these side effects and, most importantly, display a different mode of action to avoid cross-resistance and be clinically relevant. TUC-1 is a novel organometallic ferronucleoside developed in our laboratory with anti-cancer activity first shown in gastrointestinal (GI) cancer cell lines⁴. The focus of this thesis is the investigation into the biological activity and mode of action of TUC-1 and derivatives evaluated in a panel of pancreatic ductal adenocarcinoma (PDAC) cell lines.

1.2 Cancer biology

Cancer is a group of diseases characterised by uncontrolled cell proliferation overcoming regulatory mechanisms that maintain normal growth as depicted in Figure 1.1. The main causes of cancer include hereditary or acquired genetic mutations, environmental exposure to carcinogenic chemicals or radiation, bacteria and viruses such as HPV and lifestyle choices such as alcohol consumption and tobacco smoking (Cancer Research UK).

Malignant cells can grow into a tumour mass compromising tissue architecture and impeding normal function. A subpopulation of these cells can exit the primary site entering the bloodstream to reach distant sites in the body, forming secondary tumours, a phenomenon known as metastasis. In almost all cases, the tumours evolve to become progressively dangerous as they become metastatic. It is reported that around 90% of all cancer deaths are caused by metastatic spread of the disease. In their seminal review, *"The hallmarks of cancer"*⁵, Hanahan and Weinberg propose eight key traits and two contributory characteristics found in all cancer cells distinguishing them from healthy cells. This characterisation is fundamental in the understanding of cancer biology, disease development and spread. These hallmarks include sustained growth factor signalling, evading tumour suppressor signalling, evading cell death, angiogenesis, epithelial-to-mesenchymal transition, deregulation of metabolism and escaping immune surveillance⁵.

Tumours can be categorised based on the cell type they originate from. The six main categories identified by the National Cancer Institute are:

1. Carcinoma: epithelial cells lining the surfaces of the body. There are two main types of carcinomas; Adenocarcinoma originating from secretory epithelial cells present in glands and organs and squamous cell carcinoma from squamous cells that line the respiratory tract, skin etc. This includes pancreatic ductal adenocarcinoma (PDAC) which is discussed in more detail in section 1.3.1.
2. Sarcoma: mesenchymal cells present in connective tissues
3. Lymphoma: lymphocytes in the lymphatic system
4. Leukaemia: blood cells particularly immature white blood cells

5. Myeloma: antibody producing plasma cells (B-cells)
6. Mixed: from cells of different origins

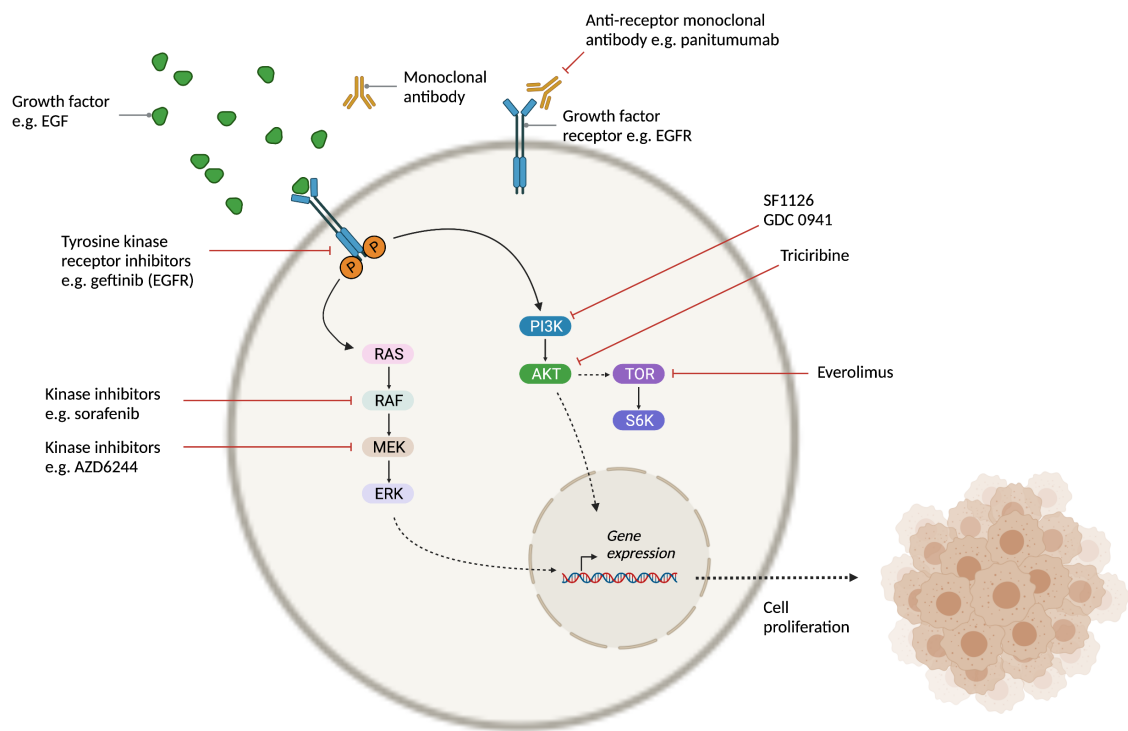


Figure 1.1. Growth factor ligands (e.g., Epidermal growth factor, EGF) binding to growth factor receptors (e.g., Epidermal growth factor receptor, EGFR) initiates signal transduction via intracellular receptor domain. Depicted here are important proliferative pathways Ras and PI3K leading to gene expression which dictates cell proliferation and survival. These pathways are regularly inhibited by different anticancer agents. (Created in BioRender.com)

1.2.1 The cell cycle and cancer

Once a mitogenic signal has been initiated by a growth factor, enabling progression past the restriction point of the cell cycle, the cell is committed to enter the S phase and DNA replication is initiated. The eukaryotic cell cycle can be divided into four distinct phases leading up to the formation of two identical daughter cells with the same and equal genetic material⁶ (Figure 1.2).

Each phase involves a series of key events that must be completed before progression to the next stage of the cycle. In the first gap phase (G1) the cell carries out the bulk biosynthesis of molecules and organelles while growing. This is followed by the synthesis phase (S) which is dominated by semi-conservative replication of DNA to produce two identical copies of chromosomes, one for each daughter cell. The centrosome is also duplicated for spindle formation in this phase⁶. The second gap phase (G2) involves cell growth in preparation for mitosis. The last phase of the cell cycle is the mitotic phase which is divided into four sub-phases that sequentially lead to successful cell division as detailed below⁶:

- i. Prophase: breakdown of nuclear envelope and nucleolus, chromosome condensation, formation of mitotic spindle between centrosomes and kinetochore binding to the chromosomes
- ii. Metaphase: chromosome alignment at the equator and assessment of kinetochore attachment by the spindle checkpoint
- iii. Anaphase: sister chromatids are separated to the opposite poles of the cell by the mitotic spindle and division of cytoplasm (cytokinesis) begins
- iv. Telophase: mitotic spindle breakdown, formation of nuclear envelope and nucleolus, chromosome decondensation and completion of cytokinesis

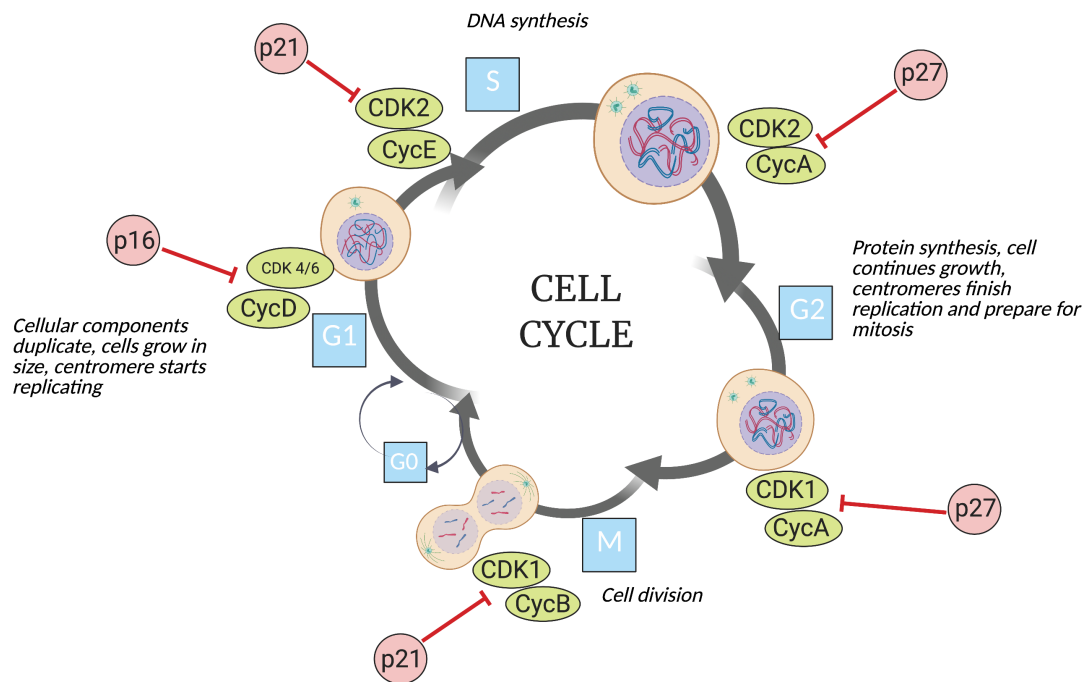


Figure 1.2. The mammalian cell cycle is divided into four distinct phases. Genetic material is duplicated in a process known as DNA synthesis (S-phase) before being divided into identical daughter cells (M-phase or mitosis). Two growth phases (G1 and G2) are placed between these two events enabling growth and allowing organelles to duplicate and reposition. Dormant cells can enter quiescence (G0) where they are not actively dividing but can resume cell cycle when stimulated. Entry into each phase of the cell cycle is governed by a group of kinases known as cyclin-dependent kinases (CDKs) and their binding partners cyclins. These are activated or inhibited by different proteins (shown in red) regulating progression through the cell cycle. (Created with BioRender.com)

Each phase of the cell cycle is tightly regulated by protein kinases and their substrates which together organise and control cell cycle progression. The two main family of proteins responsible are the cyclin dependent kinases (CDKs) and cyclins⁷ (Figure 1.2). CDKs are multifunctional kinases with different substrates, including cyclins with which they form complexes throughout the cell cycle^{8, 9}. While cyclin expression oscillates throughout the cell cycle with different cyclins expressed in different phases (Figure 1.2), CDKs are constitutively expressed but are inactive in the absence of the appropriate cyclin. Each cyclin binds a specific CDK phosphorylating multiple target proteins that coordinate reactions, such as faithful

DNA replication, and drive progression through the cell cycle⁷. The cyclins can be divided into four main groups:

- i. G1 cyclins: cyclin D binding CDK4, CDK6
- ii. G1/S cyclins: cyclin E binding CDK2
- iii. S cyclins: cyclin A binding CDK1, CDK2
- iv. M cyclins: cyclin B binding CDK1

A detailed discussion of cyclins and control of the cell cycle is beyond the scope of this thesis and the interested reader is referred to review article "*The cell cycle: a review of regulation, deregulation and therapeutic targets in cancer*" by Vermeulin *et al.* (2003). Aspects most relevant to the role of cell cycle in cancer are discussed below.

Synthesis of cyclin D subtypes is initiated by growth factor signalling which promotes phosphorylation of Rb alleviating negative regulation on transcription factor E2F promoting expression of G1/S and S cyclins. This leads to the completion of G1 and entry into S phase, at which point G1 cyclins are degraded, deactivating the active kinase complex. As hyperproliferation is one of the hallmarks of cancer, investigation into the role of cyclins and CDKs in this context revealed upregulation of cyclins, particularly cyclin D. Cyclin D is found to be upregulated in breast, oesophageal, gastrointestinal and bladder cancers¹⁰⁻¹³. In addition to this, mutations, or inactivating phosphorylation of Rb has been shown to contribute to tumorigenesis. Though this contrasts with some studies suggesting the importance of functional Rb required to exit the cell cycle, a key event for tumour progression¹⁴. In addition to the expression

of cyclins, selective phosphorylation and dephosphorylation of CDKs is required for complete kinase activity, dependent on CDK-activating kinases (CAKs) and phosphatases.

Another group of proteins called CDK inhibitors (CKIs) are responsible for regulation of CDK-cyclin complexes. CKIs are divided into two families based on structural similarity and catalytic activity: INK4 and Cip/Kip inhibitors. INK4 proteins such as p15, p16, p18 and p19 selectively inhibit CDK4 and CDK6¹⁵. These mainly induce cell cycle arrest in the G1 phase after the restriction point is surpassed. Particularly, p16 (*CDKN2A*) is a tumour suppressor protein frequently mutated in a range of different cancers such as lymphomas and sarcomas. *CDKN2A* is also frequently mutated in pancreatic ductal adenocarcinoma (PDAC) cell lines and is identified as a driver in PDAC development, discussed in more detail in section 1.3. Loss of p16 function occurs in early stage tumorigenesis, gene deletion detected in precursor lesions¹⁶. The Cip/Kip family of proteins include p21, p57 and p27, sharing sequence homology, all potent inhibitors of G1/S and S CDK-cyclin complexes inducing late G1 or S phase arrest¹⁷. The inhibitor p21 has been shown to respond to different stress stimuli including DNA damage, chemotherapeutic drugs, oxidative stress etc., inhibiting CDK2 and proliferating cell nuclear antigen (PCNA) leading to cell cycle arrest, reportedly p53 dependent¹⁸. It is commonly downregulated in different cancer cells though paradoxically the protein can function as an oncogene promoting G1 progression¹⁸.

1.2.2 DNA Replication

DNA replication is the biological process in which genomic DNA is duplicated during S phase of the cell cycle to create two copies to be split into two identical daughter cells, using the two complementary strands as template for semi-conservative replication as proposed by Watson and Crick¹⁹⁻²¹. DNA replication occurs every time the cell goes through the cell cycle to ensure the daughter cells are genetically identical. This process relies on the assembly of key replication proteins (Figure 1.3) at the origin of replication to initiate DNA synthesis²².

DNA synthesis occurs in three distinct stages, the first stage being the separation of the complementary DNA strands at the origin of replication by initiator proteins followed by helicase activity. DNA helicases, identified as mini-chromosome maintenance (MCM) proteins that, in complex with Cdc45 and GINS, break the hydrogen bonds between complementary base pairs²³. This exposes the groups that take part in hydrogen bonding to the incoming nucleotide monomers enabling correct alignment before incorporation into the newly synthesised DNA strand by DNA polymerases²⁴. Several origins are fired at the same time with some parts of the genome replicated at different times depending on the stage of the cell cycle²². Once DNA is unwound, priming enzymes, called primases, are recruited to synthesise an RNA primer needed for replication initiation as DNA polymerases are unable to catalyse *de novo* synthesis²⁴. The final stage of elongation is carried out by the multiple isoforms of DNA polymerase, each with a different functionality. While DNA polymerase ϵ carries out leading strand synthesis, Pol α primes the Okazaki fragments for elongation by Pol δ ^{25, 26}. The progression of the replication fork is

assisted by other replicative proteins including topoisomerases I and II, relieving tension on the DNA molecule ahead of the replication fork by creating transient strand breaks²⁴. Together, this multiprotein complex forms a structure called a replication fork (Figure 1.3), each fork moving in the opposite direction at any one origin.

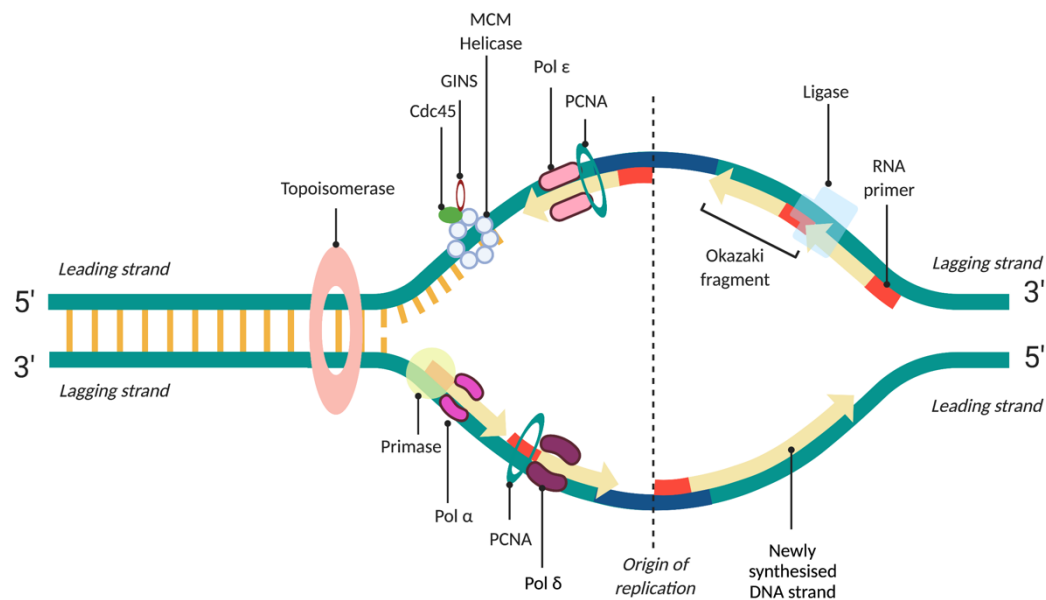


Figure 1.3. Eukaryotic DNA replication. Two bidirectional replication forks moving in the opposite direction with Pol ϵ and Pol δ carrying out replication on the leading and lagging strand respectively as Pol α initiates replication at the RNA-DNA hybrid site. In addition to polymerases, other replicative factors including topoisomerase, helicase, ligase, primase, and proliferating cell nuclear antigen (PCNA) also ensure a successful and faithful replication. (Created with BioRender.com)

Inhibition of enzymes involved in DNA replication has been explored as a potential molecular target for drugs such as Aphidicolin, an inhibitor of Pol δ and Pol α ²⁷ (Figure 1.4). Furthermore, nucleoside analogues (discussed in more detail in section 1.4.1) such as gemcitabine inhibit the process of replication through incorporation of its tri-phosphorylated form into DNA causing masked chain termination²⁸.

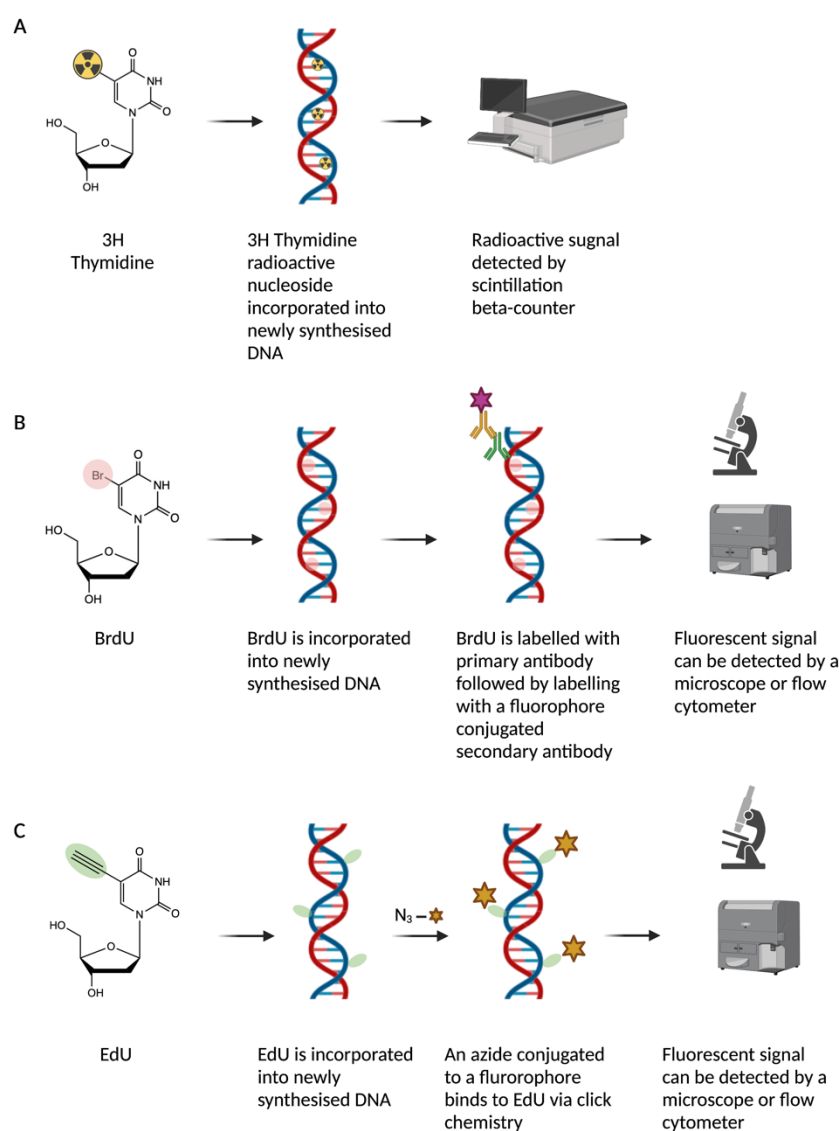


Figure 1.5. DNA analogues used as probes to monitor DNA replication. These base analogues can have a radioactive label (A), a halogen atom (B) or an alkyne group (C) that are detected via different instrumentation depending on the output after incorporation into replicating DNA. (Created with BioRender.com)

Although these analogues are accurate in their detection of any effect the drug might have on replication, the read-out is limited to the global average effect which can mask any small local differences such as the heterogeneous nature of replication forks³¹. Therefore, to study the direct effect on replication, DNA fibre fluorography is performed in this work (Chapter 5) to study replication forks at single molecule resolution³².

1.2.3 DNA damage

The term DNA damage encompasses a range of chemical modifications to DNA that can occur spontaneously from intrinsic sources such as free radicals formed as a by-product of metabolism, or this damage could arise from extrinsic sources such as irradiation and chemotherapeutics (Figure 1.6). Some common modifications include base adducts, base insertions or deletions, abasic sites, base mismatch, interstrand crosslinks, thymidine dimers, single- and double-strand breaks (SSB and DSBs)^{22, 33}. These pose a threat to genome integrity as faithful DNA replication is threatened and, if irreparable, induces cell death.

Cancer chemotherapeutics such as cisplatin commonly target genomic DNA to induce lesions such as intrastrand crosslinks³⁴ which, accompanied by other cellular effects, lead to genome instability inducing cell death which is discussed in section 1.2.5. DNA strand breaks where the phosphate-sugar backbone is broken are the most cytotoxic type of damage. DSBs can be caused by the direct action of radiomimetics and ionising radiation through free radicals³⁵. Alternatively, stalled-replication forks induced by replication inhibiting drugs such as camptothecin and nucleoside analogues also lead to the formation of DSBs^{36, 37}. As well as cytotoxicity, DSBs can also result in chromosomal damage (aneuploidy) that, if left unrepaired, can lead to abnormalities such as chromosomal structural rearrangements including fusions and translocations, a major contributory factor in early carcinogenesis³⁸. However, once detected, and left unrepaired, they trigger for cell death by initiation of apoptosis which is reportedly p53 dependent³⁹. Stalled replication forks can lead to SSBs as the fork collapses, a strong signal for checkpoint activation for repair,

assembling the 9-1-1 complex of Rad9, Rad1 and Hus1⁴⁰ (Figure 1.6). However, these SSBs can also spontaneously be converted to DSBs if there are two or more SSBs in close proximity³⁸⁻⁴⁰ during replication in the S-phase. In normal non-transformed human cells during S-phase, 1% of the total SSBs are converted to approx. 50 DSBs⁴⁰. There are many different methods that can be used to detect DNA strand breaks for example polymerase chain reaction (PCR), gel electrophoresis, Comet assay, γ H2AX biomarker etc⁴¹.

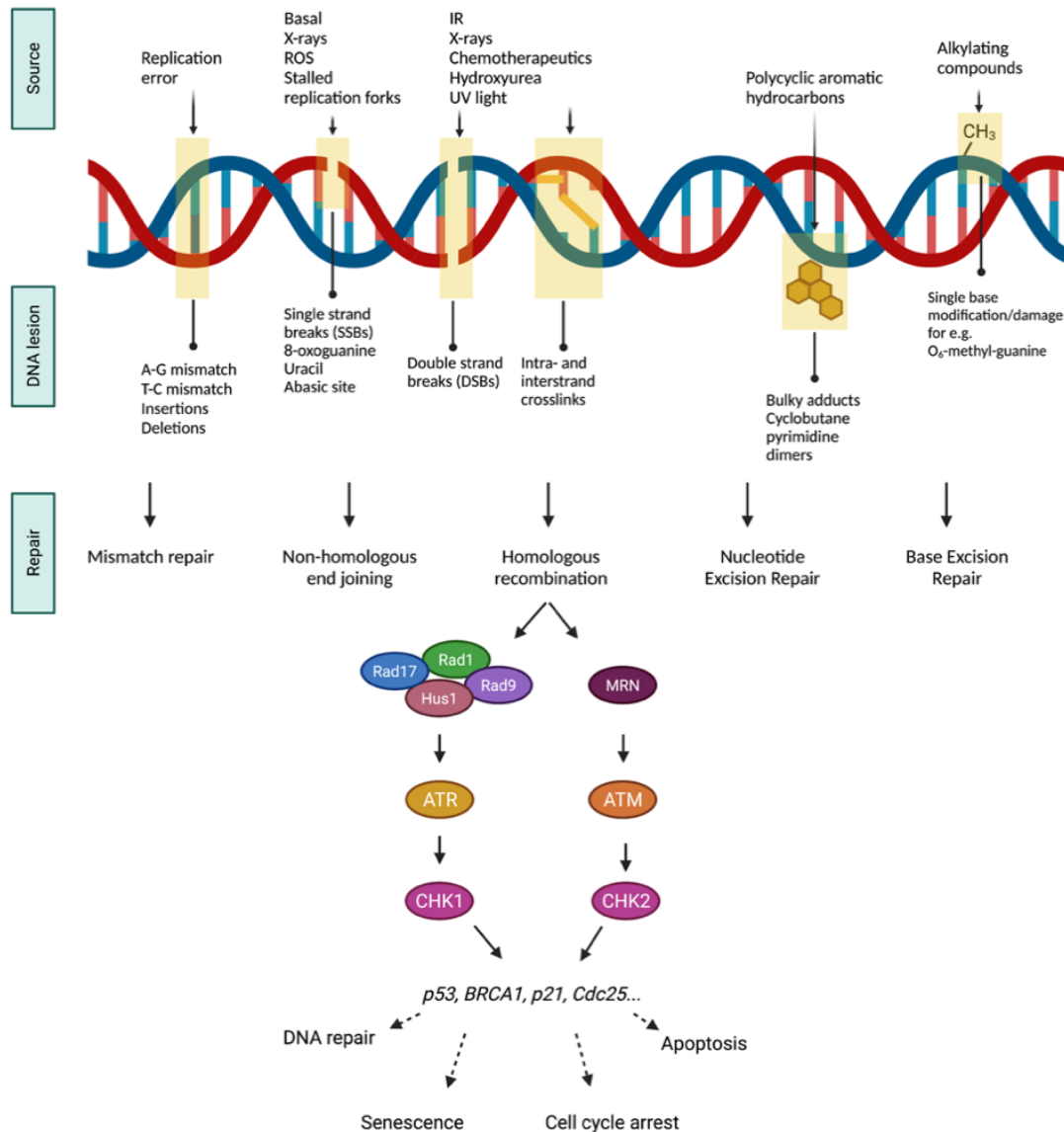


Figure 1.6. DNA damage is induced by a range of different exogenous and endogenous sources. The type of lesion is dependent on the damaging agent with some lesions, for example DNA strand breaks, posing a greater threat to genome integrity and cell survival than others. The repair pathways activated by DNA lesions are also shown with an emphasis on homologous recombination and the protein cascade that follows when DNA strand breaks are detected. (Created with BioRender.com)

1.2.4 Checkpoint proteins

DNA in eukaryotic cells is under constant surveillance for intrinsic and extrinsic DNA damage that, if detected, can trigger a range of adaptive responses including cell cycle arrest, transcriptional activation of repair proteins or, in some cases, apoptosis⁴². Throughout the cell cycle there are checkpoints that monitor the state of cell and control progression into the next stage of the cell cycle (Figure 1.7).

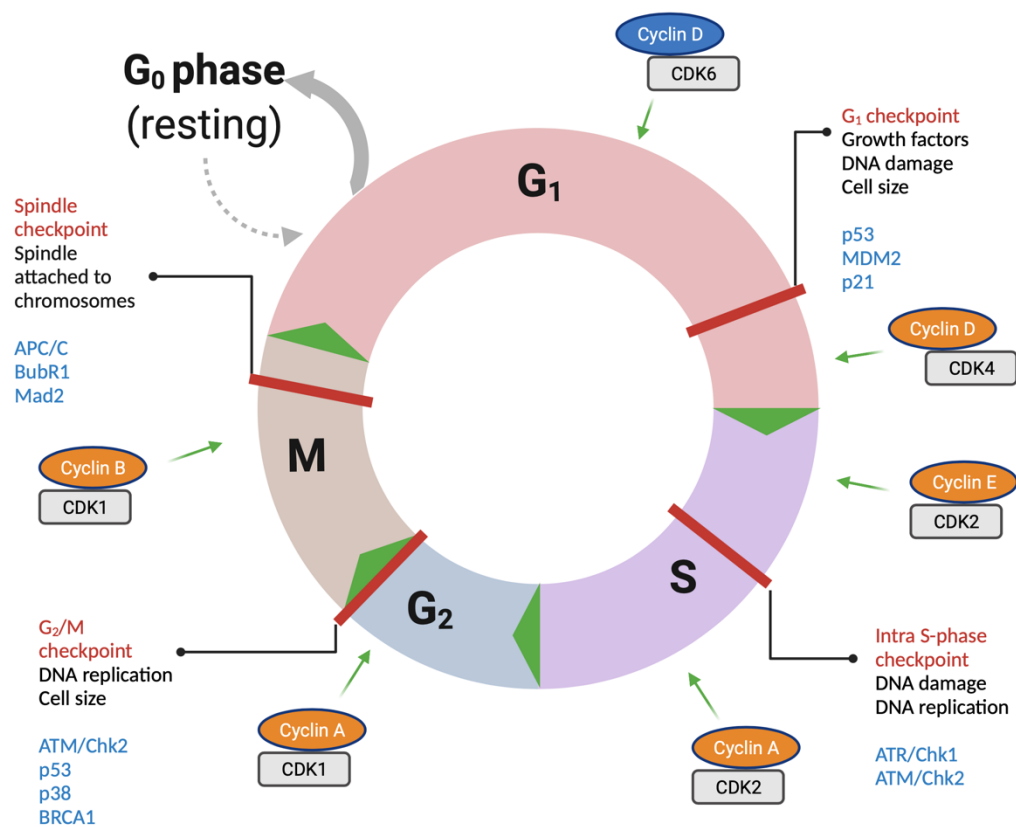


Figure 1.7. Cell cycle checkpoints regulate progression through the cycle. As cells undergo the cycle driven by cyclin-CDK complexes (orange and grey), they are monitored by the G₁, Intra-S, G₂/M and spindle checkpoints that ensure key processes are completed before allowing progression. Upon detection of any abnormality such as DNA damage, a signalling cascade is activated involving various proteins (blue) leading to cell cycle arrest. Checkpoint control is necessary for faithful, error-free DNA replication and division into two identical daughter cells. (Created with BioRender.com)

The four major checkpoints of the cell cycle occur at G1/S, Intra-S, G2/M and Anaphase⁴². Apart from the anaphase (spindle) checkpoint, they are all DNA damage checkpoints that, once activated, can lead to inhibition of replication initiation, elongation, or chromosome condensation. However, the response generated differs depending on the stage of the cell cycle and the type of checkpoint activated⁴³.

The G1 checkpoint can be activated by DNA damage, insufficient cell size or growth factors. The consequent ATM/Chk2 signalling leads to the activation of the p53/MDM2, p21 pathway as p53 is phosphorylated by ATM/ATR kinases⁴⁴. The negative regulation of p53 exerted by MDM2 ubiquitin ligase is also alleviated by these kinases leading to p53 sequestration in the nucleus and activation of targets such as the cyclin dependent kinase inhibitor p21. Inhibition of CDK2 complexes by p21 and maintenance of phosphorylated Rb (retinoblastoma) leads to G1 arrest. ATR and Chk1 expression is high in late G1 regulating the activity of cell division cycle 25 phosphatase (Cdc25), driver of G1 to S transition by activating cyclin E/CDK2 complex⁴⁴.

The S-phase checkpoint surveys the genome for DNA damage and replication errors which activates the ATM/ATR signalling cascade to inhibit origin firing, initiation of DNA replication and protecting stalled replication forks. These outcomes are implemented by different pathways including CDK2 inhibition which prevents Cdc45 assisted loading of DNA polymerase α to the replication machinery⁴⁴. Additionally, other targets of ATM and ATR kinases such as CDC7 and NBS1 have also been

identified as important downstream players in S phase arrest however the exact mechanism by which this is achieved remains elusive⁴⁴.

The G2/M checkpoint provides extra surveillance for lesions left unrepaired from S phase with CDK1 kinase being the major target⁴⁴. Activator of CDK1, Cdc25 phosphatase, is also targeted by p38 kinase leading to G2 arrest. Polo-like kinases (PLK), serine-threonine kinases regulating mitotic entry, are also implicated in the effector pathway⁴⁴. Furthermore, p53 and BRCA1 activation leads to upregulation of key effector proteins including GADD45a, p21 and 14-3-3 σ ⁴⁴. The spindle checkpoint primarily delays anaphase and segregation of chromosomes if they are not correctly aligned or attached to the spindle microtubule. The target for this checkpoint is the anaphase-promoting complex or cyclosome (APC/C) which promotes chromosome segregation⁴⁵. This is kept inactive by different proteins forming a complex with APC/C including Mad2, BubR1 and Bub3⁴⁵.

With the exception of spindle checkpoint, all checkpoints are reliant on ATM, ATR and Chk kinases that are activated by one of the many networks of DNA damage response (DDR). The first responders to DNA damage is the 9-1-1 clamp comprising of Rad9, Rad1 and Hus1 in addition to the clamp loader Rad17⁴⁶. This complex recruits protein kinases ATM and ATR for DSBs and SSBs respectively though the loading complex for ATM is different to the 9-1-1 complex observed on DSBs (Figure 1.6).

Although activation of these effector pathways leading to cell cycle arrest among other outcomes are largely p53-dependent, recent research has identified p53-independent pathways that provide an alternative route to activating downstream p53 targets. There is evidence of p53 independent initiation of apoptosis through other compensatory pathways in p53 mutant cells including activation of JNK kinase pathway⁴⁷, overexpression of pro-apoptotic factors such as BAK⁴⁸ or suppression of anti-apoptotic factors such as Bcl-2⁴⁹.

1.2.5 Cell death

Cell growth and cell death work in tandem to maintain tissue homeostasis. Regulated cell death ensures old or damaged cells resulting from trauma or disease, unable to carry out their biological function, are removed. Cell death can be classified into many different categories with the different modes displaying distinct molecular pathways of activation, responding to different environmental cues, and characterised by specific morphological changes (Figure 1.8).

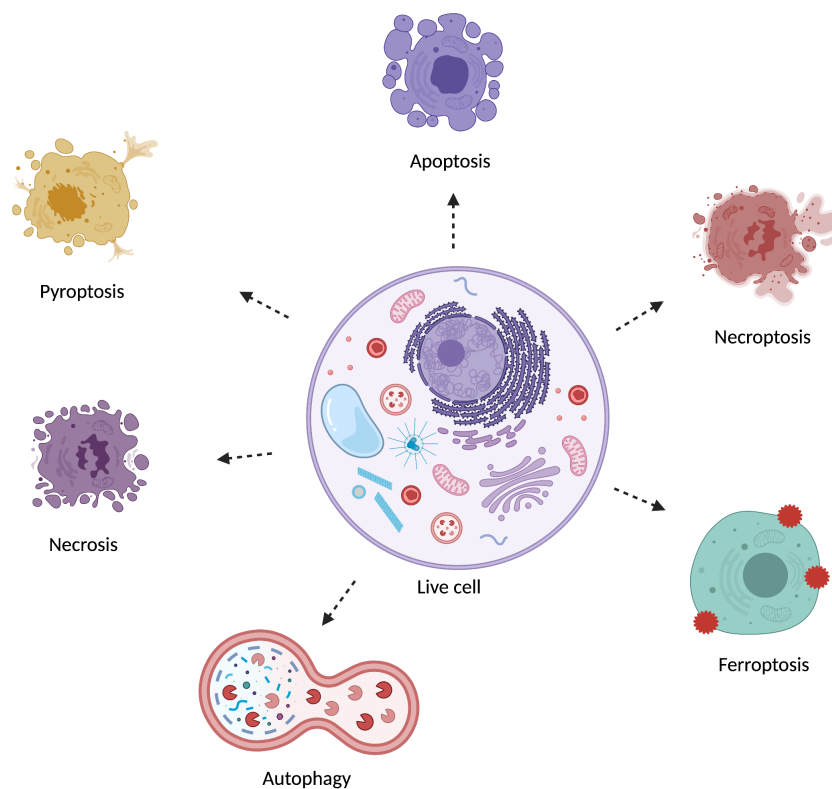


Figure 1.8. Different modes of cell death with distinct morphological outcomes. (Created in BioRender.com)

The most common mode of regulated cell death triggered by anti-cancer agents, including metallodrugs and nucleoside analogues, is apoptosis. Apoptosis, activated extrinsically or intrinsically, can be identified by morphological changes and biochemical processes unique to this mode of cell death. Three chief biochemical processes ultimately leading to cell death are membrane asymmetry, DNA fragmentation and activation of caspases, accompanied by morphological changes⁵⁰. Both extrinsic and intrinsic pathways converge when aspartate-specific cysteine proteases called caspases are activated serving as major effectors of apoptosis.

Caspases exist in their inactive form called pro-caspases that, upon necessary stimulus, are activated via cleavage between subunits and oligomerisation.

Caspases are divided into two categories based on functionalities: initiator and

executioner caspases. Initiator caspases 2, 8, 9 and 10 are largely responsible for cleavage and activation of executioner caspases that carry out degradation of cellular components such as nuclear proteins and the cytoskeleton, leading to cell death⁵¹. Apoptosis can be activated extrinsically when ligands bind death receptors such as Fas or TNFR1 receptors on cell membranes, leading to a signalling cascade as intracellular domains of receptors recruit adaptor proteins (Figure 1.9). The activated receptor complex is called the death-inducing signalling complex (DISC) activating caspase 8/10 protease which cleaves and activates of executioner caspases^{52, 53}.

Alternatively, some stimuli such as high intracellular Ca^{2+} concentration, DNA damage and oxidative stress can intrinsically activate apoptosis leading to mitochondrial membrane permeabilization via activation of pro-apoptotic BAX and BAK proteins. This allows release of proteins such as cytochrome c which, in complex with caspase 9 and Apaf-1, forms the apoptosome leading to activation of caspase 3/7 (Figure 1.9). Caspase activation is also promoted by other proteins including Smac/DIABLO and HtrA2/Omi that inhibit the XIAP, inhibitor of apoptosis⁵⁴.⁵⁵ Another less characterised mode of activation is through the endoplasmic reticulum which relies on the activity of caspase-12 activated by TNF receptor associated factor 2 (TRAF2) upon inhibition of protein synthesis⁵⁰. The main cellular phenotypes that manifest upon activation of apoptosis include pyknosis (chromatin condensation), DNA fragmentation, phosphatidylserine externalisation, nuclear condensation, activation of caspases and ROS production. These phenotypic changes remain unchanged in different cell types although there maybe differences in the stimuli, signal transduction and time taken to complete apoptosis⁵⁰.

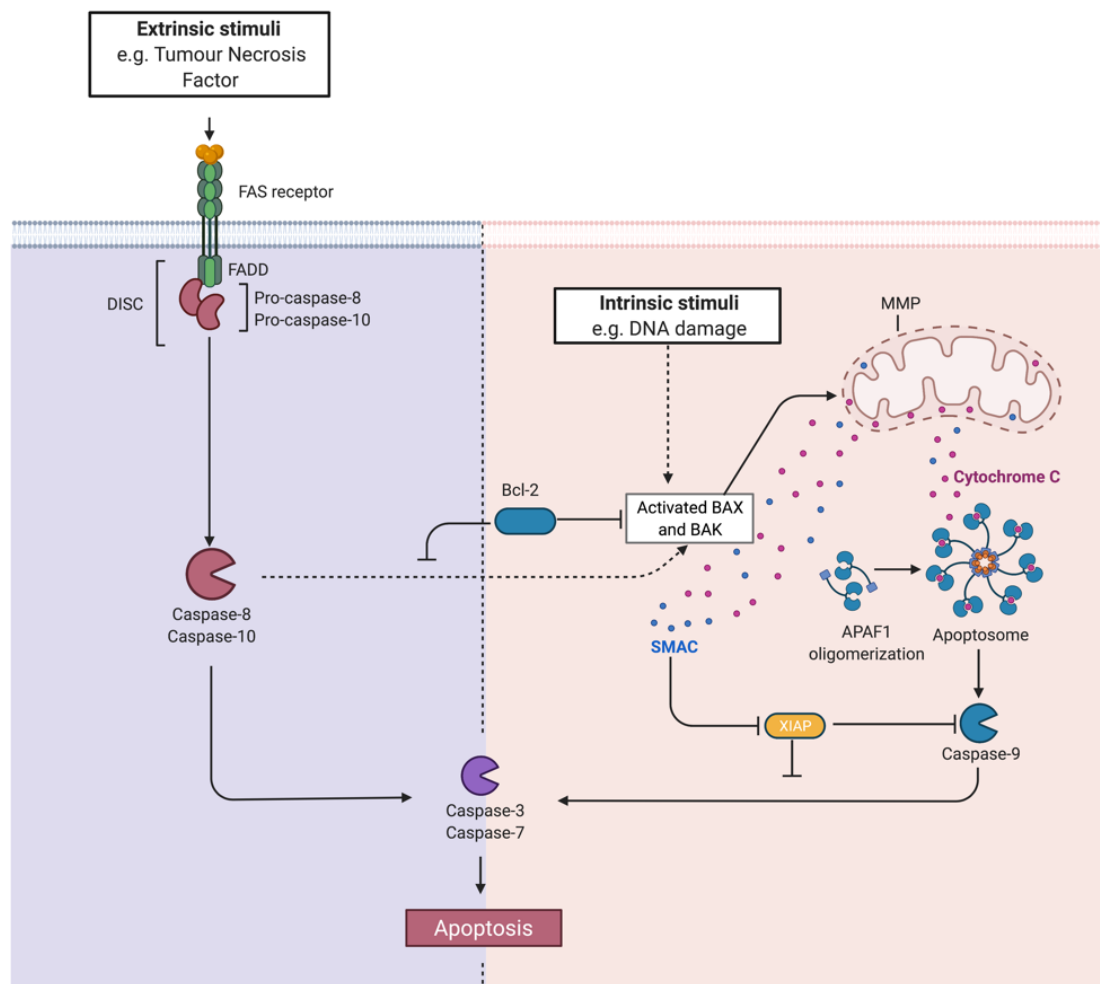


Figure 1.9. Initiation of apoptosis. Apoptosis can be triggered by different stimuli that lead to activation of the extrinsic pathway (left) or intrinsic pathway (right). Extrinsic pathway is activated by various extracellular stimuli including cytokines, such as tumour necrosis factor, which promotes ligand binding to one of the death receptors, e.g. Fas receptors, leading to assembly of the death-inducing signalling complex (DISC) which includes initiator caspases 8, 10. Intrinsic pathway is initiated by intracellular stress such as DNA damage that activates pro-apoptotic BAK and BAX proteins, subject to inhibition by anti-apoptotic Bcl-2 family of proteins. This leads to mitochondrial membrane permeabilization (MMP) and release of cytochrome c that, in complex with APAF1 and Caspase-9, form the apoptosome. The Smac/DIABLO protein promotes apoptosis by inhibiting XIAP, relieving negative regulation of Caspase-9. Both pathways converge at the cleavage of effector caspases 3 and 7 that ultimately lead to apoptosis. (Created in BioRender.com)

Evasion of apoptosis has been identified as one of the hallmarks of cancer enabling survival and hyperproliferation leading to carcinogenesis. In many cancer types, including pancreatic cancer, this is achieved through overexpression of inhibitors of apoptosis XIAP, Survivin and Bcl-2 family of proteins. This is accompanied by inhibition of pro-apoptotic proteins such as BAK and BAX, the latter reported to be regulated by p53. Thus, anticancer agents are designed to target anti-apoptotic Bcl-2

proteins among other inhibitors of apoptosis or stimulate pro-apoptotic family of proteins⁵⁶. In addition to platinum-based metallodrugs, anticancer nucleoside analogue gemcitabine has been shown to induce apoptosis as evident through presentation of DNA fragmentation and apoptotic bodies, triggered by DNA synthesis inhibition⁵⁷. Apoptosis is also initiated post DNA damage, mediated by transcription factors downstream ATM and DNA-PK including p53, E2F-1, p73, c-Abl etc. leading to transcriptional activation of BAK and BAX⁵⁸. Therefore, assessing the expression levels of these apoptotic factors can provide evidence of the mode of cell death activated upon treatment with an anticancer agent. Additionally, translocation of phospholipid phosphatidylserine (PS) from the inner to the outer leaflet of the cell membrane occurs during early apoptosis leading to membrane asymmetry, therefore serves as a key biomarker of apoptosis. This can be detected by lipid binding protein Annexin V conjugated to a highly fluorescent fluorophore detected by flow cytometry⁵⁹.

Recently, an emerging mode of cell death triggered by intracellular accumulation of Fe(II) called ferroptosis has been identified. Proposed by Dixon in 2012, it is characterised by depletion of the cysteine amino acid pool and/or inhibition of glutathione peroxidase GPX4⁶⁰. It is reported to be triggered when Fe(II) species catalyse Fenton's reaction and produce ROS, indispensable in this process, leading to excessive lipid peroxidation membrane lipids with polyunsaturated fatty acid chains⁶¹(Figure 1.10). Ferrocene, which contains Fe(II), has been shown to undergo a similar reaction catalysing the production of ROS and yielding a ferrocenium ion⁶² (Fe(III) oxidation state), therefore also potentially driving ferroptosis in cancer cells.

Cells undergoing ferroptosis also display unique morphological changes including shrinking mitochondria and depletion of inner membrane cristae, phenotypes not observed with other modes of cell death⁶³.

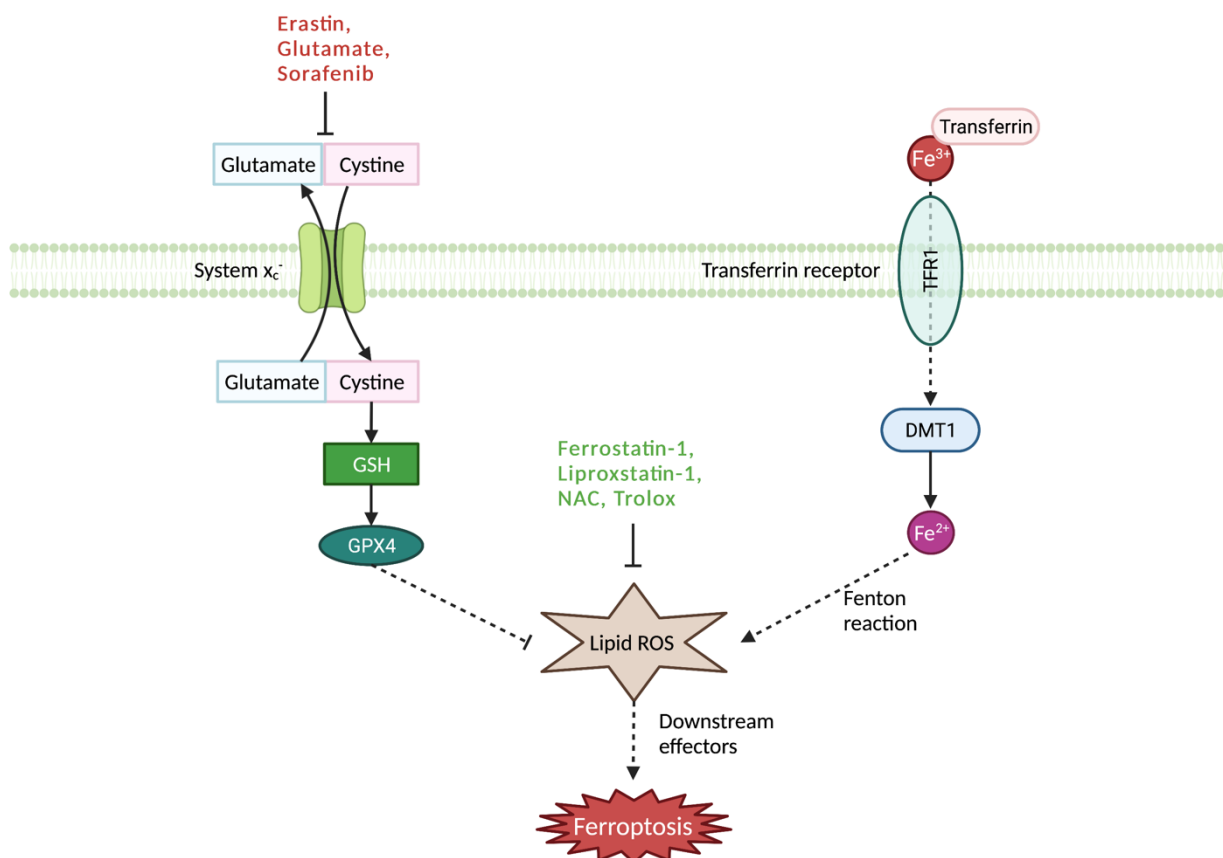


Figure 1.10. Mechanism of ferroptosis. Iron (III) bound to transferrin is transported in through transferrin receptor TFR1, reduced to Fe^{2+} in endosomes and released in the cytosol by divalent metal transporter (DMT1). Excessive Fe^{2+} catalyses Fenton's reaction generating ROS which leads to lipid peroxidation and ferroptosis via downstream effectors. Inhibition of the x_c^- antiporter, mediating the intracellular transport of cystine, also induces ferroptosis by depletion of glutathione (GSH). This results in reduced antioxidant activity of glutathione peroxidase (GPX4), leading to enhanced lipid peroxidation. Inducers (red) and inhibitors (green) of ferroptosis are also shown. (Created in BioRender.com)

As cancer cells exhibit high basal level of ROS evading ferroptotic cell death, ferroptosis can be viewed as tumour suppressive, preventing carcinogenesis. This is supported by evidence suggesting regulation of ferroptosis by tumour suppressor p53 as the protein lacking acetylation function, TP53^{3KR} induced ferroptosis but no

other modes of regulated cell death⁶⁴. Additionally, proteins involved in iron transport including divalent metal transporter 1 (DMT1), transferrin receptor 1 (TFR1), transferrin (TF), ferroportin, ferritin heavy and light chain are suggested to regulate this process⁶⁴. Ferroptosis-inducing agents such as Erastin⁶¹ trigger ferroptosis inhibiting the glutathione (GSH) antioxidant system of the cell. This is achieved when the xc⁻ antiporter system is inhibited, reducing the cysteine pool needed for GSH synthesis⁶¹. Interestingly, cells mutant for oncogenic *Ras* are more sensitive to Erastin, implicating the *Ras* signalling cascade in regulating ferroptosis.

The mechanism downstream of lipid peroxidation remains elusive, however it is proposed that continued lipid peroxidation has a detrimental effect on membrane structure and fluidity which can lead to permeabilisation⁶¹. This, coupled with GSH inhibition and elevation of intracellular ROS, induce cell death⁶¹. Anticancer agent sorafenib, used to treat liver and thyroid cancer, is the first FDA approved drug that has been shown to trigger ferroptosis. This is achieved by blocking the xc⁻ antiporter therefore inhibiting glutathione (GSH) synthesis⁶⁵. Recent studies also shown that cisplatin can also induce ferroptosis by depletion of the GSH pool and inhibition of GPX4 in HCT116 and A549 cell lines⁶⁶.

1.3 Pancreatic Cancer

Pancreatic cancer is the 10th most common type of cancer with approximately 10,000 people diagnosed each year in the UK (Pancreatic Cancer UK). The 10-year survival rate for pancreatic cancer is only 1%, unchanged since 1970s, with the incident rate expected to increase by almost two-fold in the future⁶⁷. The risk factors associated

with the disease include diabetes, pancreatitis, age, tobacco, family history, germline mutations among many others⁶⁷. Of the exocrine carcinomas, pancreatoblastoma and acinar cell carcinoma are the two major types. The histopathological precursor lesion to adenocarcinomas has been identified as pancreatic intraepithelial neoplasia (PanIN) that can be clinically detected⁶⁸. Other minor lesions include mucinous cystic neoplasm and intraductal papillary mucinous neoplasm.

1.3.1 Pancreatic ductal adenocarcinoma (PDAC)

Pancreatic ductal adenocarcinoma (PDAC) accounts for 95% of all pancreatic cancer cases, projected to become the second leading cause of cancer deaths by 2030. It is an exocrine tumour that arises from cells lining the pancreatic duct, commonly originating from the head of pancreas (Pancreatic Cancer UK). Initiation of the disease occurs as acinar cells adopt a ductal-like phenotype, upon environmental stimuli, in a process of acinar-to-ductal metaplasia (Figure 1.11). This is accompanied by mutations in key genes such as *KRAS*, *CDKN2A*, *SMAD4* and *TP53* that contribute to disease progression, detected in almost 50% of all PDAC cases. More recently, mutations in other genes such as *RBM10*, *BCORL1*, *KDM6A*, *ARID1A*, *MLL3* and *TGFBR2* have been detected in a subset of patients⁶⁹.

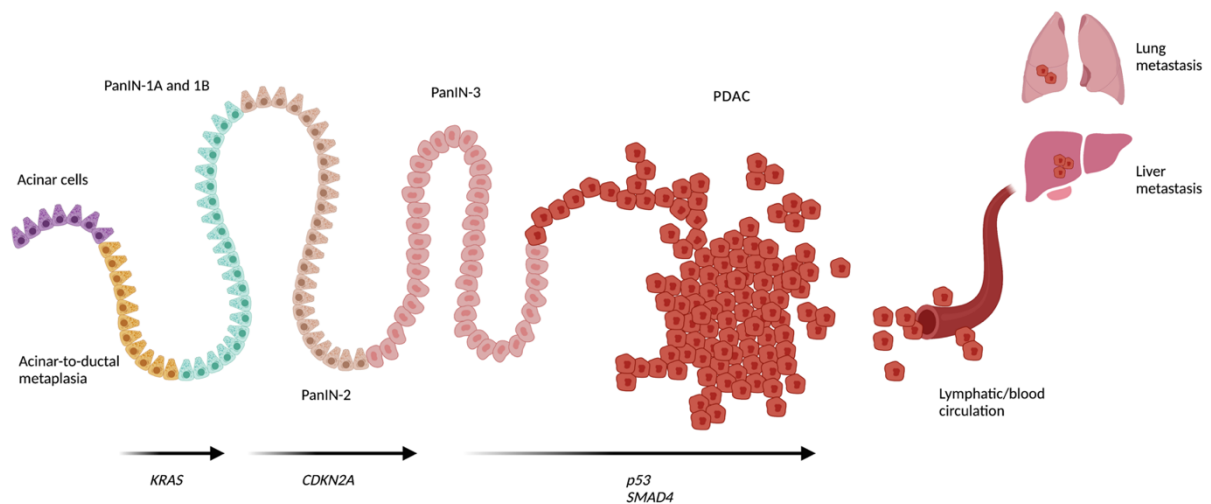


Figure 1.11. Disease progression of pancreatic ductal adenocarcinoma (PDAC) and accompanying genetic mutations. Acinary-to-ductal metaplasia is identified as an early event transforming into pancreatic intraepithelial neoplasia (PanIN), precursor to PDAC. Oncogene *KRAS* alongside tumour suppressors *CDKN2A*, *TP53* and *SMAD4* are frequently mutated in PDAC, driving disease development. (Created in BioRender.com)

PDAC is characterised by a long period of latency, lack of distinguishable symptoms followed by aggressive metastasis predominantly in the liver, contributing to the late diagnosis and poor prognosis. Due to the rapid spread of the disease, only 10% of those diagnosed qualify for resection while majority of the patients present metastatic or locally advanced tumours hence rely on chemotherapy as their primary treatment plan. There have been efforts to divide PDAC into distinguishable subsets based on the molecular characterisation of the tumour which can guide treatment. One of the proposed subsets is division based on genetic abnormalities as the tumours can be identified to have stable, unstable, locally rearranged, or scattered genome.

Additionally, with the rise of transcriptomic profiling, tumours can be classified based on their mRNA expression profile with the cells identified as quasi-mesenchymal,

squamous or basal-like. These efforts to identify molecular markers in PDAC patients can be crucial in devising personalised treatment. While nucleoside analogues such as gemcitabine are the preferred first-line treatment for PDAC, emerging cellular resistance limits their clinical benefit⁷⁰. Over the past few years, alternative surgical and treatment options like neoadjuvant therapies have been introduced albeit with limited clinical success⁶⁹.

1.4 Drug screening

Most drug candidates fail to perform at a satisfactory level in clinical trials. This high attrition rate makes preclinical studies useful tools to assess drug activity and predict clinical outcome. One of these studies is the assessment of the candidate in a range of different tumours. Platforms such as the Developmental Therapeutics Program (DTP) in collaboration with the National Cancer Institute (NCI) provide researchers with the option to submit lead compounds, synthetic or natural, for evaluation of activity in multiple cell lines. This data can be used to help predict *in vivo* efficacy and help make informed decisions to support lead compound development.

1.4.1 National Cancer Institute (NCI)

Previously, before *in vitro* testing in 2D cultures was offered by NCI, the institute tested drug efficacy in *in vivo* mouse models of leukaemia such as L1210V^{71, 72}. The inflexibility of this model to accurately evaluate drugs targeted at solid tumours led to the conception of the NCI-60 panel in 1980s, expanded over the years to investigate up to 3000 agents every year⁷³. This enabled researchers to submit their compound for assessment in a panel of cancer cell lines by evaluating its growth inhibition and lethality⁷³. The panel comprises of 60 well characterised cell lines originating from

nine tumour subtypes: leukaemia, central nervous system, lung, melanoma, kidney, breast, prostate, ovaries and colon. The test compound is tested at a single dose of 10 μ M to monitor growth inhibition (values 0-100) and lethality (values <0) in the NCI-60 panel⁷³. The protein binding sulforhodamine B (SRB) dye is used as an indicator of cell viability after drug incubation⁷⁴. Additionally, after exhibiting potent in the one-dose assay, the compound(s) may get selected for further screening in a 5-dose assay which calculates the TGI (concentration of total growth inhibition), GI₅₀ (concentration of 50% growth inhibition) and LC₅₀ (concentration for 50% cell death) of the drug candidate⁷³.

1.4.2 COMPARE algorithm

This data can be used to perform pattern recognition analysis using publicly accessible platforms such as COMPARE developed by DTP. This aims to identify compounds in the database with an activity pattern in the NCI-60 panel similar to the test compound^{73, 75}. Compounds are ranked in order of similarity and a pearsons correlation coefficient (r) is assigned to each 'hit' which is indicative of its similarity to the test compound^{73, 75}, with a correlation value of $r \geq 0.5$ considered biologically relevant in this work. If the MoA of hits identified is known, these hits can be used to define a putative MoA for the test compound. It can also inform if the compound exhibits unique behaviour therefore acts via novel MoA if no or poor correlations are found.

In addition to drug activity, NCI-60 also offers molecular characterisation of the cell lines with various datasets including microRNAs, protein expression, gene

expression, whole genome sequencing and DNA copy number⁷⁶. This enables a COMPARE analysis between cytotoxic activity and one of these various outputs to highlight genomic and/or phenotypic features important for the mode of action.

1.5 Chemotherapy

There is a range of cancer chemotherapy drugs targeting different types of cancers, all trying to contain proliferation of cancer cells selectively hence keeping the disease from local and distant spread. Cytotoxic drugs were first developed in the 1940s and this type of treatment alongside surgery and radiotherapy remains the frontline treatment for many cancer patients⁷⁷. Consisting of low molecular weight agents, it is a systemic treatment as drugs are carried to target sites through the bloodstream to inhibit cell proliferation⁷⁸. The time of administration and use of chemotherapy differs between patients, used as either neoadjuvant or adjuvant therapy. Additionally, for lymphomas and leukaemia it is the first and only line of defence, also used against recurring and metastatic cancers⁷⁸. Classical chemotherapy drugs can be classified according to their MoA belonging to one of the following classes⁷⁹:

- Alkylating drugs: introduce an alkyl group to nucleobases, commonly guanine, interrupting base-base interaction. Examples include temozolomide and trabectedin^{79, 80}.
- DNA crosslinkers: directly bind to the DNA leading to intra- and interstrand crosslinks. Most common example is platinum complexes such as cisplatin and oxaliplatin^{79, 80}.
- DNA intercalators: insertion between adjacent bases, commonly assisted by planar rings. Examples include doxorubicin, and dactinomycin^{79, 80}.

- Topoisomerase inhibitors: inhibit topoisomerase mediated relaxation of DNA topology during replication, often stabilising intermediate strand breaks. Examples include etoposide and irinotecan^{79, 80}.
- Antimetabolites: structural analogues of endogenous monomers, including nucleosides, that interfere with biosynthesis of DNA or RNA. Examples include gemcitabine, 5-FU, capecitabine^{79, 80}.
- Antitubulin agents: obstruct microtubule dynamics by binding polymerised tubulin or tubulin monomers⁸¹ preventing cell division. Examples include paclitaxel, docetaxel and vincristine⁸⁰.

Over the years, further classes of drugs have been identified including antihormonal agents, inhibitors of oncogenes, immune checkpoint modulators and inducers of synthetic lethality⁸⁰. Although there is an emergence of selective treatments (immune therapy, mRNA etc.), cytotoxic drugs are likely to remain relevant in treatment regimens⁷⁹. Common side effects of cytotoxic drugs, due to the susceptibility of replicating healthy cells, includes hair loss, anaemia, nausea, vomiting and GI mucositis⁸². The rise of chemoresistance which remains a significant clinical problem has led to the introduction of combination treatments first developed in the 1960s combining two or more agents with different MoAs, which also provided the first curative treatment for leukaemia⁷⁷.

1.5.1 Nucleoside analogues

Chemotherapy drugs used to treat pancreatic cancer include anti-metabolite nucleoside analogues gemcitabine, 5-FU or capecitabine, administered as monotherapy or in combination with radiotherapy (Figure 1.12). Drug combinations

FOLFIRINOX, FOLFOX and GemCap are also used to treat advanced stage pancreatic cancer though these regimens are associated with high toxicity⁸³.

Nucleoside analogues are structurally similar to endogenous nucleosides but contain structural modifications, such as introduction of a fluorine atom in gemcitabine⁸⁴

(Figure 1.12). These clinically beneficial agents such as gemcitabine are active in a wide range of cancers, including PDAC, improving patient outcome significantly.

Unlike alkylating agents, these analogues are cell cycle dependent⁸⁵, particularly S phase specific as they are commonly incorporated in replicating DNA during semi-conservative replication resulting in DNA synthesis inhibition by masked chain termination⁸⁴. The replication fork stalling and consequential DNA damage activates cell cycle checkpoints that are commonly implicated in chemoresistance to nucleoside analogues⁸⁴. As repair mechanisms are overwhelmed, persisting DNA damage triggers apoptosis⁸⁴.

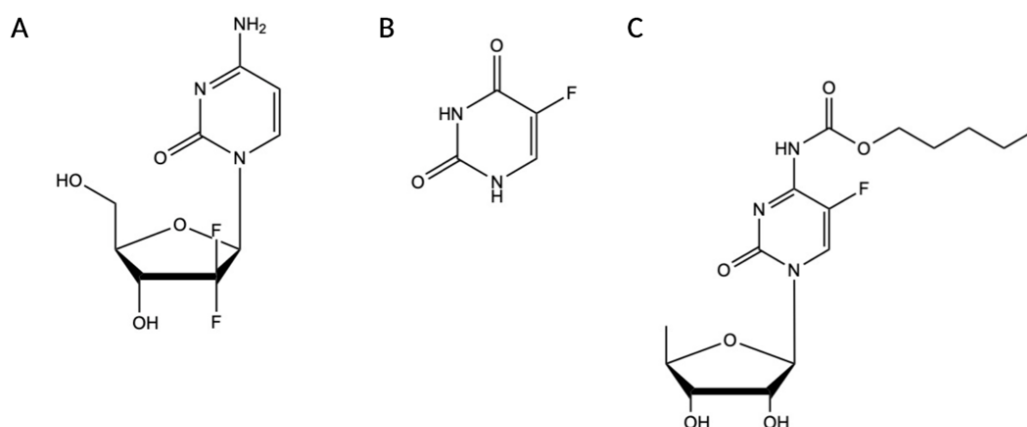


Figure 1.12. Chemical structures of nucleoside analogues (A) Gemcitabine, (B) 5-fluorouracil and (C) Capecitabine.

Nucleobase analogues, including gemcitabine, also require tri-phosphorylation in a similar manner as endogenous nucleosides (Figure 1.13), prior to DNA incorporation⁸⁶. Gemcitabine also acts as a competitive inhibitor of deoxycytidine kinase, occupying the active site inhibiting cytidine phosphorylation therefore reducing the dNTP pool⁸⁶. Phosphorylation of endogenous nucleosides and synthetic analogues such as gemcitabine occur at the hydroxyl group bonded to the ribose sugar as shown in Figure 1.13.

However, despite their *in vitro* potency, clinical efficacy of these drugs, particularly gemcitabine, remains limited due to short half-life, restricted uptake, intracellular activation and rising mechanisms of resistance observed within weeks of first administration⁸⁷. There are several pathways implicated as major drivers of gemcitabine resistance including epithelial-to-mesenchymal transition (EMT), genetic/epigenetic changes, downregulation of nucleotide transporters hCNT1, hCNT3, hEN1, upregulation of deactivating enzymes cytidine deaminase, thymidylate synthase and ribonucleotide reductase⁸⁷. Additionally, the non-specific nature of nucleoside analogues is associated with thrombocytopenia and leukopenia⁸⁸ in addition to the generic side effects of chemotherapy listed previously.

DNA replication inhibition remains an attractive strategy to target cancer cells however, the nucleoside analogues clinically available present complications including poor selectivity, resistance, intracellular activation, and metabolism⁸⁸.

Therefore, there is a pressing need for novel therapies that can overcome some of these providing improved clinical efficacy and patient outcome.

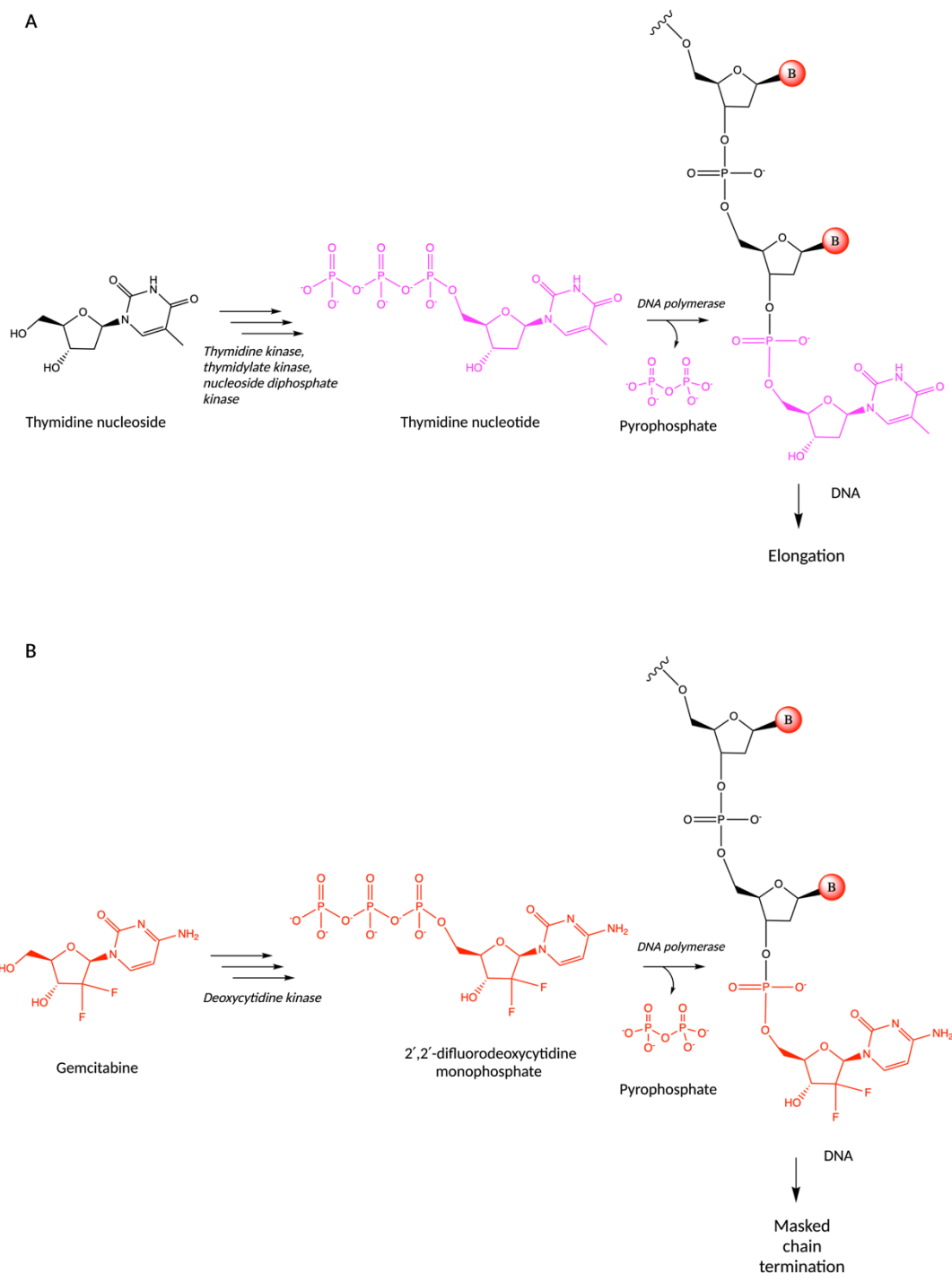


Figure 1.13. (A) Incorporation of thymidine nucleotide and (B) Gemcitabine by DNA polymerase during DNA synthesis. Endogenous deoxynucleosides, e.g., thymidine, or analogues such as gemcitabine are converted to deoxynucleoside monophosphates by nucleoside kinases, followed by further phosphorylation yielding deoxynucleoside triphosphates, called nucleotides. DNA polymerase incorporates the incoming nucleotides by forming a phosphodiester bond between the α phosphate of the monomer and free 3'-OH group of the last incorporated nucleotide, releasing a molecule of pyrophosphate in the process.

1.5.2 Metallodrugs

The clinical success of cisplatin, first discovered in 1845, has been and remains a major driver of interest in platinum-based metallodrugs (Figure 1.14). Cisplatin remains the gold standard treatment against many different types of cancers including lung, head and neck, ovarian, testicular and bladder⁸⁹. Mechanism of action of platinum-based drugs commonly includes DNA-platinum adduct formation blocking DNA replication and ROS induction, followed by activation of apoptosis^{90, 91}. This has influenced drug design with metals in the same group as platinum such as osmium⁹², ruthenium^{91, 93}, palladium and rhodium⁹⁴. However, over recent years issues with high toxicity and tumour resistance have undermined the clinical efficacy of cisplatin⁹⁴. In severe cases toxic side effects of the drug include nephrotoxicity, neurotoxicity, neutropenia, thrombocytopenia, anaemia, and cardiotoxicity^{95, 96}. To overcome these effects, research has expanded to identify novel metal structures including the application of essential metals such as iron in metallodrug design.

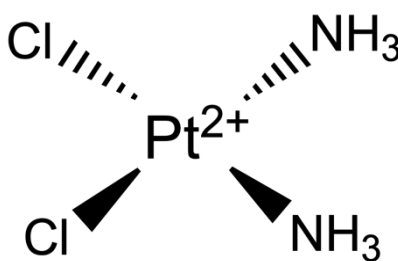


Figure 1.14. Chemical structure of metallodrug cisplatin.

1.5.3 Organometallic complexes

Organometallic complexes were first considered in 1980s as an avenue in the field of cancer and medicinal chemistry as drug candidates. Investigation to explore the anti-cancer effect of titanocene dichloride, the first organometallic complex to enter clinical trials in 1990s, revealed significant activity against cisplatin-resistant cell lines A2780CP and CH1cisR⁹⁷ (Figure 1.15). Titanocene dichloride targets DNA primarily and showed promising activity *in vitro* and *in vivo*, progressing to phase II clinical trials before it was rejected due to stability and formulation issues⁹⁸. Nonetheless, the potent activity of titanocene dichloride encouraged further research into organometallic complexes as second and third-line chemotherapeutics and as an alternative treatment for tumours resistant to established drugs such as cisplatin. This is also supported by the success of organometallic complexes such as ferrocifens⁹⁹ and ferroquine. The impressive library and success of anticancer ruthenium coordination complexes, with some entering clinical trials (e.g., NAMI-A, KP1019¹⁰⁰). Although these complexes are not identified as organometallic, their impressive activity supports the role of metals in medicine. Organometallic complexes comprise of at least one metal to carbon covalent bond providing structural flexibility as the central metal can be coordinated to different ligands in varied stereochemistry arrangements. In addition to this, their favourable physiochemical properties such as redox, physical stability, catalytic efficiency and ligand exchange means they have great potential to be explored in anti-cancer drug development¹⁰¹.

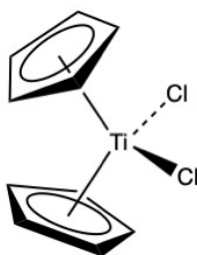


Figure 1.15. Chemical structure of titanocene dichloride.

1.5.3.1 Ferrocene

First discovered in 1951 by Kealy and Pauson¹⁰², ferrocene belongs to the family of metallocenes with the central iron (II) sandwiched between two cyclopentadienyl (Cp) rings. This complex has garnered interest due to its reversible electrochemical properties and stability in non-oxidising environment¹⁰³. Ferrocene was shown to be non-toxic to cells however the complex can be toxic upon reversible oxidation to ferrocenium ion¹⁰⁴ (Figure 1.16).

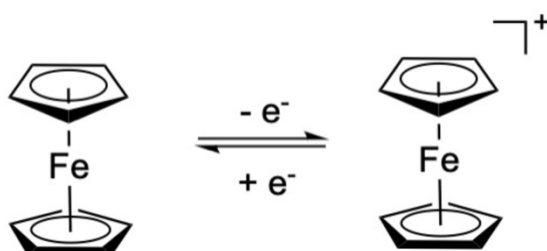


Figure 1.16. Ferrocene moiety undergoes a redox reaction yielding a ferrocenium cation.

As demonstrated by Köpf-Maier *et al.* (1984), ferrocenium salts were cytotoxic in models of Ehrlich ascites tumour as these were proposed to enhance hydroxyl radical production inducing lethal DNA damage^{105, 106}. One of the most successful applications of ferrocene in medicinal chemistry was the substitution in the skeleton of anti-cancer drug tamoxifen by Jaouen *et al.* in 1996. Tamoxifen is a selective oestrogen receptor modulator (SERM), structurally similar to oestradiol (Figure

1.17A) and clinically used to treat hormone-dependent (ER positive) breast cancer. However, through downregulation of ER receptor on cell surface membrane, among other mechanisms, led to acquire resistance against this agent¹⁰⁷. Ferrocifen is a derivative of tamoxifen as one of the three phenol rings is replaced with a ferrocene moiety (Figure 1.17B), the derivative shown to be active in both hormone-dependent and -independent breast cancer cells, MCF7 and MDA-MB-231 respectively⁹⁹. Activity in hormone-independent MDA-MB-231 cells suggest a duality in the mode of action. It has been proposed that the derivative participates in competitive oestrogen receptor binding, like tamoxifen, as well as initiating quinone methide production which targets the antioxidant system of the cell through inhibition of thioredoxin reductases⁹⁹. This work demonstrates that the ferrocene moiety can be used as a functional group or scaffold for drug design through modification of existing drugs or biomolecules.

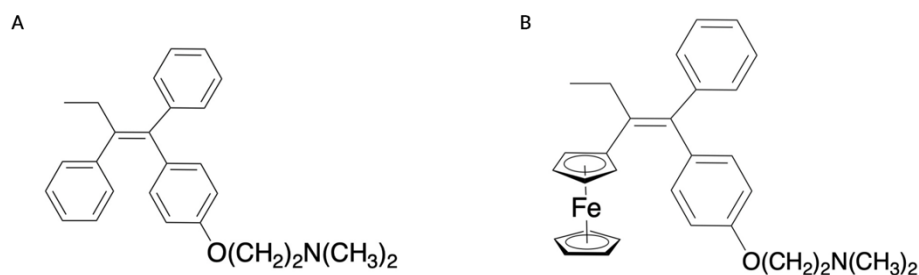


Figure 1.17. Chemical structure of anticancer drug (A) Tamoxifen and (B) its ferrocene derivative Ferrocifen.

1.5.3.2 Ferrocenyl derivatives of nucleobases

As mentioned previously (section 1.4.1), nucleoside analogues such as gemcitabine have demonstrated commercial and therapeutic success as anticancer agents,

commonly prescribed as first-line chemotherapy for pancreatic cancer. Both, pyrimidine, and purine analogues have shown activity against haematological and solid tumours. Considering the potent activity of this class of compounds, synthesis and biological activity of organometallic nucleoside derivatives have been considered.

Previously, these derivatives have shown biosensing, luminescence and monomeric properties¹⁰⁸. Ferrocenyl nucleobase derivatives are an emerging class of organometallic compounds where often ferrocene is conjugated to a nucleobase. The sandwich structure and reversible redox potential are perhaps the most important properties of this moiety for biological applications. Antitumor activity through non-covalent interaction with cellular targets has been proposed as part of the mechanism due to lack of coordination sites on the metal ion.

The first ferrocenyl-nucleobase was synthesised by Chen (1980) (Figure 1.18A) as ferrocene was *N*-substituted to yield *N*⁶-ferrocenylmethyladenine¹⁰⁹. This was followed by ferrocenyl nucleobase complex of thymine (Figure 1.18B) prepared by Price *et al.* (1996), shown to participate in electrostatic interactions with dissolved nucleic acids and perform reversible oxidation in aqueous buffer. Houlton *et al.* (1999) provide synthetic route for ferrocenyl-nucleobase conjugates of cytosine, thymine, uracil, 2-amino-6-chloropurine and N2-acetylguanine. They highlight the preferred alkylation sites for each nitrogenous base: N1 for cytosine and thymine, N3 for uracil. Another synthetic scheme and *in vitro* cytotoxicity studies with 1*N*-ferrocenylmethyl thymine (Figure 1.18C) was provided by Simenel *et al.* (2009).

Anticancer activity of their analogue was evaluated against *in vivo* model of carcinoma 755 (Ca755) achieving 70% tumour inhibition with an administered dose of 2.5 mg kg⁻¹. There was also evidence of synergy with chemotherapeutic cyclophosphamide, clinically used against a range of different cancers, leading to an increase of ~40% inhibition when co-administered with 1*N*-ferrocenylmethyl thymine (Figure 1.18C)¹¹⁰. This demonstrates that ferrocenyl nucleoside analogues can be considered as candidates for combination chemotherapy that has been more advantageous clinically than single agent treatments. Another example of impressive biological activity by ferrocenyl nucleobases is provided by Hocek *et al.* (2004) as their ferrocenylethynyl purine derivatives (Figure 1.18D) exhibit anticancer activity against T-cell lymphoblastic leukemia (CCRF-CEM), human leukemia (HL-60) and mouse lymphocytic leukemia (L1210) cell lines with IC₅₀ values in low micromolar range¹¹¹.

More recently, work by Kowalski and co-workers expand on the design and activity of ferrocenyl-nucleobases. They report the development of ferrocene-uracil analogues tested against human colon cancer (HT-29) and human breast cancer (MCF-7) cell lines. While none of the compounds were cytotoxic to HT-29 cells, the thymine derivative displayed relatively adequate activity against MCF-7 cells¹⁰³ (Figure 1.18E). Continuing their work on this class of organometallic compounds, synthesis of mono-, di- and tri-nuclear complexes with uracil was reported. Of all the derivatives tested, the di-nuclear analogue (Figure 1.18F) displayed highest activity against HT-29, comparable to cisplatin¹¹². Evaluation of sulphur-containing ferrocenyl-nucleobases highlighted structural importance of nitrogenous base thymine as

substitution of 4-thiothymine was shown to diminish activity (Figure 1.18G). This indicates the nitrogenous base is equally significant in dictating biological activity and target interaction. In addition to cytotoxicity, the thymine derivative induced phenotypic changes characteristic of apoptosis; cytoplasm condensation, nuclear envelop breakdown, blebbing and changes to cell shape¹¹³. Similar cellular effects were detected with ferrocenyl derivatives by Schmalz *et al.* (2006) as they detail enantiopure synthesis of ferrocenyl nucleosides conjugated to a five-membered ring (Figure 1.18H). Biological evaluation in Burkitt-like lymphoma cells and primary lymphoblasts led to apoptosis with an LD₅₀ between 10 to 20 μ M. Remarkably, this derivative remains active in lymphoblasts from relapsed acute lymphoblastic leukaemia, tumour resistant to established chemotherapeutics¹¹⁴.

Moving into the field of xeno nucleic acids (XNA), ferrocenyl nucleobases conjugated thymines, on each Cp ring, have been reported by Anisimov *et al.* (Figure 1.18I). These monomers are designed to mimic endogenous nucleosides that can self-polymerise¹¹⁵. Ferrocenyl glycol derivatives of XNAs have also been synthesised that can bridge organic and organometallic XNAs¹¹⁶. Perhaps biological studies could reveal whether these derivatives exhibit anticancer activity and, if so, whether they behave in a similar manner to previously designed ferrocenyl nucleosides or display a different MoA.

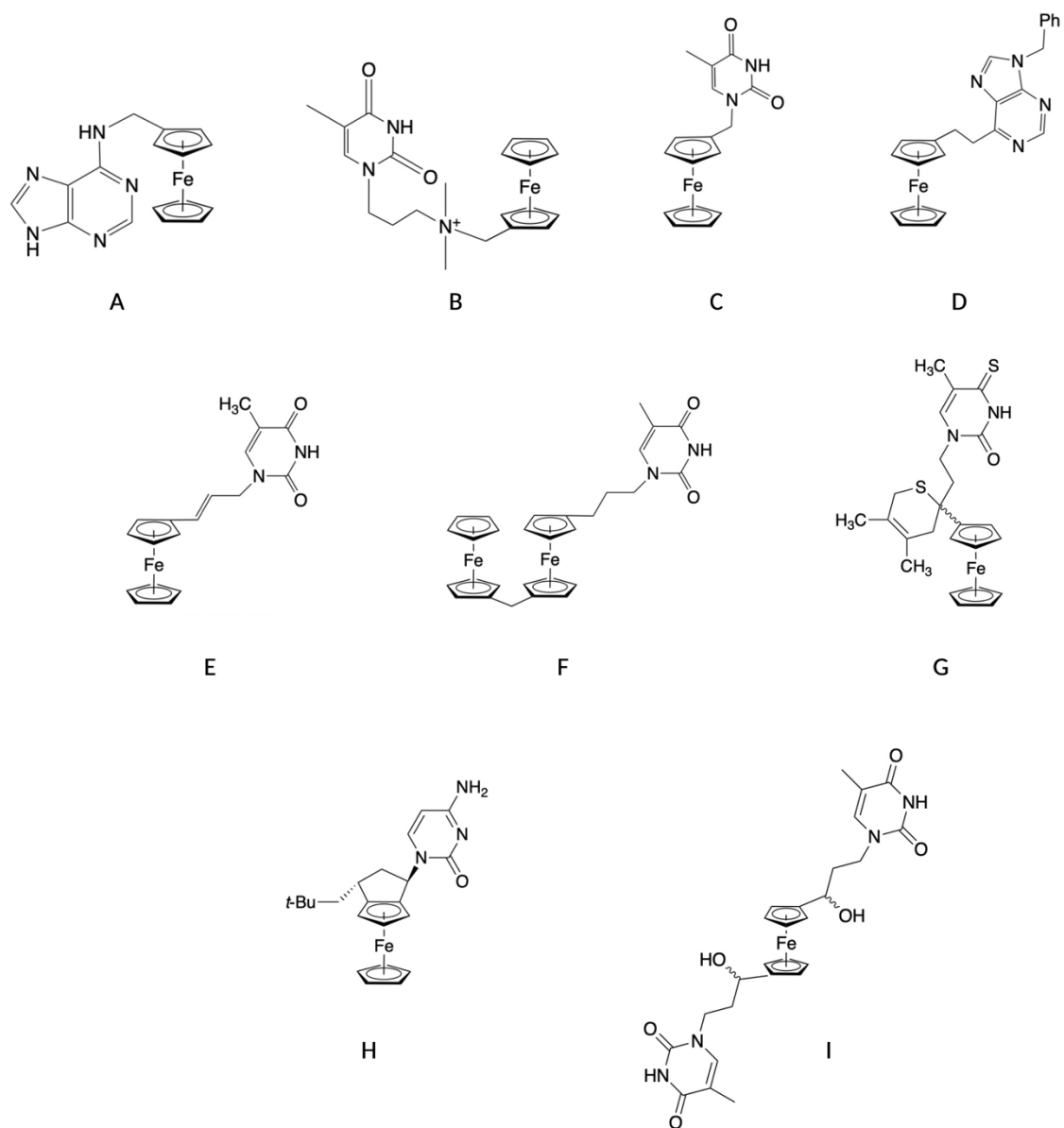


Figure 1.18. Chemical structures of ferrocenyl derivatives of nucleobases.

1.6 TUC-1

A related approach was adopted by Tucker *et al.* where the five-membered deoxyribose sugar moiety is replaced by the five-membered Cp ring of ferrocene with covalent bonding between the Cp ring and canonical nucleobase with an additional alkyl linker between the Cp ring and a hydroxyl group (Figure 1.19).

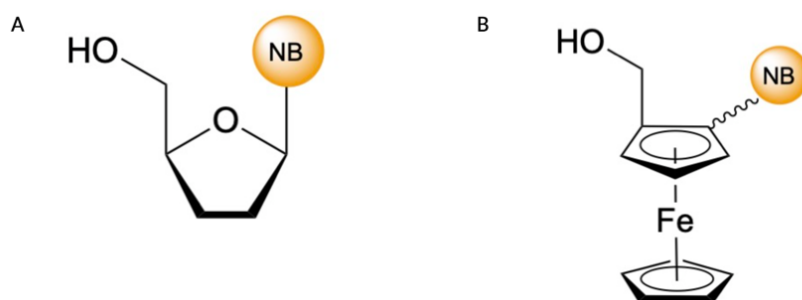


Figure 1.19. (A) Endogenous nucleosides consist of a ribose sugar unit attached to a nitrogenous nucleobase (NB) and a hydroxyl group (B) Ferronucleosides consist of a ferrocene moiety with the Cp ring replacing the ribose sugar attached to a nitrogenous nucleobase and a hydroxyl group.

As part of investigation into ferrocene nucleic acid oligomers, Tucker *et al.* synthesised bi-substituted ferrocene containing nucleoside monomers. Considering the similarity of these monomers to a nucleoside analogue and success of both nucleoside analogues and ferrocenyl compounds, the group proceeded to synthesise ferronucleosides consisting of a ferrocene bonded to a nitrogenous base and hydroxyalkyl group. Nguyen *et al.* (2014) detail the synthesis and characterisation of these analogues highlighting the importance of both functional groups⁴. Compounds devoid of either the nitrogenous base or hydroxyalkyl group had reduced cytotoxicity compared to derivatives with both functionalities, as evident by the IC₅₀ values reported⁴. From all the derivatives tested, (*S,R_p*)-1-[α -Methyl-(3-(hydroxy)propyl)]-2-

[(thyminy)ethyl]- ferrocene, referred to as TUC-1 in this thesis, was the most cytotoxic hence selected as the lead candidate for further studies (Figure 1.20A).

Activity of this compound was comparable to 5-fluorouracil when evaluated in mouse lymphocytic leukaemia (L1210), human T cell leukaemia (CEM) and HeLa cells. Additionally, TUC-1 is active in oesophageal cancer cell lines having comparable potency to cisplatin with an IC_{50} value of 6.25 μ M. To further explore the structure-activity relationship, the length of the hydroxyalkyl group was varied and biological activity of these derivatives was evaluated in human osteosarcoma cell line (HOS)¹¹⁷. Interestingly, a derivative with short linker length ($n = 1$) (Figure 1.20D), more similar to endogenous nucleosides in structure, was less active than those with longer linker length ($n = 2$) (Figure 1.20E) apparent by differences in IC_{50} values¹¹⁷.

Enantiomers of these derivatives were also evaluated with no significant toxicity observed. It is possible that the lipophilicity introduced by an additional methyl group is an important driver of cytotoxicity as well as aiding target interaction, but this remains to be determined. An inverse relationship between the linker length and half-wave potential ($E_{1/2}$) was also identified as a contributor to the activity of the complex as its oxidation to ferrocenium ion becomes favourable¹¹⁷. This is further supported by the decrease in activity observed with the ruthenocene analogue of TUC-1 (Figure 1.20F). The derivative, isostructural with identical stereochemistry to TUC-1 is 5-fold less active in MIA PaCa-2 cells¹¹⁸. The only difference between the two structures is the ability of ferrocene to undergo reversible oxidation. Iron can undergo one electron transfer reversibly that can have adverse cellular consequences such as production

of reactive oxygen species (ROS). In comparison, oxidation of ruthenium is reported to be irreversible suggesting that the ruthenocene derivative lacks the ability to effectively induce ROS and other oxidative damage. This suggests that redox activity of TUC-1 is an important factor in its potency and anticancer activity.

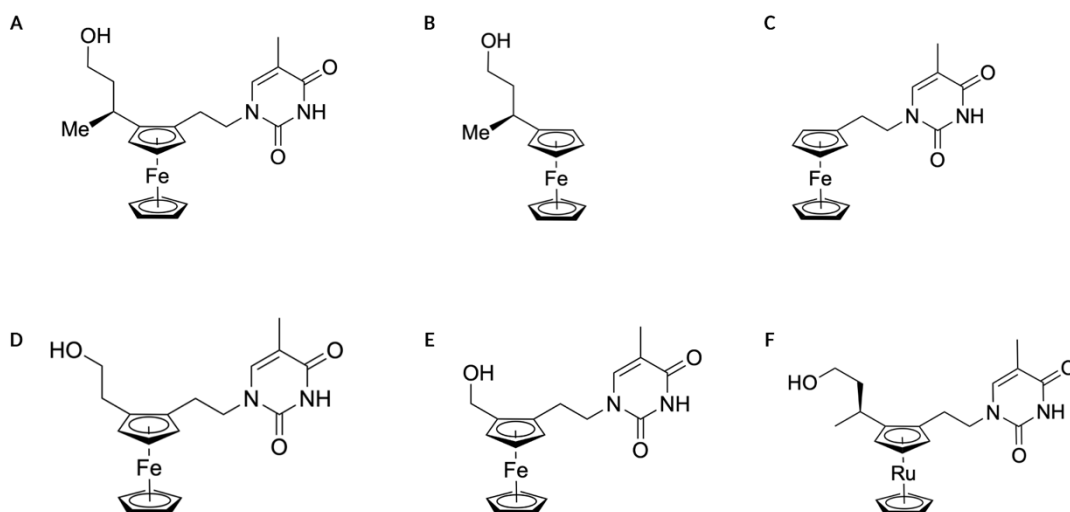


Figure 1.20. Chemical structures of (A) TUC-1 and its derivatives with lower biological activity; (B) missing nucleobase, (C) missing hydroxyalkyl group, (D, E) reduced hydroxyalkyl linker length, (F) ruthenium analogues of TUC-1.

1.7 Project Aims

Emergence of chemoresistance in PDAC, in addition to toxic side effects, has a significant impact on the clinical efficacy of frontline drugs such as gemcitabine, making tumour relapse more likely. As present anticancer agents on the market are not sufficient to tackle this evolving disease, there is a pressing need for novel therapies to treat PDAC. Before clinical studies can proceed, candidate drugs must undergo rigorous laboratory testing to decipher the processes underlying biological activity of a compound. Elucidation of the mechanism of action can also identify off-

target effects that can be used as markers for personalised medicine therefore reducing toxic side effects and improving patient prognosis.

Preliminary evidence from our laboratory at the start of the project indicated that TUC-1 had activity in PDAC cells including those resistant to gemcitabine. Therefore, the aim of this thesis is to investigate the cytotoxicity and mechanism of action of TUC-1 in a panel of PDAC cell lines. This work will build on the biological findings previously obtained and further evaluate these effects in the different cell lines to underpin similarities and differences that can aid target identification. This will involve investigating cytotoxicity in PDAC cell lines in addition to the 5-dose evaluation in the NCI-60 panel followed by COMPARE analysis. This work will assess the cellular effect of TUC-1 in PDAC cell lines with a focus on DNA replication. This will be accompanied by *in vitro* drug metabolism and pharmacokinetic (DMPK) data that will evaluate the ADME properties of TUC-1 which will inform on its *in vivo* efficacy. A synergistic relationship with a small molecule Chk1/2 kinase inhibitor is also explored to achieve greater activity at lower concentrations, reducing the possibility of potential side effects. Altogether, this work aims to provide evidence of the novel activity of TUC-1 making it a viable clinical candidate. The results chapters are divided as follows:

Chapter 3: *In vitro* Drug Metabolism and Pharmacokinetic studies (DMPK) with TUC-1. This chapter includes analysis and evaluation of data received from DMPK studies performed by Sygnature Discovery. This includes assessment of the intrinsic properties of TUC-1 in mouse, rat and human models including logD, blood stability,

hepatocyte stability, *in vitro* blood-to-plasma ratio and metabolite identification. This chapter also details *in vitro* DNA binding studies to observe the interaction between TUC-1 and double-stranded DNA.

Chapter 4: Cytotoxic evaluation of TUC-1 and derivatives *in vitro* and preliminary biological studies. Cytotoxicity of TUC-1 is established in a panel of PDAC cell lines; MIA PaCa2, BxPC3 and CFPAC-1. Derivatives of TUC-1 including the methylated analogues, regioisomer and enantiomer of TUC-1 are also evaluated in this panel. This is accompanied by investigation into cell cycle progression and identification of the mode of cell death. Analysis of NCI-60 5-dose evaluation of TUC-1 is performed to identify sensitive tumour subtypes and possible pharmacogenomic relationship. COMPARE and PILOT analysis has been performed to establish similarity with other compounds in the database allowing possible target identification.

Chapter 5: DNA replication dynamics and transcriptomic response to TUC-1. DNA strand breaks are investigated by monitoring phosphorylation of histone biomarker γ H2AX followed by evidence of inhibition of replication fork progression studied at single molecule resolution by DNA fibre fluorography. Checkpoint activation following DNA damage and replication fork stalling is presented alongside underlying transcriptomic changes.

Chapter 6: The cytotoxicity of TUC-1 is enhanced by Chk kinase inhibition. An investigation of the synergistic relationship between TUC-1 and Chk1/2 inhibitor

AZD7762. The effect of combination treatment on cellular processes including cell cycle arrest, DNA damage, DNA replication and gene expression changes are studied. The reversible activity of single and combination treatment is also evaluated.

Chapter 7: General discussion. A summary and significance of the key findings of this thesis.

Chapter 8: Appendices. This chapter provides additional supporting information related to investigations detailed in this thesis.

1.8 References

1. A. Grigorian and C. B. O'Brien, *J. Clin. Transl. Hepatol.*, 2014, **2**, 95-102.
2. M. Florescu, M. Cinteza and D. Vinereanu, *Maedica (Bucur)*, 2013, **8**, 59-67.
3. S. Horie, M. Oya, M. Nangaku, Y. Yasuda, Y. Komatsu, M. Yanagita, Y. Kitagawa, H. Kuwano, H. Nishiyama, C. Ishioka, H. Takaishi, H. Shimodaira, A. Mogi, Y. Ando, K. Matsumoto, D. Kadowaki and S. Muto, *Clin. Exp. Nephrol.*, 2018, **22**, 210-244.
4. H. V. Nguyen, A. Sallustrau, J. Balzarini, M. R. Bedford, J. C. Eden, N. Georgousi, N. J. Hodges, J. Kedge, Y. Mehellou, C. Tselepis and J. H. Tucker, *J. Med. Chem.*, 2014, **57**, 5817-5822.
5. D. Hanahan and R. A. Weinberg, *Cell*, 2011, **144**, 646-674.
6. P. Nurse, *Cell*, 2000, **100**, 71-78.
7. L. Ding, J. Cao, W. Lin, H. Chen, X. Xiong, H. Ao, M. Yu, J. Lin and Q. Cui, *Int. J. Mol. Sci.*, 2020, **21**, 1960.
8. C. J. Sherr and J. M. Roberts, *Genes Dev.*, 1999, **13**, 1501-1512.
9. K. A. Schafer, *Vet. Pathol.*, 1998, **35**, 461-478.
10. J. Hult, C. Wang, Z. Li, C. Albanese, M. Rao, D. Di Vizio, S. Shah, S. W. Byers, R. Mahmood, L. H. Augenlicht, R. Russell and R. G. Pestell, *Mol. Cell. Biol.*, 2004, **24**, 7598-7611.
11. V. M. Tut, K. L. Braithwaite, B. Angus, D. E. Neal, J. Lunec and J. K. Mellon, *Br. J. Cancer*, 2001, **84**, 270-275.
12. F. Mohammadizadeh, M. Hani, M. Ranaee and M. Bagheri, *J. Res. Med. Sci.*, 2013, **18**, 1021-1025.
13. S. Qie and J. A. Diehl, *J. Mol. Med. (Berl)*, 2016, **94**, 1313-1326.

14. W. Du and J. S. Searle, *Curr. Drug Targets*, 2009, **10**, 581-589.
15. E. T. Cánepa, M. E. Scassa, J. M. Ceruti, M. C. Marazita, A. L. Carcagno, P. F. Sirkin and M. F. Ogara, *IUBMB Life*, 2007, **59**, 419-426.
16. W. H. Liggett, Jr. and D. Sidransky, *J. Clin. Oncol.*, 1998, **16**, 1197-1206.
17. A. Cerqueira, A. Martín, C. E. Symonds, J. Odajima, P. Dubus, M. Barbacid and D. Santamaría, *Mol. Cell. Biol.*, 2014, **34**, 1452-1459.
18. T. Abbas and A. Dutta, *Nat. Rev. Cancer*, 2009, **9**, 400-414.
19. M. Meselson and F. W. Stahl, *Proc. Natl. Acad. Sci. USA*, 1958, **44**, 671-682.
20. J. H. Taylor, P. S. Woods and W. L. Hughes, *Proc. Natl. Acad. Sci. USA*, 1957, **43**, 122-128.
21. J. D. Watson and F. H. Crick, *Rev Invest Clin*, 2003, **55**, 108-109.
22. A. B. Harvey Lodish, S Lawrence Zipursky, Paul Matsudaira, David Baltimore, and James Darnell, *Mol. Cell Biol.*, Freeman, 2004.
23. T. Aparicio, A. Ibarra and J. Mendez, *Cell Div.*, 2006, **1**, 18.
24. L. A. Pray, *Nature Education*, 2008, **1**, 99.
25. N. Y. Yao and M. O'Donnell, *Cell*, 2010, **141**, 1088, 1088 e1081.
26. P. Garg, C. M. Stith, N. Sabouri, E. Johansson and P. M. Burgers, *Genes Dev.*, 2004, **18**, 2764-2773.
27. A. G. Baranovskiy, N. D. Babayeva, Y. Suwa, J. Gu, Y. I. Pavlov and T. H. Tahirov, *Nucleic Acids Res.*, 2014, **42**, 14013-14021.
28. L. de Sousa Cavalcante and G. Monteiro, *Eur. J. Pharmacol.*, 2014, **741**, 8-16.
29. A. M. Crane and S. K. Bhattacharya, *Methods Mol. Biol.*, 2013, **1014**, 65-70.
30. F. Chehrehasa, A. C. Meedeniya, P. Dwyer, G. Abrahamsen and A. Mackay-Sim, *J. Neurosci. Methods*, 2009, **177**, 122-130.

31. D. R. Iyer and N. Rhind, *PLoS Genet.*, 2017, **13**, e1006958.
32. J. Nieminuszczy, R. A. Schwab and W. Niedzwiedz, *Methods*, 2016, **108**, 92-98.
33. D. Brnzei and M. Foiani, *Nat. Rev. Mol. Cell Biol.*, 2008, **9**, 297-308.
34. A. Basu and S. Krishnamurthy, *J. Nucleic Acids*, 2010, **2010**.
35. L. F. Povirk, *ISRN Mol Biol*, 2012, **2012**.
36. J. A. Seiler, C. Conti, A. Syed, M. I. Aladjem and Y. Pommier, *Mol. Cell. Biol.*, 2007, **27**, 5806-5818.
37. B. Ewald, D. Sampath and W. Plunkett, *Mol. Cancer Ther.*, 2007, **6**, 1239-1248.
38. S. A. Sabatinos, *Nature Education*, 2010, **3**.
39. A. Mehta and J. E. Haber, *Cold Spring Harb. Perspect. Biol.*, 2014, **6**, a016428.
40. M. M. Vilenchik and A. G. Knudson, *Proc. Natl. Acad. Sci. USA*, 2003, **100**, 12871-12876.
41. G. Figueroa-Gonzalez and C. Perez-Plasencia, *Oncol. Lett.*, 2017, **13**, 3982-3988.
42. R. Visconti, R. Della Monica and D. Grieco, *J. Exp. Clin. Cancer Res.*, 2016, **35**, 153.
43. I. A. Shaltiel, L. Krenning, W. Bruinsma and R. H. Medema, *J. Cell Sci.*, 2015, **128**, 607-620.
44. M. B. Kastan and J. Bartek, *Nature*, 2004, **432**, 316-323.
45. R. Bharadwaj and H. Yu, *Oncogene*, 2004, **23**, 2016-2027.
46. B. B. Zhou and S. J. Elledge, *Nature*, 2000, **408**, 433-439.

47. L. M. McNamee and M. H. Brodsky, *Genetics*, 2009, **182**, 423-435.
48. Q. S. Tong, L. D. Zheng, L. Wang, J. Liu and W. Qian, *BMC Cancer*, 2004, **4**, 33.
49. N. Miyake, H. Chikumi, M. Takata, M. Nakamoto, T. Igishi and E. Shimizu, *Oncol. Rep.*, 2012, **28**, 848-854.
50. R. S. Y. Wong, *Journal of Experimental & Clinical Cancer Research*, 2011, **30**, 87.
51. S. Elmore, *Toxicol. Pathol.*, 2007, **35**, 495-516.
52. M. A. O'Brien and R. Kirby, *Journal of Veterinary Emergency and Critical Care*, 2008, **18**, 572-585.
53. P. Schneider and J. Tschopp, *Pharm. Acta. Helv.*, 2000, **74**, 281-286.
54. G. Kroemer, L. Galluzzi and C. Brenner, *Physiol. Rev.*, 2007, **87**, 99-163.
55. E. C. LaCasse, D. J. Mahoney, H. H. Cheung, S. Plenchette, S. Baird and R. G. Korneluk, *Oncogene*, 2008, **27**, 6252-6275.
56. C. M. Pfeffer and A. T. K. Singh, *Int. J. Mol. Sci.*, 2018, **19**.
57. P. Huang and W. Plunkett, *Semin. Oncol.*, 1995, **22**, 19-25.
58. T. Rich, R. L. Allen and A. H. Wyllie, *Nature*, 2000, **407**, 777-783.
59. G. Zhang, V. Gurtu, S. R. Kain and G. Yan, *BioTechniques*, 1997, **23**, 525-531.
60. S. J. Dixon, *Immunol. Rev.*, 2017, **277**, 150-157.
61. B. Hassannia, P. Vandenabeele and T. Vanden Berghe, *Cancer Cell*, 2019, **35**, 830-849.
62. K.-Y. A. Lin, J.-T. Lin and Y.-F. Lin, *J. Taiwan Inst. Chem. Eng.*, 2017, **78**, 144-149.

63. J. Li, F. Cao, H.-l. Yin, Z.-j. Huang, Z.-t. Lin, N. Mao, B. Sun and G. Wang, *Cell Death Dis.*, 2020, **11**, 88.
64. Y. Mou, J. Wang, J. Wu, D. He, C. Zhang, C. Duan and B. Li, *J. Hematol. Oncol.*, 2019, **12**, 34.
65. E. Lachaier, C. Louandre, C. Godin, Z. Saidak, M. Baert, M. Diouf, B. Chauffert and A. Galmiche, *Anticancer Res.*, 2014, **34**, 6417.
66. J. Guo, B. Xu, Q. Han, H. Zhou, Y. Xia, C. Gong, X. Dai, Z. Li and G. Wu, *Cancer Res. Treat.*, 2018, **50**, 445-460.
67. M. Orth, P. Metzger, S. Gerum, J. Mayerle, G. Schneider, C. Belka, M. Schnurr and K. Lauber, *Radiat. Oncol.*, 2019, **14**, 141.
68. E. A. Collisson, P. Bailey, D. K. Chang and A. V. Biankin, *Nat. Rev. Gastroenterol. Hepatol.*, 2019, **16**, 207-220.
69. A. McGuigan, P. Kelly, R. C. Turkington, C. Jones, H. G. Coleman and R. S. McCain, *World J. Gastroenterol.*, 2018, **24**, 4846-4861.
70. F. Quiñonero, C. Mesas, K. Doello, L. Cabeza, G. Perazzoli, C. Jimenez-Luna, A. R. Rama, C. Melguizo and J. Prados, *Cancer Biol. Med.*, 2019, **16**, 688-699.
71. W. R. Waud, K. S. Gilbert and J. A. Secrist, 3rd, *Cancer Chemother. Pharmacol.*, 2011, **68**, 399-403.
72. K. V. Kitaeva, C. S. Rutland, A. A. Rizvanov and V. V. Solovyeva, *Front. Bioeng. Biotech.*, 2020, **8**.
73. R. H. Shoemaker, *Nat. Rev. Cancer*, 2006, **6**, 813-823.
74. M. C. Alley, D. A. Scudiero, A. Monks, M. L. Hursey, M. J. Czerwinski, D. L. Fine, B. J. Abbott, J. G. Mayo, R. H. Shoemaker and M. R. Boyd, *Cancer*

- Res., 1988, **48**, 589-601.
75. K. D. Paull, R. H. Shoemaker, L. Hodes, A. Monks, D. A. Scudiero, L. Rubinstein, J. Plowman and M. R. Boyd, *J. Natl. Cancer Inst.*, 1989, **81**, 1088-1092.
 76. W. C. Reinhold, M. Sunshine, S. Varma, J. H. Doroshow and Y. Pommier, *Clin. Cancer. Res.*, 2015, **21**, 3841-3852.
 77. D. S. Shewach and R. D. Kuchta, *Chem. Rev.*, 2009, **109**, 2859-2861.
 78. V. T. DeVita, Jr. and E. Chu, *Cancer Res.*, 2008, **68**, 8643-8653.
 79. S. Nussbaumer, P. Bonnabry, J.-L. Veuthey and S. Fleury-Souverain, *Talanta*, 2011, **85**, 2265-2289.
 80. A. Carugo and G. F. Draetta, *Annual Review of Cancer Biology*, 2019, **3**, 385-408.
 81. L. G. Wang, X. M. Liu, W. Kreis and D. R. Budman, *Cancer Chemother. Pharmacol.*, 1999, **44**, 355-361.
 82. K. Nurgali, R. T. Jagoe and R. Abalo, *Front. Pharmacol.*, 2018, **9**, 245-245.
 83. J. Q. Fan, M. F. Wang, H. L. Chen, D. Shang, J. K. Das and J. Song, *Mol. Cancer*, 2020, **19**, 32.
 84. B. Ewald, D. Sampath and W. Plunkett, *Oncogene*, 2008, **27**, 6522-6537.
 85. C. Bastiancich, G. Bastiat and F. Lagarce, *Drug Discovery Today*, 2018, **23**, 416-423.
 86. M. L. Alvarellos, J. Lamba, K. Sangkuhl, C. F. Thorn, L. Wang, D. J. Klein, R. B. Altman and T. E. Klein, *Pharmacogenet. Genomics*, 2014, **24**, 564-574.
 87. M. Amrutkar and I. P. Gladhaug, *Cancers (Basel)*, 2017, **9**.
 88. A. J. Berdis, *Biochemistry*, 2008, **47**, 8253-8260.

89. S. Dasari and P. B. Tchounwou, *Eur. J. Pharmacol.*, 2014, **740**, 364-378.
90. S. R. W. Grazielle Fonseca de Sousa, Gisele Monteiro, *Braz. J. Pharm. Sci.*, **50**, 693-701.
91. A. Casini, C. Gabbiani, F. Sorrentino, M. P. Rigobello, A. Bindoli, T. J. Geldbach, A. Marrone, N. Re, C. G. Hartinger, P. J. Dyson and L. Messori, *J. Med. Chem.*, 2008, **51**, 6773-6781.
92. S. M. Meier-Menches, C. Gerner, W. Berger, C. G. Hartinger and B. K. Keppler, *Chem. Soc. Rev.*, 2018, **47**, 909-928.
93. I. E. Leon, J. F. Cadavid-Vargas, A. L. Di Virgilio and S. B. Etcheverry, *Curr. Med. Chem.*, 2017, **24**, 112-148.
94. L. Zeng, P. Gupta, Y. Chen, E. Wang, L. Ji, H. Chao and Z. S. Chen, *Chem. Soc. Rev.*, 2017, **46**, 5771-5804.
95. S. A. Aldossary, *Biomed. Pharmacol. J.*, 2019, **12**.
96. L. Astolfi, S. Ghiselli, V. Guaran, M. Chicca, E. Simoni, E. Olivetto, G. Lelli and A. Martini, *Oncol. Rep.*, 2013, **29**, 1285-1292.
97. C. V. Christodoulou, A. G. Eliopoulos, L. S. Young, L. Hodgkins, D. R. Ferry and D. J. Kerr, *Br. J. Cancer*, 1998, **77**, 2088-2097.
98. C. G. Hartinger, N. Metzler-Nolte and P. J. Dyson, *Organometallics*, 2012, **31**, 5677-5685.
99. G. Jaouen, A. Vessi res and S. Top, *Chem. Soc. Rev.*, 2015, **44**, 8802-8817.
100. Y. K. Yan, M. Melchart, A. Habtemariam and P. J. Sadler, *Chem. Commun.*, 2005, DOI: 10.1039/B508531B, 4764-4776.
101. G. Gasser, I. Ott and N. Metzler-Nolte, *J. Med. Chem.*, 2011, **54**, 3-25.
102. T. J. Kealy and P. L. Pauson, *Nature*, 1951, **168**, 1039-1040.

103. K. Kowalski, J. Skiba, L. Oehninger, I. Ott, J. Solecka, A. Rajnisz and B. Therrien, *Organometallics*, 2013, **32**, 5766-5773.
104. M. Patra and G. Gasser, *Nat. Rev. Chem.*, 2017, **1**, 0066.
105. D. R. van Staveren and N. Metzler-Nolte, *Chem. Rev.*, 2004, **104**, 5931-5986.
106. H. K. a. E. W. N. Petra Kopf-Maier, *Angew. Chem. Int. Ed. Engl.*, 1984, **23**, 456-457.
107. S. Ali, M. Rasool, H. Chaoudhry, P. N Pushparaj, P. Jha, A. Hafiz, M. Mahfooz, G. Abdus Sami, M. Azhar Kamal, S. Bashir, A. Ali and M. Sarwar Jamal, *Bioinformation*, 2016, **12**, 135-139.
108. K. Kowalski, *Coord. Chem. Rev.*, 2016, **317**, 132-156.
109. S.-C. Chen, *J. Organomet. Chem.*, 1980, **202**, 183-189.
110. A. A. Simenel, E. A. Morozova, L. V. Snegur, S. I. Zyкова, V. V. Kachala, L. A. Ostrovskaya, N. V. Bluchterova and M. M. Fomina, *Appl. Organomet. Chem.*, 2009, **23**, 219-224.
111. M. Hocek, P. Stepnicka, J. Ludvík, I. Císarová, I. Votruba, D. Reha and P. Hobza, *Chemistry*, 2004, **10**, 2058-2066.
112. J. Skiba, K. Kowalski, A. Prochnicka, I. Ott, J. Solecka, A. Rajnisz and B. Therrien, *J. Organomet. Chem.*, 2015, **782**, 52-61.
113. J. Skiba, R. Karpowicz, I. Szabó, B. Therrien and K. Kowalski, *J. Organomet. Chem.*, 2015, **794**, 216-222.
114. P. James, J. Neudörfl, M. Eissmann, P. Jesse, A. Prokop and H.-G. Schmalz, *Org. Lett.*, 2006, **8**, 2763-2766.
115. I. Anisimov, S. Saloman, A. Hildebrandt, H. Lang, D. Trzybiński, K. Woźniak, D. Šakić, V. Vrčec and K. Kowalski, *Chempluschem*, 2017, **82**, 859-866.

116. J. Skiba, Q. Yuan, A. Hildebrandt, H. Lang, D. Trzybiński, K. Woźniak, R. K. Balogh, B. Gyurcsik, V. Vrčec and K. Kowalski, *ChemPlusChem*, 2018, **83**, 77-86.
117. J. L. Kedge, H. V. Nguyen, Z. Khan, L. Male, M. K. I. Hodges, Holly V. Roberts, Nikolas J., S. L. Horswell, Y. Mehellou and J. H. R. Tucker, *Eur. J. Inorg. Chem.*, 2017, **2017**, 466-476.
118. M. K. Ismail, K. A. Armstrong, S. L. Hodder, S. L. Horswell, L. Male, H. V. Nguyen, E. A. Wilkinson, N. J. Hodges and J. H. R. Tucker, *Dalton Trans*, 2020, **49**, 1181-1190.

Chapter 2 – Materials and Methods

2.1 Compound synthesis

TUC-1 and its derivatives were synthesised, purified, and provided by the Tucker group in School of Chemistry. The synthesis scheme is detailed in previously published literature¹⁻³.

2.2 Cell culture

Pancreatic adenocarcinoma cell lines were obtained from the European Collection of Authenticated Cell Cultures (ECACC). Cell lines used: Human primary pancreatic adenocarcinoma BxPC-3 (ECACC 93120816); Human Caucasian pancreatic adenocarcinoma CFPAC-1 (ECACC 91112501); Human Caucasian pancreatic carcinoma MIA-Pa-Ca-2 (ECACC 85062806). Cell lines were cryopreserved in cryovials (Greiner Bio-One, Cat. no. 122263) containing 1 mL growth medium with 10% DMSO (Sigma-Aldrich, Cat. no. D2650) at -80°C.

All cell lines were thawed and grown in 75cm² tissue culture flasks (Greiner Bio-One, Cat. no. 658170) as monolayers; MIA Pa-Ca-2 cells were cultured in Dulbecco's Modified Eagle Medium (DMEM) (FisherScientific, Cat. no. 11500416), supplemented with 10% (vol/vol) foetal bovine serum (Sigma-Aldrich, Cat. no. F7524), 100 U/mL penicillin, 100 mg/mL streptomycin, and 2 mmol/L L-glutamine (Thermo Fisher Scientific, Cat. no. 10378016); BxPC3 were cultured in Roswell Park Memorial Institute medium (RPMI-1640) (FisherScientific, Cat. no. 11544446),

supplemented with 10% (vol/vol) foetal bovine serum (Sigma-Aldrich, Cat. no. F7524), 100 U/mL penicillin, 100 mg/mL streptomycin, and 2 mmol/L L-glutamine (Thermo Fisher Scientific, Cat. no. 10378016); CFPAC1 were cultured in RPMI-1640 (FisherScientific, Cat. no. 11544446), supplemented with 10% (vol/vol) foetal bovine serum (Sigma-Aldrich, Cat. no. F7524), 100 U/mL penicillin, 100 mg/mL streptomycin, and 2 mmol/L L-glutamine (Thermo Fisher Scientific, Cat. no. 10378016). All cells were maintained at 37 °C in a 5% CO₂ humidified incubator and subcultured twice weekly before confluency. Subculturing was performed by removing cell culture media followed by PBS wash (5 mL) (Thermo Fisher Scientific, Cat. No. 10010023), addition of trypsin EDTA (3 mL) (Thermo Fisher Scientific, Cat. no. 25300062) and incubation at 37 °C in a 5% CO₂ for 5 min. Trypsin EDTA solution is inactivated by addition of fresh growth medium (6 mL) followed by centrifugation at 180 g for 5 min to pellet the cell suspension. Cells were resuspended in 1 mL fresh growth medium and counted using a hemacytometer to determine cell density per mL. Cells were seeded at a density of 2×10^5 cells/mL in 15 mL fresh growth medium and incubated at 37°C in a 5% CO₂ humidified chamber until 80-90% confluent. All cells were cultured up to passage 20 before disposal and routinely tested for mycoplasma contamination.

2.3 Cell viability

2.3.1 Cell seeding

Following trypsin EDTA exposure, inactivation, centrifugation, and cell counting as described previously, cells were resuspended in fresh growth medium (12 mL) to achieve a cell density of 5×10^4 cells/mL. Cells were seeded in a 96-well plate (Starlab, Cat. no. CC7682-7596) with 100 μ L cell suspension per well (5000 cells per well) and incubated at 37°C, 5% CO₂ overnight to allow cell adhesion.

2.3.2 Drug exposure

2.3.2.1 Cytotoxicity studies

For cytotoxicity studies, PDAC cells, MCF-7, HCT116 and human osteosarcoma cell lines were exposed to TUC-1 and some or all TUC-1 derivatives; NMe TUC-1, OMe TUC-1, TUC-1* and regioisomer 2-(S). Gemcitabine (Sigma-Aldrich, Cat. no. G6423) and Cisplatin (Sigma-Aldrich, Cat. no. P4394) were used as control compounds. TUC-1 and its derivatives were dissolved in sterile-filtered DMSO (Sigma-Aldrich, Cat. no. D2650) to provide a stock solution of 40 mM. Gemcitabine was dissolved in DMSO to provide a stock solution of 100 μ M and cisplatin was dissolved in 0.9% sodium chloride solution (w/w) to provide a stock solution of 2 mM. Additionally, 0.1% Triton X-100 (Merck, Cat. no. T8787) was used as a positive control and fresh growth media with 0.1% sterile-filtered DMSO used as negative vehicle control. All compounds were diluted in fresh growth medium to a final working concentration of 200 μ M (200 nM for Gemcitabine). Exposures were prepared in sterile eppendorfs by performing a 1:2 dilution to produce a range of 0-200 μ M (0-200 nM for Gemcitabine). After removing growth medium, cells were treated with the compounds

at a range of 0-200 μ M by adding 100 μ L/well of the prepared exposures. Cells were incubated at 37°C, 5% CO₂ for 72 hours before addition of methylthiazolyldiphenyl-tetrazolium bromide (MTT) reagent (Merck, Cat. no. M5655). Cells were exposed to each concentration in triplicate and three independent biological repeats were performed for each compound. Experiment plate setup is provided in Appendices (Figure S1).

2.3.2.2 Ferroptosis

MIA PaCa-2 cells were exposed to TUC-1 in the presence or absence of Ferrostatin-1 (Merck, Cat. no. SML0583). An inducer of ferroptosis, Erastin (Strattech, Cat. no. B1524-APE) was used as the positive control in the presence or absence of Ferrostatin-1. Erastin was dissolved in sterile filtered DMSO (Sigma-Aldrich, Cat. no. D2650) to produce a stock solution of 10 mM. Ferrostatin-1 was dissolved in sterile filtered DMSO (Sigma-Aldrich, Cat. no. D2650) to produce a stock solution of 10 mM prior to dilution in fresh growth media (10 μ M) to produce a working solution. TUC-1 and Erastin exposures were prepared in fresh growth media and growth media containing Ferrostatin-1 (10 μ M). TUC-1 (40 mM) and Erastin stock solutions (10 mM) were diluted in fresh growth media and ferrostatin-1 working solution separately to a working concentration of 200 μ M which was further diluted to give a range of 0-200 μ M. After removing growth medium, MIA Pa-Ca-2 cells were treated with the prepared exposures (TUC-1 0-200 μ M \pm Ferrostatin-1 10 μ M or Erastin 0-200 μ M \pm Ferrostatin-1 10 μ M) by adding 100 μ L/well of the prepared exposures. Additionally, 0.1% sterile-filtered DMSO in fresh growth media was used as negative vehicle control. Cells were incubated at 37°C, 5% CO₂ for 72 hours before addition of

methylthiazolyldiphenyl-tetrazolium bromide (MTT) reagent (Merck, Cat. no. M5655). Cells were exposed to each concentration in triplicate and three biological repeats were performed for each compound. Experiment plate setup is provided in Appendices (Figure S2).

2.3.2.4 Combination studies

MIA Pa-Ca-2 cells were treated with TUC-1 combined with Chk kinase inhibitor AZD7762 (Stratech, Cat. no. A5919-APE). AZD7762 was dissolved in sterile filtered DMSO (Sigma-Aldrich, Cat. no. D2650) to produce a stock solution of 10mM which was diluted in sterile filtered DMSO to a concentration of 100 μ M. The cytotoxicity of AZD7762 was investigated over a range of 0-200 nM following methodology described previously (Section 2.3.2.1). Two treatment strategies were employed to investigate the effect of combination treatment.

First, a range of different concentrations of TUC-1 (0-200 μ M) were combined with fixed concentrations of AZD7762 (10, 20, 30, 40 or 50 nM). AZD7762 stock solution was diluted in fresh growth media to produce working solutions of concentrations 10, 20, 30, 40 and 50 nM. TUC-1 was diluted in each working solution to give a range of 0-200 μ M. After removing growth medium, MIA Pa-Ca-2 cells were treated with the prepared exposures (e.g. AZD7762 10 nM + TUC-1 0-200 μ M) by adding 100 μ L/well of the prepared exposures. Additionally, 0.1% sterile-filtered DMSO in fresh growth media was used as negative vehicle control. Cells were incubated at 37°C, 5% CO₂ for 72 hours before addition of methylthiazolyldiphenyl-tetrazolium bromide (MTT) reagent (Merck, Cat. no. M5655). Cells were exposed to each concentration in

triplicate and three biological repeats were performed for each compound.

Experiment plate setup is provided in Appendices (Figure S3).

Next, fractions of IC₅₀ of TUC-1 (9 µM) and AZD7762 (90 nM) were combined, maintaining equipotency, in the following ratios in fresh growth medium from TUC-1 200 µM and AZD7762 100 µM stock solutions prepared in fresh media:

4 IC₅₀ TUC-1 + 4 IC₅₀ AZD7762

2 IC₅₀ TUC-1 + 2 IC₅₀ AZD7762

1 IC₅₀ TUC-1 + 1 IC₅₀ AZD7762

0.75 IC₅₀ TUC-1 + 0.75 IC₅₀ AZD7762

0.5 IC₅₀ TUC-1 + 0.5 IC₅₀ AZD7762

0.25 IC₅₀ TUC-1 + 0.25 IC₅₀ AZD7762

Additionally, single agent exposures were prepared in fresh growth medium as follows:

8 IC₅₀ TUC-1

8 IC₅₀ AZD7762

4 IC₅₀ TUC-1

4 IC₅₀ AZD7762

2 IC₅₀ TUC-1

2 IC₅₀ AZD7762

1.5 IC₅₀ TUC-1

1.5 IC₅₀ AZD7762

1 IC₅₀ TUC-1

1 IC₅₀ AZD7762

0.5 IC₅₀ TUC-1

0.5 IC₅₀ AZD7762

After removing growth medium, MIA Pa-Ca-2 cells were treated with the prepared exposures (combination or single agent) by adding 100 µL/well of the prepared exposures. Additionally, 0.1% sterile-filtered DMSO in fresh growth media was used as negative vehicle control. Cells were incubated at 37°C, 5% CO₂ for 72 hours

before addition of methylthiazolyldiphenyl-tetrazolium bromide (MTT) reagent (Merck, Cat. no. M5655). Cells were exposed to each concentration in triplicate and three biological repeats were performed for each compound. Experiment plate setup is provided in Appendices (Figure S4).

2.3.3 MTT assay

Cell viability was assessed using the MTT assay which assesses the metabolic activity of cells as viable cells with functional succinate dehydrogenases will metabolise and convert MTT to purple formazan crystals⁴. Following the 72-hour treatment, methylthiazolyldiphenyl-tetrazolium bromide (MTT) reagent (Merck, Cat. no. M5655) was diluted from 5 mg/mL (in PBS) to 0.5 mg/mL in fresh growth media. After removing the drug exposures, MTT reagent was added, 100 µL per well, and the plate(s) incubated at 37°C, 5% CO₂ for 3 hours. After incubation, the MTT reagent was removed and DMSO (Merck, Cat. no. 472301) was added, 100 µL per well, to solubilise the purple formazan crystals and the plate left on the plate shaker for 10 min. The coloured solution was read and quantified using Tecan Infinite 200 PRO (Tecan, Switzerland) with absorbance measured at 490 nm.

2.3.4 Statistical analysis

For each drug concentration, mean and standard deviation was calculated in Microsoft Excel (USA) from the absorbance values obtained from the three independent biological experiments performed in triplicate. This was repeated for the negative control (unexposed) wells. All mean absorbance values were normalised by deducting the mean of the positive control (0.1% triton x-100) from the mean

absorbance values of all exposures and negative control. Percentage viability for each exposure was calculated as shown in equation 1.

$$\frac{[Mean\ absorbance]_{treatment}}{[Mean\ absorbance]_{negative\ control}} \times 100 \quad \text{Equation 1}$$

GraphPad Prism (USA) was used to create dose-response curves and IC_{50} determination by non-linear regression (Variable slope – four parameters). The IC_{50} is the concentration of a drug needed to inhibit 50% cell growth⁵ therefore an indicator of efficacy reported for all drug compounds in this thesis.

For combination studies, combination indexes were calculated to determine the nature of the relationship between TUC-1 and AZD7762. A combination of drugs can have an additive, antagonistic or synergistic relationship (Figure 2.1).

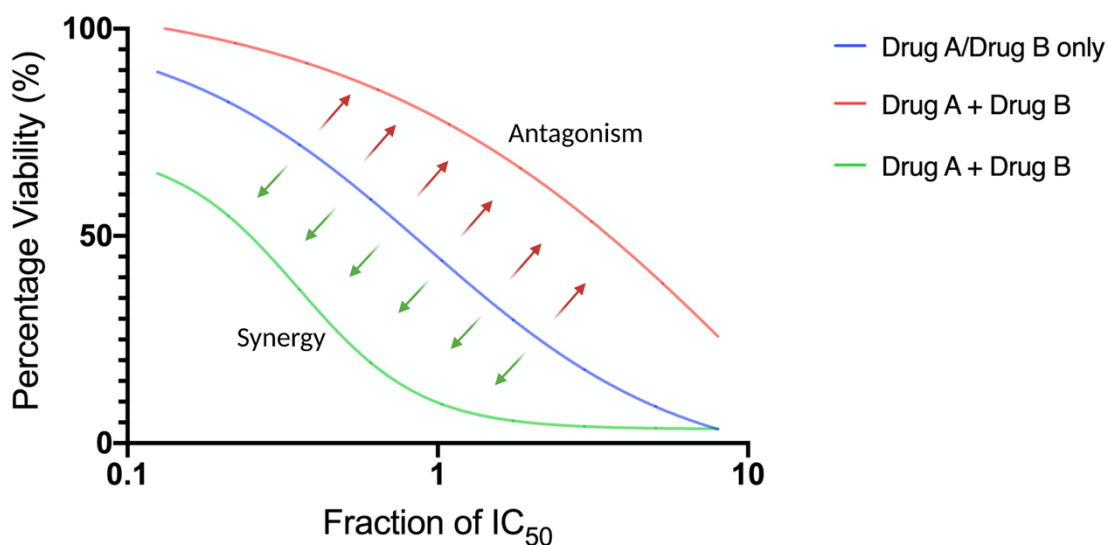


Figure 2.1. Example concentration response curves of single agent and fixed potency combination treatment. No curve shift representing no drug interaction (blue), right curve shifting showing antagonism (red) and left curve shifting showing synergy (green).

Additivity is achieved when two drugs produce a biological response that is the sum of the two administered individually⁶. In contrast to this, an antagonistic relationship is when the two drugs compete or block the effect of each other leading to reduced cytotoxicity⁶. Drug synergy or supra-additivity is achieved when drugs combined produce a greater biological response than the additive effect⁶. Many models have been proposed to evaluate drug combinations and their effectiveness. One of the most popular “null” models is Loewe additivity which assumes no interaction between the drugs administered at equal potency (e.g. IC₅₀) resulting in the same biological response as observed individually^{6, 7}. This is illustrated in equation (1) assuming drugs A and B do not interact and can be substituted for one another therefore the biological response is purely additive^{6, 8}:

$$0.5 \times \text{IC}_{50} A + 0.5 \times \text{IC}_{50} B = \text{IC}_{50} A = \text{IC}_{50} B \quad \text{Equation 2}$$

In case of a synergistic relationship, the biological response is greater than the additive effect and can be investigated experimentally by combining the two drugs at different equipotent fractions (e.g., 0.25/0.5/1.5 x IC₅₀). The extent to which the two drugs interact in synergy is indicated by Combination Indexes (CI) calculated as the ratio of the biological response achieved in combination compared to single treatment⁷. This is illustrated by equation (2) used to calculate CI values for each combination dose of TUC-1 and AZD7762 in this work:

$$\frac{\text{Percentage viability of combination treatment}}{\text{Percentage viability of TUC-1 alone}} \quad \text{Equation 3}$$

A CI value of 1 represents additivity whereas $CI < 1$ and $CI > 1$ indicate a synergistic and antagonistic relationship respectively⁷.

2.4 Cell cycle analysis

2.4.1 Cell preparation and drug exposure

PDAC cells were seeded at a density of 3×10^5 cells/mL in a 6-well plate and incubated at 37°C, 5% CO₂ overnight. For TUC-1 and TUC-1* exposures detailed in Chapter 4, stock solution (10 mM in DMSO) was diluted in fresh growth media to final concentrations of 1.25, 2.5, 5, 10 and 20 µM for TUC-1 and 5 µM for TUC-1*. For the combination treatment detailed in Chapter 6 Section 6.2.2, TUC-1 stock solution (10 mM in DMSO) was diluted in fresh growth medium to prepare single agent treatment (1, 5 µM) or combined with AZD7762 (stock solution 20 µM in DMSO) to produce combination exposures; TUC-1 1 µM + AZD7762 10, 20, 30 nM and TUC-1 5 µM + AZD7762 10, 20, 30 nM. Additionally, 0.1% sterile-filtered DMSO in fresh growth media was used as negative vehicle control. After removing growth medium, treatment was added cells, 2 mL per well, and the plates incubated at 37°C, 5% CO₂ for 24 hours. To investigate recovery for the combination treatment, drug exposures were removed, cells were washed with PBS (x3) and incubated in fresh growth medium for 24 hours prior to processing. Cells were exposed to each concentration in triplicate and three biological repeats were performed for each compound.

2.4.2 Sample processing and detection

Cells were harvested using standard trypsin EDTA procedure followed by collection in falcon tubes and centrifugation at 180 g for 5 min at room temperature to obtain

cell pellet. After washing with 1 mL PBS, the cells were fixed by resuspending the cell pellet in 250 μ L PBS and, while vortexing, 1.5 mL ice-cold 70% ethanol was added dropwise. The samples were stored at 4°C overnight. The following day, ethanol was removed, and cell pellets were obtained via centrifugation at 1500 RPM for 5 min at room temperature. After washing with 1 mL PBS, each sample was resuspended in 500 μ L PBS. Total RNA was digested by addition of 50 μ L of RNase A (Thermo Fisher Scientific, Cat. no. EN0531) solution (1 mg/mL in PBS). Next, 5 μ L of propidium iodide (1 mg/mL in dH₂O) (Merck, Cat. no. P4864) was added and samples were incubated for 30 min at room temperature. The samples were transferred to round-bottom polystyrene tubes prior to detection. Flow cytometry enables analysis of single cells in suspension by monitoring the fluorescence of probes or stains such as propidium iodide and light scattering⁹. The samples were analysed by flow cytometry using the Attune™ NxT Flow Cytometer (Thermo Fisher Scientific, USA) monitoring propidium iodide fluorescence (ex/em 535/617 nm) in YL2 channel.

2.4.3 Statistical analysis

The raw data was analysed using FlowJo (BD Bioscience, USA), gating for live cells and singlets followed by determination of percentage population in each phase of the cell cycle. Statistical differences were assessed in GraphPad Prism (USA) by performing 2-way ANOVA followed by Tukey's multiple comparison t-test.

2.5 Quantitation of apoptosis by Annexin V binding

Annexin V is an anticoagulant that binds to cell membrane lipid phosphatidylserine (PS) as it is translocated from the inner to the outer cell membrane during apoptosis¹⁰. PS externalisation is used as a biomarker to identify apoptosis as the mode of cell death as annexin V, conjugated to fluorescent probe pacific blue, binding produces a fluorescent signal detected by flow cytometry¹⁰.

2.5.1 Cell preparation and drug exposure

MIA Pa-Ca-2 cells were seeded at a density of 3×10^5 cells/mL in a 6-well plate and incubated at 37°C, 5% CO₂ overnight. An additional 3 wells were seeded for auto fluorescent, annexin V-pacific blue conjugate only and propidium iodide only controls. TUC-1 exposures were prepared the following day as stock solution (10 mM in DMSO) was diluted in fresh media to produce the following exposures: TUC-1 5, 10, 15, 20 and 25 µM. After removing growth medium, treatment was added to cells, 2 mL per well, or fresh growth media with 0.1% sterile-filtered DMSO for controls and the plates were incubated at 37°C, 5% CO₂ for 24 hours. Cells were exposed each concentration of TUC-1 in triplicate and three biological repeats were performed.

2.5.2 Sample processing and detection

Cells were harvested after 24 hours using standard trypsin EDTA procedure followed by collection in eppendorf tubes and centrifugation at 180 g for 5 min at room temperature to obtain cell pellet. Cells were washed with ice-cold PBS (300 µL per sample) followed by counting and resuspended in annexin binding buffer (Invitrogen, Cat. no. 15541947) to a density of 1×10^6 cells/mL. This was followed by addition of

5 µL Annexin V Pacific Blue conjugate (Invitrogen, Cat. no. A35122) and 1 µL propidium iodide counterstain to 100 µL cell suspensions. The samples were incubated for 15 min at room temperature before addition of 400 µL annexin binding buffer. Samples were placed on ice and protected from light before detection by flow cytometry. The samples were analysed by flow cytometry using the Attune™ NxT Flow Cytometer (Thermo Fisher Scientific, USA) monitoring propidium iodide fluorescence (ex/em 535/617 nm) in YL2 and annexin V Pacific Blue conjugate (ex/em 410/455 nm) in VL-1 channels.

2.5.3 Statistical analysis

The raw data was analysed using FlowJo (BD Bioscience, USA), counting all events excluding debris, gating out auto fluorescent events. Statistical differences between each treatment category were determined in GraphPad Prism (USA) by performing 2-way ANOVA followed by Dunnett's multiple comparison t-test.

2.6 UV-vis spectroscopy for DNA binding

The reaction mixture consisted of equimolar concentrations of calf-thymus DNA (Invitrogen, Cat. no. 15633019) and TUC-1 (200 μ M) in PBS placed in a 1 cm quartz cuvette (Fisher Scientific, Cat. no. 10594175) and incubated up to 72 hours. Measurements were taken at time intervals (24h, 48h and 72h) on UV-2600 (Shimadzu, UK) at wavelengths 250-350 nm to monitor any potential binding event. Solutions of TUC-1 (200 μ M), ctDNA (200 μ M) and PBS were used as controls.

2.7 Detection of gamma-H2AX

Phosphorylation of amino acid Serine-139 of the H2AX protein was detected following labelling with antibodies and detection through flow cytometry and confocal microscopy. The fluorescence intensity of the label is indicative of the extent of DSB damage, as each H2AX foci is representative of a DSB in a 1:1 ratio.

2.7.1 Flow cytometry

2.7.1.1 Cell preparation and drug exposure

MIA PaCa-2 cells were seeded at a density of 3×10^5 cells/mL in a 6-well plate and incubated at 37°C, 5% CO₂ overnight. Cells were exposed to TUC-1 single agent (10 μ M) (Chapter 5 Section 5.2.2) or TUC-1 combined with AZD7762 (TUC-1 5 μ M, AZD7762 30 nM, TUC-1 5 μ M + AZD7762 10, 20 and 30 nM) (Chapter 6 Section 6.2.4). Drug exposures were prepared the following day with TUC-1 stock solution (10 mM in DMSO) diluted to 5 and 10 μ M in fresh growth media, AZD7762 stock solution (20 μ M in DMSO) diluted to 30 nM in fresh growth media and TUC-1 5 μ M

combined with AZD7762 10, 20 and 30 nM. Topoisomerase II inhibitor etoposide (Merck, Cat. no. E1383) was used as a positive control with stock solution (10 mM in DMSO) diluted to 5 μ M in fresh growth media. After removing growth medium, treatment was added to cells, 2 mL per well, or fresh growth media with 0.1% sterile-filtered DMSO for untreated controls and the plates were incubated at 37°C, 5% CO₂ for 24 hours. For combination treatment, recovery was allowed by removing drug exposure, PBS wash (x3) and addition of fresh growth medium. The plates were incubated for an additional 24 hours prior to processing. Cells were exposed each compound and concentration in triplicate and three biological repeats were performed.

2.7.1.2 Sample processing and detection

Cells were harvested after treatment had finished using standard trypsin/EDTA procedure followed by collection in falcon tubes and centrifugation at 180 g for 5 min at room temperature to obtain cell pellet. After washing with 1 mL PBS (Thermo Fisher Scientific, Cat. No. 10010023), the cells were fixed by resuspending the cell pellet in 250 μ L PBS and, while vortexing, 1.5 mL ice-cold 70% ethanol was added dropwise. The samples were stored at 4°C overnight. The following day, ethanol was removed, and cell pellets were obtained via centrifugation at 1500 RPM for 5 min at room temperature. Cell pellets were resuspended in 0.25 % triton X-100 (Sigma, Cat. No. T8787) and incubated at room temperature for 10 min. Following permeabilization, the samples were centrifuged, resuspended in 200 μ L blocking solution (2% BSA in PBS) (Sigma, Cat. No. 05470) and incubated for 30 min at room temperature. An aliquot of the untreated sample was kept separately, unstained to

be used as an auto-fluorescent control. Blocking solution was removed by centrifugation and cells were exposed to 100 μ L anti-gamma H2AX (phospho S139) antibody (1:500) (Abcam, Cat. no. ab26350) in blocking solution for 1h at room temperature. The primary antibody was removed, and cells were washed with PBS. An aliquot of the untreated sample exposed to primary antibody only was taken to be used as single stain control. Subsequently cells were exposed to 100 μ L secondary antibody goat anti-mouse (FITC) antibody (1:200) (Thermo Fisher Scientific, Cat. no. 62-6511) in blocking solution for 1h in the dark at room temperature. An aliquot from the untreated sample stained with the secondary antibody only was taken to be used as single stain control. After removing the secondary antibody by centrifugation, the cells were washed with PBS and resuspended in 1 mL blocking solution and analysed by flow cytometry using the AttuneTM NxT Flow Cytometer (Thermo Fisher Scientific, USA) monitoring FITC fluorescence (ex/em 490/525 nm) in the BL-1 channel.

2.7.1.3 Statistical analysis

The raw data was analysed using FlowJo (BD Bioscience, USA), gating for live cells and singlets followed by determination of percentage population in each phase of the cell cycle. Statistical differences between different exposures were assessed in GraphPad Prism (USA) by performing 2-way ANOVA followed by Tukey's multiple comparison t-test.

2.7.2 Confocal microscopy

2.7.2.1 Cell preparation and drug exposure

MIA PaCa-2 cells were seeded at a density of 3×10^5 cells/mL on glass bottom dishes (Thermo Fisher Scientific, Cat. no. 150680) incubated at 37°C, 5% CO₂ overnight. Cells were exposed to TUC-1 single agent (10 µM) (Chapter 5 Section 5.2.2) or TUC-1 combined with AZD7762 (TUC-1 5 µM, AZD7762 30 nM, TUC-1 5 µM + AZD7762 10, 20 and 30 nM) (Chapter 6 Section 6.2.4). Drug exposures were prepared the following day with TUC-1 stock solution (10 mM in DMSO) diluted to 5 and 10 µM in fresh growth media, AZD7762 stock solution (20 µM in DMSO) diluted to 30 nM in fresh growth media and TUC-1 5 µM combined with AZD7762 10, 20 and 30 nM. Topoisomerase II inhibitor etoposide was used as a positive control with stock solution (10 mM in DMSO) diluted to 5 µM in fresh growth media. After removing growth medium, treatment was added to cells, 2 mL per well, or fresh growth media with 0.1% sterile-filtered DMSO for untreated controls and the dishes were incubated at 37°C, 5% CO₂ for 24 hours. For combination treatment, recovery was allowed by removing drug exposure, PBS wash (x3) and addition of fresh growth medium. The dishes were incubated for an additional 24 hours prior to processing. Cells were exposed each compound and concentration in triplicate and three biological repeats were performed.

2.7.2.2 Sample processing and detection

Once treatment was complete, cells were washed with 500 µL ice-cold PBS and fixed by the addition of 300 µL 4% paraformaldehyde (in PBS) (Alfa Aesar, Cat. no.

J61899.AK) for 10 min at room temperature on a shaker. Following fixation, cells were permeabilised with 500 μ L of 0.1% triton x-100 (Sigma, Cat. No. T8787) for 10 min at room temperature. After washing twice with PBST wash buffer (0.05 % Tween in PBS) (Sigma, Cat. No. P9416), cells were blocked with 2% BSA (Sigma, Cat. No. 05470) in PBST for 1h at room temperature. In the meantime, a humidified chamber was assembled, to prevent the samples from drying through evaporation when staining, by layering parafilm on top of wet tissue papers in a plastic container. Cells were washed with PBST (x3) and incubated with 100 μ L anti-gamma H2AX (phospho S139) antibody (1:500) (Abcam, Cat. no. ab26350) overnight at 4°C in a humidified chamber. The following day, cells were washed with PBST (x3) and incubated with 100 μ L goat anti-mouse (FITC) antibody (1:200) (Thermo Fisher Scientific, Cat. no. 62-6511) for 1h in the dark at room temperature. After another PBST wash, cells were incubated with 100 μ L propidium iodide (0.01 mg/mL) for 10 min. Samples were washed with PBST (x3) and coverslips (Thermo Fisher Scientific, USA) were applied using hydromount mounting media. The slides were allowed to dry for 1h in the dark at room temperature. The slides were read using Nikon A1R Inverted Confocal/TIRF microscope (Nikon, Japan) using a x100 oil-immersion objective.

2.7.2.3 Statistical analysis

The images were analysed in Fiji (ImageJ) (SciJava, USA) by splitting the multi-channels for single fluorophore images and merging for final images.

2.8 DNA fibre fluorography

2.8.1 Cell preparation and drug exposure

MIA PaCa-2 cells were grown to sub-confluency in a 6-well plate and treated with the compounds of interest. Cells were exposed to TUC-1 single agent (5, 10 and 25 μM) (Chapter 5 Section 5.2.3) or TUC-1 combined with AZD7762 (TUC-1 5 μM , AZD7762 30 nM, TUC-1 5 μM + AZD7762 10, 20 and 30 nM) (Chapter 6 Section 6.2.3). Drug exposures were prepared with TUC-1 stock solution (10 mM in DMSO) diluted to 5, 10 and 25 μM in fresh growth media, AZD7762 stock solution (20 μM in DMSO) diluted to 30 nM in fresh growth media and TUC-1 5 μM combined with AZD7762 10, 20 and 30 nM. After removing growth medium, treatment was added to cells, 2 mL per well, or fresh growth media with 0.1% sterile-filtered DMSO for untreated controls and the plates were incubated at 37°C, 5% CO₂ for 24 hours. Next, 40 minutes before the end of treatment, cells were pulse-labelled with 20 μL of 2.5 mM CldU and incubated for 20 min. Subsequently, 222 μL of CO₂-equilibrated IdU was added and incubated for an additional 20 min. After removing cell medium, cells were washed twice with ice-cold PBS. Cells were harvested by trypsinisation, resuspended in 1 mL ice-cold PBS without neutralisation of trypsin with media and kept on ice for the duration of the experiment. Cells were counted and optimised with ice-cold PBS to an optimal density of 50×10^4 cells/mL. Cells were exposed each compound and concentration in triplicate and three biological repeats were performed.

2.8.2 Spreading DNA fibres

Microscope slides (Fisher Scientific, Cat. no. 12372098) were labelled, placed on a paper towel and 2 μ L of each sample was placed near the frosting. The drop was left to dry for 4-5 min before 7 μ L of spreading buffer (200 mM Tris pH 7.4, 50 mM EDTA, 0.5% SDS) was placed directly on top of the sample and stirred with a pipette tip. After incubating the slides for 2 min at RT, the slides were tilted briefly at a small angle, to allow the drop to move down the slide at a slow and steady pace letting the excess liquid run off the slides. Slides were allowed to air-dry for 2 min at RT before being placed in a coplin jar filled with a mixture of methanol and acetic acid (3:1) to allow DNA fixation and deproteination. After an incubation period of 10 min, the slides were allowed to air-dry.

2.8.3 Immunostaining

Slides were placed in a black tray, keeping away from light, and washed twice with dH₂O followed by rinsing with freshly made 2.5 M HCl (x2) before incubation with 2.5 M HCl for 75 min for denaturation, making single-stranded DNA accessible to antibodies. After two rinses with PBS and two washes with blocking solution (1% BSA and 0.1% Tween 20 in PBS), the samples were incubated in blocking solution for 30 min at RT. The blocking solution was removed, and samples were immunolabelled with 115 μ L primary antibodies; mouse anti-BrdU antibody (1:500) (BD Bioscience, Cat. no. 347580) to detect IdU analogue and rat anti-BrdU (1:2000) (Abcam, Cat. no. ab6326) to detect CldU analogue. Each slide was covered with a coverslip and incubated in the dark for 1 h at room temperature. Samples were rinsed three times with PBS followed by antibody-antigen fixation with 0.5 mL of 4%

paraformaldehyde for 10 min at RT, slides covered with coverslips. Samples were rinsed with PBS (x3) and washed with blocking solution (x3), 115 μ L of secondary antibodies were added; goat anti-rat Alexafluor 555 (1:500) (Thermo Fisher Scientific, Cat. no. A-21434) and goat anti-mouse Alexafluor 488 (1:500) (Thermo Fisher Scientific, Cat. no. A-11029). Each slide was covered with a coverslip and incubated in the dark for 2h at room temperature. This was followed by two PBS rinse (x2), washing with blocking solution (x3) and rinse with PBS (x2). Coverslips were placed over the slides using Shandon Immu-Mount (Thermo Fisher Scientific, Cat. no. 9990402) and allowed to air-dry for 10 min. Slides were covered with foil and stored at -20°C and defrosted for at least 1h at room temperature before imaging.

2.8.4 Statistical analysis

The images were captured using Leica DM6000 with a 40x oil immersion objective and analysed using Fiji (ImageJ) (SciJava, USA). At least 1000 fibres per condition were counted from three independent biological repeats, by measuring the combined length (μ m) of the red and green label. The fibre length is converted to kB by conversion multiple 2.59 kB (1 μ m = 2.59 kB) previously reported¹¹. Statistical differences between different exposures were assessed in GraphPad Prism (USA) by performing two-tailed t-test.

2.9 Western blot analysis

2.9.1 Preparation of cell lysates and drug exposure

MIA PaCa-2 cells were seeded at a density of 3×10^5 cells/mL and incubated in 5% CO₂, 37°C overnight. The following day, drug exposures were prepared from TUC-1 stock solution (10 mM in DMSO): TUC-1 10 µM for 2, 7 and 24 hours. Control compounds hydroxyurea and aphidicolin (gifted by de Bruin Lab, UCL, UK) (stock solutions 1 mM and 250 µM in DMSO respectively) were diluted to 0.5 and 2.4 µM in fresh growth media respectively. Additionally, 0.1% sterile-filtered DMSO in fresh growth media was used as a negative vehicle control. Once completed, treatment was removed and cells washed once with ice-cold PBS, before 200 µL of RIPA buffer (Tris-HCl pH 7.5 20 mM; NaCl 150 mM; EDTA 1 mM; EGTA 1 mM; NP40 1 %; NaDoc 1 %) mixed with 1 µL phosphatase inhibitor cocktails (1:1000) (Sigma, Cat. no. P5726, P0044) and 1 µL protein kinase inhibitor cocktails (1:1000) (Sigma, Cat. no. 20-116) was added. The cells were harvested by scraping and centrifuged at 10000 RPM for 5 min at 4°C, retaining the supernatant.

2.9.2 Electrophoresis using SDS-PAGE

Following protein quantification by standard Bradford assay¹², proteins were denatured by heating at 96°C for 3 min in 1X Laemmli buffer. Equal amount of samples (30 µg) were loaded on SDS-PAGE gel (NuPAGE 4-12% Bis-Tris Gel) (Thermo Fisher Scientific, Cat. no. NP0322BOX) in 1X NuPAGE™ MOPS SDS Running Buffer 20X (Thermo Fisher Scientific, Cat. no. NP0001), run gel at 80 V for 30 min then at 130 V until the proteins are resolved. The separated proteins were transferred to 0.2 µM nitrocellulose membrane (Thermo Fisher Scientific, Cat. no.

77012) electrophoretically in transfer buffer (25 mM Tris; 190 mM glycine; 10% ethanol), run transfer at 100 V for 1h.

2.9.3 Protein detection

The nitrocellulose membrane was blocked in immobilon (Millipore, Cat. no. WBAVDP001) for 1h at RT. Once the desired bands were cut, the membrane was incubated with the following antibodies diluted in 5% BSA; rabbit anti-phospho-Chk1 (Ser345) antibody (1:1000) (Cell Signalling, Cat. no. 2341), rabbit anti-phospho-Chk2 (Thr68) antibody (1:1000) (Cell Signalling, Cat. no.2661), rabbit anti-phospho-Histone H2A.X (Ser139) antibody (1:250) (Cell Signalling, Cat. no. 9718), rabbit anti-phospho-RPA2 (Ser4/8) (1:1000) (Abcam, Cat. no. ab87277), rabbit anti-vinculin antibody (1:10000) (Abcam, Cat. no. ab129002) and mouse anti-GAPDH (1:1000) (Genetex, Cat. no. GTX627408), at 4°C overnight. After washing three times with PBST (PBS + 0.2% Tween20), the membrane strips were incubated with secondary antibodies conjugated to horseradish peroxidase (HRP); goat anti-mouse HRP (1:4000) (Fisher Scientific, Cat. no. PA1-74421), goat anti-rabbit HRP conjugated (1:4000) (Fisher Scientific, Cat. no. PI-31460) were used diluted in 5% non-fat milk in PBST. The membranes were incubated for 1h at room temperature and visualised using Luminata reagent (MerckMillipore, Cat. no. WBLUR0100) onto Amersham Hyperfilm ECL (GE Healthcare Life Sciences, Cat. no. 28906836).

2.9.4 Statistical analysis

The image was analysed, and densitometry analysis was performed in Fiji (ImageJ) (SciJava, USA).

2.10 Gene expression analysis

2.10.1 Sample preparation and drug exposure

Cells were seeded at a density of 3×10^5 cells/mL and incubated in 5% CO₂, 37°C overnight. The following day, cells were treated with drug exposures prepared by diluting TUC-1 and TUC-1* stock solutions (10 mM in DMSO) to 10 µM in fresh growth media. Additionally, 0.1% sterile-filtered DMSO in fresh growth media was used as negative vehicle control. Cells were harvested following standard trypsin EDTA protocol followed by RNA extraction using the RNeasy Mini Kit (Qiagen, Cat. no. 74104) following manufacturers guidelines. This was followed by cDNA synthesis using Tetro CDNA synthesis kit (Bioline, Cat. no. BIO-65042) following manufacturers guidelines. Cells were exposed each compound and concentration in triplicate and three biological repeats were performed.

2.10.2 PCR Array

Gene expression changes of 84 key genes related to cell cycle progression were investigated through Qiagen RT² Profiler™ PCR Array Human Cell Cycle following the manufacturer's specification (Qiagen, Cat. no. 330231). The entire PCR array was conducted in three separate times for MIA PaCa-2 and once for BxPC3 and CFPAC-1.

2.10.3 Targeted qPCR

Primers for gene clusters identified in STRING analysis and p53 homologs, p63 and p73, were designed in Primer3 (<https://primer3.ut.ee>) following the parameters set by default, primer sequences synthesised (Sigma-Aldrich, UK) detailed in Table 2.1. A

green fluorescent cyanine dye, SYBR Green, with a high affinity for dsDNA was used to quantify gene expression level. Reaction mixture included 50 ng cDNA, 0.5 μ M primer, Brilliant III SYBR Green Master Mix (dNTPs, MgCl_2 and sure start Taq DNA polymerase) (Agilent, Cat. No. 600892), 30 nM ROX reference dye, made up to total volume of 20 μ L with dH_2O . Standard PCR cycling condition for Agilent Aria MX thermocycler were used as recommended by the manufacturer and shown in Table 2.3. A typical PCR protocol includes a denaturation step followed by primer annealing and extension.

Table 2.1. Sequences of primers used for qPCR analysis of STRING clusters including p53 homologs, p63 and p73, and housekeeping genes B2M and TBP.

Gene	Forward Primer	Reverse Primer
BRCA2	GTTTCCACACCTGTCTCAGC	GGTGGAGGTAAAGGCAGTCT
SERT1	GCCGTTTCCTGATTGGTTGT	AGACCCTTGCTCAGCATCTT
HUS1	GACTTGGTGTAGTAGCCAGAA	CGGGGTGAACACACTGAAAT
GADD45A	CACTGTCGGGGTGTACGAAG	CCTGGATCAGGGTGAAGTGG
Casp3	GCCTCTTCCCCATTCTCAT	CTTCCATGTATGATCTTTGGTTCC
MDM2	CGAGCTTGGCTGCTTCTG	GTACGCACTAATCCGGGGAG
CDKN1A	GCCGAAGTCAGTTCCTTGTG	CATGGGTTCTGACGGACATC
CDK2	CATCTTTGCTGAGATGGTGACT	ACTTGGCTTGTAATCAGGCAT
CCNE1	CCCATCATGCCGAGGGAG	CACGTTTGCCTTCCTCTTCC
CDK7	CTCGGGCAAAGCGTTATGAG	CTCTGGCCTTGTAACGGTG
CCNT1	TGGAAAATAGCCCATCCCGT	GTGAGACGTTAAGACGCTGC
CCNG2	AGGTGAGGCTACAGTGATTCC	AGGCACAGATGCCAAACCTA
RBBP8	CTCAGAAAGTGCTCGCTTCC	TCTGCAGAGTTAGGGCTTCC
p63	GCTTATCAACCCTCAGCAGC	ACAATGCTGCAATCTGTGGG
p73	GACGGAATTCACCACCATCC	CCTCATCAGCTTTTCGGTCG
B2M	TTTGGCTCACAGTGTAAGGG	GTCACCCCAACTATGCCATT
TBP	CCGGCTGTTTAACTTCGCTT	CACACGCCAAGAAACAGTGA

Table 2.2. Standard qPCR reaction mixture for genes of interest.

Brilliant III SYBR Green MasterMix	10 μ L
Forward Primer	2 μ L
Reverse Primer	2 μ L
ROX reference dye (2 μ M)	0.3 μ L
cDNA	1 μ L (50 ng)
H ₂ O	4.7 μ L

Table 2.3. PCR cycling program used for Brilliant III SYBR Green Master Mix.

Cycles	Duration	Temperature (°C)
1	3 minutes	95
40	5 seconds	95
	10 seconds	60

2.10.4 p53 Sequencing

Primers designed in Primer3, synthesised (Sigma-Aldrich, UK) and used to sequence and identify p53 missense substitution mutations in PDAC cell lines are shown in Table 2.4. Both sets of primers were used to sequence all three PDAC cell lines covering the mutational regions of interest.

Table 2.4. Sequences of primers used for p53 sequencing in PDAC cell lines.

	Forward Primer	Reverse Primer
Set 1	TCGACATAGTGTGGTGGTGC	AAAGCTGTTCCGTCCCAGTA
Set 2	ACTTTTCGACATAGTGTGGTGG	TCAAAGCTGTTCCGTCCCA

DNA template for each cell line was prepared following RNA extraction and cDNA synthesis described earlier. This was followed by amplification of the region of interest using the Phusion high-fidelity PCR kit (Thermo Fisher Scientific, Cat. no. F553L) and following the manufacturers guidelines. The amplified DNA was diluted in RT-PCR grade water to achieve the desired concentration (3 ng per 10 μ L reaction volume) for sequencing. Each reaction mixture consisted of cDNA template from each cell line, primers, and RT-PCR grade water (Thermo Fisher Scientific, Cat. no. AM9935) to make final volume of 10 μ L (Table 2.5). The samples were submitted to University of Birmingham Genomic Facility for sequencing.

Table 2.5. Reaction mixture for p53 sequencing.

DNA template (100-200 bp)	3 ng
Primer (Forward)	3.2 pmol
Primer (Reverse)	3.2 pmol
RT-PCR grade water	Make up to 10 μ L

2.10.5 Statistical analysis

The results were relatively quantified using the delta delta Ct, $2^{-\Delta\Delta Ct}$, method¹³. For PCR array, *GAPDH* was used as an endogenous control while *B2M* was the chosen endogenous control for the targeted qPCR assays as the expression levels of these housekeeping genes were stable in treated and untreated samples. For p53 sequencing, the raw files were analysed in SnapGene (<https://www.snapgene.com/snapgene-viewer/>).

2.11 References

1. M. K. Ismail, Z. Khan, M. Rana, S. L. Horswell, L. Male, H. V. Nguyen, A. Perotti, I. Romero-Canelón, E. A. Wilkinson, N. J. Hodges and J. H. R. Tucker, *ChemBioChem*, 2020, **21**, 2487-2494.
2. J. L. Kedge, H. V. Nguyen, Z. Khan, L. Male, M. K. I. Hodges, Holly V. Roberts, Nikolas J., S. L. Horswell, Y. Mehellou and J. H. R. Tucker, *Eur. J. Inorg. Chem.*, 2017, **2017**, 466-476.
3. H. V. Nguyen, A. Sallustrau, J. Balzarini, M. R. Bedford, J. C. Eden, N. Georgousi, N. J. Hodges, J. Kedge, Y. Mehellou, C. Tselepis and J. H. R. Tucker, *J. Med. Chem.*, 2014, **57**, 5817-5822.
4. T. Mosmann, *J. Immunol. Methods*, 1983, **65**, 55-63.
5. S. Aykul and E. Martinez-Hackert, *Anal. Biochem.*, 2016, **508**, 97-103.
6. K. R. Roell, D. M. Reif and A. A. Motsinger-Reif, *Front. Pharmacol.*, 2017, **8**, 158-158.
7. L. Zhao, J. L. S. Au and M. G. Wientjes, *Front. Biosci., Elite Ed.*, 2010, **2**, 241-249.
8. S. Lederer, T. M. H. Dijkstra and T. Heskes, *Front. Pharmacol.*, 2018, **9**.
9. K. M. McKinnon, *Curr Protoc Immunol*, 2018, **120**, 5.1.1-5.1.11.
10. L. C. Crowley, B. J. Marfell, A. P. Scott and N. J. Waterhouse, *Cold Spring Harb Protoc*, 2016, **2016**.
11. J. Nieminuszczy, R. A. Schwab and W. Niedzwiedz, *Methods*, 2016, **108**, 92-98.
12. M. M. Bradford, *Anal. Biochem.*, 1976, **72**, 248-254.
13. K. J. Livak and T. D. Schmittgen, *Methods*, 2001, **25**, 402-408.

Chapter 3 – *In vitro* Drug Metabolism and Pharmacokinetic studies (DMPK) with TUC-1

3.1 Introduction

Pharmacological assessment of a drug is the combination of two main disciplines: pharmacokinetics (PK) and pharmacodynamics (PD). While PK aims to understand the movement and modification to the drug by a biological system, PD is the study of the effect of the drug at the site of action¹. Drug metabolism and pharmacokinetic (DMPK) studies of a lead compound encompass the absorption, distribution, metabolism, and excretion (ADME) properties that, altogether, predict the *in vivo* bioavailability, efficacy, and safety of a drug.

This chapter evaluates DMPK properties of TUC-1 including Log D, aqueous kinetic solubility, stability in hepatocytes and blood, plasma protein binding, blood-plasma ratio, and identification of the top 3 metabolites. These parameters are determined in human (mixed sex or male), mouse (male) and rat (male) models and statistically significant species differences for TUC-1 are reported, control compounds shown for comparison. The experimental work presented in this chapter was carried out by Sygnature Discovery, a leading contract research organisation and data analysed as part of this thesis is reported in this chapter with raw data presented in appendices. Below follows a discussion of the parameters quantified and a description of the methods used to obtain the data presented.

Log D is an important PK parameter indicative of the lipophilicity of a compound. The concentration of the test compound at equilibrium in aqueous (phosphate buffer saline) and lipophilic (octanol) phases are quantified by liquid chromatography-mass spectrometry (LC/MS). If ionisable groups are present, Log D is dependent on the pH of the aqueous phase therefore the pH that the assay was undertaken is also specified. For TUC-1, log D was measured at the physiological pH 7.4 and was calculated as shown in equation 1:

$$\text{Log } D_{7.4} = \log \frac{[TUC-1]_{\text{octanol}}}{[TUC-1]_{\text{buffer}}} \quad \text{Equation 1}$$

Log D value of >3.5 is indicative of high lipophilicity and poor aqueous solubility which may result in high plasma protein binding². A log D value of 1-3 is considered optimal for oral drugs as it allows tissue permeability, solubility, and associated with slow drug metabolism. Lipophilic compounds with a log D value of > 5 have been associated with poor clearance, accumulation in lipid rich tissues and toxicity which is often clinically unfavourable².

Kinetic aqueous solubility, influenced by Log D, pH, and temperature, is an important property that can impede *in vitro* assays, oral administration and absorption of a compound³. Kinetic solubility assays measure the rate of precipitation following dilution of compound in an aqueous buffer. Kinetic solubility values of < 1 µM are indicative of insolubility while values between 1-100 µM are considered moderately soluble and values greater than 100 µM indicate that compounds are highly aqueously soluble. For TUC-1 kinetic solubility, a turbidimetric assay was performed

which quantifies dispersion of light because of precipitation. Solubility was measured in phosphate buffer saline (pH 7.4) with 2% v/v DMSO.

Compound stability in blood and hepatocytes is also paramount as it directly impacts bioavailability and therapeutic window of a drug. Blood stability measures the rate of degradation in blood *in vitro* which helps predict *in vivo* compound stability. Typically the percentage compound remaining over time and half-life is calculated following quantification by MS⁴. The liver is the primary site of drug metabolism *in vivo*. Almost 60% of the marketed drugs undergo metabolism by hepatocytes mediated by cytochrome P450 enzymes⁵. Therefore, clearance of test compound by primary hepatocytes *in vitro* is indicative of potential for drug metabolism *in vivo*.

To investigate clearance by metabolism of TUC-1, hepatic stability assay was performed measuring *in vitro* intrinsic clearance (CL_{int}) and half-life ($t_{1/2}$) by quantifying the rate of compound disappearance in primary hepatocyte cultures via MS. Half-life, the time taken for drug concentration to decrease by half⁶, is indicative of the rate of metabolism and clearance from the body. It is critical to understand the half-life of a drug so that the dosing regimen can be designed to ensure adequate blood levels for clinical benefit. Typically only 3% of the initial drug is found in circulation following 5 half-lives⁶. Intrinsic clearance, combined with half-life, serves as an indicator of the rate of hepatic metabolism. This can be used to predict *in vivo* hepatic clearance using the well stirred model⁷. Additionally, compounds can be identified as high, medium, or low clearance based on the classification system shown in Table 3.1⁷. Hepatic clearance studies were carried out in cryopreserved

primary hepatocytes from human (mixed sex), mouse C57Bl6 (male) and rat/Sprague Dawley (male) species.

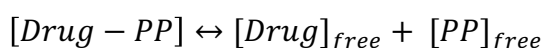
Table 3.1. Clearance categories for compounds based on species specific intrinsic clearance by hepatocytes.
*Values (assuming fraction unbound = 1) at or below lower limit of experiment

Clearance	Intrinsic Clearance ($\mu\text{L}/\text{min}/10^6$ cells)				
Category	Human	Monkey	Dog	Rat	Mouse
Low	<3.5*	<5.2	<1.9*	<5.1	<3.3*
High	>19.0	>28.3	>10.5	>27.5	>17.8

Most drugs are subjected to biotransformation by hepatocytes. These catalytic transformations are divided into two phases: Phase I and Phase II metabolism. Phase I metabolism is the chemical modification of the drug via oxidation, hydrolysis, or reduction, yielding a polar metabolite^{8,9}. Phase I reactions are catalysed principally by cytochrome P450 enzymes, particularly CYP 1-4 families^{8,9}. Prodrugs rely on metabolism to form the active metabolite, for example, codeine which is dealkylated to morphine and norcodeine by CYP2D6 and CYP3A4 respectively¹⁰. Phase II reactions involve conjugation with a polar moiety such as amino acids, glucuronide, glutathione, and sulphate, resulting in water-soluble metabolites that are readily excreted either by the kidney (urine) or the liver (bile)^{8,9}. This is mediated by a different group of enzymes including: glucuronyl transferases, sulfotransferases, glutathione S-transferases and N-acetyltransferases^{8,9}. It is important to identify these resulting metabolites as, if toxic, they can lead to adverse side effects which are clinically unfavourable. In this chapter, major metabolites of TUC-1 are identified following hepatocyte exposure and quantification by MS.

Blood-plasma ratio is the distribution of the drug found in whole blood compared to plasma¹¹. Many drugs strongly bind red blood cells in whole blood, reducing the plasma concentration which leads to inaccurate estimation of other PK parameters such as clearance. Distribution of the drug in each biofluid is quantified by LC/MS with a value > 1 indicative of high red blood cell affinity and possible sequestration¹².

Drugs can also interact with plasma proteins (PP) which also affect distribution and bioavailability as drug-PP complexes cannot passively diffuse across cell membranes. There are different types of proteins that may bind to a drug such as globulins, lipoproteins, albumin¹ and α -1 acid glycoprotein¹³. Generally, acidic, or neutral drugs favour albumin while basic drugs interact with α -1 acid glycoprotein⁶. If this interaction is reversible, the protein-bound and free drug exist in an equilibrium:



Therefore, higher plasma protein binding (PPB) means less free drug is available for passive diffusion hence lower penetrance⁵. Conversely, a high free drug concentration can result in faster metabolism, clearance, and shorter half-life. Drug bound to plasma proteins serves as a reservoir, releasing the drug in a controlled manner to maintain an optimal free drug concentration, delaying metabolism and clearance hence retained long enough to exert its biological effect. PPB percentage of <85% is clinically favourable⁵. PPB can be measured by different assays including rapid equilibrium dialysis (RED)¹⁴ used to monitor PPB of TUC-1. This involves two adjacent chambers partitioned by a membrane as protein and drug sample is added

to one vessel. The free drug can move across the membrane while protein-bound drug is unable to diffuse. Time is given to establish equilibrium before detecting protein-bound and free drug concentrations.

3.2 Results

The results presented in this section have been statistically analysed with standard deviations shown. However, the data points represent $n=2$ as only two independent biological repeats were performed by Sygnature Discovery.

3.2.1 Log $D_{7.4}$ and kinetic aqueous solubility

Log $D_{7.4}$ of TUC-1 was measured by quantifying distribution at equilibrium of the compound between phosphate buffer at pH 7.4 and octanol phases. As shown in Figure 3.1, log $D_{7.4}$ of TUC-1 was 2.76 ± 0.04 compared to 2.60 ± 0.0003 for verapamil and 1.21 ± 0.002 for the beta-blocker propranolol, widely used and orally prescribed drugs¹⁵. The antifungal agent ketoconazole¹⁶ was used as a control compound with poor aqueous solubility giving a log D value of 3.38 ± 0.02 (Figure 3.1).

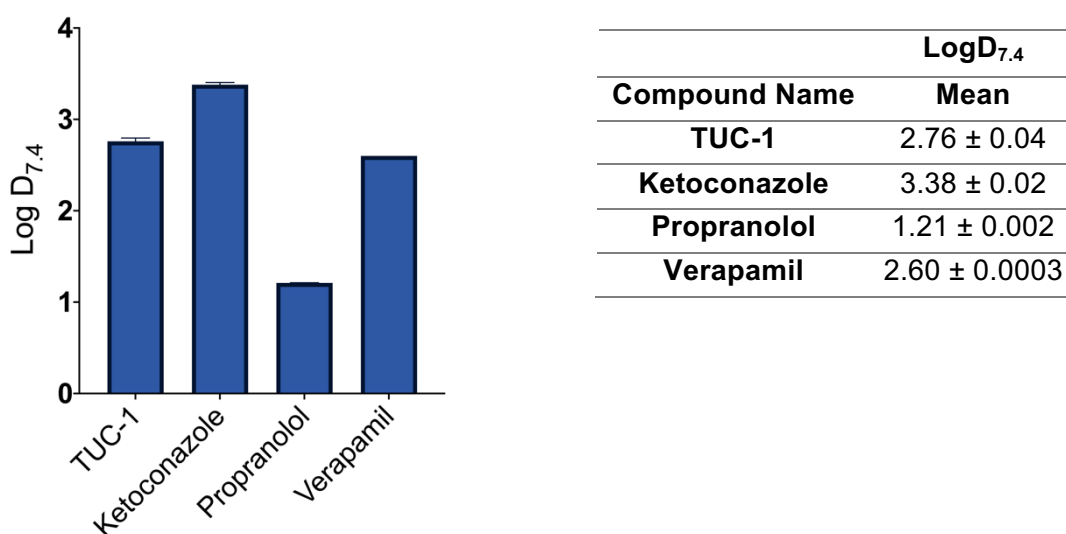


Figure 3.1. Calculated log D (pH 7.4) of TUC-1 compared to control compounds. The results represent the mean of two independent biological experiments (\pm SD, $n = 2$).

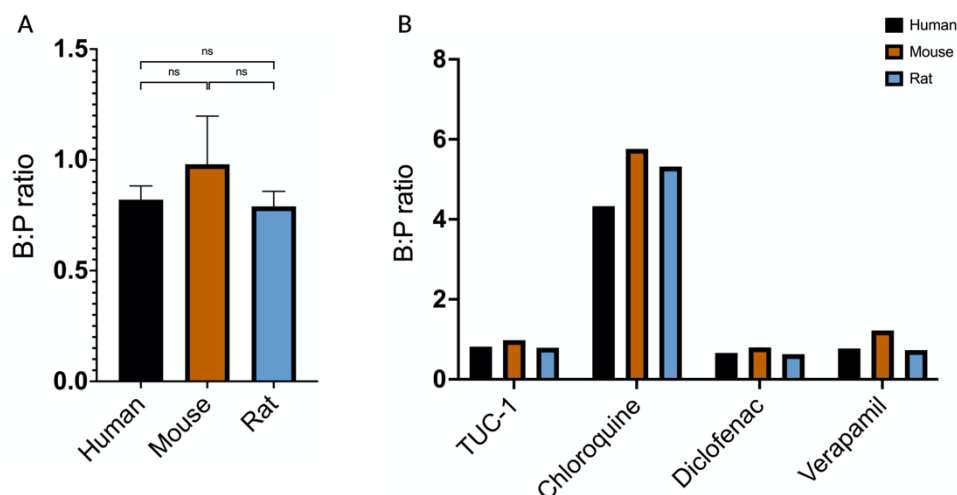
Next, the kinetic aqueous solubility of TUC-1 was investigated by diluting 20 mM DMSO stock solution in PBS (pH 7.4) containing 2% v/v DMSO prior to UV detection. As shown in Table 3.2, TUC-1 was highly soluble with a kinetic solubility of >200 μ M, which is comparable to the anti-inflammatory drug diclofenac. In comparison, the basic control compound 4,5-Diphenylimidazole¹⁷ and the antifungal agent ketoconazole had kinetic solubility values of 25 and 132 μ M respectively.

Table 3.2. Kinetic aqueous solubility of TUC-1 compared to control compounds.

Compound	Kinetic Solubility (μ M)
TUC-1	>200
Diclofenac	>200
DPI	25
Ketoconazole	132

3.2.2 Blood-plasma ratio and plasma protein binding

Distribution of TUC-1 in whole blood and plasma was investigated in human (male), mouse C57Bl6 (male) and rat/Sprague Dawley (male) models. As shown in Figure 3.2, TUC-1 blood-to-plasma ratios were 0.82, 0.98 and 0.79 in human, mouse, and rat models respectively with no statistically significant difference between species (P = 0.43, one-way ANOVA followed by Tukey's multiple comparison test). This is compared to diclofenac, an anti-inflammatory drug¹⁸, and verapamil with ratios of 0.66, 0.80 and 0.63 for diclofenac, and 0.77, 1.22 and 0.73 for verapamil in human, mouse, and rat models respectively (Figure 3.2). Additionally, the antimalarial drug chloroquine was used as an additional control because of its known high affinity for red blood cells¹⁹. This was confirmed with high blood-to-plasma ratios, reported to be 4.33, 5.76 and 5.32 in human, mouse, and rat models respectively (Figure 3.2).



Blood plasma ratio			
	Human	Mouse	Rat
TUC-1	0.82	0.98	0.79
Chloroquine	4.33	5.76	5.32
Diclofenac	0.66	0.80	0.63
Verapamil	0.77	1.22	0.73

Figure 3.2. Blood-plasma ratio of (A) TUC-1 and (B) control compounds in human (male), mouse (male) and rat (male) models. The results represent the mean of two independent biological experiments (\pm SD, $n = 2$).

Plasma protein binding of TUC-1 was studied in *in vitro* human (mixed sex), mouse C57Bl6 (male) and rat/Sprague Dawley (male) models. In the data shown (Figure 3.3, Table 3.3), percentage of drug bound to plasma proteins is indicative drug-protein complex concentration hence informing about the PPB of TUC-1. Percentage of TUC-1 bound to plasma proteins was 94.7 ± 0.3 , 91.5 ± 0.0 and 89.0 ± 0.1 in human, mouse, and rat models respectively. This is compared to the PPB of verapamil, calcium channel blocker clinically used to treat angina²⁰, as 93.8 ± 0.1 , 91.7 ± 0.4 and $90.9 \pm 0.3\%$ of the total drug bound to plasma proteins in human,

mouse, and rat models respectively (Figure 3.3). Warfarin, an anticoagulant clinically used to treat blood clots²¹, has been previously shown to strongly bind to plasma proteins resulting in a low free drug concentration and narrow therapeutic window²¹. This agent was used as a positive control in this data which confirms its high affinity for plasma proteins with percentage bound values of >99.0, 94.0 and >99.0% in human, mouse, and rat models respectively (Figure 3.3). Table 3.3 also shows the fraction unbound of each compound calculated as a ratio of the free (unbound) compound compared to the total plasma concentration²². Similar values were obtained for TUC-1 and clinical drug verapamil. The fraction unbound for TUC-1 was 0.053 ± 0.003 , 0.085 ± 0.0 and 0.110 ± 0.001 compared to 0.062 ± 0.001 , 0.083 ± 0.004 and 0.091 ± 0.003 for verapamil in human, mouse, and rat models respectively. Differences between each species for each compound were identified as statistically significant as determined using one-way ANOVA followed by Tukey's multiple comparison test.

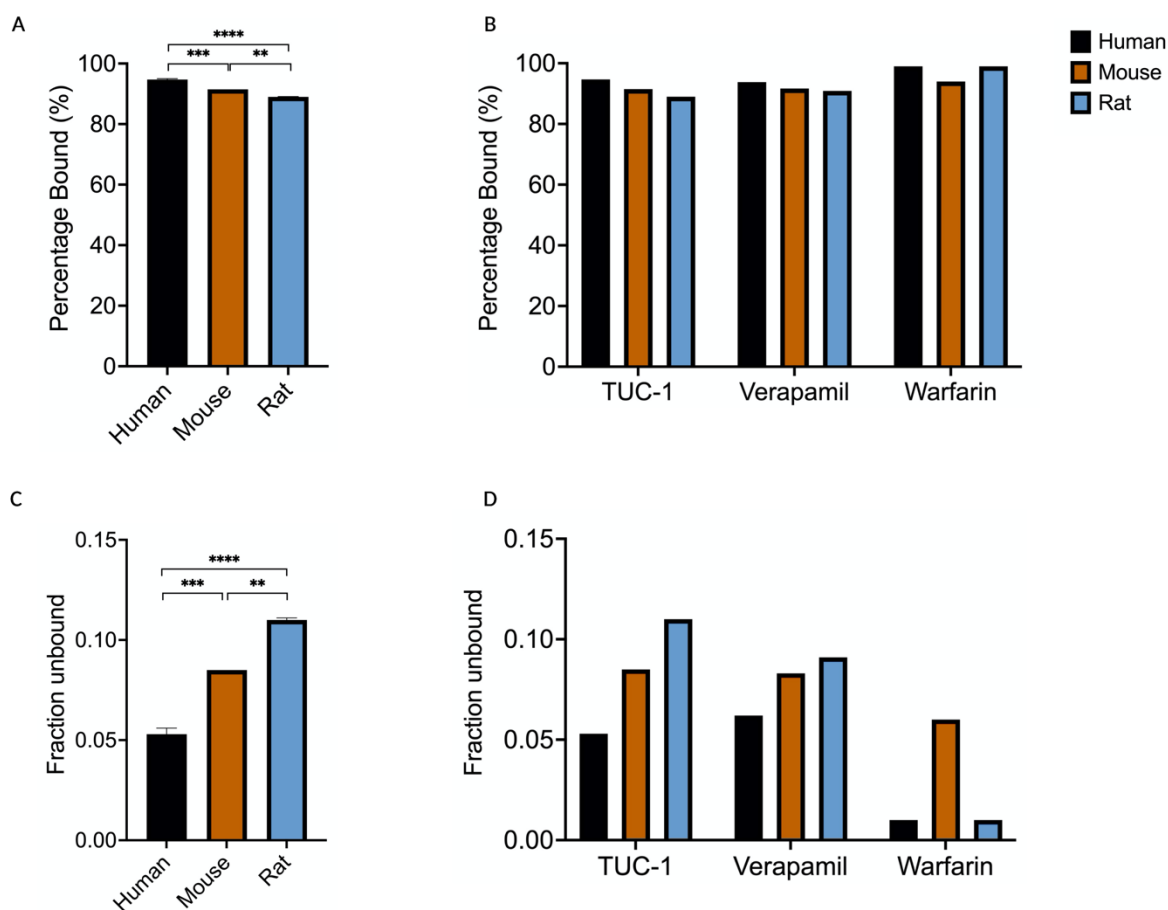


Figure 3.3. Plasma protein binding of TUC-1 showing (A) the percentage of compound and (C) fraction unbound in human (mixed), mouse (male) and rat (male) models compared to control compounds verapamil and warfarin (B, D). The results represent the mean of two independent biological experiments (\pm SD, $n = 2$). *** and **** Statistically significant differences, $P < 0.001$ and 0.0001 respectively as assessed by one-way ANOVA followed by Tukey's multiple comparisons test.

Table 3.3. Fraction unbound and percentage bound (%) values of TUC-1 and control compounds verapamil and warfarin in human, mouse, and rat models. The results represent the mean of two independent biological experiments (\pm SD, $n=2$).

Compound	Fraction Unbound			Percentage Bound (%)		
	Human	Mouse	Rat	Human	Mouse	Rat
TUC-1	0.053±0.003	0.085±0.0	0.110±0.001	94.7±0.3	91.5±0.0	89.0±0.1
Verapamil	0.062±0.001	0.083±0.004	0.091±0.003	93.8±0.1	91.7±0.4	90.9±0.3
Warfarin	<0.010±0.0	0.060±0.004	<0.010±0.0	>99.0±0.0	94.0±0.0	>99.0±0.0

3.2.3 TUC-1 stability

Stability of TUC-1 was investigated in whole blood samples and primary hepatocyte cultures to investigate stability in the blood and hepatic metabolism respectively. The blood stability of TUC-1 was evaluated in blood samples from human (male), mouse C57BL6 (male) and rat/Sprague Dawley (male) species. TUC-1 and positive control compounds were incubated in blood at 37°C for 60 minutes and the percentage of compound remaining quantified by MS. The percentage remaining was calculated compared to sample at 2 minutes which was set to 100%.

As shown in Figure 3.4A, TUC-1 displays considerable blood stability with 79.4% of the compound remaining after 60 minutes incubation with human blood sample. This was also observed for mouse and rat species with 105.6 and 87.5% compound remaining after 60 minutes. No statistically significant differences were found between species ($P = 0.07$, one-way ANOVA). Blood stability is also evident when compared to control compounds (Figure 3.4B) that show a steady decline in percentage remaining over 60-minute incubation. The half-life of TUC-1 in the blood sample of the three species was also calculated and reported as >144.2, >180.0 and >180.0 minutes in human, mouse, and rat models respectively (Table 3.4). This is compared to the control compound propantheline with a half-life of 65.9 ± 0.3 and 23.1 ± 0.2 minutes in human and mouse models respectively. Imidapril was also used as a positive control for rat species and had a half-life in blood of 7.5 ± 0.1 minutes (Table 3.4).

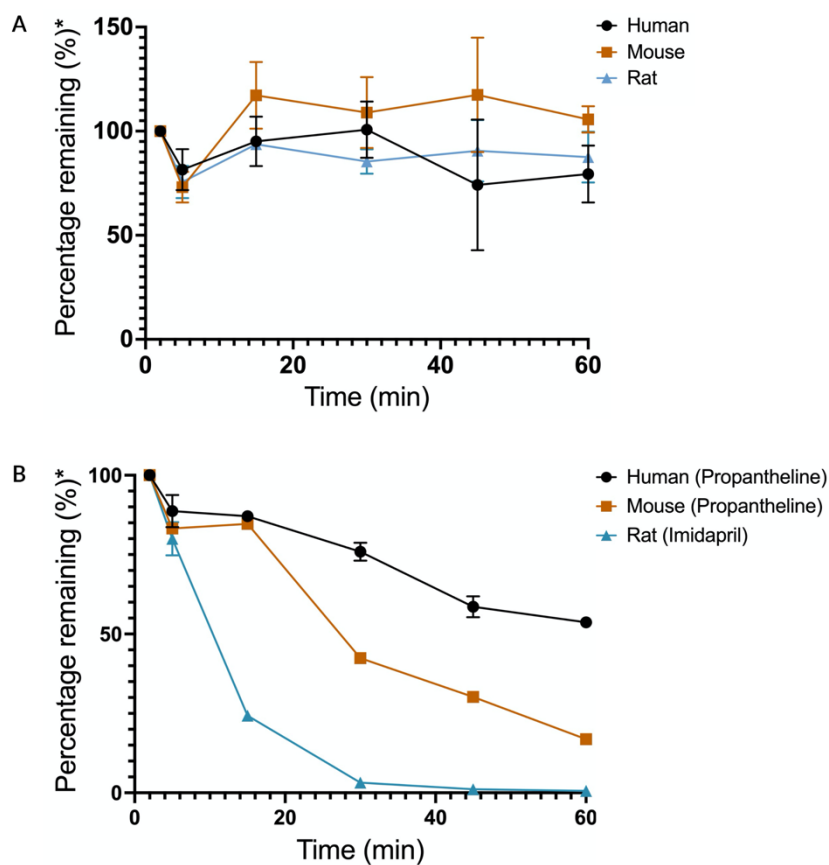
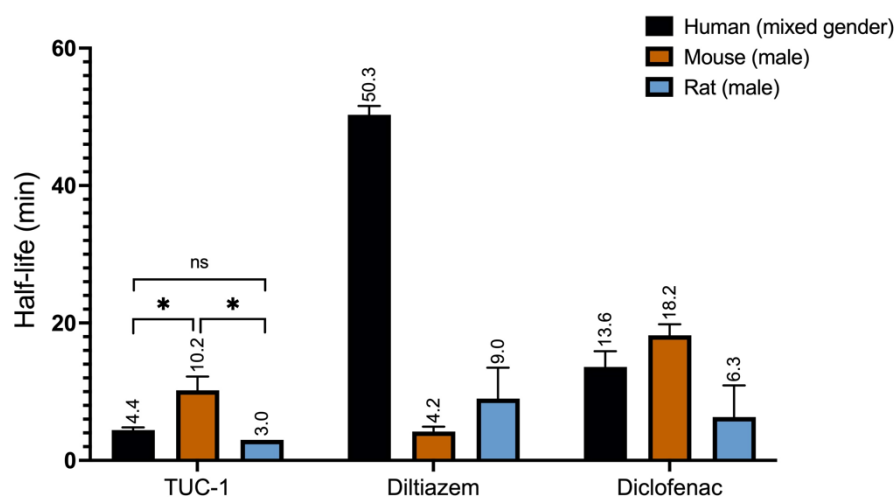


Figure 3.4. Blood stability of (A) TUC-1 and (B) control compounds propantheline and imidapril in human, mouse, and rat blood. The results represent the mean of two independent biological experiments (mean \pm SD, n = 2)
 *Percentage remaining calculated with 2-minute sample as 100%.

Table 3.4. Half-life of TUC-1 in human, mouse, and rat blood (n=2, mean \pm SD) compared to control compounds.

Compound Name	Blood Stability - Half-Life (min)		
	Human	Mouse	Rat
TUC-1	>144.2	>180.0	>180.0
Propantheline	65.9 \pm 0.3	23.1 \pm 0.2	-
Imidapril	-	-	7.5 \pm 0.1

TUC-1 hepatocyte clearance was evaluated in cryopreserved primary hepatocytes from human (mixed sex), mouse C57Bl6 (male) and rat/Sprague Dawley (male) species. The two parameters calculated in this assay were half-life and intrinsic clearance of test compound. As shown in Figure 3.5, TUC-1 had a half-life of 4.4 ± 0.4 , 10.2 ± 2.0 and <3.0 minutes in human, mouse, and rat species respectively. While the difference in half-life between human and mouse was statistically significant ($P = 0.03$, one-way ANOVA followed by Tukey's multiple comparison test), the difference between human and rat was not statistically significant ($P = 0.53$). Compared to the control compounds shown in Figure 3.5, TUC-1 had the shortest half-life in all three species tested.



	Half-Life (min)		
	Human	Mouse	Rat
TUC-1	4.4±0.4	10.2±2.0	<3.0
Diltiazem	50.3±1.3	4.2±0.7	9.0±4.5
Diclofenac	13.6±2.3	18.2±1.6	6.3±4.6

Figure 3.5. Half-life of TUC-1 and control compounds as assessed in cryopreserved hepatocytes from human (mixed sex), mouse (male) and rat (male). The results represent the mean of two independent biological experiments (mean \pm SD, n = 2). * Statistically significant inter-species differences are assessed for TUC-1 ($P < 0.05$, one-way ANOVA followed by Tukey's multiple comparison test).

Following this, *in vitro* intrinsic clearance (CL'_{int}) by the hepatocytes was calculated. TUC-1 had the highest CL'_{int} in rat followed by human and mice with values of >460.0, 370.5 and 172.3 $\mu\text{L}/\text{min}/\text{million cells}$ respectively (Figure 3.6). According to the intrinsic clearance classification model (Table 3.1), TUC-1 can be classified as high clearance in human, mouse, and rat models.

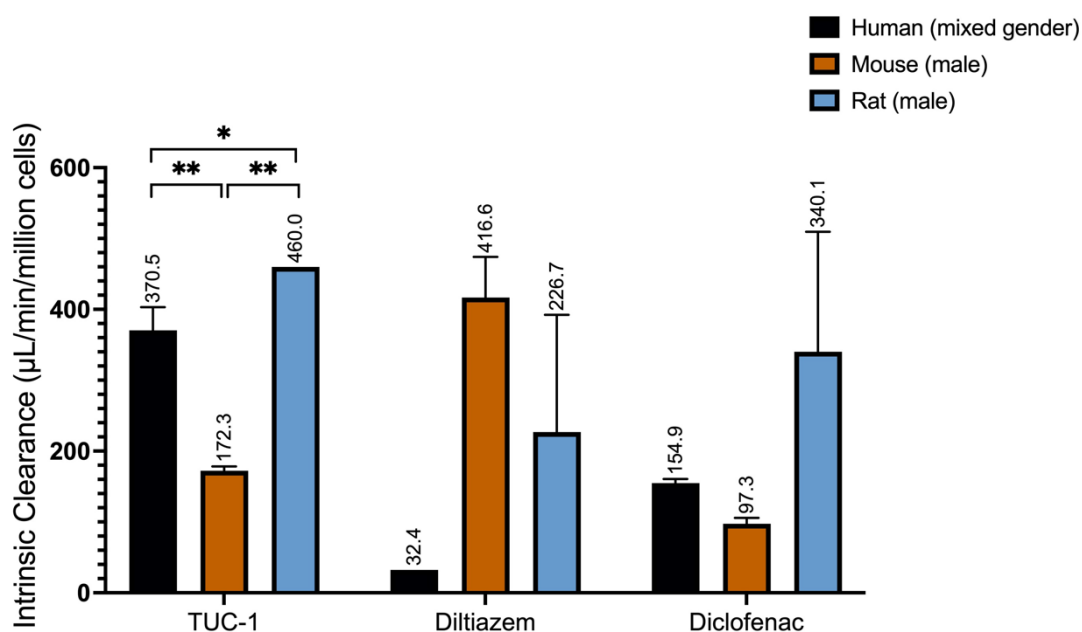


Figure 3.6. Intrinsic clearance of TUC-1 and control compounds as assessed in cryopreserved hepatocytes from human (mixed sex), mouse (male) and rat (male). The results represent the mean of two independent biological experiments (\pm SD, n = 2). *, ** Statistically significant inter-species differences are assessed for TUC-1 (P<0.05, one-way ANOVA followed by Tukey's multiple comparison test).

Human *in vitro* intrinsic clearance can be used to predict *in vivo* hepatic clearance using the well stirred model⁷. This was calculated by scaling up *in vitro* CL'_{int} to *in vivo* CL_{int} , 442 μ L/min/million cells (Equation 2) and calculating *in vivo* hepatic clearance (Equation 3):

$$CL_{int} = \frac{N_H}{N_S} CL'_{int} \quad \text{Equation 2}$$

$$CL_{hepatic} = \frac{Q \times CL_{int}}{Q + CL'_{int}} \quad \text{Equation 3}$$

Where:

CL'_{int} = *in vitro* intrinsic clearance (370.5 $\mu\text{L}/\text{min}/\text{million cells}$)

CL_{int} = *in vivo* intrinsic clearance ($\mu\text{L}/\text{min}/\text{million cells}$)

N_H = number of hepatocytes in an average human liver (1.8×10^{11} cells)

N_S = number of hepatocytes in *in vitro* assay (0.21×10^6 cells)

$CL_{hepatic}$ = hepatic clearance ($\text{mL}/\text{min}/\text{kg}$)

Q = hepatic blood flow rate (901 h^{-1})

Therefore, the *in vivo* hepatic clearance of TUC-1 is calculated to be 313 $\text{mL}/\text{min}/\text{kg}$, similar to the intrinsic clearance determined *in vitro*. Following this, the hepatic extraction ratio was calculated (Equation 4) which is an indicator of the fraction of drug removed from systemic circulation during a single pass of blood through the liver, values ranging from 0 (no elimination) to 1 (complete elimination)²³.

$$E_H = \frac{fu \times CL_{int}}{Q_H + fu \times CL_{int}} \quad \text{Equation 4}$$

Where:

CL_{int} = *in vivo* intrinsic clearance (442 $\mu\text{L}/\text{min}/\text{million cells}$)

fu = fraction unbound (TUC-1 0.053)

Q_H = hepatic blood flow rate (901 h^{-1})

E_H = hepatic extraction ratio

The hepatic extraction ratio for TUC-1 is calculated to be 0.025 indicative of low hepatic elimination.

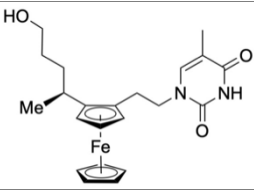
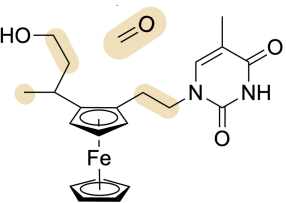
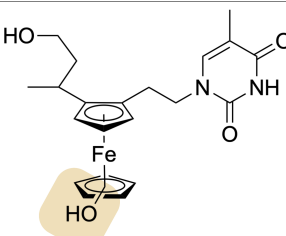
3.2.4 Metabolite identification

The three most prevalent metabolites of TUC-1 were identified using human (mixed sex), mouse C57Bl6 (male) and rat/Sprague Dawley (male) hepatocytes. Metabolites were identified following 1 μ M TUC-1 treatment of hepatocytes and MS analysis.

Metabolite data is presented as percentage of the total compound related MS response in the test sample. As shown in Table 3.5, a glucuronide metabolite of TUC-1 (M2) was the major metabolite identified in human hepatocytes and represented 76% of the compound in the test sample. This metabolite was also observed in rat hepatocytes where it comprised 96% of metabolites identified. In contrast, it was not a major metabolite in mouse hepatocytes where it formed 16% of metabolites identified.

The only other metabolite detected in human hepatocytes was M1, a hydroxylation metabolite at an indetermined position on the alkyl chain of TUC-1 which represented 24% of TUC-1 metabolites. Metabolite M1 was also detected in mouse and rats albeit to a lesser extent, forming 16 and 4% of metabolites respectively. TUC-1 was not as readily metabolised by mouse hepatocytes with 64% of parent compound recovered. Additionally, low levels (3%) of a different glucuronide metabolite (M3) following hydroxylation of the ferrocene ring of TUC-1 was only detected in mouse hepatocytes.

Table 3.5. Summary of the top three metabolites with tentative structures assigned, quantification is based on the mass spectrometric (MS) response; quantification of these metabolites is quoted as a percentage of total compound related material in the test sample.

Peak Identifier	Ion (m/z)	Fragment ions	Assignment	Percentage profile (%)		
				Human	Mouse	Rat
TUC-1	410	359, 345, 299, 284		ND	64	ND
M1	424	359, 343, 331, 317, 299, 298		24	16	4
M2	586	460, 410, 345, 284	Glucuronide of TUC-1	76	16	96
M3	602	426, 345	 Glucuronide	ND	3	ND

3.3 Discussion

This chapter has evaluated DMPK properties of TUC-1 studied *in vitro* in human, mouse, and rat models with the aim to assess its suitability as a drug candidate and to identify a suitable *in vivo* model for efficacy and safety studies. TUC-1 exhibits lipophilicity in the optimal range ($1-3^{24}$) with a clinically favourable log $D_{7.4}$ of 2.76 which is comparable to the predicted log D_7 of 1.76 and 0.87 for the nucleoside analogues gemcitabine and 5-fluorouracil respectively

(<https://disco.chemaxon.com/calculators/demo/plugins/logd/>).

Previously, a negative correlation between log D and drug efficacy has been established by linear regression for anti-cancer agent camptothecin and its analogues²⁵. It has been proposed that physiochemical properties like log D are at least as important as *in vitro* IC_{50} values for the prediction of *in vivo* drug efficacy²⁵. It is also known that highly lipophilic drugs ($\log D > 5$) have reduced systemic clearance increasing the potential for drug-induced toxicity²⁵. Additionally, TUC-1 is also highly soluble in aqueous medium ($>200 \mu\text{M}$) which is also an important property for drug formulation as insoluble anticancer agents such as paclitaxel (aqueous solubility $< 0.1 \text{ mg/mL}^{26, 27}$) creates challenges for drug delivery. A drug showing solubility $>10 \mu\text{M}$ is considered eligible for pre-clinical assessment²⁸. Considering these factors, TUC-1 with a log $D_{7.4}$ 2.76 ± 0.04 and aqueous solubility $> 200 \mu\text{M}$ is a clinically viable candidate providing a balance between lipophilicity which will assist intestinal absorption and aqueous solubility that supports clearance.

Additionally, the human and rat blood to plasma ratios of TUC-1 were also similar compared to mouse although the interspecies differences were not statistically significant. As all blood to plasma ratios were below 1, it suggests TUC-1 does not bind red blood cells however there is evidence of plasma protein binding (PPB). This was confirmed by rapid equilibrium dialysis where TUC-1 showed strong binding to plasma proteins. Anticancer agents display a wide range in their PPB as some agents such as bleomycin show no binding compared to strong binding agents like vinblastine²⁹. Cisplatin has a similar PPB compared to TUC-1, >90% plasma protein bound³⁰, whereas nucleoside analogue gemcitabine exhibits low PPB (10%) (http://www.bccancer.bc.ca/drug-database-site/Drug%20Index/Gemcitabine_monograph.pdf).

Plasma protein concentration is highly variable between patients as some PPs, for example α -1 acid glycoprotein, are generally elevated in cancer cells. However, the degree of elevation varies between patients. This dictates the free drug concentration that is available for biological activity. Therefore, PPB is considered clinically significant in cases where the drugs bind PPs irreversibly or binding is PP concentration dependent. Drugs like camptothecin undergo conversion and drug formulation controls unbound drug concentration²⁹. Hence, without investigating these factors and determination of tissue permeability, PPB cannot be indicative of the efficacy of TUC-1.

TUC-1 also demonstrates good blood stability unlike control compound propantheline which displays instability supported by *in vivo* evidence of poor systemic

bioavailability leading to rapid distribution and elimination³¹. This suggests TUC-1 is not subjected to enzymatic degradation in the plasma which directly impacts bioavailability. While TUC-1 is stable in the blood, it is metabolically unstable in human, rat and to a lesser extent mouse hepatocytes. Rapid metabolism is accompanied with high intrinsic clearance which suggests biotransformation of TUC-1 may limit bioavailability of the parent compound *in vivo*^{32, 33}. However, the intrinsic clearance of TUC-1 in mouse and rat models is comparable to existing drugs diltiazem and diclofenac which supports the clinical suitability of TUC-1.

Metabolite profile evaluation is performed in drug development to identify species differences in metabolism to support *in vivo* model development and to identify potentially toxic metabolites. In cancer development, drug metabolism has been implicated in promoting multidrug resistance. For example, glutathione conjugation to cisplatin results in ABC transporter mediated efflux of the drug impeding its therapeutic effect³⁴. Additionally, upregulation of drug inactivating cytochrome P450s CYP3A4, CYP2C8 and CYP3A5 have been identified as one of the major factors promoting resistance to taxane family of chemotherapeutics³⁵.

In this study, a glucuronide of TUC-1 was the major metabolite in both human and rat but not mouse hepatocytes, confirming the importance of phase II metabolism. Although the exact chemical structure of the metabolite (M2) could not be determined, glucuronidation of the hydroxy alkyl chain of TUC-1 seems most likely. Glucuronidation involves conjugation of glucuronic acid to a substrate, either untransformed drug or phase I metabolite, increasing the hydrophilicity of the drug

prior to elimination. Anticancer drug irinotecan also undergoes inactivating glucuronidation catalysed by uridine diphosphate glucuronosyltransferase UGT1A1³⁶. Genetic polymorphism in UGT1A1, particularly the UGT1A1*28 variant, has been shown to improve irinotecan sensitivity and patient outcome³⁶. Altogether, this does not exclude TUC-1 as a potential candidate as, in addition to irinotecan, clinically used anticancer agents such as nucleoside analogue 5'-deoxy-5-fluorouridine and metalloid drug cisplatin, are also commonly biotransformed by hepatocytes yielding 4 and 31 different metabolites respectively³⁷.

Species differences were also identified in the hepatic metabolism of TUC-1 which can be attributed to different metabolic pathways and isoforms of cytochrome P450 enzymes. For example, human hepatocytes express CYP2D6, 2C19, 2C9 and 3A4 exclusively, not found in mouse and rat hepatocytes³⁷. Differences in phase I metabolism between species are likely to explain the qualitative differences in formation of metabolite M1 (alkyl chain oxidation) and the formation of metabolites M3 (glucuronidation of ring hydroxylation metabolite) for TUC-1 which was only identified in mouse hepatocytes (Figure 7). Interspecies differences in metabolism are a common observation previously reported for many drugs such as flutamide and β -lapachone³⁷⁻³⁹. Qualitative differences were also observed in the major metabolite M2 of TUC-1 where the rat hepatic metabolic profile is more similar to human hepatocytes. In contrast, TUC-1 was overall metabolised to a lesser extent than the other two species where TUC-1 remained largely untransformed (64%). The existing data suggest that the rat would be preferable for studies of TUC-1 *in vivo* and this will be valuable when the project reaches the stage of evaluating toxicology.

However, genetically modified mice are the chosen pre-clinical model for pancreatic cancer⁴⁰. These mice carry mutations in key genes such as *KRAS* implicated in the development of PDAC thus provide a model accurately mimicking disease pathology⁴⁰. Therefore, evaluation of TUC-1 efficacy in this *in vivo* model would provide a better preclinical assessment of its activity against PDAC. The results presented here will be invaluable in interpreting efficacy data in such mouse models. While most pharmacokinetic properties of TUC-1 are clinically favourable, others such as poor metabolic stability and high metabolism, as observed with other chemotherapeutic agents such as gemcitabine⁴¹, can present a potential hinderance.

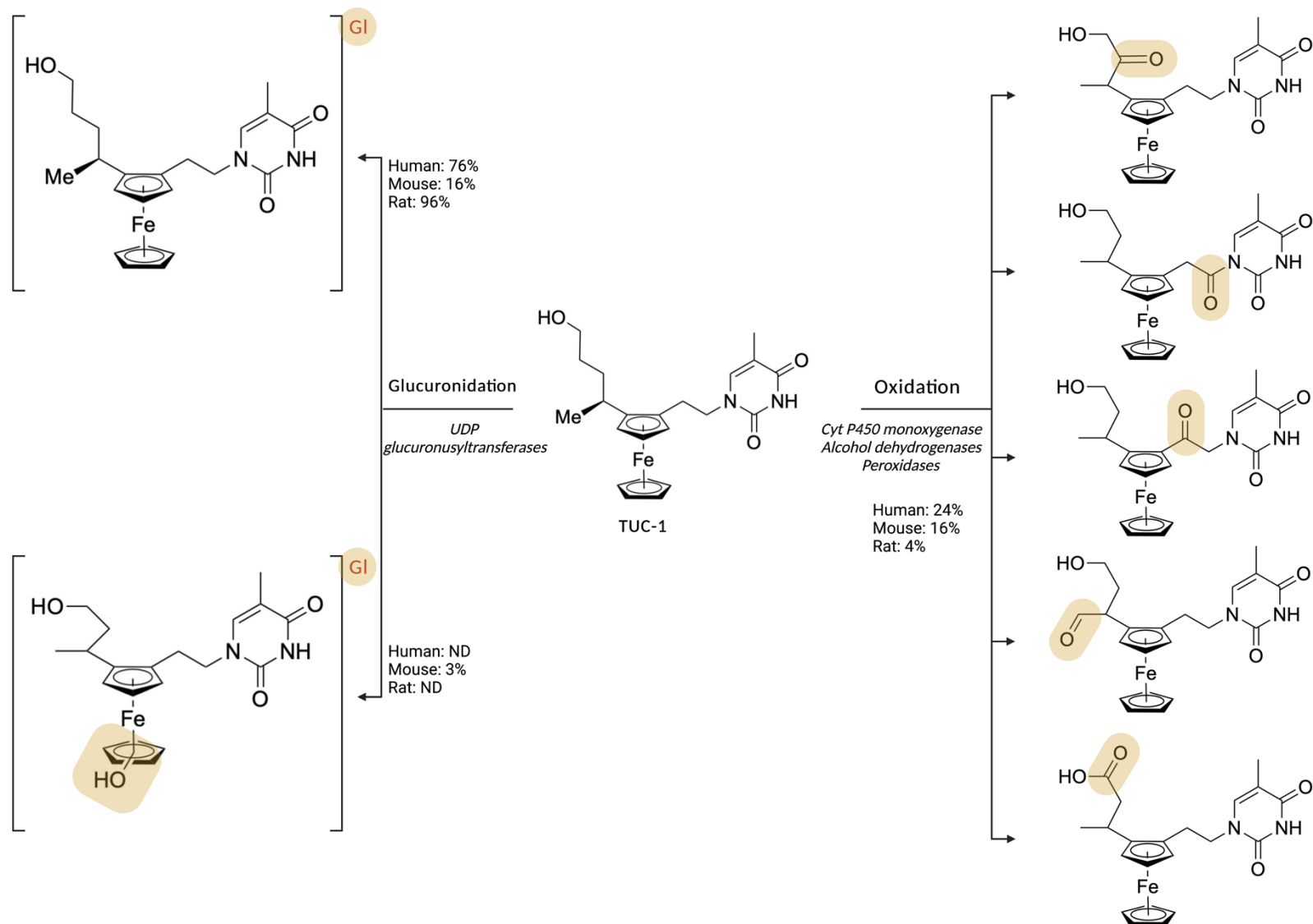


Figure 7. Metabolic pathways proposed for TUC-1 showing formation and percentage profile of each metabolite and their tentative structures. (Created in BioRender.com)

3.4 Future work

Although comparable to existing drugs, TUC-1 shows high metabolic clearance by hepatocytes and short hepatic half-life, following phase II metabolism. DMPK evaluation of the methylated derivatives of TUC-1 (discussed in Chapter 4) may provide a better kinetic profile as the candidate glucuronidated alkyl hydroxyl group is shielded by the methyl group potentially preventing formation of metabolite M2 and increasing hepatic stability.

Similarly, PK parameters are also dependent on the enantiomer as previously observed with anti-inflammatory drug etodolac³⁹ as the *R* enantiomer underwent glucuronidation more readily than *S*³⁹. Therefore, a metabolic profile of the enantiomer of TUC-1, TUC-1*, would provide a useful comparison to predict *in vivo* response to each enantiomer. A gene expression analysis of enzymes involved in Phase I and Phase II metabolism following hepatocyte exposure would also be useful in identifying the enzymes involved in the metabolism of TUC-1.

Additionally, *in vitro* evaluation of TUC-1 tissue permeability by performing a Caco-2 permeability assay would provide insight into the rate of intestinal absorption and efflux⁴² to support the impressive Log D_{7.4}, solubility and blood stability demonstrated earlier. This can also be used to predict a suitable mode of administration.

Interspecies comparison has identified *in vitro* rat model as having similar DMPK properties as human model in response to TUC-1 compared to mouse. This data can be used to conduct *in vivo* investigation in PDAC cell line derived xenograft mouse model, available commercially, to assess TUC-1 PK and PD parameters. Although

the *in vitro* data presented earlier demonstrates similarity between human and rat models, rats are not as well characterised and challenging to administer dose due to size. Therefore, either *KRAS* mutated, or xenograft mouse models would be preferable taking into account the *in vitro* DMPK in interpretation of the data.

3.5 References

1. N. Mehrotra, M. Gupta, A. Kovar and B. Meibohm, *Int. J. Impotence Res.*, 2007, **19**, 253-264.
2. A. Andrés, M. Rosés, C. Ràfols, E. Bosch, S. Espinosa, V. Segarra and J. M. Huerta, *Eur. J. Pharm. Sci.*, 2015, **76**, 181-191.
3. T. Sou and C. A. S. Bergström, *Drug Discovery Today: Technol.*, 2018, **27**, 11-19.
4. L. Di, E. H. Kerns, Y. Hong and H. Chen, *Int. J. Pharm.*, 2005, **297**, 110-119.
5. R. T. Scheife, *Dicp*, 1989, **23**, S27-31.
6. J. L. Davis, in *Equine Internal Medicine (Fourth Edition)*, eds. S. M. Reed, W. M. Bayly and D. C. Sellon, W.B. Saunders, 2018, DOI: <https://doi.org/10.1016/B978-0-323-44329-6.00002-4>, pp. 79-137.
7. J. B. Houston, *Biochem. Pharmacol.*, 1994, **47**, 1469-1479.
8. L. A. Stanley, in *Pharmacognosy*, eds. S. Badal and R. Delgoda, Academic Press, Boston, 2017, DOI: <https://doi.org/10.1016/B978-0-12-802104-0.00027-5>, pp. 527-545.
9. J. P. Tillement and D. Tremblay, in *Compr. Med. Chem. II*, eds. J. B. Taylor and D. J. Triggle, Elsevier, Oxford, 2007, DOI: <https://doi.org/10.1016/B0-08-045044-X/00117-6>, pp. 11-30.
10. P. R. Ortiz de Montellano, *Future Med. Chem.*, 2013, **5**, 213-228.
11. J. J. Novak, W. Burchett and L. Di, *Biopharm. Drug Dispos.*, 2021, **42**, 234-241.
12. H. Mamada, K. Iwamoto, Y. Nomura and Y. Uesawa, *Mol. Divers.*, 2021, **25**, 1261-1270.

13. M. Pellegatti, S. Pagliarusco, L. Solazzo and D. Colato, *Expert Opin. Drug Metab. Toxicol.*, 2011, **7**, 1009-1020.
14. N. J. Waters, R. Jones, G. Williams and B. Sohal, *J. Pharm. Sci.*, 2008, **97**, 4586-4595.
15. A. S. Nies and D. G. Shand, *Circulation*, 1975, **52**, 6-15.
16. G. A. Jacobs, M. Gerber, M. M. Malan, J. L. du Preez, L. T. Fox and J. du Plessis, *Drug Deliv.*, 2016, **23**, 631-641.
17. F. Xu, N. Wang, Y. Tian and G. Li, *J. Heterocycl. Chem.*, 2013, **50**, 668-675.
18. D. W. Scholer, E. C. Ku, I. Boettcher and A. Schweizer, *Am. J. Med.*, 1986, **80**, 34-38.
19. Y. Bergqvist and B. Domeij-Nyberg, *J. Chromatogr.*, 1983, **272**, 137-148.
20. S. R. Kelley, T. J. Kamal and M. E. Molitch, *Am. J. Physiol.*, 1996, **270**, E96-E100.
21. J. P. Hanley, *J. Clin. Pathol.*, 2004, **57**, 1132.
22. E. Mullokandov, J. Ahn, A. Szalkiewicz and M. Babayeva, 2014.
23. J. Nguyen-Lee, C. T. Nguyen-Buckley and A. Bagdasarjana, in *Pharmacology and Physiology for Anesthesia (Second Edition)*, eds. H. C. Hemmings and T. D. Egan, Elsevier, Philadelphia, 2019, DOI: <https://doi.org/10.1016/B978-0-323-48110-6.00032-6>, pp. 645-656.
24. M. Lapins, S. Arvidsson, S. Lampa, A. Berg, W. Schaal, J. Alvarsson and O. Spjuth, *J. Cheminf.*, 2018, **10**, 17.
25. C. Nanavati and D. E. Mager, *J. Pharm. Sci.*, 2016, **105**, 1561-1566.
26. M. S. Surapaneni, S. K. Das and N. G. Das, *ISRN Pharmacol*, 2012, **2012**, 623139.

27. T. Konno, J. Watanabe and K. Ishihara, *J. Biomed. Mater. Res. A*, 2003, **65**, 209-214.
28. C. Fink, D. Sun, K. Wagner, M. Schneider, H. Bauer, H. Dolgos, K. Mäder and S. A. Peters, *Clin. Pharmacol. Ther.*, 2019, **107**.
29. T. Bohnert and L. S. Gan, *J. Pharm. Sci.*, 2013, **102**, 2953-2994.
30. J. Wang, J. Tao, S. Jia, M. Wang, H. Jiang and Z. Du, *Pharmaceuticals (Basel)*, 2021, **14**.
31. C. W. Vose, G. C. Ford, S. J. Grigson, N. J. Haskins, M. Prout, P. M. Stevens, D. A. Rose, R. F. Palmer and H. Rudel, *Br. J. Clin. Pharmacol.*, 1979, **7**, 89-93.
32. P. Baranczewski, A. Stańczak, K. Sundberg, R. Svensson, A. Wallin, J. Jansson, P. Garberg and H. Postlind, *Pharmacol. Rep.*, 2006, **58**, 453-472.
33. S. S and S. Vuppu, *J. Pharm. Biomed. Anal.*, 2020, **179**, 113000.
34. H. Zahreddine and K. Borden, *Front. Pharmacol.*, 2013, **4**.
35. S. M. Maloney, C. A. Hoover, L. V. Morejon-Lasso and J. R. Prosperi, *Cancers (Basel)*, 2020, **12**.
36. M. Takano and T. Sugiyama, *Pharmacogenomics Pers. Med.*, 2017, **10**, 61-68.
37. N. Muhamad and K. Na-Bangchang, *Drug Des., Dev. Ther.*, 2020, **14**, 1401-1444.
38. J. Magdalou, V. Chajes, C. Lafaurie and G. Siest, *Drug Metab. Dispos.*, 1990, **18**, 692-697.
39. D. R. Brocks and F. Jamali, *J. Pharm. Sci.*, 1991, **80**, 1058-1061.
40. M. Herreros-Villanueva, E. Hijona, A. Cosme and L. Bujanda, *World J.*

- Gastroenterol.*, 2012, **18**, 1286-1294.
41. J. Ciccolini, C. Serdjebi, G. J. Peters and E. Giovannetti, *Cancer Chemother. Pharmacol.*, 2016, **78**, 1-12.
42. S. O'Hagan and D. B. Kell, *PeerJ*, 2015, **3**, e1405-e1405.

Chapter 4 – Cytotoxic evaluation of TUC-1 and derivatives *in vitro* and preliminary biological studies

4.1 Introduction

TUC-1, a novel ferronucleoside, has previously shown anti-cancer activity against different cancer cell lines originating from solid tumours including those derived from the gastrointestinal tract with IC₅₀ values comparable to clinically used metallodrug cisplatin¹. Pancreatic ductal adenocarcinoma (PDAC), another solid tumour, remains of the most difficult cancers to treat showing resistance to clinically used nucleoside analogue gemcitabine², as discussed in detail in Chapter 1. This creates a clinically unmet need for novel agents that, alone or in combination with other agents, can target this disease. Therefore, in this chapter, cytotoxicity of TUC-1 and derivatives is assessed in a panel of PDAC cell lines compared to gemcitabine and cisplatin. Selectivity is also probed by evaluating activity in non-tumorous fibroblasts MRC5.

Previous TUC-1 structure-activity relationship studies by Tucker *et al.* discussed in Chapter 1 Section 1.6, have shown presence of both hydroxyalkyl chain and thymidine nitrogenous base is important for anticancer activity¹. Additionally, reducing the hydroxyalkyl linker length, making it structurally similar to endogenous nucleosides, diminishes cytotoxicity of the compound³. The metallocene atom was also identified as an important component as demonstrated by the lower activity of the iso-structural ruthenium analogue of TUC-1⁴. This suggests reversible redox

property of the ferrocene moiety also contributes to the cytotoxicity, reduced upon ruthenium substitution with its irreversible redox⁴. Together these data suggest a MoA different from conventional nucleoside analogues. This is further investigated in this chapter as methylated derivatives of TUC-1 are evaluated for cytotoxicity. As discussed in Chapter 1 Section 1.5.1, endogenous nucleosides undergo catalytic phosphorylation by kinases yielding nucleoside triphosphates, substrates for DNA polymerases during DNA replication⁵. Nucleoside analogue gemcitabine also undergoes a similar conversion at the primary alcohol prior to DNA incorporation and inhibition of DNA synthesis.

To investigate whether TUC-1 behaves in a similar manner as nucleosides and their analogues, with activation by tri-phosphorylation upon cell entry, methylated derivatives were synthesised in our laboratory⁶ (Figure 4.1A, B). While methylation of the primary alcohol (Figure 4.1A) would block any catalytic phosphorylation by thymidine kinase, methylated thymidine (Figure 4.1B) would exclude any base-base interactions via hydrogen bonding. In addition to PDAC cells, these derivatives are also evaluated in human osteosarcoma cell lines HOS (TK+) and 143B (TK-) isogenic except for their expression of thymidine kinase (TK), enzyme that phosphorylates thymidine nucleosides⁶.

The regioisomer of TUC-1, 2-(S) (Figure 4.1D), with identical lipophilicity but different substitution pattern of hydroxyalkyl group and nitrogenous base is also assessed. Enantiomers of a drug, with chiral centre(s) commonly exhibit different biological activity and separate pharmacokinetic and pharmacodynamic profiles. This

complexity makes single enantiomer formulations clinically desirable. Almost 50% of the drugs distributed are chiral with half of these sold as single enantiomer formulations^{7, 8}. Many chiral drugs on the market are sold as single enantiomer formulations for example Fluticasone, a respiratory agent⁹. As TUC-1 is a chiral compound, it is assigned S,R_p chirality with enantiomer TUC-1* in R,S_p configuration (Figure 4.1C). To compare the activity of the enantiomers, cytotoxicity of TUC-1* is also evaluated in PDAC cell lines.

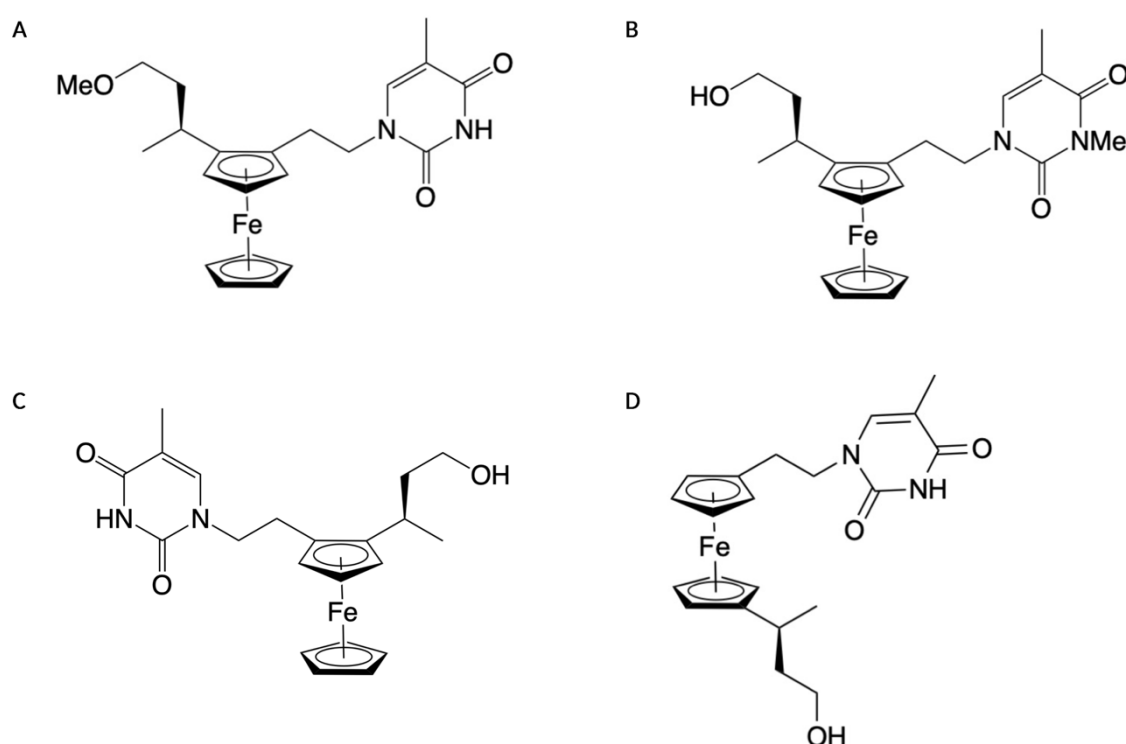


Figure 4.1. Chemical structure of (A) OMe TUC-1, (B) NMe TUC-1, (C) TUC-1* and (D) Regioisomer 2-(S)

TUC-1 was also submitted to the National Cancer Institute (USA) for testing in the NCI-60 panel of cells¹⁰, described previously (Chapter 1, Section 1.4). This chapter presents data analysis of the 5-dose evaluation which includes the COMPARE

algorithm¹¹ to identify compounds with a similar activity pattern as TUC-1 and possible pharmacogenomic relationships. This is complemented by PRISM (Pattern Recognition Integrated with Structural Med-chem) analysis which combines COMPARE results with pharmacophore identification lead organisation tool (PILOT) with hits displaying suitable rigidity are aligned to identify common pharmacophoric regions potentially assisting target interaction.

Nucleoside analogues have been shown to trigger cell cycle arrest following inhibition of DNA synthesis and DNA damage¹². In the presence of excessive DNA damage, due to mutated and/or overwhelmed repair systems, cell death by apoptosis is triggered¹². Therefore, the effect of TUC-1 on the cell cycle distribution is investigated with identification of apoptosis as the mode of cell death triggered.

4.2 Results

4.2.1 TUC-1 Cytotoxicity

Cytotoxicity of TUC-1 was evaluated in a panel of PDAC cell lines, MIA PaCa-2, BxPC3 and CFPAC-1. Viability was assessed using the colorimetric MTT assay in cells treated with increasing concentrations of TUC-1 (0 – 200 μM) for 72 hours. The half maximal inhibitory concentration (IC_{50}) was determined as described in the Materials and Methods. The results demonstrate that TUC-1 leads to a marked inhibition of PDAC cell growth compared to vehicle control. As presented in Figure 4A, TUC-1 was cytotoxic to all cell lines studied, exhibiting IC_{50} values in the low micromolar range (2 – 9 μM), which is comparable to cisplatin (Table 4.1). The IC_{50} values calculated from the concentration response curves (Figure 4.2) for the PDAC cell lines investigated were 9.2 ± 3.0 , 4.4 ± 3.9 and 2.4 ± 2.7 μM in MIA PaCa-2, BxPC3 and CFPAC-1 respectively. The IC_{50} value obtained for cisplatin in MIA PaCa-2 cells was similar to TUC-1, observed to be 5.6 ± 0.8 μM . Previous work in our laboratory shows that the activity of cisplatin is also of similar potency in BxPC3 and CFPAC-1 with IC_{50} values of 1.0 and 4.9 μM respectively (Table 4.1).

Cytotoxicity of TUC-1 was also compared to gemcitabine with an IC_{50} value of 21.7 ± 2.7 nM in MIA PaCa-2 cells and 16.0 and 5.5 nM in BxPC3 and CFPAC-1 respectively (Table 4.1). Based on these results, MIA PaCa-2 cells were selected as a representative cell line for extensive mechanistic work.

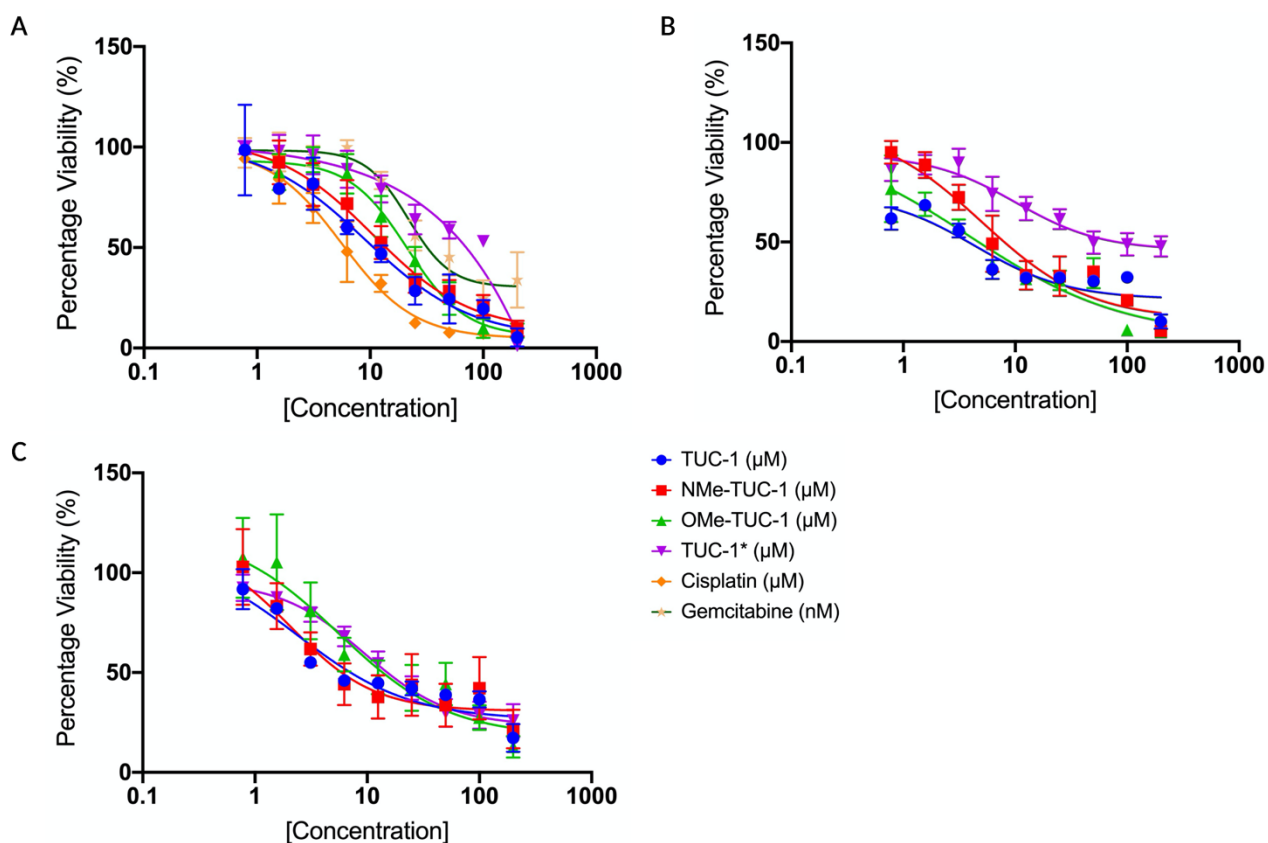


Figure 4.2. Concentration response curves for TUC-1 and its derivatives in (A) MIA PaCa-2, (B) BxPC3 and (C) CFPAC-1 cell lines as assessed by the MTT assay following a 72-hour treatment. The results represent the mean of three independent biological experiments (\pm SD, $n=3$). IC_{50} values calculated from non-linear regression (Variable slope – four parameters).

Table 4.1. IC_{50} values of TUC-1 and its derivatives expressed in μ M in MIA PaCa-2, BxPC3 and CFPAC-1 cell lines. Also shown are the IC_{50} values of clinical drugs cisplatin (μ M) and gemcitabine (nM) in PDAC cell lines. The results represent the mean of three independent biological repeats (\pm SD, $n=3$).

[†]Data obtained previously in our laboratory

	TUC-1 (μ M)	TUC-1* (μ M)	OMe-TUC-1 (μ M)	NMe-TUC-1 (μ M)	Cisplatin (μ M)	Gemcitabine (nM)
MIA PaCa-2	9.2 ± 3.01	>100	21.3 ± 2.7	10.6 ± 3.3	5.6 ± 0.8	21.7 ± 2.7
BxPC3	4.4 ± 3.9	12.0 ± 6.0	4.0 ± 5.2	5.1 ± 2.5	1.0^{\dagger}	16.0^{\dagger}
CFPAC-1	2.4 ± 2.7	9.5 ± 1.6	5.6 ± 4.0	2.1 ± 2.2	4.9^{\dagger}	5.5^{\dagger}

Cytotoxicity of TUC-1 and its methylated derivatives, OMe-TUC-1 and NMe-TUC-1 was evaluated in human osteosarcoma cell lines HOS and 143B cell lines (Figure 4.3). As shown in Table 4.2, IC₅₀ values of 2.1, 2.7 and 1.4 μ M were obtained for TUC-1, OMe-TUC-1 and NMe-TUC-1 respectively in HOS cells. As protected derivatives were equally active in HOS cells, positive for thymidine kinase expression (TK⁺), their activity was investigated next in a TK⁻ cell line. The 143B osteosarcoma cell line was used for this purpose as these cells are negative for thymidine kinase expression (TK⁻) but otherwise isogenic with HOS. IC₅₀ value of all derivatives was higher in this cells with values of 5.1, 5.8 and 4.3 μ M obtained for TUC-1, OMe-TUC-1 and NMe-TUC-1⁶. Previous work in our laboratory has also evaluated the activity of dimethyl-TUC-1 with similar IC₅₀ values obtained, as shown in Table 4.2. Additionally, this work also examined the activity of the regioisomer of TUC-1, 2-(S), with substitution on both Cp rings. This derivative was non-toxic to HOS and 143B cells with IC₅₀ values of 56.7 and >100 μ M respectively (Figure 4.3, Table 4.2).

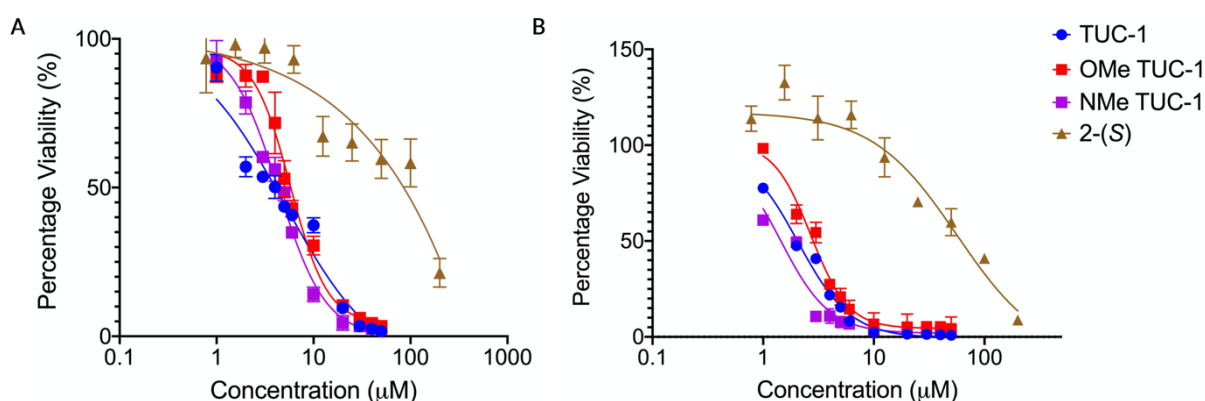


Figure 4.3. Concentration response curves for TUC-1 and its derivatives in human osteosarcoma cell lines (A) 143B (thymidine kinase negative) and (B) HOS (thymidine kinase positive) as assessed by the MTT assay following a 72-hour treatment. The results represent the mean of three independent biological experiments (\pm SD, n=3). IC₅₀ values calculated from non-linear regression (Variable slope – four parameters).

Table 4.2. IC₅₀ values of TUC-1 and non-phosphorylatable analogues of TUC-1 expressed in μ M in TK positive (HOS1) and TK negative (143B) osteosarcoma cell lines. Also shown are the IC₅₀ values of gemcitabine in nM. The values in parentheses are the 95% CI, the results represent the mean from three independent biological experiments (n=3).

*Data obtained previously in our laboratory

Compound	IC ₅₀ (μ M)	
	HOS (TK+)	143B (TK-)
TUC-1	2.1 (1.9-2.3)	5.1 (3.7-8.8)
OMe-TUC-1	2.7 (2.3-3.0)	5.8 (5.2-6.5)
NMe-TUC-1	1.4 (1.2-1.7)	4.3 (4.0-4.7)
Dimethyl TUC-1	2.6 (2.3-2.9)	7.3 (6.2-9.2)
2-(S)	56.7	>100
Gemcitabine (nM)	0.1 (0.01-0.37)	15.6

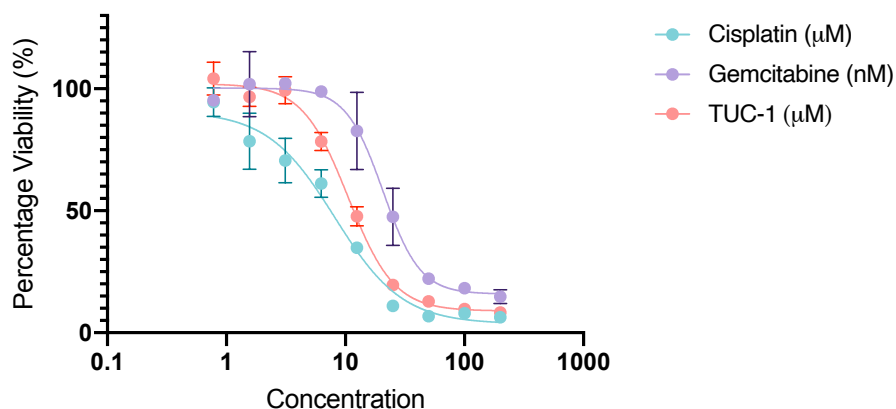
Cytotoxicity of methylated derivatives of TUC-1, OMe-TUC-1 and NMe-TUC-1 was also evaluated in PDAC cell lines as shown in Figure 4.2. Both derivatives showed activity in all cell lines with IC₅₀ values in the low micromolar range (2.1-21.3 μ M) (Table 4.1). IC₅₀ values of 21.3, 4.0 and 5.6 μ M were observed for OMe-TUC-1 in MIA PaCa-2, BxPC3 and CFPAC-1 respectively. NMe-TUC-1 was equally active with values of 10.6, 5.1 and 2.1 μ M obtained for MIA PaCa-2, BxPC3 and CFPAC-1 respectively. Interestingly, the enantiomer of TUC-1, TUC-1*, was not toxic to MIA PaCa-2 cells with an IC₅₀ value of >100 confirming the importance of stereochemistry in toxicity of TUC-1 (Figure 4.2A, Table 4.1). However, intriguingly TUC1* was active albeit it to a lesser extent than TUC-1 in other PDAC cell lines tested, with an IC₅₀ value of 12.0 \pm 6.0 and 9.5 \pm 1.6 μ M in BxPC3 and CFPAC-1 respectively.

Cytotoxicity of TUC-1 was also assessed in the non-immortalised, normal lung tissue fibroblasts, MRC5. The results show that TUC-1 is cytotoxic to MRC5 cells with an IC₅₀ value of 10.6 \pm 1.2 μ M (Figure 4.4). Both cisplatin and gemcitabine were also active in MRC5 cells with IC₅₀ values of 8.2 \pm 1.1 μ M and 20.7 \pm 1.5 nM respectively (Figure 4.4). The selectivity index (SI), defined as the ratio of the toxic concentration

compared to active concentration, was calculated for each compound using Equation 1:

$$SI = \frac{IC_{50} \text{ MRC5 cells}}{IC_{50} \text{ PDAC cells}} \quad \text{Equation 1}$$

As shown in Table 4.3, all SI values were below the threshold value of 10, indicative of low selectivity¹³. The selectivity index of TUC-1 was 1.2, 2.4 and 4.4 for MIA PaCa-2, BxPC3 and CFPAC-1 respectively with the highest selectivity for CFPAC-1. This is compared to cisplatin with SI values of 1.5, 8.2 and 1.7 for MIA PaCa-2, BxPC3 and CFPAC-1 respectively. Gemcitabine displayed the lowest SI values for all three PDAC cell lines; 0.95, 1.3 and 3.8 for MIA PaCa-2, BxPC3 and CFPAC-1 respectively.



	TUC-1 (μM)	Cisplatin (μM)	Gemcitabine (nM)
MRC5	10.6 ± 1.2	8.2 ± 1.1	20.7 ± 1.5

Figure 4.4. (A) Dose response curves of TUC-1 (μM), cisplatin (μM) and gemcitabine (nM) in MRC5 fibroblasts as assessed by the MTT assay following a 72-hour treatment. (B) IC₅₀ values of TUC-1 (μM), cisplatin (μM) and gemcitabine (nM) evaluated in MRC5 cells. The results represent the mean of three independent biological repeats (±SD, n=3). IC₅₀ values calculated from non-linear regression (Variable slope – four parameters).

Table 4.3. Selectivity index of TUC-1, cisplatin, and gemcitabine for PDAC cell lines.

	Selectivity index (SI)		
	TUC-1	Cisplatin	Gemcitabine
MIA PaCa-2	1.2	1.5	0.95
BxPC3	2.4	8.2	1.3
CFPAC-1	4.4	1.7	3.8

4.2.2 NCI-60 screen

TUC-1 was submitted for evaluation of activity in the NCI panel of 60 cancer cell lines originating from 9 different cancer types. Cells were treated for 48 hours with 10 µM TUC-1 for single concentration and 100, 10, 1, 0.1 and 0.01 µM TUC-1 for five concentration evaluations. Cell viability was quantified using the sulforhodamine (B) SRB assay¹⁴. At the end of the experiment, three parameters (GI₅₀, TGI, LC₅₀) were calculated for each cell line tested using the following equations 2-4. The raw data for all 60 cell lines is summarised in Figure 4.5:

GI₅₀: concentration of drug resulting in 50% reduction of cell growth

$$\frac{\text{test growth} - \text{time zero growth}}{\text{control growth} - \text{time zero growth}} \times 100 = 50 \quad \text{Equation 2}$$

TGI: concentration of drug resulting in total growth inhibition

$$\text{test growth} = \text{time zero growth} \quad \text{Equation 3}$$

LC₅₀: concentration of drug resulting in 50% cell death

$$\frac{\text{test growth} - \text{time zero growth}}{\text{time zero growth}} \times 100 = -50 \quad \text{Equation 4}$$

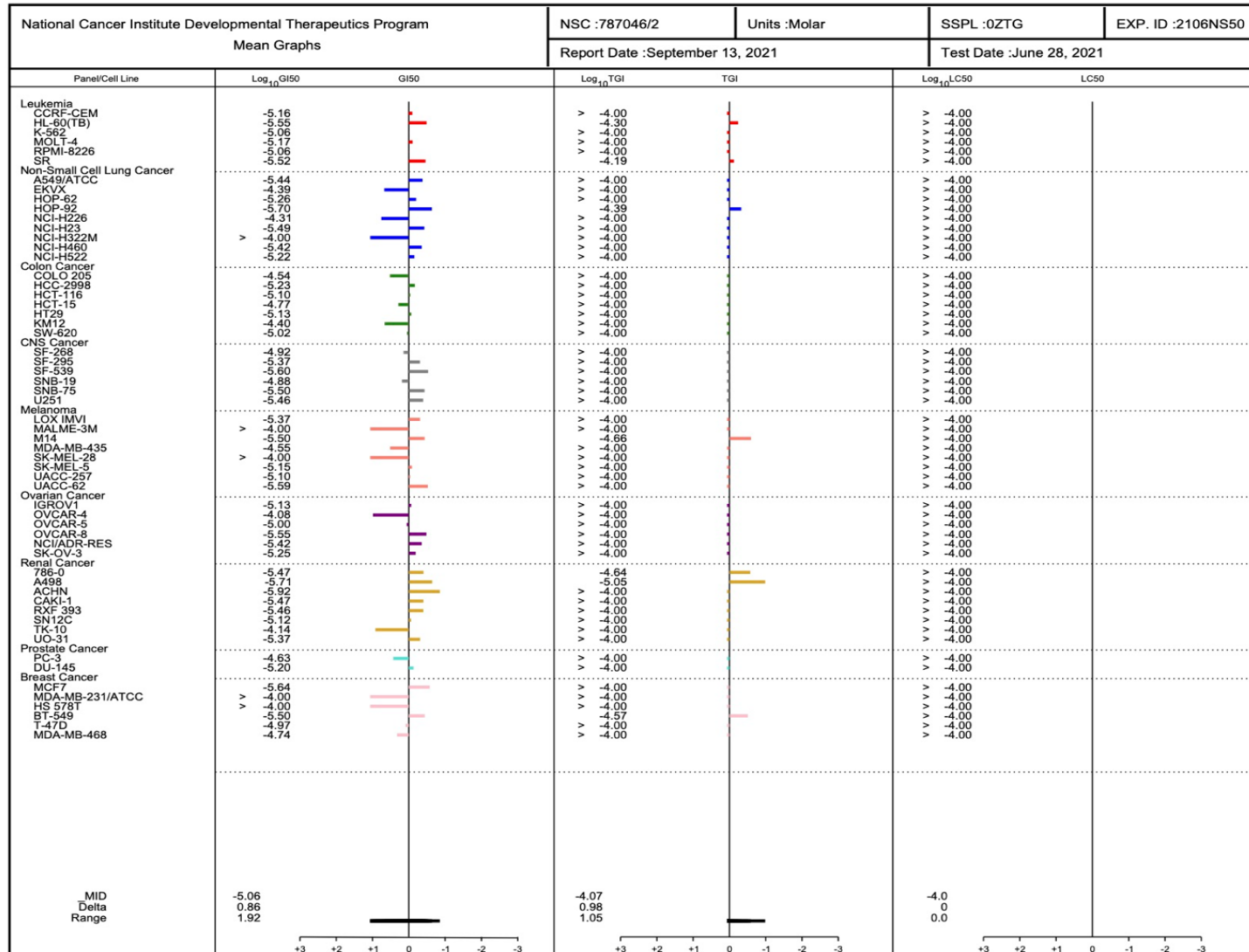


Figure 4.5. Mean graphs for TUC-1 showing GI₅₀, TGI and LC₅₀ endpoints for each cell line in the NCI-60 panel. Bars showing deviation from the mean (-5.06) with bars to the right represent net cell growth and sensitivity with bars to the left indicating cell death and low sensitivity. No bar indicates no net growth. Data provided by National Cancer Institute Developmental Therapeutics Program.

As shown in Figure 4.6, TUC-1 displayed activity comparable to cisplatin while the uneven GI₅₀ distribution of gemcitabine is influenced by low sensitivity of some cell lines, discussed below, in the NCI-60 panel. The mean GI₅₀ (μM) values calculated for TUC-1, cisplatin and gemcitabine were 19.6 ± 29.6, 19.6 ± 15.0 and 13.5 ± 33.4 respectively. Higher concentration values were obtained for the other two endpoints, TGI and LC₅₀, as expected to achieve complete inhibition and cell death over a 48-hour treatment respectively.

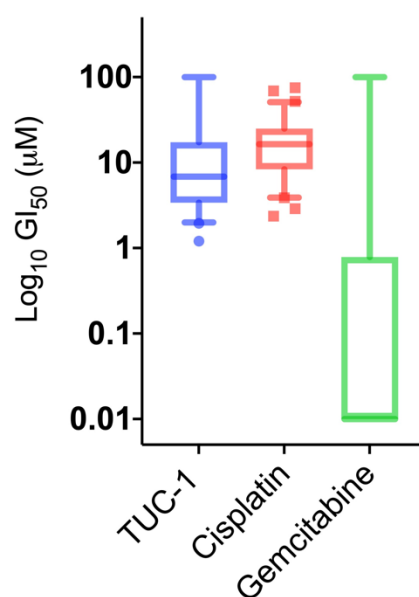


Figure 4.6. Box and whisker plot showing GI₅₀ distribution of TUC-1 compared to cisplatin and gemcitabine as determined by the NCI-60 evaluation. Box and whisker plots show the mean (line splitting the box), interquartile range (box), 5 and 95 percentile range (whiskers) with values falling outside this range plotted as individual points.

Table 4.4. Mean GI₅₀, TGI and LC₅₀ values (+ SD) obtained for TUC-1 in the NCI-60 panel compared to metalloid cisplatin and nucleoside analogue gemcitabine.

[†]Data received from NCI/DTP: September 2021

^{**}Data obtained from NCI database
(ND: Not Determined, >100)

	GI ₅₀ (μM)	TGI (μM)	LC ₅₀ (μM)
TUC-1[†]	19.5 ± 29.6	92.0 ± 22.6	ND
Cisplatin^{**}	19.6 ± 15.0	61.6 ± 21.8	92.7 ± 11.7
Gemcitabine^{**}	13.5 ± 33.4	74.0 ± 43	95.1 ± 21.2

The mean GI₅₀ was also calculated for the different cancer subtypes (Table 4.5).

Values lower than the overall mean GI₅₀ (19.5 µM) is indicative of potential sensitivity of cancer cell lines derived from a specific organ to TUC1. Table 4.5 shows TUC-1 to be the most potent in Leukaemia cell lines followed by cell lines derived from CNS cancers, Renal cancers, Prostate cancers, Ovarian cancers, and Colon cancer, displaying a broad spectrum of activity.

Table 4.5. Mean GI₅₀, TGI and LC₅₀ values (\pm SD) obtained for TUC-1 in different tumour subtypes of the NCI-60 panel.

Cancer subtype	GI₅₀ (µM)
Leukaemia	6.2 \pm 2.6
Non-small cell lung cancer	23.8 \pm 33.7
Colon cancer	16.6 \pm 13
CNS cancer	6.4 \pm 4.8
Melanoma	31.7 \pm 43
Ovarian cancer	18.8 \pm 31.6
Renal cancer	12.2 \pm 24.4
Prostate cancer	14.9 \pm 12.1
Breast cancer	39.1 \pm 47.6

Following this, it was investigated which cell lines displayed higher sensitivity to TUC-1 compared to gemcitabine and cisplatin. Figure 4.7 shows the GI₅₀ values obtained for each cell line in the NCI-60 panel for TUC-1, cisplatin, and gemcitabine. A GI₅₀ value of 100 is indicative of poor activity as 50% growth inhibition was not achieved at the highest concentration tested (100µM). The distribution shown in Figure 4.7 shows a multi-modal distribution of cell line sensitivity to TUC-1 and gemcitabine. In contrast, sensitivity to cisplatin showed a normal distribution of response. The cell lines least sensitive to gemcitabine were HS578T, SK-MEL-2, SK-MEL-28, EKVX, IGROV1, OVCAR-4 and TK-10 (Table 4.6). Interestingly, four of these cell lines were sensitive to TUC-1 with GI₅₀ values of 7.4, 40.7, 72.4 and 83.2 for cell lines IGROV1,

EKVX, TK-10 and OVCAR-4 respectively, as shown in Table 4.6. The five cell lines in the NCI-60 panel were least sensitive to TUC-1 (Table 4.7) were: MDA-MB-231, HS 578T, MALME-3M, SK-MEL-28 and NCI-H322M. Interestingly, gemcitabine was shown to be active with a lower GI_{50} value in only two of these cell lines (Table 4.7). The cell lines least sensitive to TUC-1 belonged to the tumour subtypes breast cancer, melanoma, and non-small cell lung cancer. This was also observed for gemcitabine in addition to ovarian and renal cancer. Interestingly, out of the 18 cell lines most sensitive to TUC-1, 11 (63%) are reported to have a *TP53* mutation (Appendices Table S3). The effect of p53 expression on the activity of TUC-1 is investigated later in this thesis (Chapter 5, Section 5.2.4).

The distribution shown in Figure 4.7 can be split into four clusters for TUC-1: least sensitive (GI_{50} 100 μ M), moderately sensitive (GI_{50} 10-80 μ M), sensitive (GI_{50} 5-10 μ M) and most sensitive (GI_{50} < 5 μ M), indicating a differential effect on cells suggesting the possibility of a cell specific response and a specific cellular target for TUC-1.

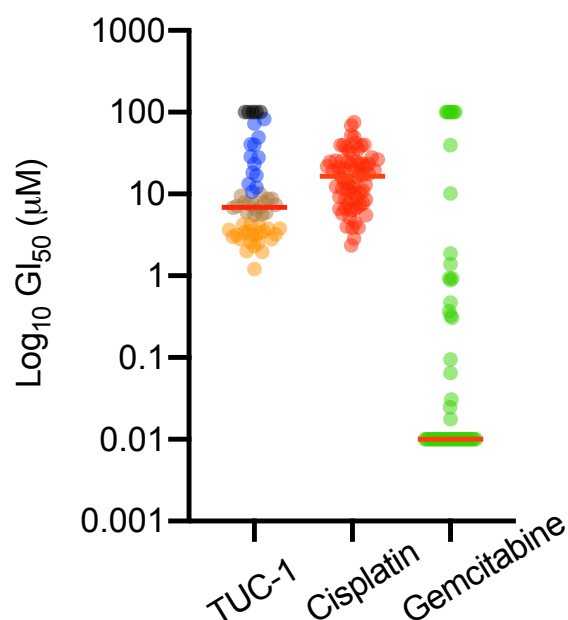


Figure 4.7. Scatter graph showing GI_{50} value for each cell line following treatment with TUC-1, Cisplatin and Gemcitabine (0.01-100 μ M, 48 hours). The median value for each drug is indicated (red line). Four clusters are identified for TUC-1; least sensitive (GI_{50} 100 μ M) (black), moderately sensitive (GI_{50} 10-80 μ M) (blue), sensitive (GI_{50} 5-10 μ M) (brown) and most sensitive (GI_{50} < 5 μ M) (orange).

Table 4.6. List of cell lines in the NCI-60 panel least sensitive to gemcitabine (GI_{50} 100 μ M). GI_{50} values calculated for TUC-1 for these cell lines are also shown.

*Data received from NCI/DTP: September 2021

**Data obtained from NCI database

Cell line	Tumour subtype	Gemcitabine GI_{50} (μ M)**	TUC-1 GI_{50} (μ M)*
HS578T	Breast cancer	100	100
SK-MEL-2	Melanoma	100	ND
SK-MEL-28	Melanoma	100	100
EKVX	Non-small cell lung cancer	100	40.7
IGROV1	Ovarian cancer	100	7.4
OVCAR-4	Ovarian cancer	100	83.2
TK-10	Renal cancer	100	72.4

Table 4.7. List of cell lines in the NCI-60 panel least sensitive to TUC-1 (GI_{50} 100 μ M). GI_{50} values calculated for gemcitabine for these cell lines are also shown.

*Data received from NCI/DTP: September 2021

**Data obtained from NCI database

Cell line	Tumour subtype	TUC-1 GI_{50} (μ M)*	Gemcitabine GI_{50} (μ M)**
MDA-MB-231/ATCC	Breast cancer	100	0.92
HS 578T	Breast cancer	100	100
MALME-3M	Melanoma	100	ND
SK-MEL-28	Melanoma	100	100
NCI-H322M	Non-small cell lung cancer	100	0.025

The GI_{50} endpoint data obtained for TUC-1 was used in the COMPARE algorithm, a tool used to provide mechanistic insight into the MoA by comparing the activity profile of TUC-1 with all other compounds in the NCI/DTP standard agents database which consists of 171 compounds and synthetic compounds database consisting of more than 40,000 compounds. Compounds with a similar pattern of GI_{50} activity to TUC-1 were identified and a Pearson correlation coefficient (r) used as a statistical indicator of the degree of similarity.

In total, 214 correlations were obtained when compared against the standard agents (GI_{50}) database. Compounds were split into the following categories based on their mechanism of action: DNA alkylating agents, DNA synthesis inhibitors, Topoisomerase inhibitors, DNA binding agents, Protein synthesis inhibitors, Antimetabolites, Tubulin targeting, Antifols, Selective estrogen receptor modulators, DNA methyltransferase inhibitors, Metabolic inhibitors, Mitochondria targeting, Protein kinase inhibitors and Apoptosis inducers. As shown in Figure 4.8A, TUC-1 had the most positive correlations with DNA alkylating agents (35%) followed by DNA synthesis inhibitors (21%) and Topoisomerase inhibitors (15%). Following this,

standard agents (GI₅₀) compounds with a correlation coefficient of $r \geq 0.5$ were selected and combined with compounds ($r \geq 0.5$) identified in COMPARE against synthetic agents (GI₅₀) (Figure 4.8B). As observed earlier, highest correlations were obtained with DNA alkylating agents (37%), DNA synthesis inhibitors (20%), Topoisomerase inhibitors (29%), DNA binding agents (8%), Antimetabolites (4%), and Antifols (2%). This suggests that TUC-1 may also behave in a similar manner with DNA as the primary target in the mechanism of action, as expected from nucleoside analogues.

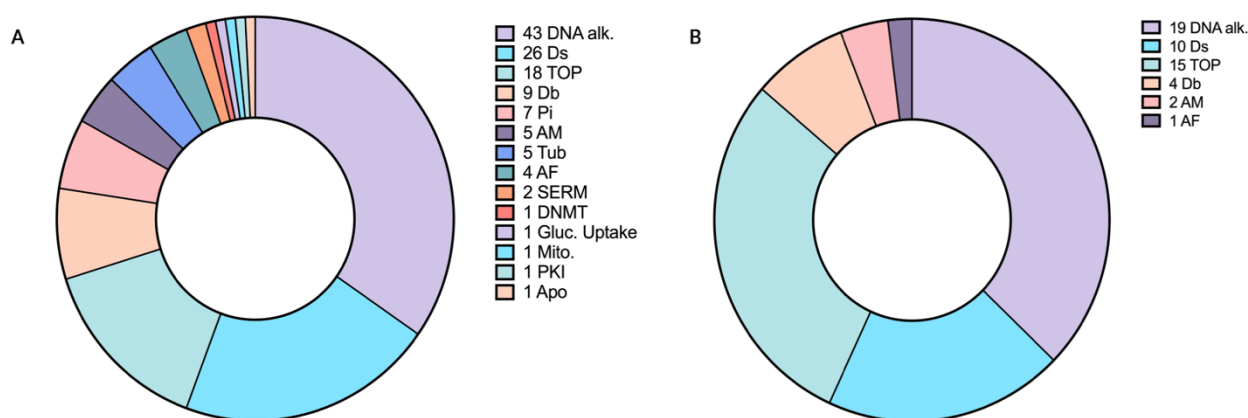


Figure 4.8. COMPARE analysis of TUC-1 showing similarity of pattern of activity in NCI-60 panel against compounds in the NCI database with the GI₅₀ endpoint. (A) All 214 correlations ($r > 0$) identified in the COMPARE analysis against standard agents database, split into 14 categories based on the MoA. (B) Biologically relevant correlations ($r \geq 0.5$) when compared against standard and synthetic agents database are shown split into 6 categories based on the MoA. (DNA alk: DNA alkylating agent; Ds: DNA synthesis inhibitor; TOP: Topoisomerase inhibitor; Db: DNA binder; Pi: protein synthesis inhibitor; AM: antimetabolite; Tub: tubulin inhibitor; AF: antifolate; SERM: selective estrogen receptor modulator; DNMT: DNA methyltransferase inhibitor; Gluc. Uptake: glucose uptake inhibitor; Mito: mitochondrial targeting; PKI: protein kinase inhibitor; Apo: apoptosis inducer).

The compounds in the standard agents database with the highest, biologically relevant correlation ($r \geq 0.5$) with TUC-1, divided by endpoint, are shown in Table 4.8 compared to PCC with COMPARE against gemcitabine and cisplatin. TUC-1 displays

a higher PCC with the top hits compared to gemcitabine and cisplatin suggesting a MoA different from established chemotherapeutics.

Table 4.8. COMPARE analysis using the standard agents GI₅₀ and TGI endpoints. Compounds with the highest Pearson's correlation coefficient when compared against TUC-1 are shown. The PCC values of these hits when compared against cisplatin and gemcitabine are also shown.

	Endpoint	Compound	Pearson's correlation coefficient (PCC)	Mechanism of action	Cisplatin PCC	Gemcitabine PCC
TUC-1	GI ₅₀	Aphidicolin Glycinate	0.71	Antimetabolite, DNA synthesis inhibitor	0.56	0.61
	TGI	Rapamycin	0.65	Protein kinase inhibitor, mTOR inhibitor	0.33	0.03

PRISM analysis identified compounds with higher correlation coefficient values ($r > 0.7$) than those recognised in the standard and synthetic agents databases earlier. Interestingly, these included agents with a ferrocene moiety as shown in Figure 4.9a-d, signifying its contribution towards anticancer activity. PILOT alignment of the highest correlators with rigid conformations identified two compounds: NSC 759878 and NSC 740475. Alignment of these compounds (Figure 4.10) has identified key features common to both compounds including positive ionisable group, hydrophobic residues, hydrogen bond donors and acceptors. As these groups are also a part of the structure of TUC-1, perhaps they are biologically significant in assisting target interaction.

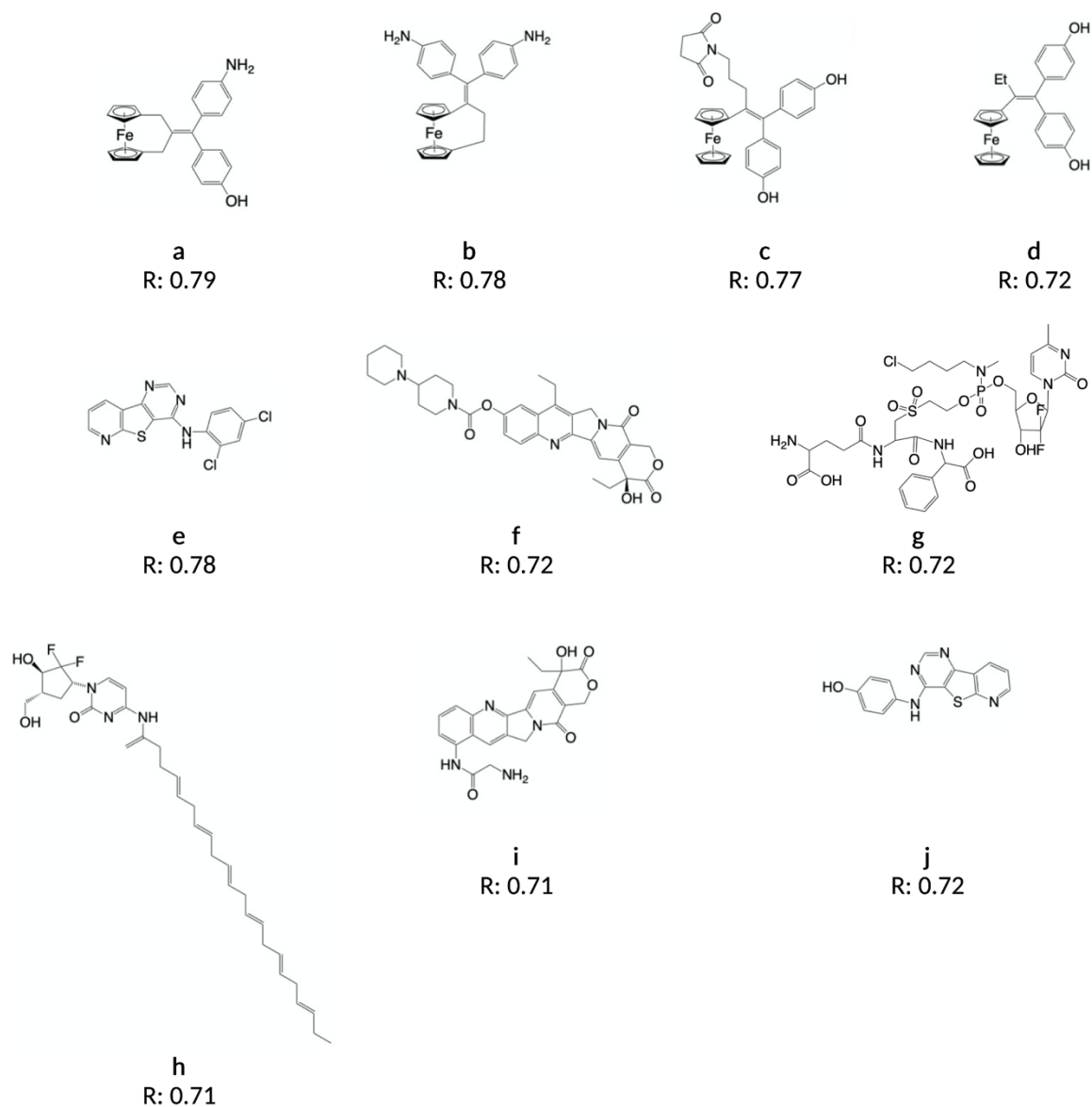


Figure 4.9. PRISM analysis of TUC-1 GI_{50} data identified compounds with a similar pattern of activity in the NCI-60 panel of cell lines. Compounds with a correlation coefficient $r > 0.7$ are shown acknowledged by their NSC number; a) NSC 756998, b) NSC 754385, c) NSC 791461, d) NSC 748141, e) NSC 778770, f) NSC 759878, g) NSC 740475, h) NSC 782349, i) NSC 619232, j) NSC 778776.

Data retrieved: October 2021

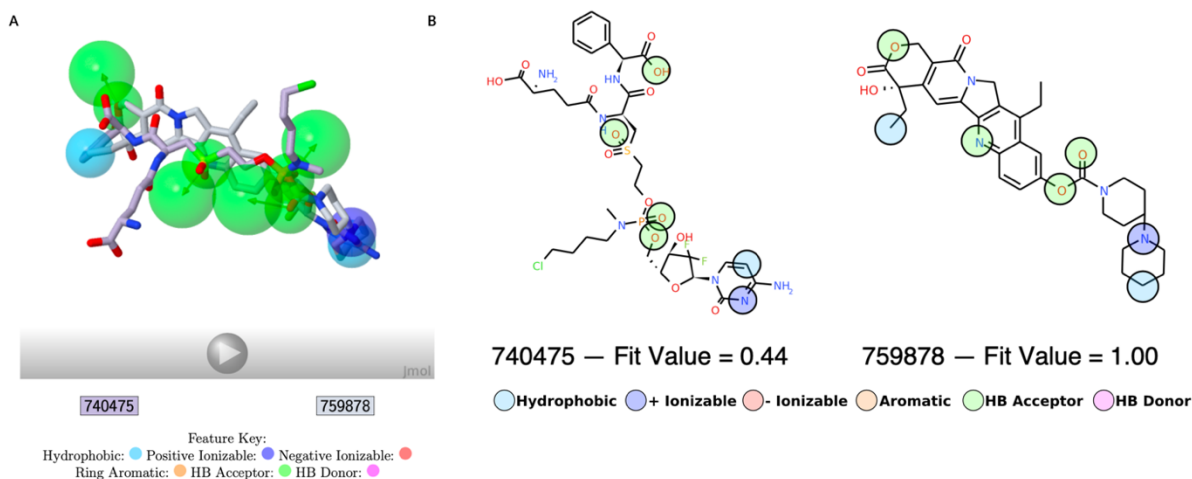


Figure 4.10. PILOT analysis of compounds with suitable rigid structures identified in PRISM showing similar pattern of activity in NCI-60 panel and high correlation coefficient with TUC-1. Three-dimensional (A) and two-dimensional (B) pharmacophore overlap of NSC 759878 and NSC 740475 with mapped features colour coded.

COMPARE program also allows pharmacogenomic analysis to determine if activity of TUC-1 in the NCI-60 panel correlates with levels of specific transcripts. Using the GI_{50} data obtained for TUC-1, a COMPARE analysis was performed with microarray data provided by NCI/DTP including genes commonly mutated in cancer. Figure 4.11B shows 25 genes with the highest correlation returned after COMPARE analysis with TUC-1 (GI_{50} endpoint) which include some key players in tumorigenesis such as *FGFR*, *TP53*, *MDM2* and *MYC*. Protein functional analysis of the top 25 genes in STRING revealed significant connections (Figure 4.11A) with a ppi enrichment value of $1.06e-07$ indicating the connections in the network are not random and biologically relevant. Gene ontology analysis identified p53 binding (GO:0002039) and protein kinase activity (GO:0019199, GO:0004713, GO:0004672) molecular functions as the most enriched in this set of genes. This demonstrates although individually none of the genes returned displayed a correlation of biological

significance ($r>0.5$) individually, as a network of genes they are functionally important, possibly contributing to the activity of TUC-1.

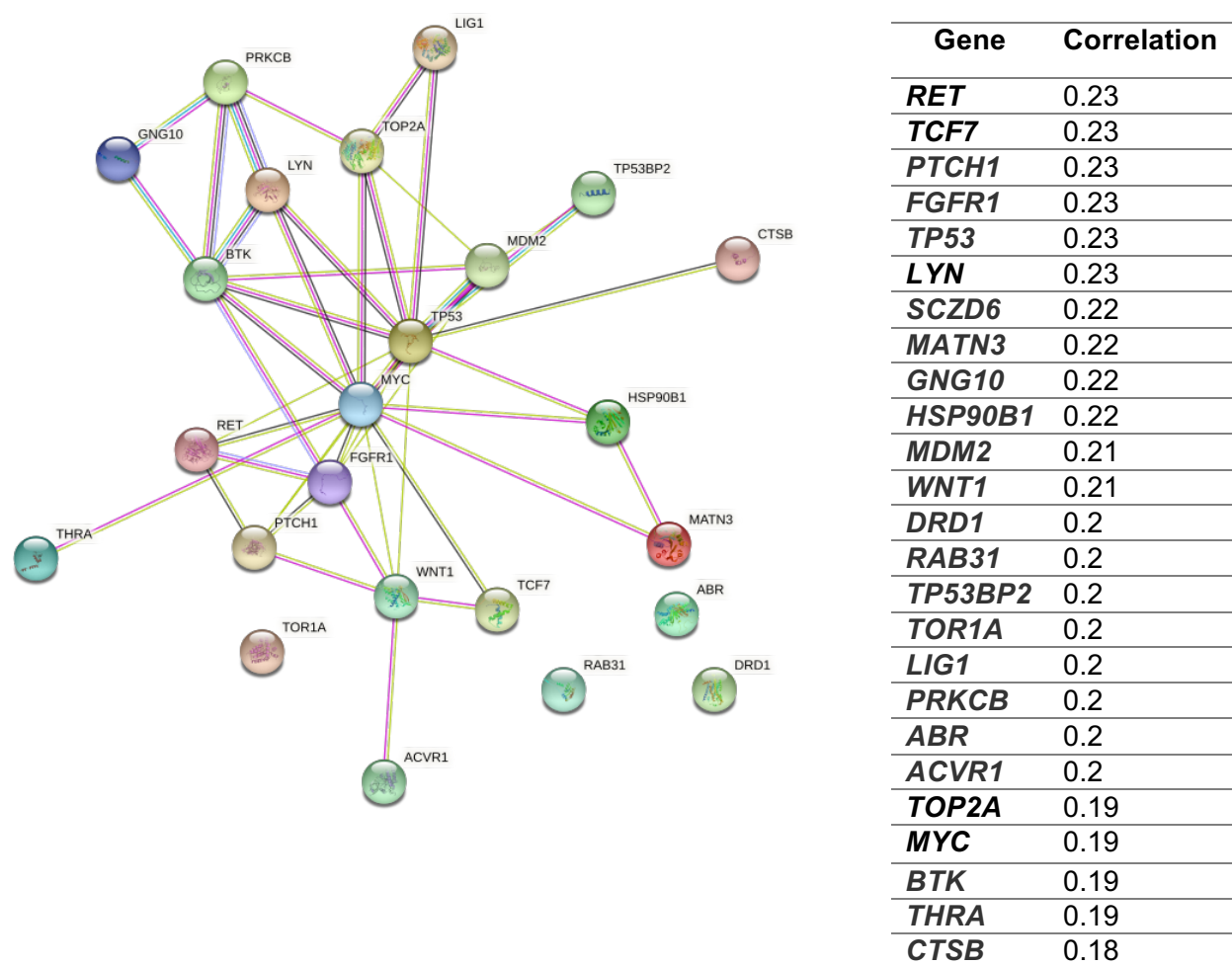


Figure 4.11. (A) STRING network analysis (<https://string-db.org>) of the top 25 genes identified in the COMPARE analysis of TUC-1 GI₅₀ data against microarray dataset provided by NCI/DTP. Interconnecting lines within the network represent predicted molecular actions activation, inhibition, binding, catalysis, phenotype, posttranslational modification, reaction and transcriptional regulation. (B) List of top 25 genes identified in the COMPARE analysis of TUC-1 GI₅₀ data against microarray dataset provided by NCI/DTP.

4.2.3 Cell cycle inhibition

Chemotherapy drugs commonly leads to cell cycle inhibition in cancer cell lines *in vitro* because of genotoxic stress. Nucleoside analogues such as gemcitabine have been shown to arrest the cell cycle in the G1 phase due to inhibition of DNA synthesis preventing progress through S phase. To determine whether the cytotoxic effect of TUC-1 is also mediated through cell cycle inhibition, PDAC cells were stained with propidium iodide (PI) to quantify DNA content and therefore cell cycle phase. Analysis was performed in MIA PaCa-2, BxPC3 and CFPAC-1 cells treated with TUC-1 (5 μ M for 24 hours). The results shown in Figure 4.15 indicate cell cycle inhibition by TUC-1 with arrest in S phase of the cell cycle. The percentage of cells arrested in S phase was 37.38 ± 5.8 , 44.44 ± 13.1 and $50.13 \pm 3.2\%$ in MIA PaCa-2, BxPC3 and CFPAC-1 respectively, all differences were statistically significant compared to untreated controls ($P < 0.01$). A concentration dependent effect was also established in MIA PaCa-2 cells after treatment with increasing concentrations of TUC-1 (1.25, 2.5, 5, 10 and 20 μ M, 24 hours). The percentage of cells in S phase arrest following treatment with 1.25, 2.5, 5, 10 and 20 μ M TUC-1 was 28.2 ± 2.4 , 29.6 ± 4.9 , 38.0 ± 7.9 , 57.6 ± 9.1 and $71.6 \pm 10.1\%$ respectively, compared to $16.4 \pm 4.9\%$ in untreated control (Figure 4.12). Cell cycle regulation is an interplay between CDK-cyclin, CAKs and CKIs among others. Data presenting changes in expression of cell cycle related genes in cells treated with TUC-1 is presented later in the thesis (Chapter 5, Section 5.2.4).

PDAC cell lines were also treated with the enantiomer TUC-1* (5 μ M for 24 hours). As shown in Figure 4.13, in MIA PaCa-2 cells, there was no difference in cell cycle

distribution between untreated and TUC-1* treated samples whereas S phase arrest was observed following treatment with TUC-1, as seen previously. The percentage of MIA PaCa-2 cells arrested in S phase after TUC-1* treatment was 22.0 ± 5.5 compared to 18.4 ± 1.9 for untreated samples. In contrast to this, treatment with TUC-1* led to S phase arrest in BxPC3 and CFPAC-1 cells which suggests molecular characteristics of PDAC cell lines govern responsiveness to drugs and is also consistent with the toxicity of TUC-1* seen in these cell lines. The percentage of BxPC3 and CFPAC-1 cells arrested in S phase following treatment with TUC-1* was 50.1 ± 3.2 and 34.2 ± 5 respectively (Figure 4.13B, C). TUC-1 treatment also led to S phase arrest in the two cell lines as shown earlier.

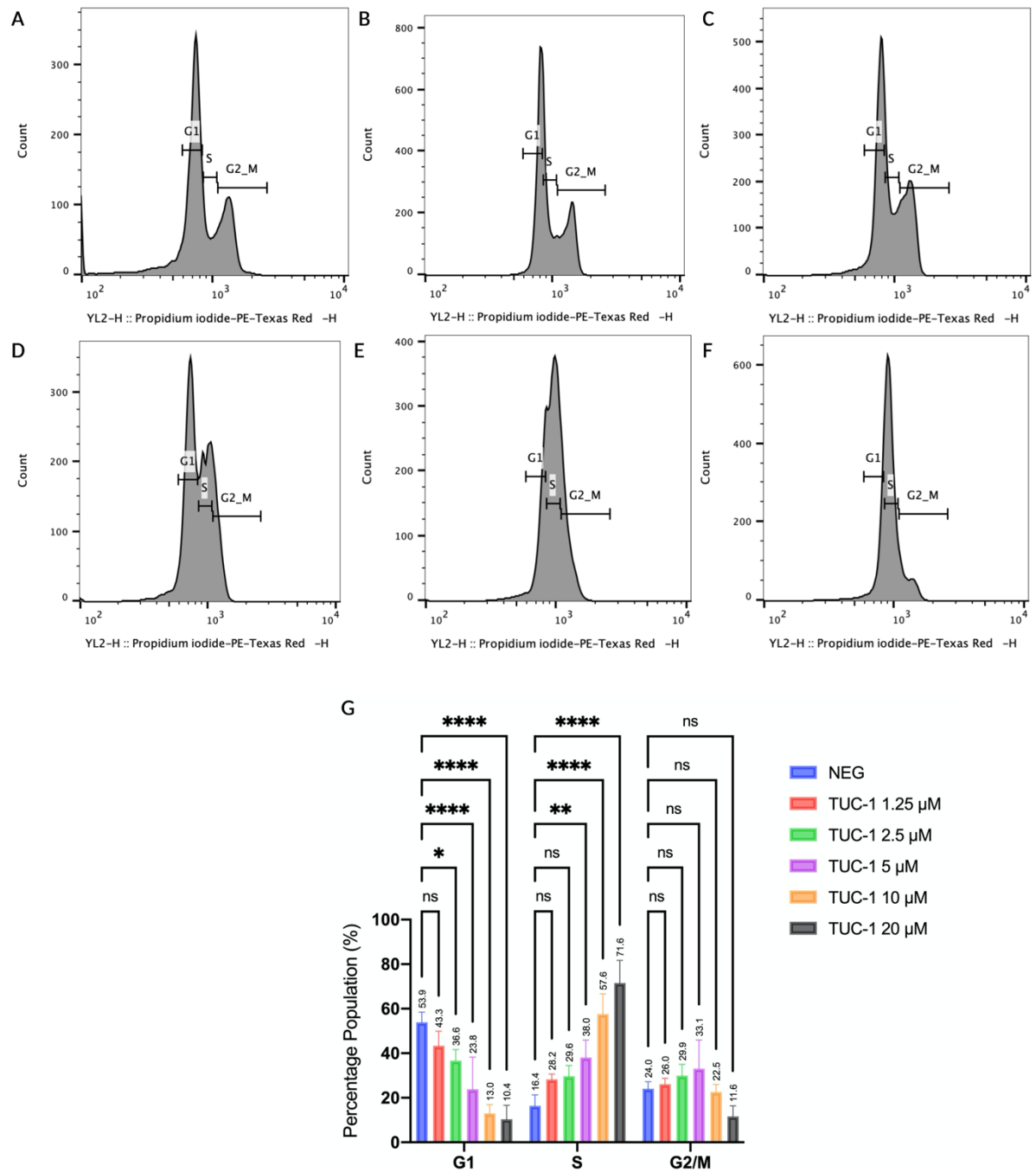


Figure 4.12. Cell cycle distribution of MIA PaCa-2 cells after treatment with TUC-1. Representative histograms from cells treated with (A) 0, (B) 1.25, (C) 2.5, (D) 5, (E) 10 and (F) 20 μ M TUC-1 for 24 hours followed by propidium iodide staining and analysis by flow cytometry. (G) Quantification and graphical representation of the results representing mean of three independent biological repeats (\pm SD, $n=3$). *, **, *** and **** statistically significantly different ($P<0.05$, $P<0.01$, $P<0.001$ and $P<0.0001$ respectively) as assessed by 2-way ANOVA followed by Tukey's multiple comparison t-test.

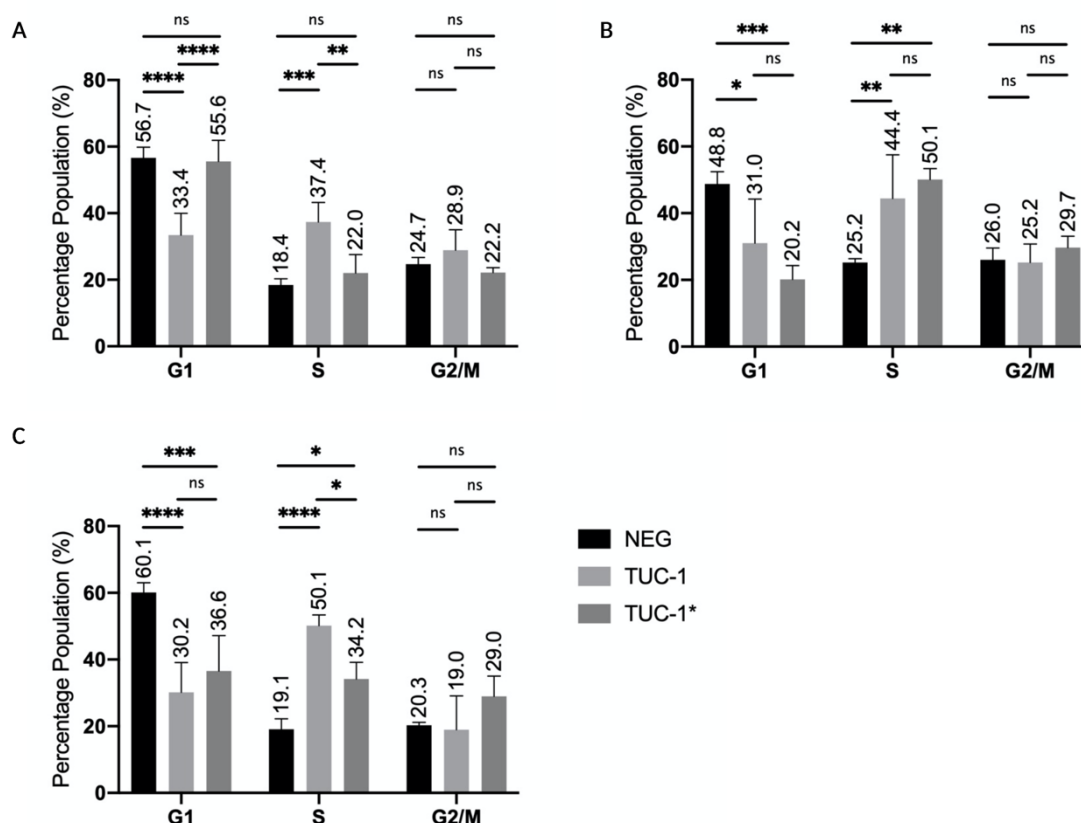


Figure 4.13. Cell cycle distribution of PDAC cell lines (A) MIA PaCa-2, (B) BxPC3 and (C) CFPAC-1 following treatment with TUC-1 and TUC-1* (5 μ M, 24 hours) and staining with propidium iodide followed by analysis by flow cytometry. The results represent the mean of three independent biological repeats (\pm SD, $n=3$). *, **, *** and **** statistically significantly different ($P<0.05$, $P<0.01$, $P<0.001$ and $P<0.0001$ respectively) as assessed by 2-way ANOVA followed by Tukey's multiple comparison t-test.

4.2.4 Cell death

Ferroptosis is a mode of cell death induced by excessive iron accumulation and consequential lipid peroxidation. It was investigated whether the ferrocene moiety of TUC-1 catalyses a fenton-like reaction intracellularly leading to cell death via ferroptosis. Erastin, an inducer of ferroptosis was used as a positive control. Cells were treated with increasing concentrations of TUC-1 or erastin (0-200 μ M) in the presence or absence of ferrostatin-1 (10 μ M, 72 hours), an inhibitor of ferroptosis. Cell viability was assessed by an MTT assay described previously. As shown by the

difference in the concentration-dependent curves in Figure 4.14B, MIA PaCa-2 cells treated with erastin in the presence of ferrostatin-1 had a higher percentage viability overall compared to treatment with erastin alone. The IC_{50} value increases from 0.28 μM to 2.7 μM with the inhibitor, almost ten times higher in the presence of ferrostatin-1 confirming the induction of ferroptosis by erastin. MIA PaCa-2 cells treated with TUC-1 in the presence of ferrostatin-1 displayed no change in cell viability compared to single treatment (Figure 4.14A) with IC_{50} values of 9.2 μM and 11 μM in the absence and presence of ferrostatin-1 respectively.

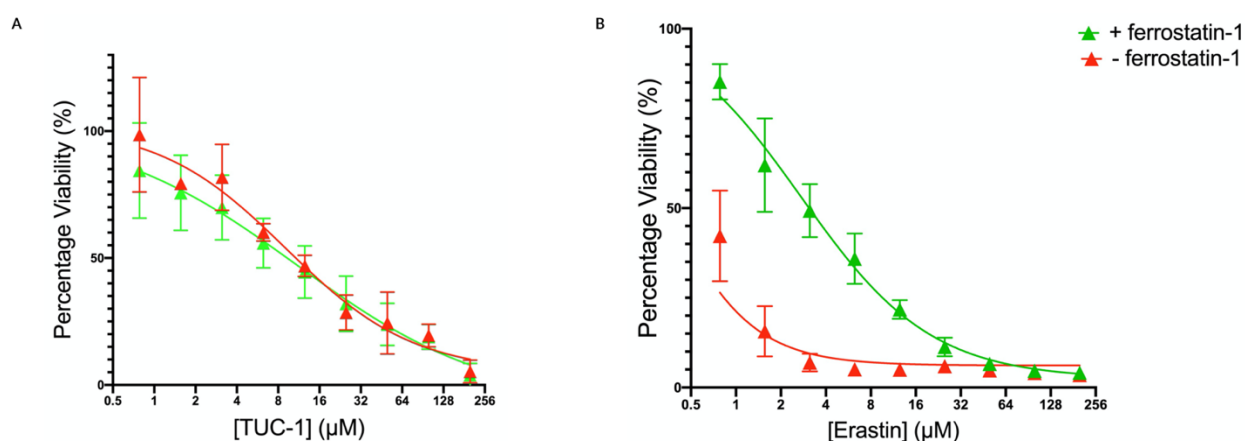


Figure 4.14. Concentration response curves for (A) TUC-1 and (B) Erastin in the presence or absence of ferrostatin-1 (10 μM) evaluated in MIA PaCa-2 cells, assessed by the MTT assay following a 72-hour treatment. The results represent the mean of three independent biological experiments ($\pm SD$, $n=3$). IC_{50} values calculated from non-linear regression (Variable slope – four parameters).

Nucleoside mimics such as gemcitabine and 5-fluorouracil commonly trigger apoptosis¹⁵ therefore the ability of TUC-1 to induce cell death by apoptosis was investigated. Externalisation of phosphatidylserine following induction of apoptosis was used as a biomarker by labelling with Pacific Blue conjugated Annexin V. MIA PaCa-2 cells were treated with increasing concentrations of TUC-1 (5, 10, 15, 20 and 25 μ M) for 72 hours. As shown in Figure 4.15A-F, the number of cells entering early apoptosis increases in a concentration-dependent manner. The population of cells in early apoptosis increases from 8.5% in untreated control to 13.4, 21.7, 31.4, 38.2 and 50.4% for TUC-1 5, 10, 15, 20 and 25 μ M respectively (Figure 4.15G). A similar trend was observed for percentage of cells entering late apoptosis. The population of cells in late apoptosis increased from 9.3% in untreated control to 12.4, 16.7, 20.2, 32.0 and 33.2% for TUC-1 5, 10, 15, 20 and 25 μ M respectively (Figure 4.15G). These results suggest apoptosis is the mode of regulated cell death triggered by TUC-1 in a concentration-dependent manner.

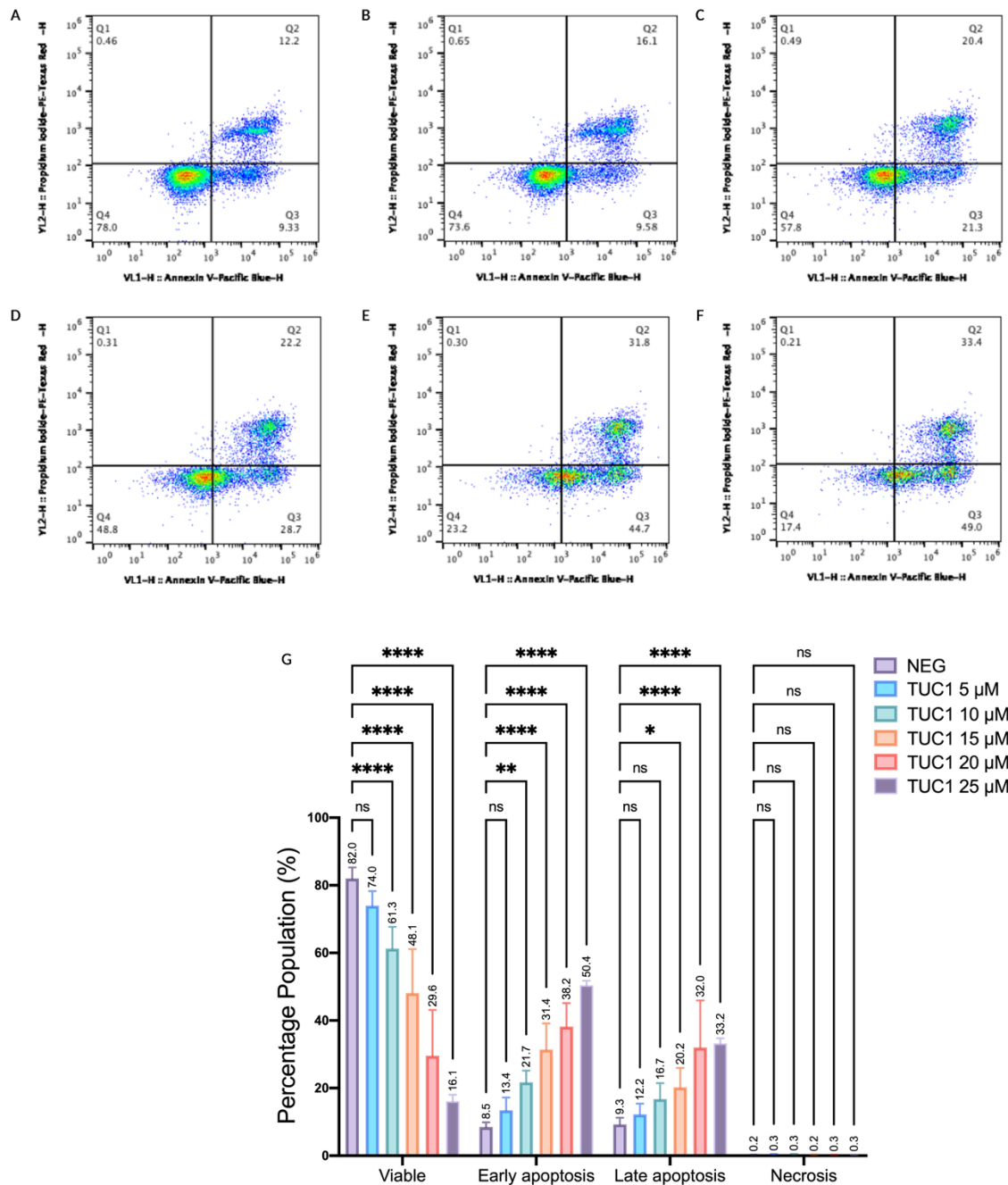


Figure 4.15. TUC-1 induces apoptosis in MIA PaCa-2 cells. Cell death was monitored by labelling with Annexin V Pacific Blue conjugate and propidium iodide following treatment with (A) 0, (B) 5, (C) 10, (D) 15, (E) 20 and (F) 25 μ M TUC-1 for 72 hours. The representative cytograms (A-F) show four different populations of cells: viable (Q4), early apoptotic (Q3), late apoptotic (Q2) and necrotic (Q1). (G) Bar graph showing percentage population of cells in different stages of apoptosis following treatment with TUC-1. The results represent the mean of three independent biological repeats (\pm SD, $n=3$). *, **, *** and **** statistically significantly different ($P<0.05$, $P<0.01$, $P<0.001$ and $P<0.0001$ respectively) as assessed by 2-way ANOVA followed by Dunnett's multiple comparison t-test.

4.3 Discussion

This chapter has evaluated the cytotoxicity of TUC-1 in three PDAC cell lines establishing low micro molar IC_{50} values ($<10\ \mu M$), with CFPAC-1 identified as the most sensitive cell line. Activity of TUC-1 is comparable to cisplatin, clinically used to treat different types of cancer¹⁶⁻¹⁸. Although gemcitabine was more potent by an order of magnitude compared to TUC-1 and cisplatin, previous work in our laboratory has established activity of TUC-1 in gemcitabine resistant sub clones of MIA PaCa-2 cells with an IC_{50} value of $3.7\ \mu M$ (NJH personal communication). As both drugs remain clinically significant, chemoresistance via different cellular mechanisms such as metabolic inactivation and reduced uptake, reduces the efficacy of these agents^{19, 20}. This suggest a lack of cross-resistance which could be clinically advantageous, with TUC-1 a candidate for further investigation for the potential treatment of gemcitabine resistant PDAC. Nucleosides require triphosphorylation prior to DNA incorporation and this is also a part of the MoA of antiviral and anticancer nucleoside analogues including gemcitabine. Gemcitabine inhibits DNA synthesis following incorporation resulting in masked chain termination, evading repair leading to irreparable lesions²¹.

Previous SAR studies have shown reducing alkyl linker length has a negative impact on the cytotoxicity of TUC-1³. In this chapter, it was investigated whether TUC-1 requires phosphorylation for anti-cancer activity. The hydroxyl group most likely to be subjected to phosphorylation was protected by methylation in addition to the secondary amine on the nitrogenous base. Evaluation in TK positive (HOS) and negative (143B) cell lines show these methylated derivatives to be cytotoxic at a

similar potency as TUC-1, with IC₅₀ values generally higher in TK negative cells. These derivatives were also equally active in PDAC cell lines at micromolar IC₅₀ values. In contrast to TUC-1, the positive control gemcitabine showed a 156-fold increase in IC₅₀ value in thymidine kinase negative cells. Together these data strongly support the hypothesis that the ferronucleoside TUC-1 does not require catalytic phosphorylation for cytotoxicity and it is not part of its mode of action⁶.

Conversion to gemcitabine monophosphate by deoxycytidine kinase is a rate-limiting step in the activation of gemcitabine as it competes with deoxycytidine²².

Phosphorylated gemcitabine metabolite is a substrate for deoxycytidine deaminase (dCD), a pyrimidine metabolic enzyme, leading to drug inactivation by conversion to difluorodeoxyuridine²². Studies have shown upregulation of dCD contributes to acquired gemcitabine resistance²³. Elevated expression and activity of dCD is found in pancreatic cancers with poor prognosis and accelerated disease progression²⁴. By bypassing the need for phosphorylation, TUC-1 displays unique behaviour compared to gemcitabine and other nucleoside analogues making it a potentially important clinically viable drug candidate especially for treatment of cancers with resistance to existing nucleoside analogues.

Previous work in our laboratory has also evaluated the activity of the regioisomer of TUC-1 in HOS and 143B cell lines. The regioisomer was not toxic to these cells with IC₅₀ values >50 µM, suggesting lipophilicity alone does not govern the cytotoxicity of TUC-1 and that the substitution pattern is important. These data are reinforced by previous structure activity relationship studies^{1, 3, 6}. Moreover, TUC-1 cytotoxicity was

also evaluated in non-immortalised normal lung tissue MRC5 fibroblasts. Although TUC-1 was found to be cytotoxic to these cells, the selectivity indexes for PDAC were >1 suggesting some evidence for preferential activity in PDAC cells compared to non-cancerous cells. Furthermore, the SI of TUC-1 was comparable to or better than both cisplatin and gemcitabine. These findings are not surprising as MRC5 cells are rapidly dividing with a population doubling time of 34 hours, a higher turnover rate than MIA PaCa-2 (40 hours) and BxPC3 (48-60 hours)²⁵.

As discussed later, DNA replication is the primary target of TUC-1 leading to cell death therefore cells undergoing rapid cell divisions will be susceptible to any agent targeting replication. Although the effect of anticancer drugs on rapidly dividing healthy cells has been identified as a major disadvantage of chemotherapeutics however in many cases the benefits outweigh the side effects. Furthermore, MRC5 cells are derived from lung tissue, different from PDAC cell lines that are derived from pancreatic tissue, which limits direct comparison. It is to be noted, tissue of origin and cell type can also influence selectivity as reported previously in literature^{26, 27}.

Therefore, a non-cancerous cell line originating from pancreatic tissue would offer a more accurate representation and assessment of selectivity. This is supported by the NCI-60 evaluation, discussed later, where the IC_{50} value of 5.4 μ M was reported in non-small cell lung cancer cell line A549, half the value obtained for the non-cancerous counterpart MRC5.

Chirality has been shown to play an important role in drug action as enantiomers with identical molecular and structural formulae may exhibit different biological activities

leading to separate pharmacokinetic and pharmacodynamic profiles⁷. In a racemic mixture, an enantiomer may not only be inactive but can counteract the active enantiomer. This, coupled with complex PK and PD, makes single enantiomer formulations clinically favourable. The FDA requires the stereochemistry of novel chiral agents to be well defined and tested during early drug development⁹. The enantiomer of TUC-1, TUC-1*, was inactive in MIA PaCa-2 cells but interestingly retained some activity in BxPC3 and CFPAC-1 cells, albeit with IC₅₀ values higher compared to TUC-1. Cell line differences in sensitivity may be attributed to different molecular characteristics of each cell line, a phenomenon known to exist not only between different cell lines but within subpopulations of a parental cell line²⁶. The work by Amrutkar *et al.* further supports this as differential expression of gemcitabine deactivating enzyme deoxycytidine deaminase in PDAC cell lines MIA PaCa-2, BxPC3 and PANC-1 led to different cytotoxic profiles².

Differential activity is also evident in the NCI-60 evaluation which clearly showed that some cancer cell lines were more sensitive to TUC-1. Overall, cell lines derived from leukaemia's were the most sensitive group within the NCI-60 panel. HL-60(TB) cell line had the lowest IC₅₀ (4.3 µM) value. However, in contrast RPMI-8226 another leukaemia cell line was resistant to TUC-1 (> 100µM). This effect was also observed with other cancer subtypes. Mean GI₅₀ comparison with cisplatin and gemcitabine also shows that overall, the potency of TUC-1 is comparable to these clinically successful and widely used drugs. GI₅₀ distribution of TUC-1 and gemcitabine identified cell lines least sensitive to each compound with a GI₅₀ value of ≥ 100 µM. Interestingly, TUC-1 was active in 4 out of the 7 cell lines least sensitive to

gemcitabine. This data, supported by the SAR studies with methylated derivatives mentioned earlier, suggests that the MoA of TUC-1 is different from common nucleoside analogues indicative of target interaction. The GI₅₀ distribution for TUC-1 also shows four clusters to exist ranging from least to most sensitive. This reinforces cell line differences in response to TUC-1, previously observed in PDAC cell lines with the enantiomer TUC-1*. This was not observed for cisplatin which shows a normal distribution.

Tumours originating from the same tissue become heterogeneous as they evolve leading to many subtypes, each responsive to a specific drug. This is evident as some cell lines such as MCF-7 in the breast cancer panel was very sensitive to TUC-1 (GI₅₀ 2.3 µM) whereas MDA-MB-231 another breast cancer cell line was resistant to TUC-1 (GI₅₀ ≥100 µM). This was also previously demonstrated by the NCI-60 evaluation of Imatinib which revealed a relatively high mean GI₅₀ value of 15 mM, however it was 1000-fold more selective towards K-562 cells with GI₅₀ 0.02 mM²⁸. As this is the only cell line with the target BCR-Abl fusion gene, this demonstrates target-specific agents can have a differential effect in the panel leading to least and most sensitive clusters as observed with TUC-1²⁸. Various contributory factors such as genotype, protein expression, metabolic potential etc., play an important role in cellular response to a drug. Cells with a high genome instability and mutational load are particularly sensitive to anticancer agents²⁹. The significance of mutational load in drug sensitivity was previously demonstrated by Pavel and Korolev²⁹ as they evaluated the activity of 24 drugs in Cancer Cell Line Encyclopedia panel with almost half the drugs showing significant activity for cell lines with a high mutational load²⁹.

Therefore, a deeper -omics approach is needed to identify reproducible molecular features that distinguish each cell line, beyond tissue of origin and cancer type. This will enable identification of common features that dictate sensitivity to TUC-1.

GI₅₀ and TGI endpoint data was also used to perform COMPARE analysis against the standard agents and synthetic compounds database to identify 'hits' with a similar pattern of activity in the NCI-60 panel of cell lines. This is used to aid identification of the potential MoA. COMPARE algorithm has been previously successful in identifying MoA of novel compounds such as indenoisoquinolines, that correlated strongly with camptothecin and were found to similarly target topoisomerase I, later entering clinical trials^{30, 31}. Analysis identified different classes of drugs with the DNA alkylating agents, DNA synthesis inhibitors and topoisomerase inhibitors having the greatest number of correlations. Although a caveat to this is the unequal representation of all classes of drugs in the databases resulting in some drugs such as DNA alkylating being pulled more frequently.

COMPARE analysis indicates DNA replication as the primary target of TUC-1 as the most significant correlations ($r \geq 0.5$) were found with agents inhibiting DNA synthesis or directly targeting DNA. The work by Gormen *et al.* provides an interesting comparison as the ferrocenophane and ferrocene derivatives with two phenol rings were evaluated in the NCI-60 panel followed by COMPARE analysis³². These derivatives also correlated strongly with agents causing DNA damage and/or inhibiting replication including aphidicolin glycinates³². The amine derivative synthesised by the group also had a high correlation coefficient ($r = 0.78$) with TUC-1

as identified by the PRISM analysis. As both structures only share the ferrocene moiety, perhaps it plays an important role in directing the MoA towards DNA replication among other effects. The pharmacogenomic relationship was also probed between common cancer related genes expressed in NCI-60 cell lines and activity of TUC-1. Gene ontology analysis of molecular functions of the top 25 genes revealed p53 binding and protein kinase activity as the functions related to this set of genes with a ppi enrichment value of $1.06\text{e-}07$ suggesting a biological connection, potentially key players in the MoA of TUC-1.

The effect of TUC-1 on cell cycle distribution was also studied in all PDAC cell lines which shows S phase arrest as part of the mechanism, similar to gemcitabine³³ and 5-FU³⁴. Additionally, a parallel effect was observed with the enantiomer TUC-1* in CFPAC-1 and BxPC3 but not MIA PaCa-2 cells. As DNA replication initiation and elongation dominates S-phase of the cell cycle, this data indicates TUC-1 interferes the replication machinery by target interaction, supported by the SAR studies mentioned previously^{1, 3}.

Investigation into the mode of cell death showed concentration-dependent initiation of apoptosis, most likely triggered following cell cycle arrest. MIA PaCa-2 cells enter early and late apoptosis in a concentration-dependent manner leading to cell death, as observed with other nucleoside analogues^{15, 34}. Interestingly, the compound did not initiate iron-dependent ferroptosis as co-treatment with the inhibitor ferrostatin-1 did not impact the cytotoxicity of TUC-1. This is compared to positive control erastin, an inducer of ferroptosis, which was significantly less cytotoxic when co-treated with

ferrostatin-1. It has been reported previously, iron-containing agents such as ferric ammonium citrate do not always lead to ferroptosis as other contributory factors such as cell origin, delivery and accumulation of these agents are equally important.

4.4 Future work

This chapter has highlighted cell line differences can have a profound impact on sensitivity to chiral agents. To identify these influential functional phenotypic differences, a proteomics approach can be adopted to identify up or downregulation of proteins, changes in cellular compartments, presence, or absence of metabolic enzymes among other changes. This would also aid target identification by identifying key proteins important for biological activity. To eliminate differences in tissue origin and assess the selectivity of TUC-1, activity can be evaluated in a normal pancreatic duct epithelial cells such as H6c7³⁵. This would enable direct comparison with the cancerous counterpart allowing any off-target effects to be identified.

The NCI-60 evaluation is a useful tool for early drug discovery allowing evaluation of activity while enabling further analysis by COMPARE. Additionally, the cytotoxic assays performed in PDAC cell lines are also indicative of biological activity informing further mechanistic work. This work can be used to perform *in vivo* studies in xenograft models of PDAC to evaluate dosage, toxicity and efficacy. K-ras wild-type and mutant models of mice would be useful in studying the effect of this PDAC driver mutation on the activity of TUC-1.

4.5 References

1. H. V. Nguyen, A. Sallustrau, J. Balzarini, M. R. Bedford, J. C. Eden, N. Georgousi, N. J. Hodges, J. Kedge, Y. Mehellou, C. Tselepis and J. H. R. Tucker, *J. Med. Chem.*, 2014, **57**, 5817-5822.
2. M. Amrutkar, N. T. Vethe, C. S. Verbeke, M. Aasrum, A. V. Finstadsveen, P. Sántha and I. P. Gladhaug, *Cancers*, 2020, **12**, 3628.
3. J. L. Kedge, H. V. Nguyen, Z. Khan, L. Male, M. K. I. Hodges, Holly V. Roberts, Nikolas J., S. L. Horswell, Y. Mehellou and J. H. R. Tucker, *Eur. J. Inorg. Chem.*, 2017, **2017**, 466-476.
4. M. K. Ismail, K. A. Armstrong, S. L. Hodder, S. L. Horswell, L. Male, H. V. Nguyen, E. A. Wilkinson, N. J. Hodges and J. H. R. Tucker, *Dalton Trans.*, 2020, **49**, 1181-1190.
5. C. R. Burke and A. Luptak, *Proc. Natl. Acad. Sci. USA*, 2018, **115**, 980-985.
6. M. K. Ismail, Z. Khan, M. Rana, S. L. Horswell, L. Male, H. V. Nguyen, A. Perotti, I. Romero-Canelón, E. A. Wilkinson, N. J. Hodges and J. H. R. Tucker, *ChemBioChem*, 2020, **21**, 2487-2494.
7. J. McConathy and M. J. Owens, *Prim. Care Companion J. Clin. Psychiatry*, 2003, **5**, 70-73.
8. N. Chhabra, M. L. Aseri and D. Padmanabhan, *Int. J. Appl. Basic Med. Res.*, 2013, **3**, 16-18.
9. W. H. Brooks, W. C. Guida and K. G. Daniel, *Curr. Top. Med. Chem.*, 2011, **11**, 760-770.
10. R. H. Shoemaker, *Nat. Rev. Cancer*, 2006, **6**, 813-823.
11. D. W. Zaharevitz, S. L. Holbeck, C. Bowerman and P. A. Svetlik, *J. Mol. Graph*

- Model*, 2002, **20**, 297-303.
12. D. Sampath, V. A. Rao and W. Plunkett, *Oncogene*, 2003, **22**, 9063-9074.
 13. A. Quispe-Mauricio, D. C, J. C, M. Posso and A. W, *Revista peruana de medicina experimental y salud publica*, 2006, **23**, 265-269.
 14. M. C. Alley, D. A. Scudiero, A. Monks, M. L. Hursey, M. J. Czerwinski, D. L. Fine, B. J. Abbott, J. G. Mayo, R. H. Shoemaker and M. R. Boyd, *Cancer Res.*, 1988, **48**, 589-601.
 15. P.-H. Jiang, Y. Motoo, N. Sawabu and T. Minamoto, *World J. Gastroenterol.*, 2006, **12**, 1597-1602.
 16. J. Guigay, J. Fayette, A. F. Dillies, C. Sire, J. N. Kerger, I. Tennevet, J. P. Machiels, S. Zanetta, Y. Pointreau, L. Bozec Le Moal, S. Henry, A. Schilf and J. Bourhis, *Ann. Oncol.*, 2015, **26**, 1941-1947.
 17. D. A. Fennell, Y. Summers, J. Cadranel, T. Benepal, D. C. Christoph, R. Lal, M. Das, F. Maxwell, C. Visseren-Grul and D. Ferry, *Cancer Treat Rev.*, 2016, **44**, 42-50.
 18. G. W. Sledge, Jr., P. J. Loehrer, Sr., B. J. Roth and L. H. Einhorn, *J. Clin. Oncol.*, 1988, **6**, 1811-1814.
 19. Y. Nakano, S. Tanno, K. Koizumi, T. Nishikawa, K. Nakamura, M. Minoguchi, T. Izawa, Y. Mizukami, T. Okumura and Y. Kohgo, *Br. J. Cancer*, 2007, **96**, 457-463.
 20. S. Schmidtova, K. Kalavska and L. Kucerova, *Curr. Oncol. Rep.*, 2018, **20**, 88.
 21. M. L. Alvarellos, J. Lamba, K. Sangkuhl, C. F. Thorn, L. Wang, D. J. Klein, R. B. Altman and T. E. Klein, *Pharmacogenet. Genomics*, 2014, **24**, 564-574.
 22. E. Mini, S. Nobili, B. Caciagli, I. Landini and T. Mazzei, *Ann. Oncol.*, 2006, **17**,

v7-12.

23. T. Neff and C. A. Blau, *Exp. Hematol.*, 1996, **24**, 1340-1346.
24. C. Bengala, V. Guarneri, E. Giovannetti, M. Lencioni, E. Fontana, V. Mey, A. Fontana, U. Boggi, M. Del Chiaro, R. Danesi, S. Ricci, F. Mosca, M. Del Tacca and P. F. Conte, *Br. J. Cancer*, 2005, **93**, 35-40.
25. E. L. Deer, J. González-Hernández, J. D. Coursen, J. E. Shea, J. Ngatia, C. L. Scaife, M. A. Firpo and S. J. Mulvihill, *Pancreas*, 2010, **39**, 425-435.
26. T. Tsuruo and I. J. Fidler, *Cancer Res.*, 1981, **41**, 3058-3064.
27. E. Biscop, A. Lin, W. V. Boxem, J. V. Loenhout, J. D. Backer, C. Deben, S. Dewilde, E. Smits, Bogaerts and Annemie, *Cancers*, 2019, **11**, 1287.
28. S. L. Holbeck, J. M. Collins and J. H. Doroshow, *Mol. Cancer Ther.*, 2010, **9**, 1451-1460.
29. A. B. Pavel and K. S. Korolev, *Sci. Rep.*, 2017, **7**, 1938-1938.
30. G. Kohlhagen, K. D. Paull, M. Cushman, P. Nagafuji and Y. Pommier, *Mol. Pharmacol.*, 1998, **54**, 50-58.
31. Y. Pommier and M. Cushman, *Mol. Cancer Ther.*, 2009, **8**, 1008-1014.
32. M. Gormen, P. Pigeon, S. Top, E. A. Hillard, M. Huche, C. G. Hartinger, F. de Montigny, M. A. Plamont, A. Vessieres and G. Jaouen, *ChemMedChem*, 2010, **5**, 2039-2050.
33. D. Namima, S. Fujihara, H. Iwama, K. Fujita, T. Matsui, M. Nakahara, M. Okamura, M. Hirata, T. Kono, N. Fujita, H. Yamana, K. Kato, H. Kamada, A. Morishita, H. Kobara, K. Tsutsui and T. Masaki, *In Vivo*, 2020, **34**, 3195-3203.
34. C. Focaccetti, A. Bruno, E. Magnani, D. Bartolini, E. Principi, K. Dallaglio, E. O. Bucci, G. Finzi, F. Sessa, D. M. Noonan and A. Albini, *PloS one*, 2015, **10**,

e0115686-e0115686.

35. H. Ouyang, L. Mou, C. Luk, N. Liu, J. Karaskova, J. Squire and M. S. Tsao, *Am. J. Pathol.*, 2000, **157**, 1623-1631.

Chapter 5 – DNA replication dynamics and transcriptomic response to TUC-1

5.1 Introduction

Previous work in our laboratory, using the alkaline comet assay, has shown that TUC-1 induces single strand breaks in cultures of MIA PaCa-2 cells. Data shown in Chapter 4 demonstrated that TUC-1 causes cell cycle arrest. In this chapter, data is presented that further examines the ability of TUC-1 to induce both single and double DNA strand breaks as a potential mechanistic trigger of cell cycle arrest.

Phosphorylation of histone variant H2AX at Serine-139¹, serves as a biomarker for DSBs detected via immunofluorescent labelling and foci formation observed by microscopy and/or flow cytometry². Nucleoside analogues such as gemcitabine have been shown to induce DNA DSBs following incorporation into nascent DNA which leads to marked increase in phosphorylated H2AX, γ H2AX, foci formation³. This effect has been attributed to gemcitabine-induced stalled replication forks and replication termination³. Therefore, presence of γ H2AX is also indicative of replication fork stalling as reported previously for nucleoside analogues cytarabine, troxacitabine and gemcitabine⁴.

Unstable replication forks, slow fork progression and/or fork collapse, as a result of direct inhibition of replication fork machinery or presence of DNA lesions, result in single stranded DNA that are converted to DSBs⁵. To study replication forks at single molecule resolution, DNA fibre fluorography was used which also uses base

analogues to pulse-label replicating DNA in cells however, instead of average cellular assessment, replication forks can be visualised as local individual entities⁶.

Sequential labelling and immunodetection of two thymidine analogues, chloro-deoxyuridine (CldU) and iodo-deoxyuridine (IdU) allows visualisation of different phenotypes that arise from slow/stalled replication forks, replication termination, origin firing and direction of replication⁶.

Stalled replication forks, in addition to DNA damage, can trigger intra-S checkpoint⁷ to enable repair and initiate fork restart. As detailed in Chapter 1 Section 1.2.3, various DNA damage response (DDR) proteins are involved in checkpoint activation including ATM and ATR kinases that activate Chk1 and Chk2 kinases respectively, these transducers relay the signal to downstream effector proteins. While the ATR-Chk1 axis is activated in response to SSBs and other lesions, ATM-Chk2 pathway is activated in response to DSBs^{7, 8}, although there is substantial substrate overlap between the two pathways. Western blot analysis, performed in this chapter, for the phosphorylated form of protein kinases Chk1, Chk2, and their substrates H2AX and RPA were used to confirm the checkpoint response in cells treated with TUC-1.

Previously, the assembly of ATM and MRN complex (Mre11-Rad50-Nbs1) has been shown to assemble at stalled replication forks and initiate repair following exposure to nucleoside analogues⁴. This has been proposed as one of the chemoresistance mechanisms enabling cancer cell proliferation after repair⁴. To investigate if this occurs following TUC-1 induced replication fork stalling and S-phase arrest, gene expression array to monitor transcriptomic changes of genes involved in DNA

damage response (DDR) and cell cycle regulation. Quantitative PCR array was performed in all three PDAC cell lines to investigate if the transcriptional response is conserved or if there are cell line differences as highlighted earlier with TUC-1* activity and differential TUC-1 sensitivity in NCI-60 panel of cell lines (Chapter 4).

Targeted qPCR analysis was also performed with genes identified in the array as significantly changed in at least two PDAC cell lines, forming a functional network as identified in STRING (<https://string-db.org>). This platform allows evaluation of gene expression results by performing protein-protein interaction analysis to identify physical or functional associations. Following this, the role of tumour suppressor p53 in orchestrating this transcriptomic response in PDAC cell lines was probed by confirming the mutational status of these cell lines by gene sequencing. Expression level of p53 homologs, p63 and p73, was also evaluated following treatment with TUC-1 to identify possible compensatory mechanisms regulating expression of p53 target proteins.

5.2 Results

5.2.1 DNA binding

TUC-1 interaction with double-stranded calf-thymus DNA was monitored through UV-vis spectroscopy over a time course of 72 hours with measurements taken at 24-hour intervals. The ctDNA, in the absence of TUC-1, had an absorbance maximum at 254 nm while TUC-1 exhibits maximum absorption at a wavelength of 268 nm (Figure 5.1). As TUC-1 and ctDNA were combined at equimolar concentrations (220 μM), an additive effect was observed in contrast to the hyperchromic effect commonly observed at 260 nm in the event of intercalation⁹. It is evident that TUC-1 does not directly bind or interact with DNA and therefore it is not part of the MoA.

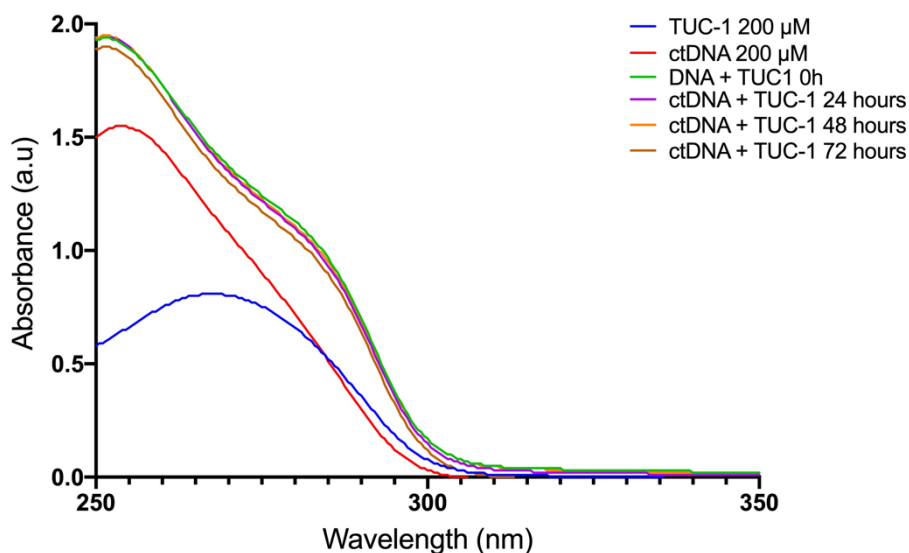


Figure 5.1. UV absorption spectra of TUC-1 in the presence of calf-thymus DNA (ctDNA), measurements taken at 0, 24, 48 and 72 hours.

5.2.2 DNA strand breaks

Previously we have shown that TUC-1 induces DNA single strand breaks in a concentration dependent manner as investigated by the alkaline comet assay (Figure 5.2). Treatment of MIA PaCa-2 cells with increasing concentrations of TUC-1 (0-5 μ M, 24 hours) led to a concentration-dependent increase in percentage tail intensity, indicative of SSBs. The mean % tail DNA values were 0.38 ± 0.11 , 0.93 ± 0.02 , 5.90 ± 1.3 and $14.2 \pm 1.25\%$ for cells treated with 0, 1, 2.5 and 5 μ M TUC-1 respectively (Figure 5.2A), compared to $29.0 \pm 0.3\%$ for positive control gemcitabine (50 nM, 24 hours). Furthermore, pulse-labelling cells with EdU revealed SSBs to be present in newly synthesised DNA (Figure 5.2B) as indicated by the presence of EdU (green signal) in the comet tails. Whereas this effect was absent in cells treated with 4-Nitroquinoline that induces SSBs by stabilising the transient strand breaks created by topoisomerases¹⁰.

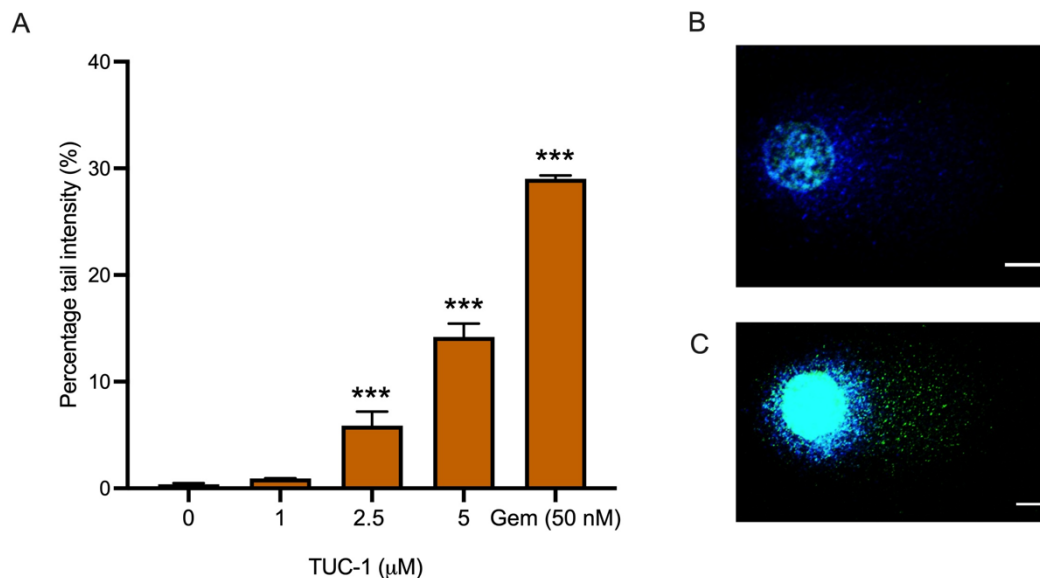


Figure 5.2. TUC-1 induced DNA single strand breaks in newly synthesised DNA. (A) Concentration-dependent increase in single stranded DNA breaks following treatment with TUC-1 (0-5 μ M, 24 hours) as assessed by the comet assay. Pulse labelling with EdU (green signal) prior to treatment confirms that single strand breaks occur in newly synthesised DNA following treatment with (B) TUC-1 (5 μ M, 24 hours) but not when treated with (C) NQO (2.1 μ M, 24 hours), genotoxic chemical, where only non-EdU DNA counterstained with Hoechst (blue signal) is visible in the comet tail. The results represent the mean of three independent biological experiments (\pm SD, $n = 3$), *** significantly different from untreated control ($P < 0.001$, 1-way ANOVA followed by a *post-hoc* Dunnett's t-test) (Scale bar = 10 μ M, Magnification 40X).

Formation of DNA DSBs results in phosphorylation of histone protein H2AX by checkpoint kinases ATM/ATR. Therefore, phosphorylation of H2AX, detected by immunofluorescence, is a sensitive biomarker of DSBs in cells. It is proposed the phosphorylated protein recruits DNA damage proteins such as Chk kinases following detection¹. After 24-hour treatment with TUC-1 (10 μ M), flow cytometry was performed to quantify levels of γ H2AX. The results show levels of γ H2AX are elevated in all three PDAC cell lines compared to negative control. This was quantified as an increase in median fluorescence intensity (MIF, Figure 5.3). Fold change in TUC-1 treated samples was calculated compared to untreated control with etoposide (5 μ M, 24 hour), an inhibitor of topoisomerase II¹¹, used as a positive control. For MIA PaCa-2 the increase in MIF hence DSB formation was 4.3-fold higher compared to untreated control whereas the fold changes calculated for

BxPC3, and CFPAC-1 were 3.4 and 2.5 respectively. Based on these fold changes, MIA PaCa-2 cells were most susceptible to TUC-1-induced DSBs which can be attributed to cell line differences discussed in Chapter 4.

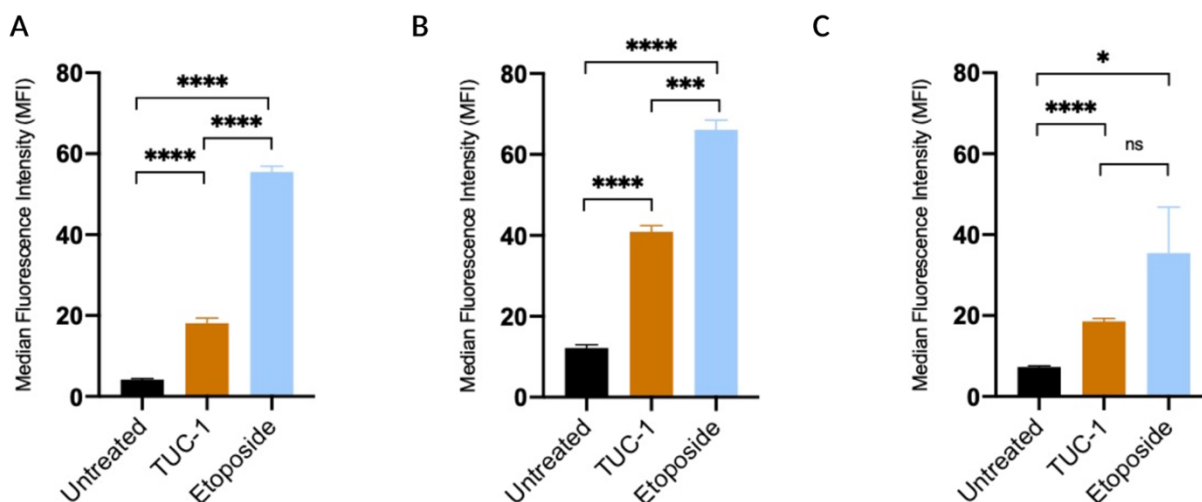


Figure 5.3. TUC-1 induces DNA double strand breaks in genomic DNA of PDAC cell lines MIA PaCa-2 (A), BxPC3 (B) and CFPAC-1 (C) as detected by γ H2AX phosphorylation, a biomarker for DNA double strand breaks, immunolabelled and detected by flow cytometry. Following treatment with TUC-1 (10 μ M, 24h) the median fluorescent intensity (MFI) increased in all cell lines compared to untreated control, indicative of elevated levels of γ H2AX. Etoposide (5 μ M, 24h) was used as a positive control. The results represent mean of three independent biological repeats (\pm SD, n = 3). *, ** and **** Statistically significant differences, P<0.05, 0.001 and 0.0001 respectively (Unpaired t-test).

Immunofluorescence labelling of γ H2AX foci by confocal microscopy imaging enables visualisation of the spatial distribution of DSBs in nuclei and was therefore used to further study formation of γ H2AX. In untreated cells only very faint H2AX foci were observed indicative of basal level of DSB induction induced by endogenous sources (Figure 5.4A). Treatment with TUC-1 (10 μ M, 24 hours) results in a dramatic increase in the number of γ H2AX foci confirming formation of DSBs observed by flow cytometry (Figure 5.4D) and providing evidence of the spatial distribution in the cell. The γ H2AX foci appear to be located in the nucleus exclusively, except the nucleolus,

as identified by PI counterstaining. Cells treated with etoposide as a positive control (5 μ M, 24 hours) also exhibiting intense γ H2AX foci (Figure 5.4G).

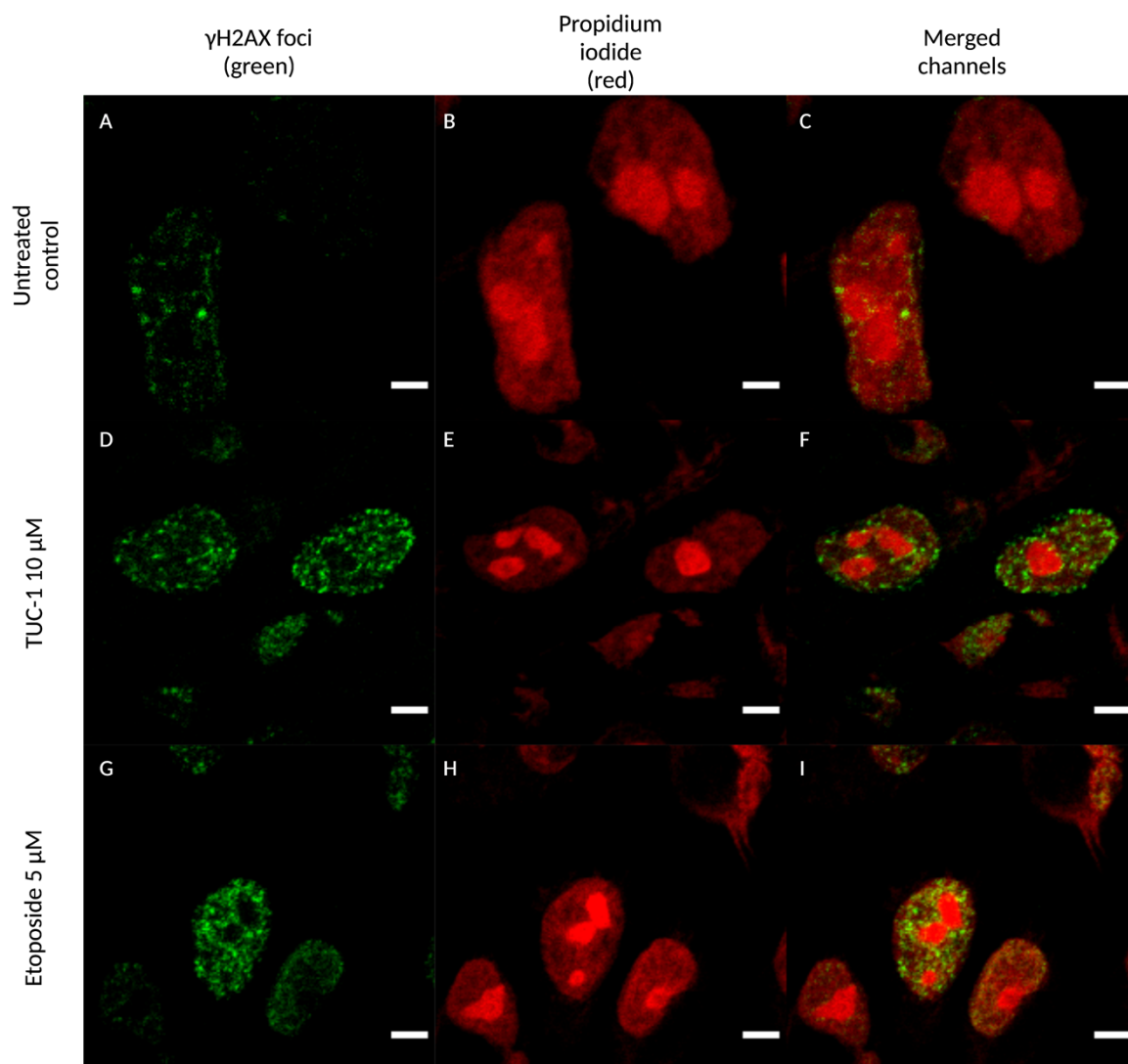


Figure 5.4. Representative images of MIA PaCa-2 cells exposed to TUC-1 (10 μ M, 24h) and positive control Etoposide (5 μ M, 24h) stained for γ H2AX with antibodies (green fluorescence) and counterstained with propidium iodide (red fluorescence). Cells treated with TUC-1 have higher γ H2AX foci formation compared to untreated control indicative of more DNA double strand breaks (Scale bar = 5 μ m, Magnification 100X).

5.2.3 DNA fibre fluorography

DNA fibre fluorography was performed to assess replication fork dynamics by labelling replication forks with thymidine analogues, CldU and IdU, in a sequential manner during treatment with TUC-1. Immunodetection with analogue-specific antibodies allows visualisation of replication forks and incorporated CldU and IdU are labelled red and green respectively (Figure 5.5A). Active replication forks appear as red and green tracts allowing the fork direction to be identified⁶. Additionally, replication dynamics such as new origins, elongation, termination, and fork collapse can also be monitored through this strategy⁶. For this experiment, overall fibre lengths, red and green signal combined, were monitored after treatment with TUC-1.

MIA PaCa-2 cells were treated with increasing concentrations of TUC-1 (5, 10 and 25 μ M) for 24 hours. At the end of the treatment, cells were pulse-labelled with CldU followed by IdU for 20 min each, labelled with antibodies and visualised through immunofluorescence microscopy (Figure 5.5A). Fibre lengths measured in micrometre (μ m) was converted to kB of DNA as described previously⁶. In untreated MIA PaCa-2 cells, mean fibre length was observed to be 2.34 ± 0.8 kB (range 0.73–5.60). In contrast, cells treated with TUC-1 had statistically significantly shorter fibres ($P < 0.001$) for all concentrations investigated. Following treatment with 5 and 10 μ M TUC-1 mean fibre lengths were observed to be 0.56 ± 0.20 (range 0.19–2.17) and 0.28 ± 0.12 (range 0.08–1.53) kB respectively (Figure 5.5B).

Representative images of DNA-fibres from each experimental condition are shown in Figure 5.5D-G. The red (CldU) and green (IdU) labels are approximately the same

length, a ratio of 1:1, for untreated control as expected for unperturbed DNA replication. Treatment with 25 μ M TUC-1 resulted in complete replication arrest, as evident in the images, leading to unquantifiable fibres (Figure 5.5G). The speed of DNA-replication, as determined from the mean fibre lengths, were 0.12 ± 0.04 , 0.028 ± 0.01 and 0.014 ± 0.006 kB/minute for untreated control, 5 and 10 μ M treatments respectively (Figure 5.5C). This provides evidence that TUC-1 induces replication stress by fork stalling, an upstream event leading to fork collapse that is translated into DNA strand breaks as evident by γ H2AX foci formation presented earlier.

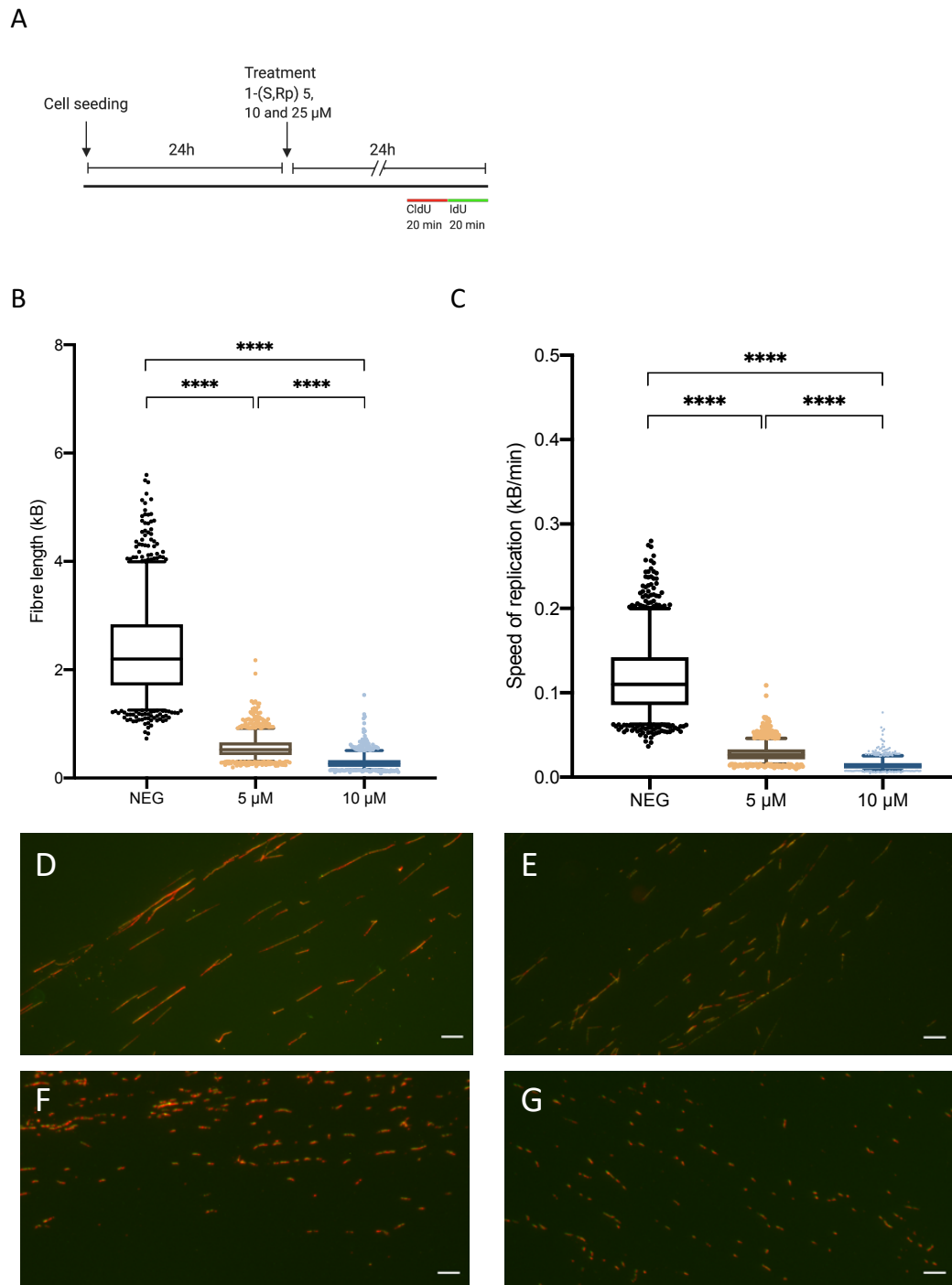


Figure 5.5. TUC-1 inhibits DNA replication assessed at single molecule resolution by DNA fibre fluorography. (A) Schematic of experimental design: cells were seeded and treated with increasing concentrations of TUC-1 (5, 10 and 25 µM) for 24h before labelling with thymidine analogues CldU (red) followed by IdU (green) (Created with BioRender.com). (B) Total fibre length measured in (kB) and (C) Speed of replication (kB/min) had a concentration dependent decrease upon treatment with TUC-1. Representative images of DNA fibres following treatment with (D) untreated control, (E) TUC-1 5 µM, (F) TUC-1 10 µM and (G) TUC-1 25 µM. Box and whisker plots show the mean (line splitting the box), interquartile range (box), 5 and 95 percentile range (whiskers) with values falling outside this range plotted as individual points. The results represent the mean of three independent biological experiments ($n = 3$) with 1072, 1406 and 1189 DNA fibres analysed for untreated control, 5 µM and 10 µM TUC-1 respectively. Treatment with 25 µM TUC-1 led to complete inhibition of replication and unquantifiable DNA fibres. **** Statistically significant ($P < 0.0001$) as assessed by a two-tailed t-test (Scale bar 10 µm, Magnification 40X)

5.2.4 Checkpoint activation

Next it was investigated whether checkpoint activation occurs following replication fork stalling in TUC-1 treated cells. Expression and phosphorylation status of key checkpoint kinases Chk1, Chk2, H2AX and RPA was determined. PCR array performed in MIA PaCa-2 cells, presented later (Section 5.2.4), shows gene expression of both Chk kinases to be upregulated following treatment with TUC-1 (10 μ M, 24 hours). As shown in Figure 5.6A, treatment with 10 μ M TUC-1 for 2h, 7h and 24h also leads to phosphorylation of Chk 1 and 2 kinases and their substrate RPA. Consistent with the data presented in section 5.2.1, phosphorylation of H2AX was also confirmed. Preliminary quantification of the bands, by densitometry, is shown in Figure 5.6B and confirms the increase in phosphorylated protein content in samples treated with TUC-1 compared to untreated controls. The ratios of expression of phosphorylated proteins in TUC-1 treated samples compared to negative control was 2.24, 3.74, 2.44 and 2.13 for pChk1, pChk2, pRPA and H2AX respectively.

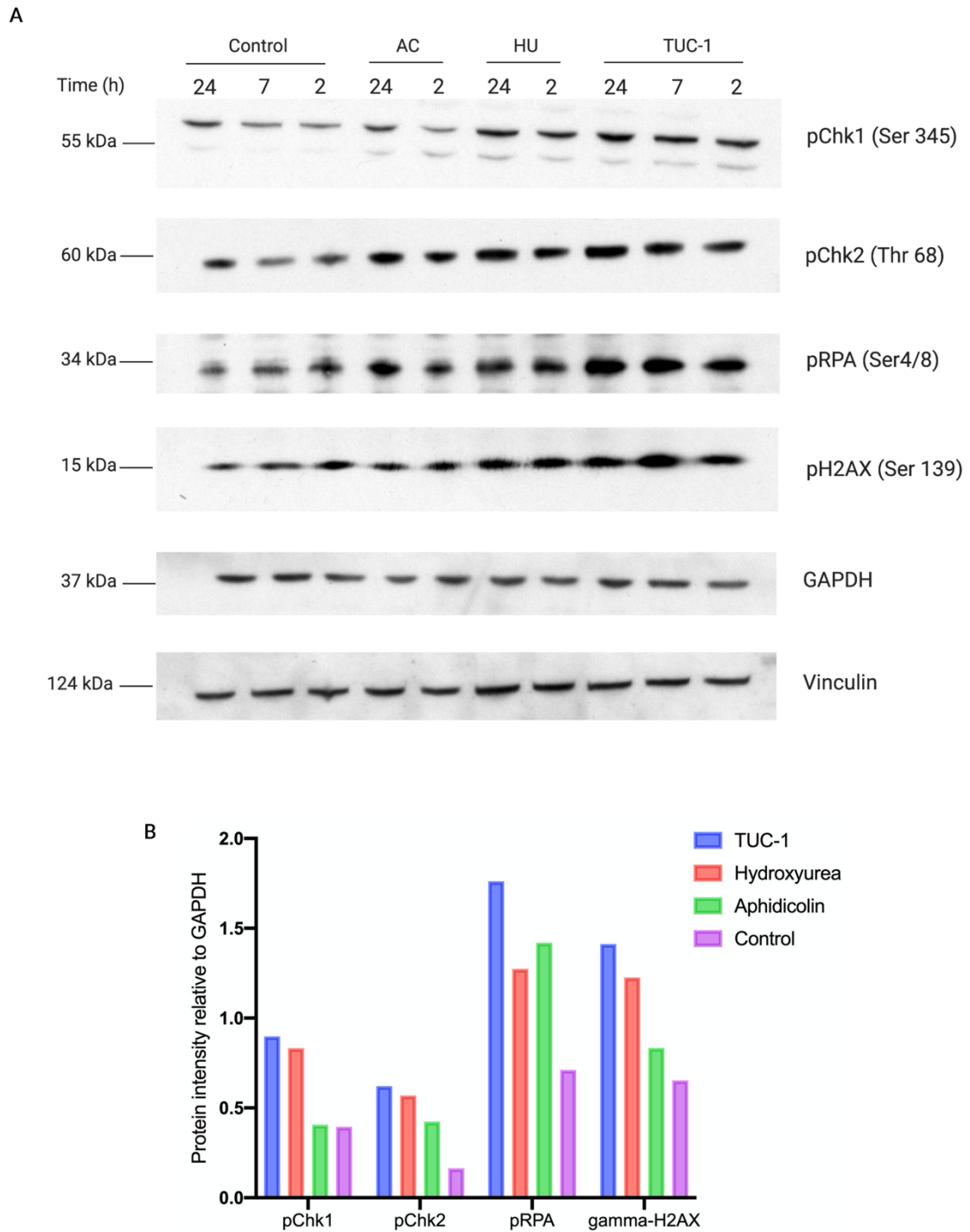


Figure 5.6. (A) Western blotting for DNA damage response proteins including phosphorylated Chk kinases, H2AX and RPA in MIA PaCa-2 cells treated with 10 μ M TUC-1 for 2, 7 and 24 hours. Cells were also treated with 0.5 μ M Hydroxyurea (HU) and 2.4 μ M Aphidicolin (AC) for 2 and 24 hours as positive controls. GAPDH and vinculin were used as loading controls. (B) Corresponding densitometric analysis with bar chart showing protein level relative to GAPDH in each sample. The results represent one biological repeat (n = 1).

5.2.5 Gene expression analysis

Quantitative PCR of a panel of 84 genes involved in DNA damage response and cell cycle progression was performed. This is to investigate the transcriptomic changes following replication fork stalling and DNA double strand breaks following treatment with TUC-1 (10 μ M, 24 hours) compared to untreated control. Altogether, 53 out of the 84 genes investigated were upregulated (Appendices Table S4), 39 (63%) of these genes were statistically significant (Figure 5.7), data normalised to GAPDH housekeeping gene. Importantly, upregulation was observed in checkpoint kinases *ATM*, *Chk1* and *Chk2* and key players of the DDR pathway including *MRE11A*, *RAD1*, *HUS1*, *RAD17*. These data suggests that a strong DNA damage response is activated following treatment with TUC-1 in MIA PaCa-2 cells.

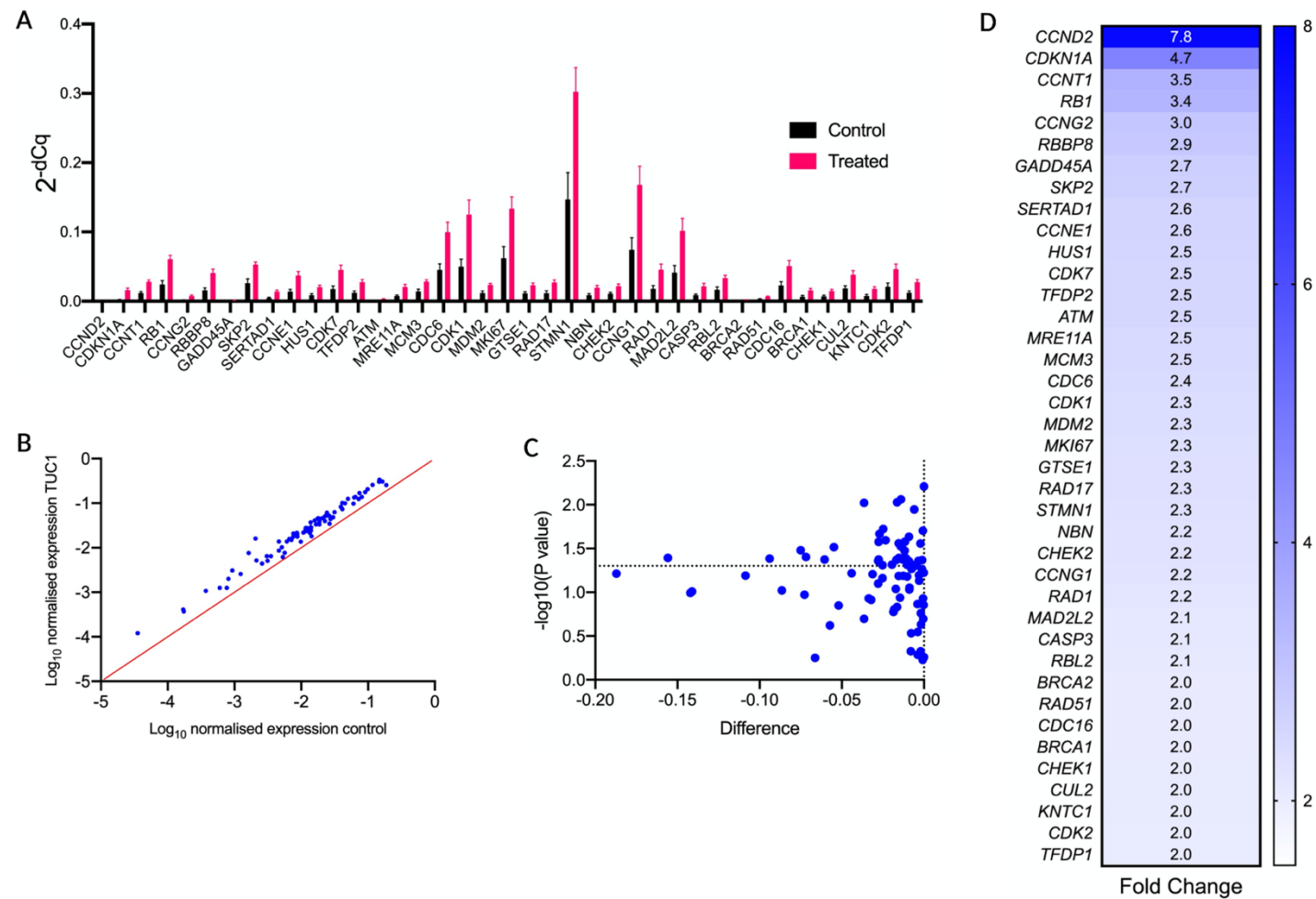


Figure 5.7. List of 39 genes related to DNA-repair that are statistically significantly upregulated in MIAPaCa2 cells following treatment with TUC-1 (10 μ M, 24 hours). A) Expression in control and treated cells expressed as 2^{-dCq} relative to *GAPDH*. B) Log normalised plot of data, C) volcano plot and D) Fold changes. The results represent the mean of three independent biological experiments (mean \pm SD, n=3), statistical significance ($P < 0.05$) assessed by unpaired t-test.

The qPCR array was also performed in BxPC3 and CFPAC-1 to determine if the core DDR signalling initiated by TUC-1 is conserved. The overall changes in gene expression were lower in BxPC3 and CFPAC1, with only 7 and 15 of the 84 genes upregulated (fold change ≥ 1.5) respectively as shown in Figure 5.8.

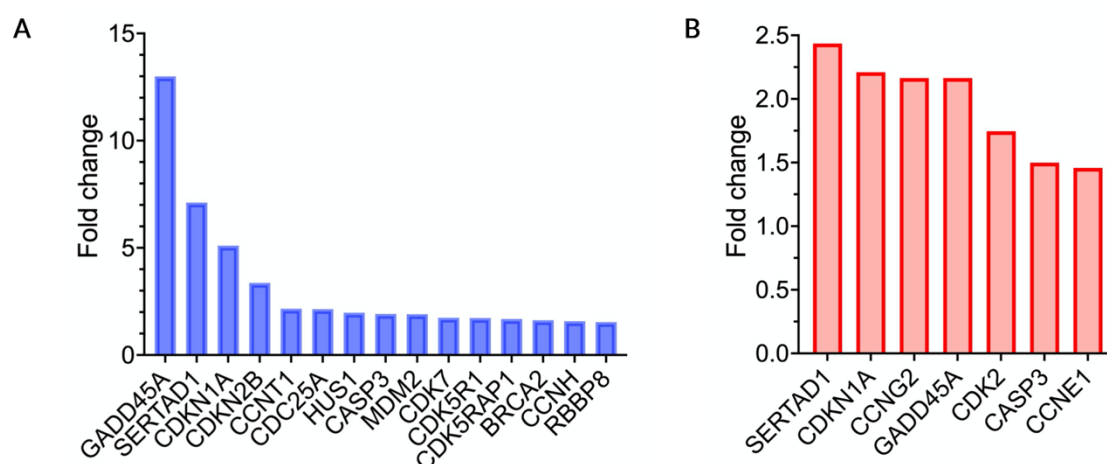


Figure 5.8. List of genes upregulated in the qPCR array (fold change > 1.5) in CFPAC-1 (A) and BxPC3 (B). The results represent one biological repeat plotted as $2^{-\Delta Cq}$ relative to *GAPDH*.

Comparing the expression pattern in all three PDAC cell lines, it was found out of the 39 genes significantly changed in MIA PaCa-2, 13 were induced in either BxPC3 and CFPAC1 or both at a fold change of 1.5 or greater (Appendices Table S4). Analysis of this list of genes in STRING¹² was performed to establish potential protein-protein interaction networks. The network identified by STRING (Figure 5.8A) was assigned a ppi enrichment value of $p < 1.0e-16$ indicative of biological relevance. Additionally, gene ontology analysis revealed cell cycle regulation and DNA damage response as the biological processes coordinated by this network (GO terms: GO:0051726, GO:0007049, GO:0000079, GO:0006974 and GO:0045786). By Kmeans clustering,

2 main clusters (Figure 5.9A) were identified with the genes falling into two categories; DNA damage response (*SERTAD1*, *RBBP8* and *HUS1*) or cell cycle regulation (*GADD45A*, *MDM2*, *CDKN1A*, *CCNG2*, *CDK2*, *CCNE1*, *CDK7*, *CCNT1* and *CASP3*).

This gene network was validated by targeted qPCR in all three PDAC cell lines. As shown in Figure 5.9B there is an evident increase in cell cycle inhibitors *CDKN1A* and *GADD45A* in all three cell lines, normalised to B2M, consistent with cell cycle arrest observed in Chapter 4. For MIA PaCa-2, all the genes showed 1.5 or greater fold change, whereas this was true for 6 and 8 out of the 13 genes for BxPC3 and CFPAC-1 respectively. Interestingly, apart from *CDKN1A* and *SERT1*, none of the genes were upregulated (fold change > 1.5) in MIA PaCa-2 cells treated with the enantiomer of TUC-1, TUC-1* (10 µM, 24 hours) (Figure 5.9B). These two genes showed a greater fold change following treatment with TUC-1 compared to TUC-1*.

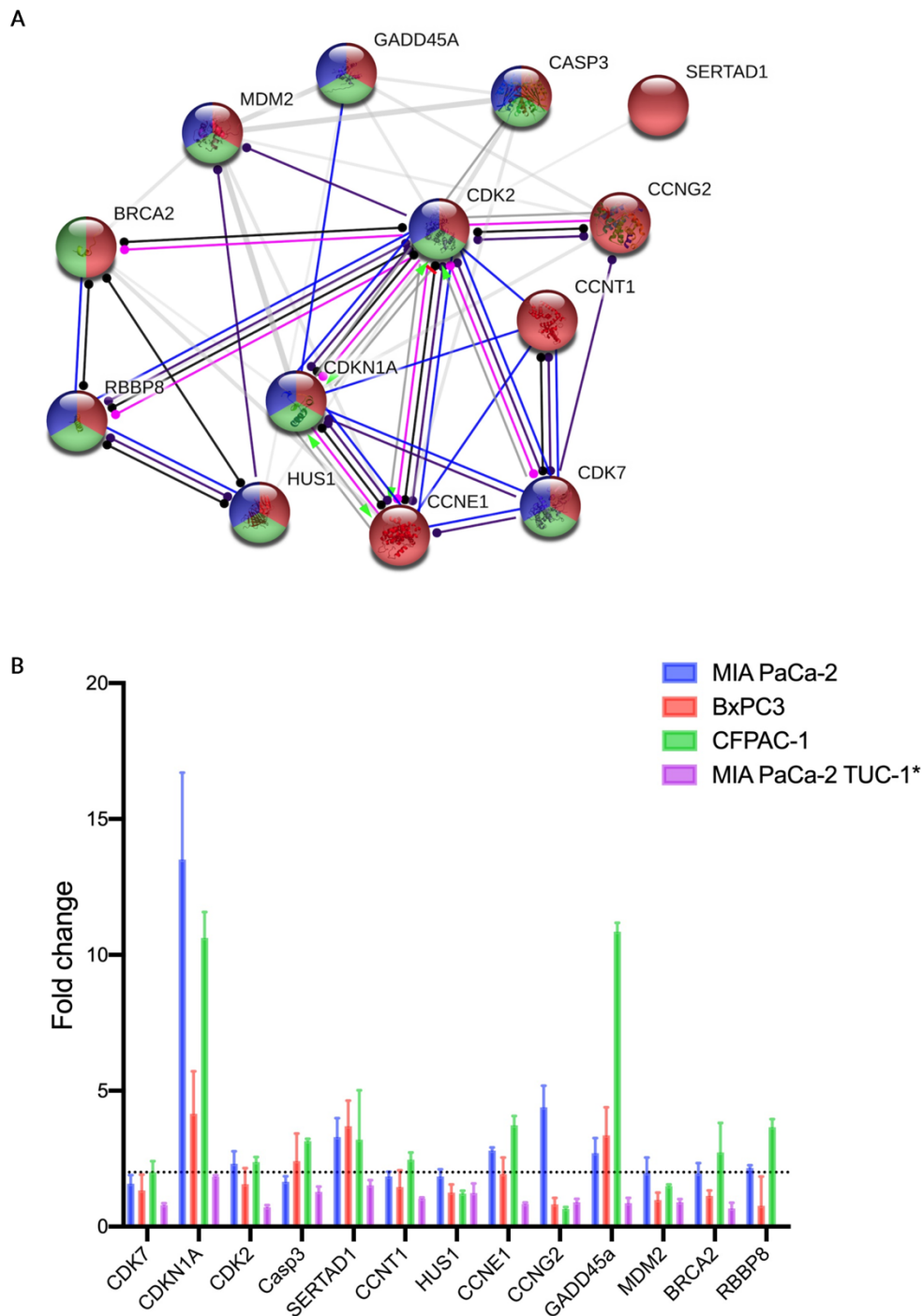


Figure 5.9. TUC-1 induces a conserved transcriptional response in PDAC cell lines MIA PaCa-2, BxPC3 and CFPAC-1. (A) STRING functional protein network (<https://string-db.org>) of the 13 genes significantly changes in MIA PaCa-2 and at least one other PDAC cell line when treated with TUC-1 (10 μ M, 24 hours). Within the network major GO-terms represented included: GO:0051726 regulation of cell cycle (coloured red), GO:0045786 negative regulation of cell cycle (coloured blue) and GO:0006974 cellular response to DNA damage stimulus (coloured green). Interconnecting lines within the network represent predicted molecular actions: activation, inhibition, binding, catalysis, phenotype, posttranslational modification, reaction and transcriptional regulation. (B) Relative gene expression analysis of the 13 gene STRING network in MIA PaCa-2, BxPC3, CFPAC-1 and MIA PaCa-2 treated with TUC-1* assessed by qPCR. The results represent the mean of three independent biological repeats ($n = 3$, \pm SD).

To further investigate if the induction of p21 (*CDKN1A*) among other p53 targets in the STRING network (*CDK2*, *MDM2*, *CASP3*, *CDKN1A*, *GADD45A*, *CCNG2*, *CCNE1*) was p53 dependent as reported in literature¹³, qPCR was performed under the same treatment conditions with human colon cancer cell lines HCT116, wild-type and p53-mutant (null), different in p53 expression but otherwise isogenic. It was found that there were little differences in gene expression levels between these two cell lines with a slightly enhanced *CDKN1A* expression in p53 wild-type cells (Figure 5.10). The three PDAC cell lines are also reported to have mutant non-functional p53¹⁴, this was verified by p53 sequencing (Appendices Figure S7). The following missense substitution mutations were detected in the cell lines in agreement with the mutations reported in Cosmic database¹⁴:

- i. MIA PaCa-2: cytosine to thymine at position 742
- ii. BxPC3: adenine to guanine at position 659
- iii. CFPAC-1: thymine to cytosine at position 724

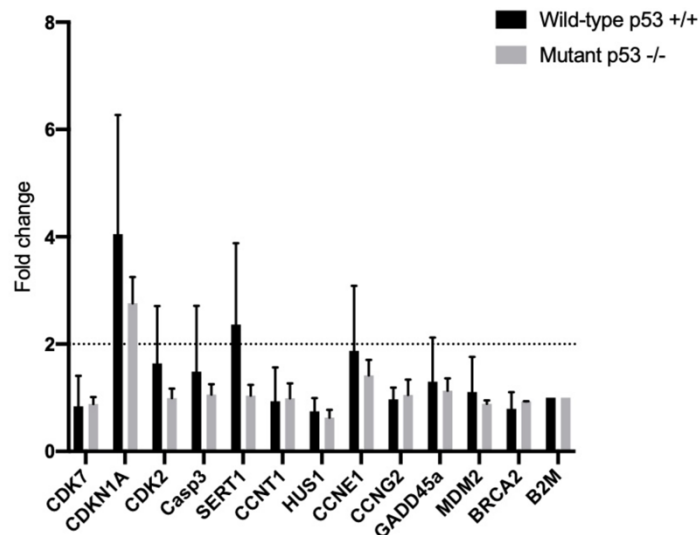


Figure 5.10. Gene expression changes following treatment with TUC-1 (10 μ M, 24 hours) are independent of p53 status. Relative gene expression analysis of 12 genes part of the conserved STRING protein network, identified previously, in p53 wild type (HCT116 $^{+/+}$) and p53 mutant (HCT116 $^{-/-}$) human colon cancer cell lines.

Altogether, this confirms that p21 (*CDKN1A*) upregulation is, if not completely then partially, independent of p53. Next, expression level of p53 homologs p63 and p73 was investigated to determine if expression levels of these isoforms changed in response to treatment with TUC-1 providing a compensatory route to activating p53-responsive genes identified in the qPCR array. As shown in Figure 5.11, treatment with TUC-1 (10 μ M, 24 hours) led to induction of p73 in MIA PACA-2 and CFPAC-1 as well as p53 mutant cell line HCT116 $^{-/-}$. Interestingly, expression levels of p63 remained quite low in all cell lines except p53 WT cell line HCT116 $^{+/+}$. This could mean, in line with literature, p73 could be providing an alternative route to activating p53 targets in response to DNA damage leading to cell cycle arrest and consequently apoptosis as shown previously.

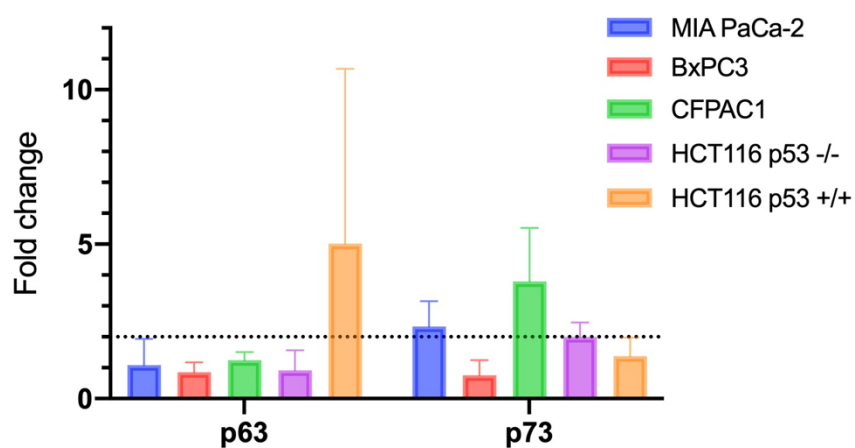


Figure 5.11. Relative gene expression analysis of p53 homologs, p63 and p73 in MIA PaCa-2, BxPC3, CFPAC-1, HCT116 p53^{+/+} and HCT116 p53^{-/-} cell lines as assessed by qPCR. Homolog p73 is differentially upregulated in most cell lines including p53 mutant cells after treatment with TUC-1 (10 μ M, 24 hours). The results represent the mean of three independent biological repeats ($n = 3$, \pm SD).

5.3 Discussion

This chapter has evaluated the ability of TUC-1 to induce DNA damage in PDAC cell lines MIA PaCa-2, CFPAC-1 and BxPC3. The formation of SSB and DSBs has been detected by the comet assay and γ H2AX foci formation respectively. Presence of DSBs in all three PDAC cell lines can be attributed to inactivating mutations present in key tumour suppressor proteins including *p53*, *SMAD4* and *CDKN2A* which, coupled with activation of oncogene *KRAS*, limits the DNA repair potential of these cells¹⁵.

The intra-S phase checkpoint, described in Chapter 1 Section 1.2.4, serves as the main DNA damage checkpoint in the cell cycle protecting genome integrity and ensuring faithful replication by regulating replication forks. ATR kinase and its downstream targets including Chk1 dominate intra-S checkpoint response, playing a key role in SSB detection⁷. H2AX, widely used as a biomarker for DSBs is a substrate for ATM and ATR kinases¹⁶ which, upon phosphorylation, recruits signal transducers Chk1 and Chk2 that are part of the DNA damage response (DDR) pathway. ATM kinase is recruited to DSBs by the MRN complex¹⁶, discussed later, leading to substrate phosphorylation which includes H2AX, Chk1, Chk2, 53BP1 and BRCA1.¹⁶ γ H2AX foci has also been implicated in assisting DSB repair via homologous recombination¹⁷. Therefore, the presence of this marker in PDAC cell lines following TUC-1 exposure is not only indicative of the presence of DSBs but also the initiation of repair.

Further evidence that supports this role include colocalization of γ H2AX with other sensory proteins that initiate ATM/ATR-dependent repair including components of the MRN complex MRE11, Rad50 and NBS1^{18, 19}. Carboxy terminus of γ H2AX serves as a docking site for repair proteins particularly MDC1 which, in complex with γ H2AX, forms a recognition site for the MRN complex leading to ATM activation and downstream DDR effector proteins¹⁶. Additionally, H2AX is phosphorylated by ATR upon SSB detection following replication stress during S phase of the cell cycle therefore this event is also important in monitoring DNA replication by stabilising replication forks²⁰. Altogether, this demonstrates DNA single- and double strand breaks induced by TUC-1 activate checkpoint response and DDR leading to S phase arrest observed earlier (Chapter 4)

DNA replication dominates the S phase of the cell cycle as pre-replicative complexes, assembled at the origin of replication during G1 phase, are converted to active multiprotein replication forks^{21, 22} as detailed in Chapter 1 Section 1.2.2. Different factors including nucleotide depletion can impede S phase progression by replication fork stalling which may result in fork collapse dependent on the duration of the blockade²². It has also been previously reported that replication fork stalling caused by hydroxyurea can be reversed by fork restart with long exposure leading to collapse and formation of DSBs²³. To decipher if DSBs observed earlier and the decrease in the rate of EdU incorporation observed previously (NJH personal communication) are a result of TUC-1 induced replication stalling, DNA replication forks were studied at single molecule resolution by DNA fibre fluorography²⁴. This experiment demonstrated concentration-dependent replication fork stalling as a

crucial part of the MoA of TUC-1 with complete inhibition observed with 25 μ M. Nucleoside analogues such as gemcitabine have been reported to induce replication fork stalling after incorporation as the steric clash with the analogue prevents fork progression³. The presence of γ H2AX at stalled replication forks have also been reported to coincide with gemcitabine incorporation into DNA suggesting a role in fork stabilisation³, the exact role remains elusive.

Inhibition of replication machinery and consequential replication fork stalling by other agents such as hydroxyurea and aphidicolin is also accompanied by an increase in γ H2AX foci formation, observed with TUC-1^{20, 25}. DNA polymerase and helicase uncoupling at stalled replication forks leads to single stranded DNA that is coated with Replication protein A (RPA) providing a signal of distress to the intra-S checkpoint⁷. These SSBs are converted to DSBs leading to recruitment of the MRN and 9-1-1 complex to the site of stalled forks, as evident by the transcriptomic changes discussed later. The subsequent activation Chk1 inhibits Cdc25A preventing new origin firing and CDK2-mediated S phase progression²⁶.

To determine whether TUC-1 induced replication fork stalling, and DNA damage activates checkpoint response, immunoblot analysis for phosphorylated Chk1 and Chk2 was performed. Additionally, protein expression of γ H2AX and phosphorylated RPA was also assessed to validate the quantitative data obtained earlier and verify the presence of single stranded DNA following fork stalling. The results show high protein expression of both Chk kinases, γ H2AX and phospho-RPA after treatment with TUC-1 confirming checkpoint activation. Elevated level of phospho-RPA

confirms the fork stalling mechanism suggested earlier as ahead of stalled replication forks, MCM helicases continue to unwind the DNA leading to SSBs stabilised by phospho-RPA which recruits the 9-1-1 clamp of Rad9, Rad1 and Hus1 to initiate repair as discussed later^{27, 28}. Gene upregulation of MCM3, MCM2, Rad1 and Hus1 was evident in the MIA PaCa-2 qPCR array following treatment with TUC-1 further confirming this.

Transcriptomic changes in PDAC cell lines that accompany these events were also assessed by quantitative PCR following treatment with TUC-1. The results show statistically significant upregulation of key genes involved in the detection of DNA damage, cell cycle regulation and initiation of the DDR pathways. These include *MRE11A* and *NBS1*, components of the MRN complex (*MRE11*, *RAD50* and *NBS1*) which binds stalled replication forks and DSBs leading to recruitment of ATM kinase to the site of damage²⁹. The 9-1-1 complex of *RAD9*, *HUS1* and *RAD1*, first responders to DNA damage, plays a key role in checkpoint activation³⁰. Both *HUS1* and *RAD1* had elevated expression following treatment with TUC-1. This complex leads to activation of Chk1 by ATR, as evident in the immunoblot analysis, which also promotes replication fork stabilisation³⁰. Phospho-RPA bound to ssDNA is replaced by *RAD51*, one of the significantly upregulated genes. Rad51 stabilises ssDNA, protecting it from nuclease activity assisted by BRCA2, which was also upregulated in the array³¹. This promotes fork reversal and repair by homologous recombination³¹. Altogether, this data supports the immunoblot analysis suggesting a robust DDR and checkpoint response is activated by TUC-1. Compared to MIA PaCa-2 cells, fewer changes were observed in BxPC3 and CFPAC-1.

Gene ontology analysis of the 13 genes significantly upregulated in at least two PDAC cell lines identified two clusters: DDR and cell cycle regulation. A targeted qPCR of this network showed all genes to be upregulated (fold change > 1.5) in MIA PaCa-2 cells whereas less changes were observed in CFPAC-1 and BxPC3. Reinforcing the inactivity of TUC-1* in MIA PaCa-2 cells (Chapter 4, Section 4.2.1), only 2 out of the 13 genes showed a fold change > 1.5 following treatment with the enantiomer. The lack of a transcriptomic response confirms the cell line sensitivity and superior activity of TUC-1 as discussed in Chapter 4. *GADD45a* and *CDKN1A*, negative regulators of the cell cycle and downstream targets of tumour suppressor p53, had the highest expression level in all three PDAC cell lines. *GADD45a* has also been identified as an inducer of apoptosis following genotoxic stress, mode of cell death observed earlier in cells treated with TUC-1.

To investigate the role of p53 in activating these genes, qPCR studies were performed in p53 wild-type (WT) and p53 mutant HCT116 cell lines to look at expression changes in the same network of 13 genes. As these cell lines were isogenic except for their p53 status, it was reasoned that any changes will be attributed to p53 status. However, no significant changes were observed between the wild-type and mutant cells indicating activation of DDR, intra-S checkpoint and subsequent cell cycle arrest is p53 independent in these cells. Missense mutations in *TP53* are found in 50-75% PDAC malignancies³², it is reported to be an important event in tumour progression by promoting metastasis and growth.

PDAC cell lines used for gene expression analysis were all reported to be mutant for p53 resulting in non-functional protein¹⁴. To verify this, p53 sequencing was performed in MIA PaCa-2, CFPAC-1 and BxPC3 which confirmed the mutational status of these cell lines. Altogether, this data suggests that activation of DNA damage response including the key downstream target *CDKN1A* was p53 independent. This is clinically important as drugs that rely on wild type p53 or stabilise the mutant version of the protein will be ineffective or lead to hyper proliferation and chemoresistance as observed with gemcitabine³³. Recent studies have also revealed a protective role of tumour suppressor p53³⁴ in promoting DNA processivity, enhanced in wild type p53 compared to deficient thymocytes³⁵ providing defence against fork stalling and collapse. This suggests perhaps non-functional p53 is a contributory factor in rendering PDAC cells sensitive to replication stress inducers including TUC-1.

Two emerging homologs of p53, p63 and p73, have been reported as sharing structural and functional similarity¹⁶. These homologs are also less frequently mutated in cancers with important roles in development and differentiation. Of all the structural motifs, the DNA binding domain (DBD) appears to be the most conserved between these isoforms with p73 and p63 sharing 63% and 60% structural similarity in DBD with p53 respectively¹⁶. This enables them to bind p53-responsive elements activating downstream targets leading to cell cycle arrest, cell death or senescence. There are two distinct variants for each isoform; transactivating (TA) and N-terminus truncated (Δ N), both having opposing cellular effect¹⁶. While full length TA isoforms are tumour suppressive, truncated Δ N variants have been shown to promote

tumourgenesis³⁶. TAp73 has been shown to regulate cell cycle progression by activating inhibitors p21 and p57. Additionally, the protein also inhibits proliferative genes such as Cdc25 and Cyclin B family members, preventing entry into mitosis³⁷⁻

40 .

To decipher whether these family members are interacting with p53-responsive elements leading to upregulation of gene targets, expression level of p63 and p73 was evaluated in PDAC cell lines, HCT116^{+/+} and HCT116^{-/-} cells. All samples apart from HCT116^{+/+} that were treated with TUC-1 (10 μ M, 24 hours) had elevated expression levels for p73 but not p63. Therefore, p73 could have a compensatory role in PDAC cell lines with non-functional p53 proteins, providing an alternative route for the activation of DDR, cell cycle arrest and initiation of apoptosis. Previously the inhibitor *CDKN1A* has also been shown to be activated via Sp1 sites in its promoter region⁴¹ in a p53 independent manner. In addition to this, other pathways have also been identified leading to p53 independent activation of GADD45a such as transcription activation by Oct-1 and NF-YA transcription factors⁴². This suggests that transcriptomic changes observed in PDAC cell lines following TUC-1 treatment are p53 independent with other compensatory regulators such as p73 accounting for, if not all, some of the downstream targets.

5.4 Future work

DNA fibre fluorography can be used to investigate time-dependent effect of TUC-1 on replication fork progression to establish minimum time required after treatment to initiate fork stalling. This can be achieved by measuring the total fibre length after each time point or co-administering the drug with the second analogue (IdU). It will also be interesting to determine the time required for replication forks to restart once the drug has been removed.

Though DNA fibre fluorography is a powerful tool providing single molecule resolution, the length of the DNA molecules that can be detected are limited to kilobases. Molecular combing is a technique that improves the alignment of DNA fibres providing uniform assembly on silanised coverslip, the molecules stretched at a constant rate at the liquid-air interface by the retreating meniscus⁴³. This technique has a higher limit of detection up to megabases. Future studies can perhaps focus on detecting fibres using molecular combing to provide a wider screen of origin firing and replication fork progression post TUC-1 treatment.

Additionally, gene expression analysis of the full length transactivating and -terminus truncated p73 and p63 will be useful in identifying the variant that dominates the compensatory response to DNA damage leading to activation of p53 downstream targets. Additionally, TUC-1 cytotoxic activity can be evaluated in PDAC cells pre-treated with p53 activator Nutlin which has been previously shown to alleviate cytotoxic stress induced by gemcitabine⁴². This would support the recent evidence suggesting a protective role of p53 in early tumourigenesis³⁵.

5.5 References

1. L. J. Mah, A. El-Osta and T. C. Karagiannis, *Leukemia*, 2010, **24**, 679-686.
2. G. Figueroa-Gonzalez and C. Perez-Plasencia, *Oncol. Lett.*, 2017, **13**, 3982-3988.
3. B. Ewald, D. Sampath and W. Plunkett, *Mol. Cancer Ther.*, 2007, **6**, 1239-1248.
4. B. Ewald, D. Sampath and W. Plunkett, *Cancer Res.*, 2008, **68**, 7947.
5. W. J. Cannan and D. S. Pederson, *J. Cell. Physiol.*, 2016, **231**, 3-14.
6. J. Nieminuszczy, R. A. Schwab and W. Niedzwiedz, *Methods*, 2016, **108**, 92-98.
7. D. R. Iyer and N. Rhind, *Genes*, 2017, **8**, 74.
8. J. Bartek, C. Lukas and J. Lukas, *Nat. Rev. Mol. Cell Biol.*, 2004, **5**, 792-804.
9. S. U. Rehman, Z. Yaseen, M. A. Husain, T. Sarwar, H. M. Ishqi and M. Tabish, *PLOS ONE*, 2014, **9**, e93913.
10. Z. H. Miao, V. A. Rao, K. Agama, S. Antony, K. W. Kohn and Y. Pommier, *Cancer Res*, 2006, **66**, 6540-6545.
11. Y. Pommier, E. Leo, H. Zhang and C. Marchand, *Chem. Biol.*, 2010, **17**, 421-433.
12. D. Szklarczyk, A. Franceschini, S. Wyder, K. Forslund, D. Heller, J. Huerta-Cepas, M. Simonovic, A. Roth, A. Santos, K. P. Tsafou, M. Kuhn, P. Bork, L. J. Jensen and C. von Mering, *Nucleic Acids Res.*, 2015, **43**, D447-452.
13. P. P. McKenzie, S. M. Guichard, D. S. Middlemas, R. A. Ashmun, M. K. Danks and L. C. Harris, *Clin. Cancer. Res.*, 1999, **5**, 4199-4207.
14. J. G. Tate, S. Bamford, H. C. Jubb, Z. Sondka, D. M. Beare, N. Bindal, H.

- Boutselakis, C. G. Cole, C. Creatore, E. Dawson, P. Fish, B. Harsha, C. Hathaway, S. C. Jupe, C. Y. Kok, K. Noble, L. Ponting, C. C. Ramshaw, C. E. Rye, H. E. Speedy, R. Stefancsik, S. L. Thompson, S. Wang, S. Ward, P. J. Campbell and S. A. Forbes, *Nucleic Acids Res.*, 2019, **47**, D941-D947.
15. S. Mueller, T. Engleitner, R. Maresch, M. Zukowska, S. Lange, T. Kaltenbacher, B. Konukiewitz, R. Ollinger, M. Zwiebel, A. Strong, H. Y. Yen, R. Banerjee, S. Louzada, B. Fu, B. Seidler, J. Gotzfried, K. Schuck, Z. Hassan, A. Arbeiter, N. Schonhuber, S. Klein, C. Veltkamp, M. Friedrich, L. Rad, M. Barenboim, C. Ziegenhain, J. Hess, O. M. Dovey, S. Eser, S. Parekh, F. Constantino-Casas, J. de la Rosa, M. I. Sierra, M. Fraga, J. Mayerle, G. Kloppel, J. Cadinanos, P. Liu, G. Vassiliou, W. Weichert, K. Steiger, W. Enard, R. M. Schmid, F. Yang, K. Unger, G. Schneider, I. Varela, A. Bradley, D. Saur and R. Rad, *Nature*, 2018, **554**, 62-68.
 16. A. Dupré, L. Boyer-Chatenet and J. Gautier, *Nat. Struct. Mol. Biol.*, 2006, **13**, 451-457.
 17. R. Scully and A. Xie, *Mutat. Res.*, 2013, **750**, 5-14.
 18. S. Bekker-Jensen, C. Lukas, R. Kitagawa, F. Melander, M. B. Kastan, J. Bartek and J. Lukas, *J. Cell Biol.*, 2006, **173**, 195-206.
 19. M. Downey and D. Durocher, *Cell Cycle*, 2006, **5**, 1376-1381.
 20. I. M. Ward and J. Chen, *J. Biol. Chem.*, 2001, **276**, 47759-47762.
 21. D. Y. Takeda and A. Dutta, *Oncogene*, 2005, **24**, 2827-2843.
 22. S. A. Sabatinos, *Nature Education*, 2010, **3**, 40.
 23. E. Petermann, M. L. Orta, N. Issaeva, N. Schultz and T. Helleday, *Mol. Cell*, 2010, **37**, 492-502.

24. J. Henry-Mowatt, D. Jackson, J.-Y. Masson, P. A. Johnson, P. M. Clements, F. E. Benson, L. H. Thompson, S. Takeda, S. C. West and K. W. Caldecott, *Mol. Cell*, 2003, **11**, 1109-1117.
25. A. Kurose, T. Tanaka, X. Huang, F. Traganos, W. Dai and Z. Darzynkiewicz, *Cytometry A*, 2006, **69**, 212-221.
26. N. Mailand and J. F. X. Diffley, *Cell*, 2005, **122**, 915-926.
27. L. Zou, D. Liu and S. J. Elledge, *Proc. Natl. Acad. Sci. USA*, 2003, **100**, 13827-13832.
28. Y. Kanoh, K. Tamai and K. Shirahige, *Gene*, 2006, **377**, 88-95.
29. L. Bian, Y. Meng, M. Zhang and D. Li, *Mol. Cancer*, 2019, **18**, 169.
30. E. R. Parrilla-Castellar, S. J. Arlander and L. Karnitz, *DNA Repair (Amst)*, 2004, **3**, 1009-1014.
31. K. P. Bhat and D. Cortez, *Nat. Struct. Mol. Biol.*, 2018, **25**, 446-453.
32. J. P. Morton, P. Timpson, S. A. Karim, R. A. Ridgway, D. Athineos, B. Doyle, N. B. Jamieson, K. A. Oien, A. M. Lowy, V. G. Brunton, M. C. Frame, T. R. Evans and O. J. Sansom, *Proc. Natl. Acad. Sci. USA*, 2010, **107**, 246-251.
33. C. Fiorini, M. Cordani, C. Padroni, G. Blandino, S. Di Agostino and M. Donadelli, *Biochim. Biophys. Acta.*, 2015, **1853**, 89-100.
34. C. Q. X. Yeo, I. Alexander, Z. Lin, S. Lim, O. A. Aning, R. Kumar, K. Sangthongpitag, V. Pendharkar, V. H. B. Ho and C. F. Cheok, *Cell Rep.*, 2016, **15**, 132-146.
35. I. Klusmann, S. Rodewald, L. Müller, M. Friedrich, M. Wienken, Y. Li, R. Schulz-Heddergott and M. Dobbelsstein, *Cell Rep.*, 2016, **17**, 1845-1857.
36. V. Dotsch, F. Bernassola, D. Coutandin, E. Candi and G. Melino, *Cold Spring*

- Harb. Perspect. Biol.*, 2010, **2**, a004887.
37. E. Balint, A. C. Phillips, S. Kozlov, C. L. Stewart and K. H. Vousden, *Proc. Natl. Acad. Sci. USA*, 2002, **99**, 3529-3534.
 38. M. J. Scian, E. H. Carchman, L. Mohanraj, K. E. Stagliano, M. A. Anderson, D. Deb, B. M. Crane, T. Kiyono, B. Windle, S. P. Deb and S. Deb, *Oncogene*, 2008, **27**, 2583-2593.
 39. J. Pflaum, S. Schlosser and M. Muller, *Front. Oncol.*, 2014, **4**, 285.
 40. S. A. Innocente and J. M. Lee, *Biochem. Biophys. Res. Commun.*, 2005, **329**, 713-718.
 41. K. Nakano, T. Mizuno, Y. Sowa, T. Orita, T. Yoshino, Y. Okuyama, T. Fujita, N. Ohtani-Fujita, Y. Matsukawa, T. Tokino, H. Yamagishi, T. Oka, H. Nomura and T. Sakai, *J. Biol. Chem.*, 1997, **272**, 22199-22206.
 42. D. Kranz and M. Dobbelstein, *Cancer Res.*, 2006, **66**, 10274-10280.
 43. H. Labit, A. Goldar, G. Guilbaud, C. Douarche, O. Hyrien and K. Marheineke, *BioTechniques*, 2008, **45**, 649-652, 654, 656-648.

Chapter 6 – The cytotoxicity of TUC-1 is enhanced by Chk kinase inhibition

6.1 Introduction

As demonstrated previously, immunoblot analysis of Chk1 and Chk2 following treatment with TUC-1 (Chapter 5, Section 5.2.3) showed both kinases are activated by phosphorylation by TUC-1, most likely following DNA strand breaks. In this chapter, the effect of AZD7762, a Chk1 and Chk2 inhibitor, on the potency of TUC-1 and the downstream mode of action was investigated.

Checkpoint pathways maintain genome integrity and protect against DNA damage and other abnormalities by preventing cell cycle progression, allowing repair to take place. Chk kinases serve as the main relay proteins activated by ATR and ATM kinases respectively¹. While the ATM-Chk2 axis recognises DSBs, ATR-Chk1 pathway is triggered in response to different stimuli including replication stress, strand breaks, UV radiation and SSBs². Chk kinases play a pivotal role in activating downstream signalling cascade³, leading to repair, transcription, cell cycle arrest, apoptosis². Recent data shows that constitutive activation of Chk1, by disrupting the N- and C-terminus closed conformation, has a profound effect on tumour growth leading to total growth inhibition and cell death⁴. Chk1 is transiently expressed in S and G2 phases⁵ and activity is enhanced upon fork stalling and DNA damage⁵.

Three main S phase processes regulated by Chk1 include late replication initiation, DNA elongation and stabilising stalled forks. One of the main substrates of Chk1 is

the protein phosphatase Cdc25A which catalyses removal of two phosphate groups from CDK2/cycA and CDK2/cycE complexes promoting G1 to S transition.

Phosphorylation of Cdc25A by Chk1, in response to DNA damage, leads to ubiquitination and proteasomal degradation which leads to cell cycle arrest enabling repair^{2, 6, 7}. One of the most significant roles of Chk1 in S phase is the surveillance of replication fork progression as Chk1 inhibition in this phase led to cell death⁸.

Compared to Chk1, Chk2 is stably expressed throughout the cell cycle, present in its inactive form and activated by DNA damage⁵. It is most active in G1 and G2/M phases inducing cell cycle arrest by activating downstream targets such as p53, Rb and Cdc25. Chk2 is involved in replication fork surveillance and intra-S checkpoint response⁹ facilitating DNA damage repair by homologous recombination by phosphorylating BRCA1 and BRCA2¹⁰ and participates in base excision repair by activating FoxM1 transcription factor¹¹.

Their key role in mediating DNA repair makes Chk kinases therapeutic targets to potentiate the effect of DNA damaging agents. As cancer cells rely on ATR-Chk1 and ATM-Chk2 to repair DNA lesions and support survival. Previously, Chk1 inhibitors such as UCN-01, XL844 and SB-218078 were shown to bind the ATP-binding pocket within the kinase domain¹² impairing its ability to phosphorylate downstream substrates leading to cell death. However, despite their benefits, only a select few Chk1 inhibitors enter clinical trials for example LY2603618¹³, AZD7762¹⁴ and MK-8776¹⁵. Some inhibitors like UCN-01 did not complete clinical trials as it was found to interact with plasma α -1 glycoprotein and interacted with other cellular components,

e.g. PDGF and CDK2 rendering it toxic to healthy cells^{16, 17}. Chk2 selective inhibitors, like NSC109555, have also proven to be efficacious entering clinical trials having demonstrated preclinical efficacy in PDAC cells in combination with gemcitabine^{18, 19}. The Chk1 and Chk2 dual inhibitor AZD7762 has been reported to potentiate the activity of established chemotherapeutics including paclitaxel, cisplatin, and gemcitabine. It has been shown to significantly improve the efficacy of cisplatin against osteosarcoma, breast, ovarian, head and neck cancers²⁰.

AZD7762 is an ATP-competitive inhibitor of Chk1 and Chk2, reversibly binding to the ATP binding site preventing phosphorylation of substrates such as Cdc25.

Scintillation studies reveal the inhibitor to be selective for Chk kinases over other kinases by 100-fold²¹. It has been shown to abrogate S and G2/M checkpoint responses activated by gemcitabine and topotecan²¹. Recently, combination treatment with AZD7762 and carboplatin revealed enhanced efficacy against triple negative breast cancer cells triggering mitotic catastrophe²². This provides an alternative approach to sensitize cancer cells to platinum therapies, commonly subject to resistance. The synergistic behaviour of AZD7762 with gemcitabine and irinotecan, drugs possessing unique MoA, could mean that it might also synergise with other DNA targeting agents like TUC-1 that also activate Chk kinases.

This hypothesis is supported by data showing enhanced potency of gemcitabine when combined with AZD7762, attributed to the crucial role of Chk1 in replication fork stabilisation, targeted by gemcitabine²¹ and TUC-1 as demonstrated previously (Chapter 5, Section 5.2.2). It was previously hypothesised that tumours can be

selectively sensitised to DNA damaging agents like TUC-1 by inhibiting checkpoint response²³⁻²⁵. As p53 is frequently mutated in cancers, including PDAC, this subset of tumours is defective for the p53-dependent G1 response thus rely on the intra-S and G2/M checkpoints activated by Chk1²³⁻²⁵. Therefore, Chk kinase inhibitor combined with DNA targeting agents can improve the selectivity index by preferentially targeting p53-mutant cancer cells over healthy cells with functional alternative p53-dependent repair pathways.

Considering the benefits and success of these combination studies, it was investigated if TUC-1 synergises with Chk1 and Chk2 inhibitor AZD7762, achieving cytotoxicity at lower concentrations when combined with the inhibitor. Various cellular outcomes that were previously established for TUC-1 monotherapy including cell cycle analysis, replication fork dynamics, DNA damage and transcriptomic changes are evaluated in this work following combination treatment.

Drugs that act via target interaction, for example receptor or enzyme inhibition, display reversible activity as they eventually disengage with their target²⁶. Previous SAR studies indicated a similar target interaction for TUC-1 (Chapter 4) with the central metal, hydroxyalkyl linker length, stereo- and regioisomerism identified as important structural features²⁷⁻²⁹. In this work, reversible action of TUC-1 as a single agent and in combination with AZD7762 is probed by allowing 24-hour cellular recovery before analysis of various cellular processes listed above.

6.2 Results

6.2.1 Synergy

The cytotoxicity of Chk1 and Chk2 inhibitor AZD7762 was evaluated in MIA PaCa-2 cells and to identify a non-cytotoxic concentration for TUC-1 combination studies. As shown in Figure 6.1, AZD7762 was cytotoxic to MIA PaCa-2 cells with an IC_{50} value of 91.8 ± 20.2 nM. Based on these data, non-cytotoxic concentrations up to 50 nM of AZD7762 were selected for combination studies with TUC-1.

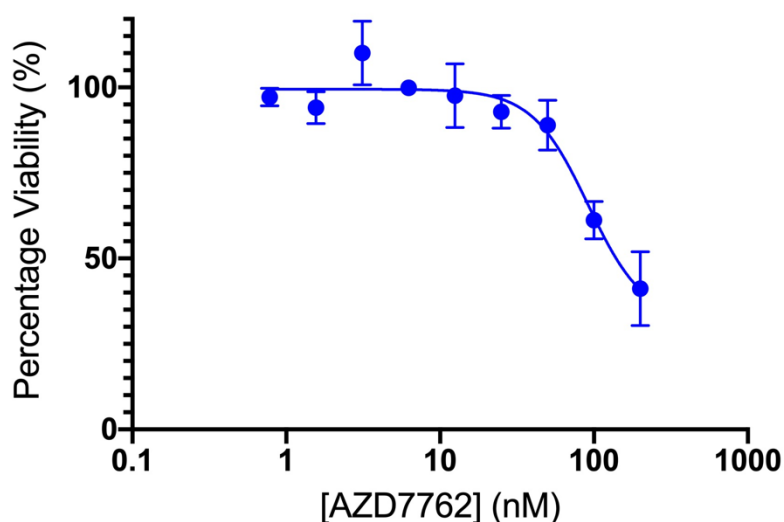


Figure 6.1. Concentration response curve for AZD7762 in MIA PaCa-2 cells as assessed by the MTT assay following a 72-hour treatment. The results represent the mean from three independent biological repeats (mean \pm SD, $n = 3$). IC_{50} value calculated from non-linear regression (Variable slope – four parameters)

Next, it was investigated if AZD7762 could potentiate the cytotoxicity of TUC-1. MIA PaCa-2 cells were treated with increasing concentrations of TUC-1 (0-200 μ M, 72 hours) in combination with constant concentrations of AZD7762 (10, 20, 30, 40 and 50 nM, 72 hours). As shown in Figure 6.2A, addition of AZD7762 has an effect on the activity of TUC-1 evident by the left shift of the IC_{50} curves, as the concentration of AZD7762 increases. The IC_{50} value of TUC-1 decreased when combined with

AZD7762, calculated as 4.1 ± 0.3 , 1.6 ± 0.7 , 1.6 ± 0.1 , 1.2 ± 0.5 , and 0.25 ± 6.8 μM for co-administration with 10, 20, 30, 40 and 50 nM AZD7762 respectively (Figure 6.2A). This is compared to the IC_{50} value of 8.9 ± 2.5 μM obtained for TUC-1 single agent treatment.

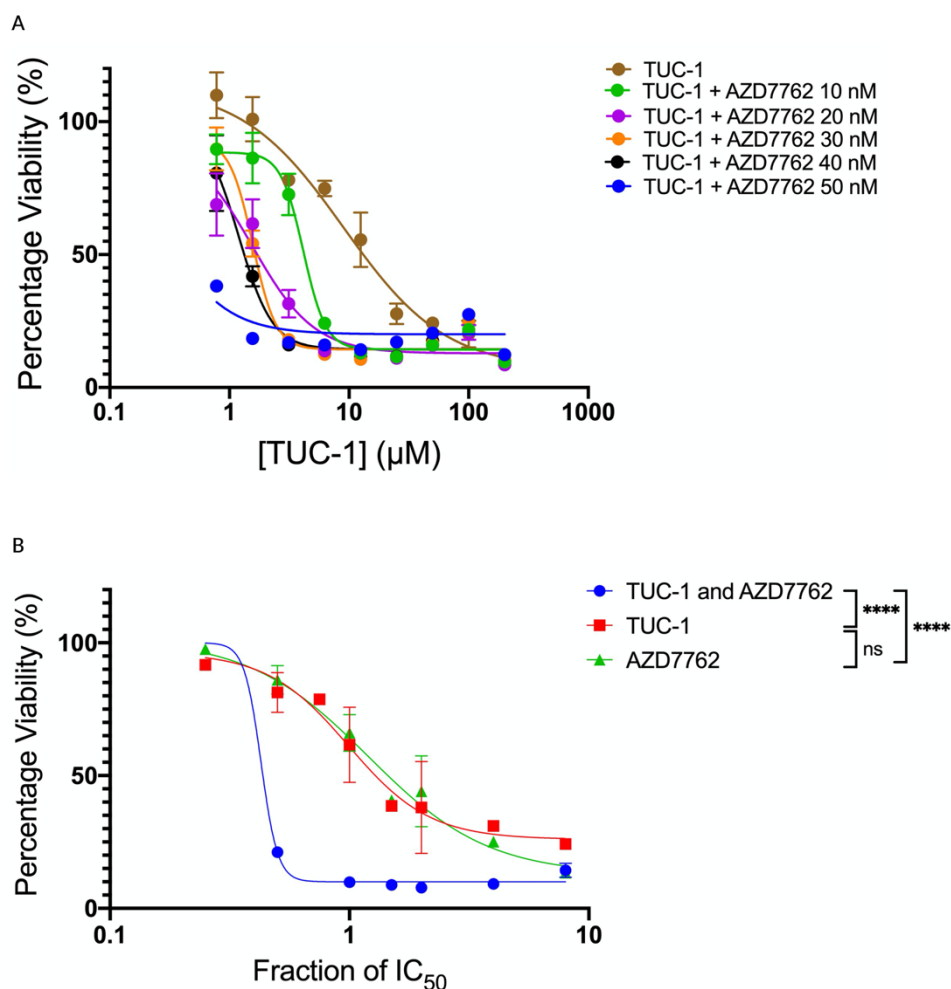


Figure 6.2. AZD7762 potentiates the activity of TUC-1 in MIA PaCa-2 cells. (A) Concentration response curves for TUC-1 combined with 10, 20, 30, 40 and 50 nM AZD7762 evaluated in MIA PaCa-2 cells assessed by the MTT assay following a 72-hour treatment. The results represent mean of one biological repeat and three technical repeats ($\pm\text{SD}$, $n=1$). IC_{50} values calculated from non-linear regression (Variable slope – four parameters). (B) Concentration response curves for single agents TUC-1, AZD7762 and fixed potency combination of the drugs in MIA PaCa-2 cells treated with different fractions of IC_{50} concentration of TUC-1 and AZD7762 for 72 hours. The results represent the mean from three independent biological repeats ($\pm\text{SD}$, $n = 3$). **** statistically significantly different ($P<0.0001$) as assessed by 2-way ANOVA followed by Tukey's multiple comparison test.

Next, the type of interaction between TUC-1 and AZD7762 was investigated to establish if the effect on cell viability was additive or synergistic. TUC-1 and AZD7762 were administered at fixed equipotent concentrations in MIA PaCa-2 cells as different fractions of individual IC₅₀ values. A more detailed outline of the experimental plan can be found in Methods and Materials (Chapter 2, Section 2.3.2.4). As shown in Figure 6.2B, the combination treatment was more cytotoxic compared to single agents as evident by the deviation of the combination treatment curve. This deviation was statistically significant (P<0.0001, 2way ANOVA followed by Tukey's post hoc test) compared to TUC-1 and AZD7762 single treatment. Whereas the single treatment curves were not statistically significant (P=0.9986).

Following this, combination indexes (CI) were calculated for each dose combination. As shown in Table 6.1, the CI values calculated were 0.26, 0.16, 0.23, 0.21, 0.3 and 0.6 for dose combinations 0.5, 1, 1.5, 2, 4 and 8. All values were below 1 confirming a synergistic relationship between TUC-1 and AZD7762 induced cytotoxicity in MIA PaCa-2 cells.

Table 6.1. Combinatory index calculated for different IC₅₀ combinations of TUC-1 and AZD7762 (Synergy: CI <1)

Dose combination (Fraction of IC₅₀)	Combination Index (CI) (compared to TUC-1)
0	1
0.5	0.3
1	0.2
1.5	0.2
2	0.2
4	0.3
8	0.6

6.2.2 Cell cycle arrest

The effect of TUC-1 combined with AZD7762 on the cell cycle was investigated to monitor checkpoint activation and subsequent cell cycle arrest in the presence of the inhibitor. Cell cycle analysis was performed following treatment with the agents and staining with propidium iodide, as detailed in Materials and Methods (Chapter 2 Section 2.4). MIA PaCa-2 cells were treated with single agents TUC-1 (1, 5 μ M) and AZD7762 (10, 20 and 30 nM) for 24 hours. The combination treatment included TUC-1 (1 and 5 μ M) combined with non-cytotoxic concentrations of AZD7762 (10, 20 and 30 nM), MIA PaCa-2 cells exposed for 24 hours before detection by flow cytometry.

As demonstrated previously (Chapter 4, Section 4.2.3) and shown in Figure 6.3A, TUC-1 single agent treatment induces S phase arrest in a concentration-dependent manner compared to untreated control. The percentage of cells in S phase was 26.5 and 38.6% following treatment with 1 and 5 μ M TUC-1 respectively, compared to 20% in untreated control. Treatment with single agent AZD7762 did not induce S phase arrest as the cell cycle distribution was not statistically significantly different to the untreated control. The percentage population in S phase was determined to be 19.3, 24.1 and 20% following treatment with 10, 20 and 30 nM AZD7762 respectively (Figure 6.3A).

AZD7762 enhanced the effect of TUC-1 on the cell cycle as the percentage population in S phase was higher compared to TUC-1 single agent treatment. The percentage population in S phase following treatment with TUC-1 1 μ M combined with AZD7762 10, 20 and 30 nM was 26.3, 25.7 and 28.4% respectively (Figure

6.3A). A concentration dependent effect was also established as a higher concentration of TUC-1 (5 μ M) combined with increasing concentrations of AZD7762 led to a statistically significantly ($P<0.01$) higher proportion of cells arrested in the S phase. This was calculated to be 42.3, 52.7 and 56.4 following treatment with TUC-1 5 μ M combined with AZD7762 10, 20 and 30 nM respectively (Figure 6.3A).

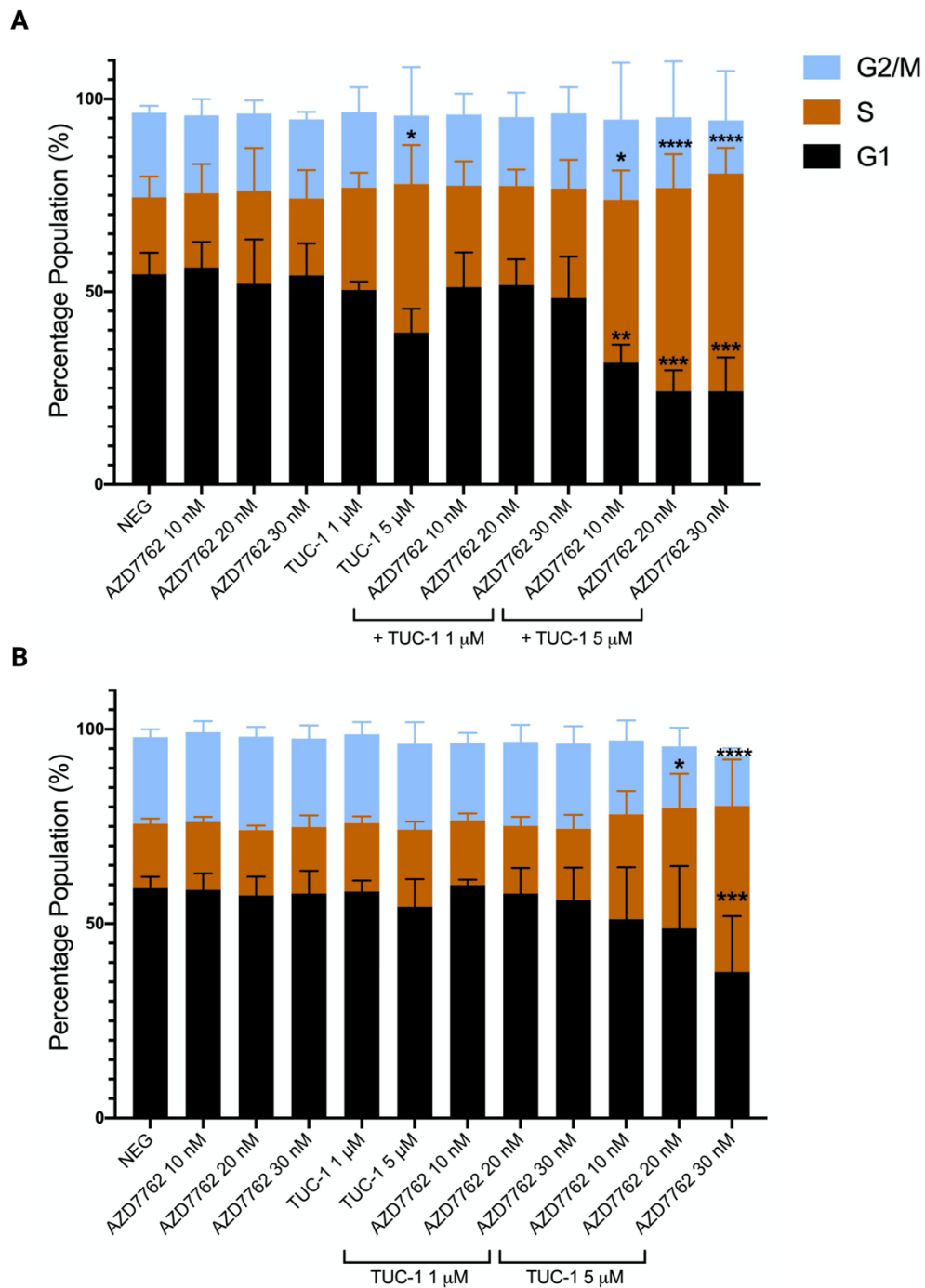


Figure 6.3. TUC-1 combined with AZD7762 has a greater effect on the cell cycle than single treatment. Cell cycle distribution of MIA PaCa-2 cells after treatment with single agents TUC-1 (1, 5 μ M), AZD7762 (10, 20, 30 nM) and TUC-1 (1, 5 μ M) combined with AZD7762 (10, 20 and 30 nM). Reversibility of TUC-1 and combination treatment is probed by performing flow cytometric analysis (A) without and (B) with 24-hour recovery. The results represent the mean of three independent biological repeats (\pm SD, n=3). *, **, *** and **** statistically significantly different ($P < 0.05$, $P < 0.01$, $P < 0.001$ and $P < 0.0001$ respectively) as assessed by 2-way ANOVA followed by Tukey's multiple comparison t-test.

To investigate if the effect of TUC-1 single agent and combination treatment on the cell cycle is reversible, MIA PaCa-2 cells were washed following 24-hour exposure and incubated in fresh media for 24 hours to allow recovery. As shown in Figure 6.3B, S phase arrest induced by TUC-1 single agent treatment (1, 5 μ M) was reversible as the cell cycle distribution post recovery was not statistically significantly different to the untreated control. The S phase population was 17.6 and 19.9% when recovery was allowed following treatment with 1 and 5 μ M TUC-1 respectively. Combination treatment with 1 μ M TUC-1 also displayed a reversible effect with 16.6, 17.4 and 18.3% percentage population in S phase following treatment with TUC-1 1 μ M combined with AZD7762 10, 20 and 30 nM (Figure 6.3B). However, combination treatment with 5 μ M TUC-1 led to a concentration-dependent increase in the number of cells irreversibly arrested in S phase as evident by a statistically significantly ($P < 0.01$) higher percentage of cells in S phase compared to untreated control. The percentage population in S phase following treatment with TUC-1 5 μ M combined with AZD7762 10, 20 and 30 nM was 27, 31 and 42.7% respectively compared to 16.6% for untreated control (Figure 6.3B).

6.2.3 Replication fork dynamics

To study the effect of TUC-1 and AZD7762 synergy on replication fork dynamics, DNA fibre fluorography was performed in MIA PaCa-2 cells following treatment with TUC-1 (5 μ M) combined with AZD7762 (10, 20 and 30 nM) for 24 hours. The experimental design was the same as described previously (Chapter 5, Section 5.2.2), with DNA fibre length and speed of replication calculated as outlined in literature³⁰.

As demonstrated previously (Chapter 5, Section 5.2.2) and shown in Figure 6.4, TUC-1 single agent treatment (5 μ M, 24 hours) induces replication fork stalling as evident by the mean fibre length of 0.31 ± 0.2 kB compared to 1.5 ± 0.7 kB for untreated control. AZD7762 single agent treatment (30 nM, 24 hours) did not have an effect on replication fork progression with mean fibre length calculated to be 1.4 ± 0.6 kB (Figure 6.4A). All combination treatments enhanced TUC-1 induced replication fork stalling as evident by the statistically significantly smaller mean fibre lengths, decreasing in a concentration dependent manner as the concentration of AZD7762 increases. This can be seen in the representative images in Figure 6.5A-F, as DNA fibres after combination treatment were shorter than TUC-1 alone. The mean fibre lengths were 0.31 ± 0.2 , 0.24 ± 0.2 and 0.17 ± 0.1 kB following treatment with TUC-1 5 μ M combined with AZD7762 10, 20 and 30 nM respectively (Figure 6.4A). This effect is also mirrored in the speed of replication, calculated to be 0.08 ± 0.03 , 0.07 ± 0.03 , 0.02 ± 0.008 , 0.02 ± 0.01 , 0.01 ± 0.01 and 0.009 ± 0.004 kB/min for untreated control, AZD7762 30 nM, TUC-1 5 μ M, TUC-1 5 μ M combined with AZD7762 10, 20 and 30 nM respectively (Figure 6.4B).

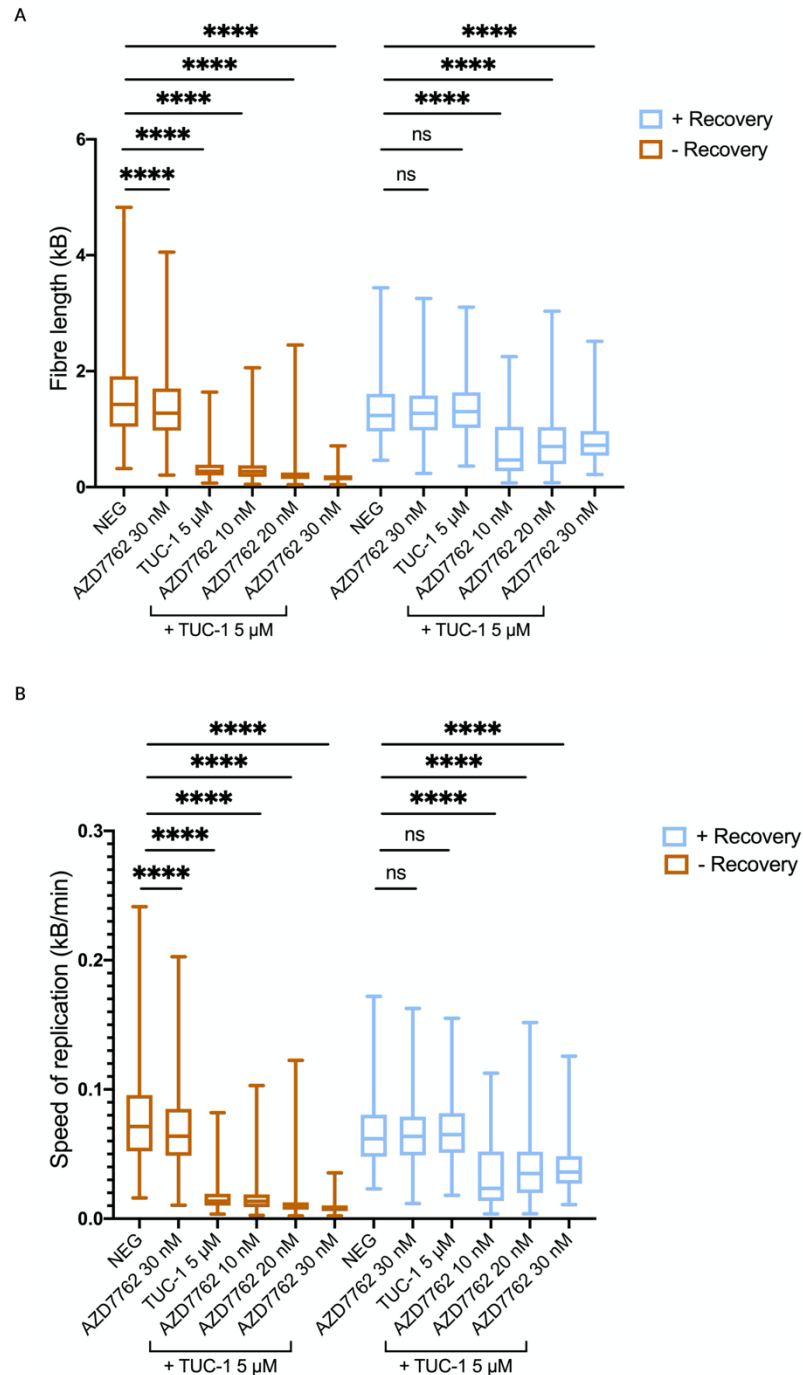


Figure 6.4. TUC-1-induced replication fork inhibition is enhanced by AZD7762. Box and whisker plot of (A) total DNA fibre length (kB) and (B) Speed of replication (kB/min) after treating MIA PaCa-2 cells with single agents TUC-1 (5 µM), AZD7762 (10, 20, 30 nM) and TUC-1 (5 µM) combined with AZD7762 (10, 20, 30 nM). Reversibility of TUC-1 and combination treatment is probed by performing DNA fibre analysis without (brown) and with 24-hour recovery (blue). Box and whisker plots show the mean (line splitting the box), interquartile range (box), 5 and 95 percentile range (whiskers) with values falling outside this range plotted as individual points. The results represent the mean of three independent biological experiments (n=3) with 692, 1143, 844, 1257, 684 and 570 DNA fibres analysed for TUC-1 (5 µM), AZD7762 (10, 20, 30 nM) and TUC-1 (5 µM) combined with AZD7762 (10, 20, 30 nM) without recovery, 622, 1046, 949, 784, 826 and 766 DNA fibres analysed for TUC-1 (5 µM), AZD7762 (10, 20, 30 nM) and TUC-1 (5 µM) combined with AZD7762 (10, 20, 30 nM) with 24-hour recovery. **** Statistically significant ($P < 0.0001$) as assessed by a two-tailed t-test.

Next, the reversibility of replication fork stalling under different experimental conditions was investigated by allowing 24-hour recovery period following treatment of MIA PaCa-2 cells with either single agents or combination treatments. Replication fork stalling with TUC-1 alone (5 μ M, 24 hours) was reversible. The mean fibre length after recovery was 1.34 ± 0.4 kB and was not statistically different to AZD7762 alone (30 nM, 24 hours) or control values of 1.3 ± 0.5 and 1.34 ± 0.5 kB respectively (Figure 6.4A).

In contrast, the combination treatment had an irreversible effect on the replication fork dynamics as forks remained stalled after the recovery period albeit to a lesser extent than pre-recovery suggesting at least some forks were able to restart and a partial recovery. This is evident by smaller mean fibre lengths of 0.7 ± 0.5 , 0.8 ± 0.5 and 0.8 ± 0.3 kB following treatment with TUC-1 5 μ M combined with AZD7762 10, 20 and 30 nM respectively (Figure 6.4A). This can be seen in the representative images in Figure 6.5G-L, DNA fibres following combination treatment appear shorter than TUC-1, AZD7762 and untreated control. This is also reflected in the speed of replication, calculated to be 0.07 kB/min for TUC-1 (5 μ M), AZD7762 (30 nM) and untreated control (Figure 6.4B). Following the reduction in fibre length, the speed of replication was also lower for combination treatments. This was calculated to be 0.03 ± 0.02 , 0.04 ± 0.02 and 0.04 ± 0.2 kB/min following treatment with TUC-1 5 μ M combined with AZD7762 10, 20 and 30 nM respectively (Figure 6.4B).

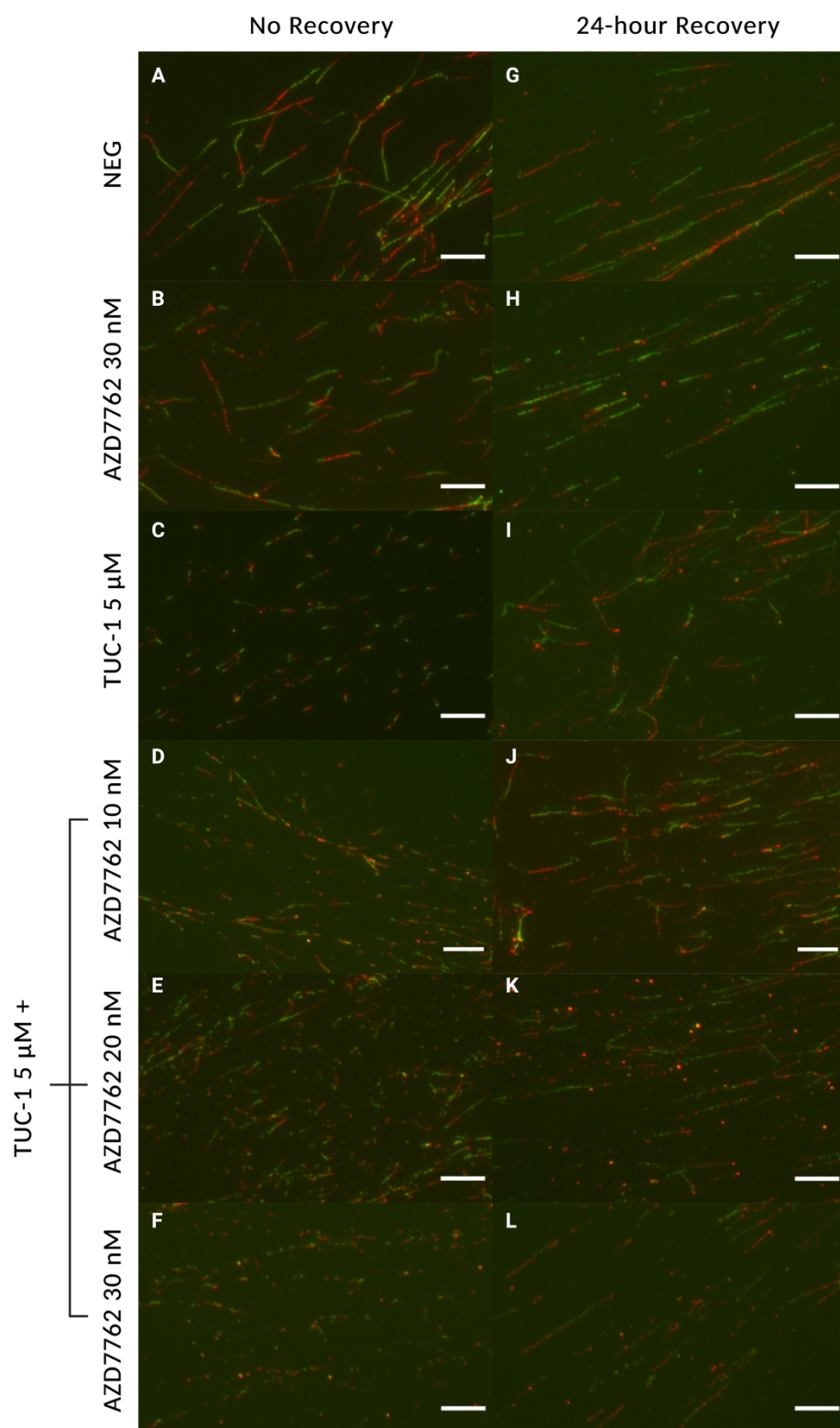


Figure 6.5. Representative images of DNA fibres from MIA PaCa-2 cells are presented following treatment with AZD7762 30 nM, TUC-1 5 µM, TUC-1 5 µM combined with AZD7762 10, 20 and 30 nM. Single agent and combination treatment reversibility is investigated by allowing 24-hour recovery. Red: CldU, Green: IdU (Scale bar = 10 µm, Magnification 40X).

6.2.4 DNA double strand breaks

It was previously established TUC-1 induces DNA strand breaks in a concentration dependent manner (Chapter 5, Section 5.2.1). As Chk1 mediated repair is inhibited by AZD7762, it was investigated if the inhibitor enhances TUC-1 induced DNA double strand breaks (DSBs). The formation of γ H2AX foci was used as a biomarker for DSBs as discussed earlier (Chapter 5). Immunofluorescence detection of the histone variant by flow cytometry and confocal microscopy was performed following single agent and combination treatment.

MIA PaCa-2 cells were exposed to TUC-1 5 μ M, AZD7762 30 nM, TUC-1 5 μ M combined with AZD7762 10, 20 and 30 nM for 24 hours followed by γ H2AX immunolabelling and detection. As determined previously and shown in Figure 6.6, TUC-1 induces DNA DSBs evident by the 1.4-fold increase in median fluorescence intensity (MFI) compared to untreated control. Whereas MFI for AZD7762 single agent treatment was lower than the untreated control with a fold change of 0.78 suggesting the inhibitor alone does not induce DSBs. However, the inhibitor combined with TUC-1 enhances γ H2AX foci formation indicative of higher levels of DSB compared to TUC-1 alone (Figure 6.6A). TUC-1 5 μ M combined with AZD7762 10, 20 and 30 nM led to 1.3, 1.6 and 2.2-fold higher MFI respectively, compared to untreated control. This effect can also be seen in the representative images (Figure 6.7A, D, G, J, M, P) as the foci formation becomes more apparent with TUC-1 and combination treatment.

Next, it was investigated if combination treatment leads to prolonged DNA strand break formation as suggested by the irreversibility seen earlier with cell cycle analysis and replication fork dynamics. The treatment was washed out and MIA PaCa-2 cells allowed to recover for 24 hours prior to detection. As shown in Figure 6.6B, the γ H2AX foci formation reaches basal level after recovery for TUC-1 single agent treatment. The fold change in MFI was 0.93 and 0.89 for TUC-1 5 μ M and AZD7762 30 nM single agents compared to untreated control (Figure 6.6B). However, γ H2AX level remains elevated in cells treated with TUC-1 in combination with AZD7762 albeit to a lesser extent compared to combination treated cells without recovery (Figure 6.8A, D, G, J, M, P). The MFI fold changes observed were 1.1, 1.3 and 1.8 following treatment with TUC-1 5 μ M combined with AZD7762 10, 20 and 30 nM respectively (Figure 6.6B).

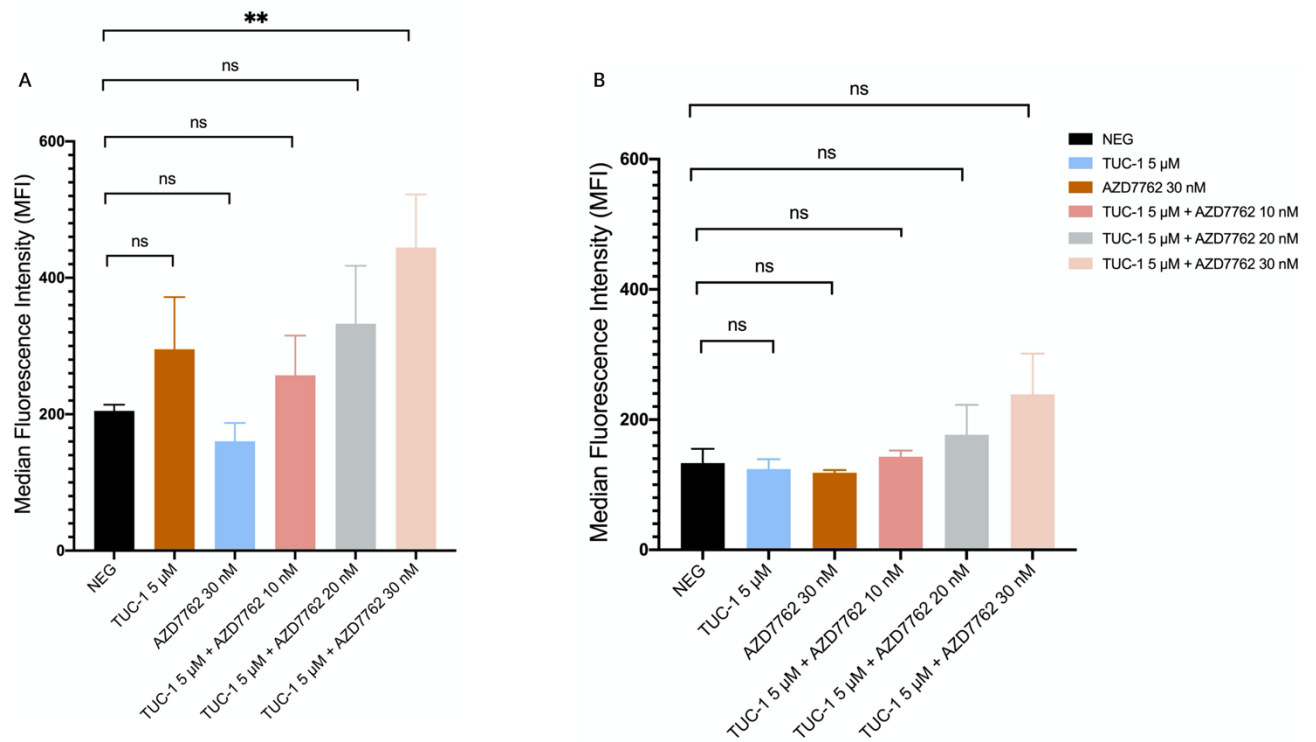


Figure 6.6. AZD7762 enhances the effect of TUC-1 on DNA double strand breaks. Induction of DSBs was detected in MIA PaCa-2 cells with (A) no recovery and (B) 24-hour recovery as detected by γ H2AX phosphorylation, a biomarker for DNA double strand breaks, immunolabelled and detected by flow cytometry. The median fluorescent intensity (MFI) increased following all combination treatments compared to untreated control, indicative of elevated levels of γ H2AX. The results represent mean of three independent biological repeats (\pm SD, $n=3$). ** Statistically significant difference ($P < 0.01$) (Unpaired t-test).

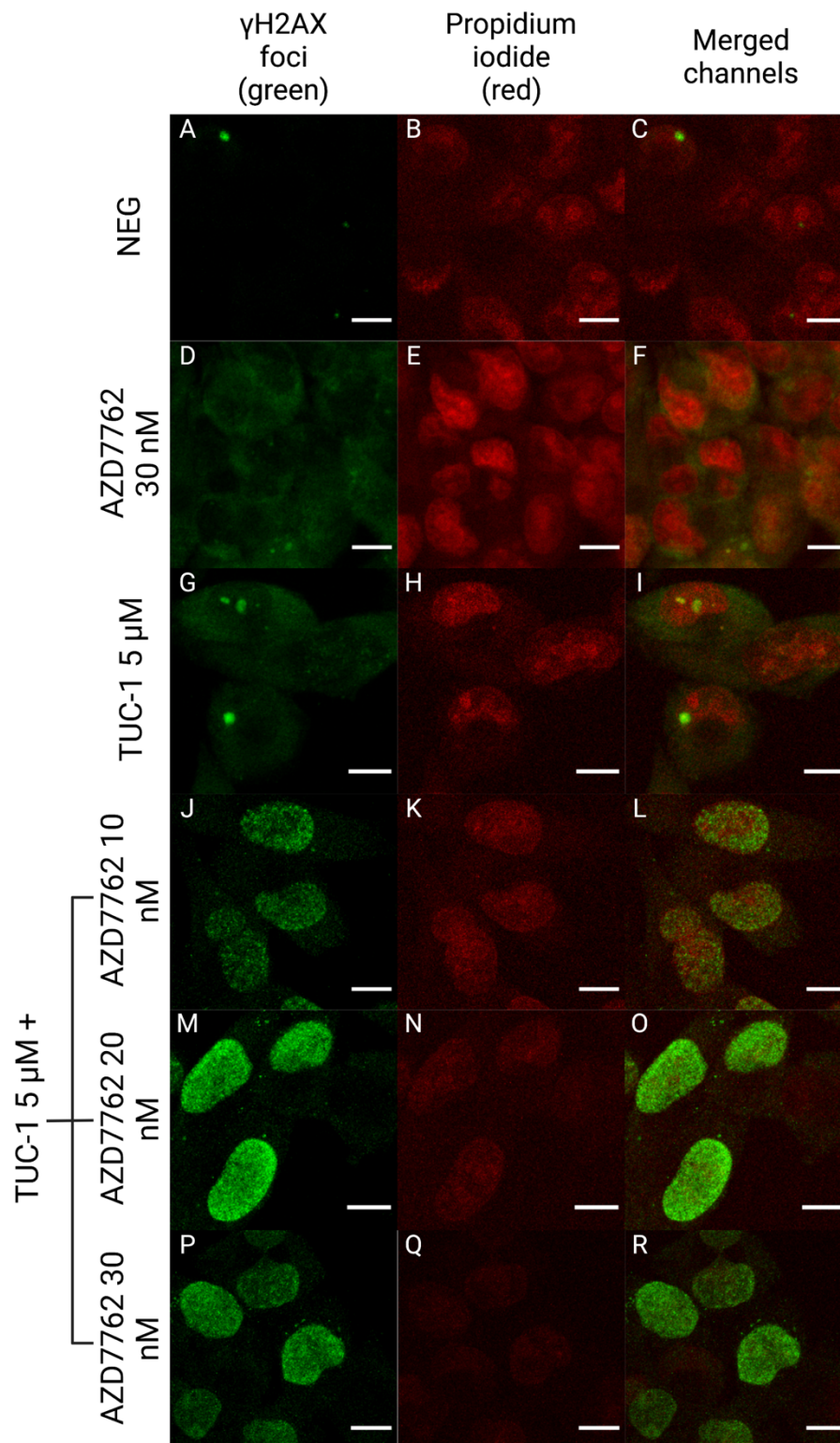


Figure 6.7. Representative images of MIA PaCa-2 cells exposed to (E-G) AZD7762 (30 nM, 24 hour), (H-J) TUC-1 (5 μ M, 24 hour) and (K-S) TUC-1 (5 μ M) combined with AZD7762 (10, 20, 30 nM, 24 hour) followed by staining for γ H2AX with antibodies (green fluorescence) and counterstained with propidium iodide (red fluorescence).

Cells treated with combination treatment have higher γ H2AX foci formation compared to untreated control and single agent treatment indicative of elevated DNA double strand breaks. (Scale bar = 10 μ m, Magnification 100X).

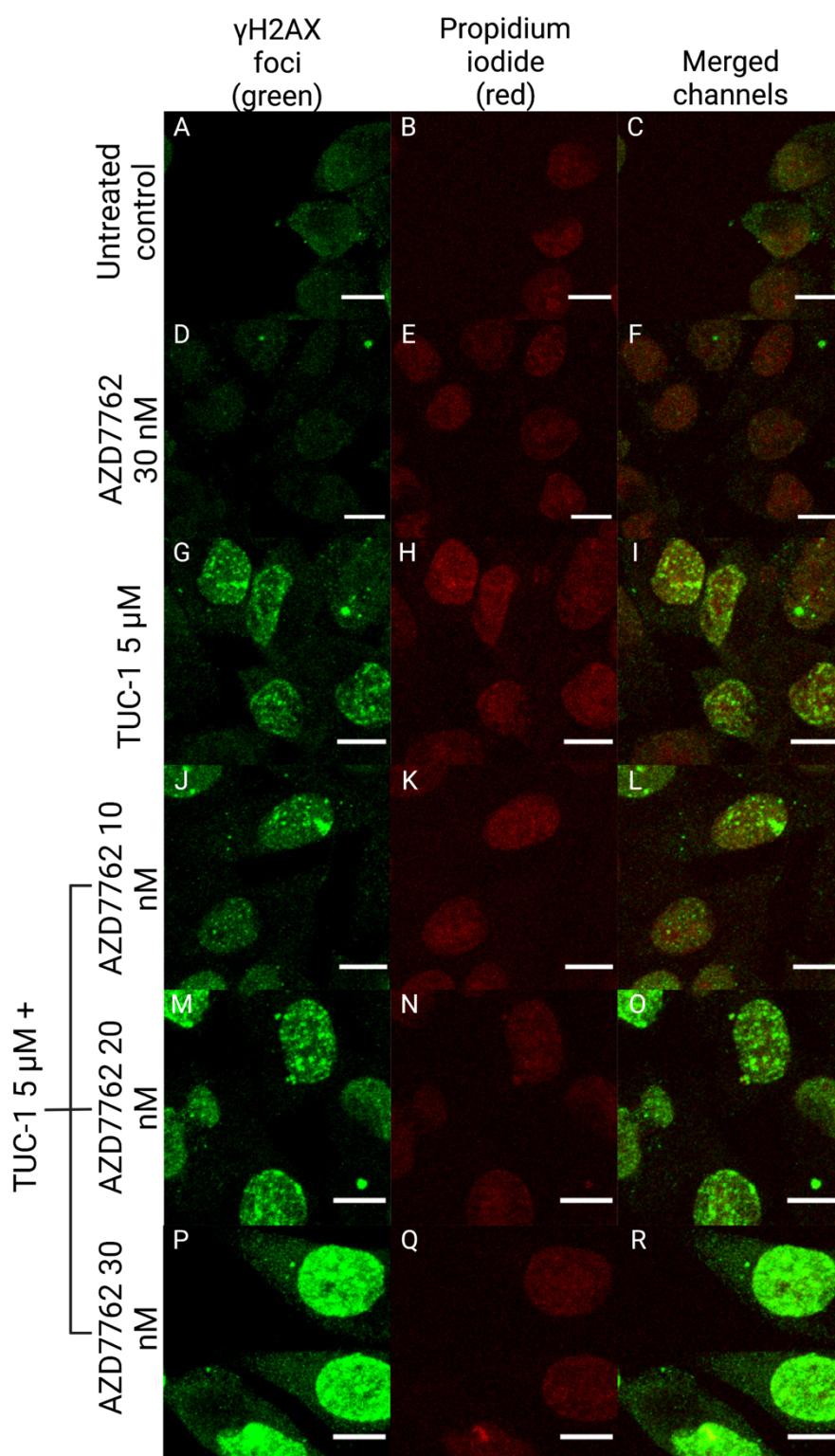


Figure 6.8. Representative images of MIA PaCa-2 cells exposed to (E-G) AZD7762 (30 nM, 24 hour), (H-J) TUC-1 (5 μM, 24 hour) and (K-S) TUC-1 (5 μM) combined with AZD7762 (10, 20, 30 nM, 24 hour). Cells were washed and allowed to recover for 24 hours before staining for γH2AX with antibodies (green fluorescence) and counterstained with propidium iodide (red fluorescence). Cells treated with combination treatment have higher γH2AX foci formation compared to untreated control and single agent treatment indicative of elevated DNA double strand breaks. (Scale bar = 10 μm, Magnification 40X).

6.2.5 Transcriptomic profile

The STRING network conserved in all three PDAC cell lines, as discussed previously (Chapter 5, Section 5.2.4), was evaluated in MIA PaCa-2 cells with the inclusion of *CHEK1* and *CHEK2* following single agent (TUC-1 5 μ M, AZD7762 30 nM) and combination (TUC-1 5 μ M and AZD7762 30 nM) treatment for 24 hours.

Gene expression changes in the network were also investigated under recovery conditions.

As shown in Figure 6.9, the number of genes upregulated after 24-hour recovery was higher compared to no recovery for all treatment conditions. For TUC-1 single treatment, 2 out of the 15 genes (*CDKN1A* and *CCNG2*) were upregulated (fold change > 1.5) prior to recovery. The transcriptomic response is more prominent after recovery as 9 out of the 15 genes (*CDKN1A*, *CDK2*, *Casp3*, *SERTAD1*, *HUS1*, *CCNE1*, *GADD45A*, *CHEK2*, *RBBP8*, *BRCA2*) were upregulated (fold change > 1.5) post recovery (Figure 6.9B) suggesting a delay in the activation of DDR and repair. Out of all the genes in the network, tumour suppressor *BRCA2* had the highest fold change of 12.9 after recovery.

Compared to TUC-1, AZD7762 single treatment led to fewer gene upregulation with only 3 (*Casp3*, *SERTAD1*, *HUS1*) and 1 (*CCNG2*) genes upregulated (fold change > 1.5) in the network with and without recovery respectively (Figure 6.9). Similarly, fewer genes were upregulated (fold change > 1.5) following combination treatment with TUC-1 (5 μ M) and AZD7762 (30 nM) compared to TUC-1 single treatment. Only 3 (*CDKN1A*, *SERTAD1*, *GADD45A*) and 2 (*CDKN1A*, *SERTAD1*) genes in the

network had elevated expression with and without recovery respectively (Figure 6.9). Cell cycle inhibitors *CDKN1A* and *GADD45A* were highly expressed in the network after recovery when treated with TUC-1 alone, as observed previously (Chapter 5, Section 5.2.4), and in combination with AZD7762. Additionally, *SERTAD1* was also consistently upregulated for all three treatment conditions after recovery.

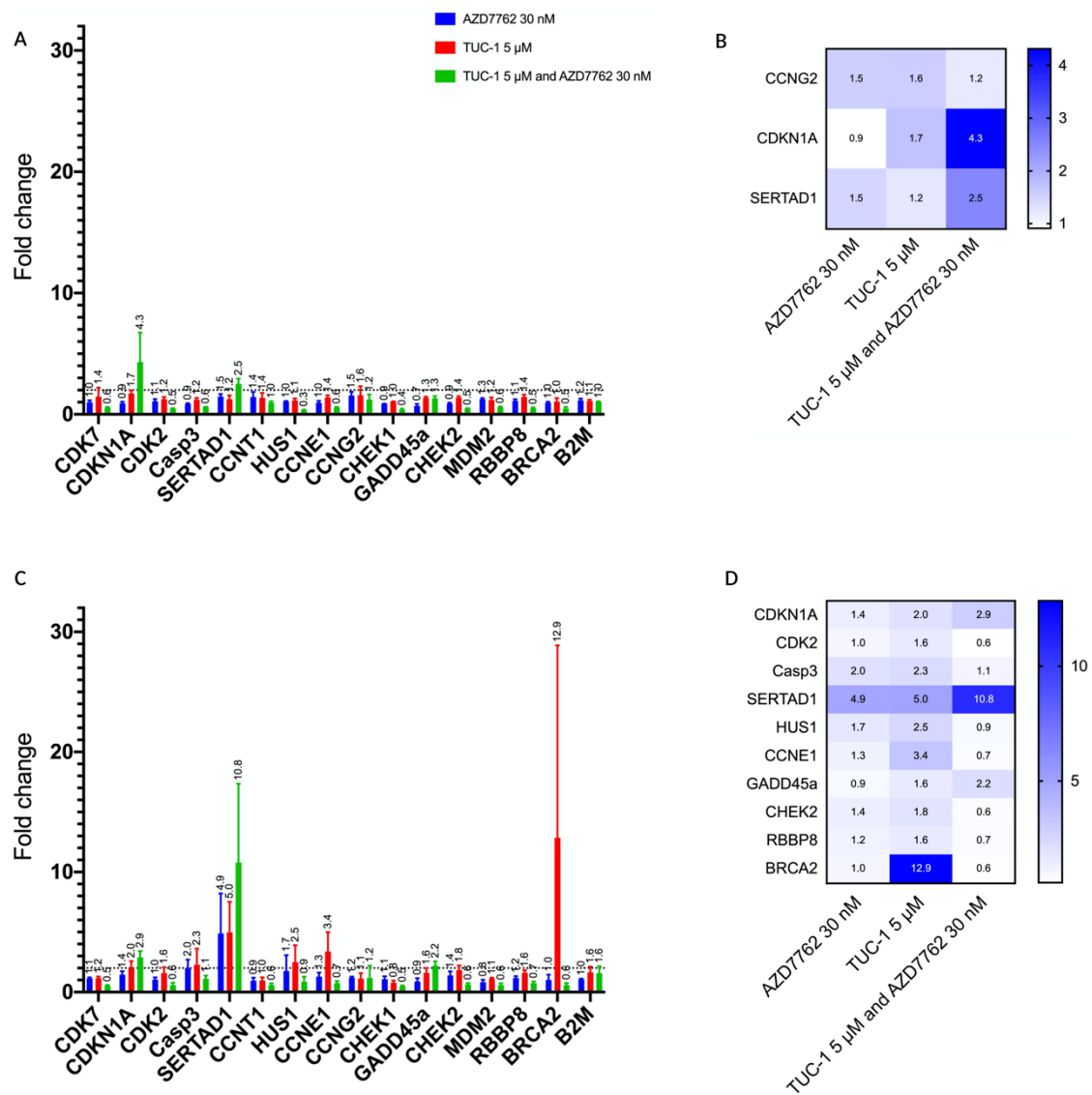


Figure 6.9. AZD7762 suppresses the DDR transcriptional response induced by TUC-1. Relative gene expression analysis of the 13 gene STRING network, in addition to *CHEK1* and *CHEK2* in MIA PaCa-2 cells assessed by qPCR. Bar graphs showing gene expression changes with (A) no recovery and after (C) 24-hour recovery. Heatmaps showing genes upregulated following either single agent or combination treatment with (B) no recovery and after (D) 24-hour recovery. The results represent the mean of three independent biological repeats ($n=3$, \pm SD).

6.3 Discussion

TUC-1 targets DNA as part of its MoA and activates the intra-S checkpoint response following replication fork stalling and DNA strand breaks. The intra-S checkpoint, activated by TUC-1, relies on the ATR-Chk1 axis to inhibit replication origin firing and stabilise stalled replication forks that, upon collapse, are converted to DNA DSBs. Chk1 also initiates DNA damage repair which enables cancer cells to survive and develop resistance to DNA damaging agents such as cisplatin. Inhibition of this pathway has been shown to promote early entry into mitosis and DNA fragmentation leading to cell death.

Inhibitors of ATR and Chk1 have been shown to synergise with anticancer agents such as platinum-based drugs and nucleoside analogues potentiating their activity in different cancers including pancreatic, lung and ovarian³¹⁻³³. Chk inhibition also provides a potential route to overcome chemo-resistance by sensitising cancer cells to genotoxic agents³⁴. In addition to overcoming resistance, this strategy also allows for these drugs to be delivered at a lower dose thereby reducing off-target interactions and toxicities commonly associated with platinum-based drugs²¹.

Cancer cells commonly possess p53 mutations and are therefore deficient in G1 checkpoint response. This is supported by evidence that shows elevated Chk1 expression in cancer cells³⁵. Inhibition of Chk1 provides another avenue to target cancer cells selectively in a manner similar to synthetic lethality, using PARP inhibitors which has been successful in *BRCA1/2* deficient tumours³⁶. Based on the success of Chk inhibitors combined with anticancer agents particularly in p53

deficient cells, it was investigated if inhibiting this response may sensitise PDAC cells, also mutant for p53³⁷, to TUC-1 enhancing its potency. AZD7762, an ATP competitive inhibitor of Chk1 and Chk2, has been shown to synergise with clinical drugs gemcitabine²¹ and cisplatin²⁰ enhancing their activity by inhibiting DNA damage repair. Combination treatment has been successful in p53 mutant cancers including head and neck cancers²⁰.

This chapter has explored the synergistic relationship between Chk1/2 kinase inhibitor AZD7762 and TUC-1. It was found that AZD7762 was cytotoxic to MIA PaCa-2 cells, it had additional effects at non-toxic concentrations. AZD7762 strongly sensitises MIA PaCa-2 cells to TUC-1 cytotoxicity. Combination indexes were below 1 (range 0.6-0.2) supported the existence of a synergistic relationship between the two agents. Interestingly, the CI values obtained with TUC-1 are lower than those previously reported for gemcitabine combined with AZD7762 evaluated in urothelial cancer cell lines³⁸ suggesting a stronger synergistic relationship is established with TUC-1 that may be clinically beneficial.

TUC-1 has been shown to activate Chk1 and Chk2 and induce S phase arrest in PDAC cells. As reported in the literature, activation of Chk kinases leads to the phosphorylation and degradation of their substrate cdc25A consequently increasing CDK2 phosphorylation³⁹. This leads to inactivation of CDK2 complexes with cyclin A and E which results in S phase arrest³⁹. In the current study, treatment with AZD7762 alone did not trigger cell cycle arrest, confirming previous observations²⁰. As DNA damaging agents such as cisplatin trigger G2/M checkpoint response and cell cycle

arrest, abrogation of this arrest was observed when combined with AZD7762, leading to mitotic catastrophe²⁰. Contrary to this, when combined with TUC-1, it did not prevent intra-S checkpoint activation and subsequent S phase arrest. Instead, accumulation in S phase increased following combination treatment in a concentration-dependent manner. Additionally, this response persisted after a 24-hour recovery period whereas cells treated with TUC-1 alone returned to their normal cell cycle distribution. This suggests co-treatment with AZD7762 makes TUC-1 induced G1/S cell cycle arrest irreversible. Furthermore, cell death is increased compared to TUC-1 treatment alone.

It was previously shown that checkpoint activation and S phase arrest induced by TUC-1 is likely caused by stalled replication forks in response to replication stress. Chk1 has been shown to inhibit new origin firing which directs replication factories to stalled forks for stabilisation and completion of replication⁴⁰. This inhibition was shown to be alleviated when Chk1 inhibitor AZD7762 was sequentially added to cultures exposed to with gemcitabine with new origin firing increasing from 3% to 9%⁴¹, leading to an increase in the number of stalled replication forks. As such DNA at stalled replication forks is converted to excessive DNA DSBs, as observed with TUC-1 and AZD7762 combined, which leads to cell death.

Our data shows replication fork stalling is also enhanced by AZD7762 in combination with TUC-1 as evident by smaller fibre lengths and lower speed of replication compared to single agent treatment. The blockade imposed on replication forks by the two agents combined persisted after 24-hour recovery reinforcing irreversibility,

hence the prolonged S phase arrest. Whereas replication forks stalled by TUC-1 alone, with uninhibited Chk1, restarted following with fibre lengths identical to negative control. Although the mean fibre lengths and speeds of replication for the combination treatment were higher after recovery, they were lower than single treatments indicative of a partially irreversible effect on the replication fork machinery when TUC-1 was combined with inhibitor AZD7762.

Fork restart, promoted by the ATR-Chk1 axis, aims to restore genome stability, and more importantly minimise DNA strand break, as observed with a decrease in γ H2AX foci formation with 24-hour recovery following TUC-1 single agent treatment. Inhibition of Chk1-mediated fork stabilisation by AZD7762 combined with TUC-1 led to a marked increase in γ H2AX foci formation compared to TUC-1 alone, an effect which persisted post recovery. This follows the irreversible replication fork stalling and S phase arrest with combination treatment.

Suppression of DDR by AZD7762 when combined with TUC-1 is also evident in the STRING gene expression changes which included *CHEK1* and *CHEK2*. Without recovery, fold changes of ≥ 1.5 signifying upregulation are fewer with combination treatment compared to TUC-1 alone. Expression of *CHEK1* and *CHEK2* decreased by a factor of 2.5 and 2.8 respectively following combination treatment compared to TUC-1 alone. However, it is important to note the major regulation of Chk kinases by post-translational phosphorylation³⁹.

Gene expression changes induced by TUC-1 alone are more apparent following recovery which suggests DDR pathways activated after treatment with TUC-1, discussed earlier in Chapter 5, repairs DSBs restoring DNA integrity leading to basal γH2AX foci and resumption of the cell cycle as observed earlier.

Earlier data indicates p53 independent induction of negative cell cycle regulator *CDKN1A*, also known as p21, by TUC-1 (Chapter 5, Section 5.2.4). The STRING analysis once again shows p21 upregulation by TUC-1 which is enhanced when TUC-1 is combined with AZD7762, consistent pre- and post-recovery. This can be attributed to the addition of AZD7762 as previous studies have shown p53-independent induction of p21, following Chk1 inhibition and elevated DNA damage^{42, 43}.

Loss of p21 has also been shown to improve sensitivity to Chk inhibitors⁴³. Another gene highly upregulated following combination treatment is *SERTAD1*, a positive regulator of the cell cycle highly expressed in pancreatic tissue⁴⁴ which, coupled with mutated negative regulator *CDKN2A* (or p16), promotes proliferation. *SERTAD1* binds to CDK4 and cyclin D complexes leading Rb (retinoblastoma) phosphorylation and alleviation of negative regulation on transcription factor E2F promoting G1 to S transition⁴⁵. This can be seen with TUC-1 and AZD7762 combination treatment which leads to an increase in S phase accumulation compared to TUC-1 alone. Though *SERTAD1* acts as an oncogene, it has been reportedly upregulated following treatment with gemcitabine, cisplatin and topotecan⁴⁶. Altogether, the lack of

transcriptomic response when TUC-1 is combined with AZD7762 explains the elevated DNA damage and stalled replication forks following Chk1 inhibition.

6.4 Future work

As reported in the literature previously²⁰, p53 mutant cells were more sensitive to AZD7762 combined with a DNA damaging agent due to the lack of G1 checkpoint response. To decipher if this stands true for combination treatment with TUC-1, activity and synergy can be probed in p53 mutant and wild-type HCT116 cells, otherwise isogenic. Additionally, as p21 plays a key role in mediating cell cycle arrest following TUC-1 induced DNA damage, loss of p21, by knockdown or siRNA, will further clarify its role in the downstream effects triggered by TUC-1. An immunoblot analysis for Chk1 and Chk2 substrate Cdc25A following combination treatment will also confirm if AZD7762 successfully inhibits the effector kinases. Furthermore, combination treatment with Chk1 and Chk2 selective inhibitors such as CHIR-124⁴⁷ and BML-277⁴⁸ would distinguish the role of each kinase in TUC-1 mediated cytotoxicity, deciding if inhibition of both kinases is required for synergy.

6.5 References

1. M. Gatei, K. Sloper, C. Sorensen, R. Syljuåsen, J. Falck, K. Hobson, K. Savage, J. Lukas, B. B. Zhou, J. Bartek and K. K. Khanna, *J. Biol. Chem.*, 2003, **278**, 14806-14811.
2. Y. Zhang and T. Hunter, *Int. J. Cancer*, 2014, **134**, 1013-1023.
3. B.-B. S. Zhou and S. J. Elledge, *Nature*, 2000, **408**, 433-439.
4. J. Wang, X. Han and Y. Zhang, *Cancer Res.*, 2012, **72**, 3786-3794.
5. C. Lukas, J. Falck, J. Bartkova, J. Bartek and J. Lukas, *Nat. Cell Biol.*, 2003, **5**, 255-260.
6. J. Falck, N. Mailand, R. G. Syljuåsen, J. Bartek and J. Lukas, *Nature*, 2001, **410**, 842-847.
7. C. S. Sørensen, R. G. Syljuåsen, J. Falck, T. Schroeder, L. Rönnstrand, K. K. Khanna, B. B. Zhou, J. Bartek and J. Lukas, *Cancer Cell*, 2003, **3**, 247-258.
8. K. Brooks and B. Gabrielli, *Cell Cycle*, 2012, **11**, 2039-2040.
9. L. Zannini, D. Delia and G. Buscemi, *J. Mol. Cell Biol.*, 2014, **6**, 442-457.
10. J. Zhang, H. Willers, Z. Feng, J. C. Ghosh, S. Kim, D. T. Weaver, J. H. Chung, S. N. Powell and F. Xia, *Mol. Cell. Biol.*, 2004, **24**, 708-718.
11. Y. Tan, P. Raychaudhuri and R. H. Costa, *Mol. Cell. Biol.*, 2007, **27**, 1007-1016.
12. B. Zhao, M. J. Bower, P. J. McDevitt, H. Zhao, S. T. Davis, K. O. Johanson, S. M. Green, N. O. Concha and B. B. Zhou, *J. Biol. Chem.*, 2002, **277**, 46609-46615.
13. G. Scagliotti, J. H. Kang, D. Smith, R. Rosenberg, K. Park, S. W. Kim, W. C. Su, T. E. Boyd, D. A. Richards, S. Novello, S. M. Hynes, S. P. Myrand, J. Lin,

- E. N. Smyth, S. Wijayawardana, A. B. Lin and M. Pinder-Schenck, *Invest. New Drugs*, 2016, **34**, 625-635.
14. E. Sausville, P. Lorusso, M. Carducci, J. Carter, M. F. Quinn, L. Malburg, N. Azad, D. Cosgrove, R. Knight, P. Barker, S. Zabludoff, F. Agbo, P. Oakes and A. Senderowicz, *Cancer Chemother. Pharmacol.*, 2014, **73**, 539-549.
 15. M. Suzuki, T. Yamamori, T. Bo, Y. Sakai and O. Inanami, *Transl. Oncol.*, 2017, **10**, 491-500.
 16. E. Fuse, H. Tanii, N. Kurata, H. Kobayashi, Y. Shimada, T. Tamura, Y. Sasaki, Y. Tanigawara, R. D. Lush, D. Headlee, W. D. Figg, S. G. Arbuck, A. M. Senderowicz, E. A. Sausville, S. Akinaga, T. Kuwabara and S. Kobayashi, *Cancer Res.*, 1998, **58**, 3248-3253.
 17. R. P. Perez, L. D. Lewis, A. P. Beelen, A. J. Olszanski, N. Johnston, C. H. Rhodes, B. Beaulieu, M. S. Ernstoff and A. Eastman, *Clin. Cancer Res.*, 2006, **12**, 7079-7085.
 18. Y. J. Kim, Y. B. Hong, C. H. Cho, Y. S. Seong and I. Bae, *Pancreas*, 2012, **41**, 804-805.
 19. H.-Q. Duong, Y. B. Hong, J. S. Kim, H.-S. Lee, Y. W. Yi, Y. J. Kim, A. Wang, W. Zhao, C. H. Cho, Y.-S. Seong and I. Bae, *J. Cell. Mol. Med.*, 2013, **17**, 1261-1270.
 20. J. Zhu, H. Zou, W. Yu, Y. Huang, B. Liu, T. Li, C. Liang and H. Tao, *Cancer Cell Int.*, 2019, **19**, 195.
 21. S. D. Zabludoff, C. Deng, M. R. Grondine, A. M. Sheehy, S. Ashwell, B. L. Caleb, S. Green, H. R. Haye, C. L. Horn, J. W. Janetka, D. Liu, E. Mouchet, S. Ready, J. L. Rosenthal, C. Queva, G. K. Schwartz, K. J. Taylor, A. N. Tse, G.

- E. Walker and A. M. White, *Mol. Cancer Ther.*, 2008, **7**, 2955.
22. H. Zhu, Z. Rao, S. Yuan, J. You, C. Hong, Q. He, B. Yang, C. Du and J. Cao, *Eur. J. Pharmacol.*, 2021, **908**, 174366.
23. C. C. Lau and A. B. Pardee, *Proc. Natl. Acad. Sci. U.S.A.*, 1982, **79**, 2942-2946.
24. S. R. Musk and G. G. Steel, *Int. J. Radiat. Biol.*, 1990, **57**, 1105-1112.
25. B. A. Teicher, S. A. Holden, T. S. Herman, R. Epelbaum, A. B. Pardee and B. Dezube, *Anticancer Res.*, 1991, **11**, 1555-1560.
26. L. Zhao, J. L. S. Au and M. G. Wientjes, *Front. Biosci., Elite Ed.*, 2010, **2**, 241-249.
27. H. V. Nguyen, A. Sallustrau, J. Balzarini, M. R. Bedford, J. C. Eden, N. Georgousi, N. J. Hodges, J. Kedge, Y. Mehellou, C. Tselepis and J. H. R. Tucker, *J. Med. Chem.*, 2014, **57**, 5817-5822.
28. J. L. Kedge, H. V. Nguyen, Z. Khan, L. Male, M. K. I. Hodges, Holly V. Roberts, Nikolas J., S. L. Horswell, Y. Mehellou and J. H. R. Tucker, *Eur. J. Inorg. Chem.*, 2017, **2017**, 466-476.
29. M. K. Ismail, Z. Khan, M. Rana, S. L. Horswell, L. Male, H. V. Nguyen, A. Perotti, I. Romero-Canelón, E. A. Wilkinson, N. J. Hodges and J. H. R. Tucker, *ChemBioChem*, 2020, **21**, 2487-2494.
30. J. Nieminuszczy, R. A. Schwab and W. Niedzwiedz, *Methods*, 2016, **108**, 92-98.
31. A. B. Hall, D. Newsome, Y. Wang, D. M. Boucher, B. Eustace, Y. Gu, B. Hare, M. A. Johnson, S. Milton, C. E. Murphy, D. Takemoto, C. Tolman, M. Wood, P. Charlton, J. D. Charrier, B. Furey, J. Golec, P. M. Reaper and J. R. Pollard,

- Oncotarget*, 2014, **5**, 5674-5685.
32. S. Liu, Y. Ge, T. Wang, H. Edwards, Q. Ren, Y. Jiang, C. Quan and G. Wang, *Oncol. Rep.*, 2017, **37**, 3377-3386.
 33. Y. Liu, Y. Li, X. Wang, F. Liu, P. Gao, M. M. Quinn, F. Li, A. A. Merlino, C. Benes, Q. Liu, N. S. Gray and K. K. Wong, *Cancer Res.*, 2017, **77**, 5068-5076.
 34. M. Bartucci, S. Svensson, P. Romania, R. Dattilo, M. Patrizii, M. Signore, S. Navarra, F. Lotti, M. Biffoni, E. Piloizzi, E. Duranti, S. Martinelli, C. Rinaldo, A. Zeuner, M. Maugeri-Saccà, A. Eramo and R. De Maria, *Cell Death Differ.*, 2012, **19**, 768-778.
 35. R. Boutros, C. Dozier and B. Ducommun, *Curr. Opin. Cell Biol.*, 2006, **18**, 185-191.
 36. T. Ubhi and G. W. Brown, *Cancer Res.*, 2019, **79**, 1730-1739.
 37. E. L. Deer, J. González-Hernández, J. D. Coursen, J. E. Shea, J. Ngatia, C. L. Scaife, M. A. Firpo and S. J. Mulvihill, *Pancreas*, 2010, **39**, 425-435.
 38. M. Isono, M. J. Hoffmann, M. Pinkerneil, A. Sato, M. Michaelis, J. Cinatl, Jr., G. Niegisch and W. A. Schulz, *J. Exp. Clin. Cancer Res.*, 2017, **36**, 1-1.
 39. M. Patil, N. Pabla and Z. Dong, *Cellular and molecular life sciences*, 2013, **70**, 4009-4021.
 40. X. Q. Ge and J. J. Blow, *J. Cell Biol.*, 2010, **191**, 1285-1297.
 41. S. McNeely, C. Conti, T. Sheikh, H. Patel, S. Zabudoff, Y. G. Pommier, G. K. Schwartz and A. Tse, *Cell Cycle*, 2010, **9**, 995-1004.
 42. H. Paculová, J. Kramara, Š. Šimečková, R. Fedr, K. Souček, O. Hylse, K. Paruch, M. Svoboda, M. Mistrík and J. Kohoutek, *Tumor Biol.*, 2017, **39**, 1010428317727479.

43. S. Origanti, S. R. Cai, A. Z. Munir, L. S. White and H. Piwnica-Worms, *Oncogene*, 2013, **32**, 577-588.
44. M. Höglund, L. Gorunova, A. Andrén-Sandberg, S. Dawiskiba, F. Mitelman and B. Johansson, *Genes Chromosomes Cancer*, 1998, **21**, 8-16.
45. S. Qiu, S. Liu, T. Yu, J. Yu, M. Wang, Q. Rao, H. Xing, K. Tang, Y. Mi and J. Wang, *BMC Cancer*, 2017, **17**, 795.
46. G. N. da Silva, L. T. Filoni, M. C. Salvadori and D. M. F. Salvadori, *Pathol. Oncol. Res.*, 2018, **24**, 407-417.
47. A. N. Tse, K. G. Rendahl, T. Sheikh, H. Cheema, K. Aardalen, M. Embry, S. Ma, E. J. Moler, Z. J. Ni, D. E. Lopes de Menezes, B. Hibner, T. G. Gesner and G. K. Schwartz, *Clin. Cancer. Res.*, 2007, **13**, 591-602.
48. Z. Xu, C. J. Vandenberg, E. Lieschke, L. Di Rago, C. L. Scott and I. J. Majewski, *Mol. Cancer Res.*, 2021, **19**, 1350-1360.

Chapter 7 – General discussion

7.1 Background

This chapter summarises the results presented in this thesis and highlights their potential future clinical significance, providing an overall conclusion on the MoA of TUC-1.

The clinical success of cisplatin has driven interest into metal-containing compounds while nucleoside analogue gemcitabine has provided another avenue to explore during drug design. The emergence of chemoresistance and toxicity associated with these agents reduces their clinical efficacy and creates demand for novel therapies that are equally or more efficacious with minimal side effects. Considering these challenges novel agents with multiple cellular targets are advantageous, explored in medicinal chemistry by combining two distinct molecules with different mechanistic profiles. The desirable physiochemical properties¹ of ferrocene have led to the synthesis of a wide range of ferrocenyl compounds, such as ferrocifen and derivatives, with impressive anti-cancer activity². Hybridisation of ferrocene with the tamoxifen scaffold resulted in dual acting ferrocifens, inhibiting estrogen receptor activity and also inducing quinone methides via ROS, superior to the parent compound². Inspired by this strategy, novel ferronucleoside analogue TUC-1 was developed in our laboratory. A ferrocene moiety replaces the pentose sugar ring in canonical nucleosides while retaining the nitrogenous base thymidine with a hydroxyl group bonded to one of the two cyclopentadiene rings³. Preliminary cytotoxicity

studies revealed anticancer activity of the compounds in multiple cancer cell lines originating from the GI tract³.

7.2 Summary and significance

This thesis has aimed to investigate the mechanism of action of TUC-1, as summarised in Figure 7.1, as a potential clinical candidate to treat pancreatic ductal adenocarcinoma (PDAC), accounting for 90% of all pancreatic cancer cases⁴. As demonstrated in Chapter 4, activity of TUC-1 is evaluated in a panel of PDAC cell lines with low micromolar IC₅₀ values comparable to cisplatin with activity in gemcitabine-resistant MIA PaCa-2 cells. In this case, TUC-1 is a viable candidate for second-line therapy following gemcitabine resistance as the current combination treatment for resistant pancreatic cancers, FOLFIRINOX, is associated with severe toxicity⁵. The cytotoxicity of TUC-1 in cancer cell lines, part of the NCI-60 panel, resistant to gemcitabine further support this application. Furthermore, TUC-1 is distinguished from conventional nucleoside analogues, such as gemcitabine, as it does not appear to be tri-phosphorylated by nucleoside kinases and incorporation into replicating DNA for cancer cell cytotoxicity⁶. This has not been established yet for other ferrocenyl nucleobases reported previously in the literature⁷⁻⁹. This provides a clinical advantage as gemcitabine resistance in PDAC is attributed to reduced expression of deoxycytidine kinase, enzyme catalysing rate-limiting monophosphorylation of gemcitabine¹⁰. As TUC-1 does not rely on this activating step, the prospect of cross-resistance is minimised. It also suggests TUC-1 is not vulnerable to cytidine deaminase inactivation in the plasma, implicated in reducing gemcitabine half-life and the concentration reaching pancreatic tissue¹⁰. Lead optimisation by various SAR studies also reinforced key structural elements such as

hydroxyalkyl linker length, stereo- and regiochemistry, iron (II) centre, identified as important for biological activity^{3, 6, 11, 12}. This alludes to a specific target interaction with the replication machinery in addition to local iron (II) catalysed induction of ROS, potentially reversible effects as evident by the recovery assays presented in Chapter 6. This is clinically important as it minimises off-target effects and toxicity in healthy cells that may result from a nonspecific MoA such as ROS generation observed with ferrocenyl compounds¹³⁻¹⁹.

Recently it has been hypothesised by Barton *et al.* that iron-sulfur (FeS) clusters that are present in DNA replication and repair proteins participate in reversible redox processes to modulate DNA charge transfer during replication²⁰⁻²². It has also been shown that binding of an iron-containing cofactor promotes ROS generation, leading to DNA cleavage and strand breaks in recently replicated DNA²², as observed with TUC-1 in Chapter 5. Additionally, oxidation of FeS clusters slows polymerase activity of DNA polymerase δ by increasing DNA binding affinity, resulting in lower processivity and replication fork stalling²². These data support the hypothesis of TUC-1 binding to DNA polymerases or other replication proteins, which interferes with the DNA charge transfer resulting in stalled replication forks as shown in Chapter 5. However, further *in vitro* investigations assessing DNA polymerase activity and related proteins are needed to definitively support this hypothesis.

As presented in Chapter 5, replication fork stalling and subsequent DNA strand breaks have been identified as major components of the MoA, accompanied by transcriptomic changes, partially p53-independent, leading to cell cycle arrest and

ultimately cell death by apoptosis. As most anticancer drugs, including oxaliplatin²³, cisplatin^{24, 25} and 5-FU²³, rely on p53-induced transcriptional response as part of their MoA²⁶, the high mutation rate of p53 promotes chemoresistance and poor efficacy. Therefore, agents that rely on p53 independent mechanisms, like TUC-1, are desirable. Significantly, the activation of Chk kinases and their downstream targets have been identified as key players activated following TUC-1 induced DNA damage and replication fork stalling.

The successful cotreatment of gemcitabine and Abraxane, a cytidine deaminase inhibitor, in pancreatic cancer patients has emphasised the advantage of combination treatment compared to single agent therapies¹⁰. Further investigations detailed in Chapter 6 show that inhibition of Chk-mediated repair by AZD7762 potentiates the activity of TUC-1. A synergistic relationship has therefore been established between the two compounds, as reported previously with gemcitabine²⁷ and cisplatin²⁸ and in the clinic with gemcitabine and Abraxane²⁹. Cotreatment with the inhibitor AZD7762 not only enhances but also irreversibly commits cells to the effects such as cell cycle arrest, DNA strand breaks and replication fork stalling, previously observed with TUC-1 single agent treatment. However, MIA PaCa-2 cells treated with TUC-1 alone were shown to revert to their physiological state observed with untreated controls once treatment was removed. As reversibility is commonly associated with inhibitors binding cell surface receptors or other cellular targets³⁰, this further supports the hypothesis of a reversible target interaction.

In vitro assessment of drug metabolism and pharmacokinetic properties of TUC-1 (DMPK studies presented in Chapter 3) also highlight clinically desirable outcomes including Log D_{7.4}, aqueous solubility, favourable blood-plasma ratio, and high blood stability. While hepatic instability shown by high clearance and short half-life is indicative of a small therapeutic window, stressing metabolically vulnerable groups such as the hydroxyl and amine groups. Although TUC-1 exhibits high plasma protein binding (PPB), the significance of this PK parameter remains contentious as 45% of newly FDA approved drugs (2003-2013) showed >95% PPB³¹. Additionally, high PPB did not correlate with free drug concentrations *in vivo* while low PPB was associated with poor oral bioavailability³¹. Additionally, the *in vitro* mouse (male) model carrying *KRAS* driver mutation is suggested as the most suitable animal model for evaluating *in vivo* activity of TUC-1 with the DMPK results used to interpret *in vivo* efficacy data.

Therefore in conclusion, TUC-1 remains a clinically viable agent for the treatment of PDAC distinctive from other tumour microenvironment targeting agents such as RO4929097, an inhibitor of angiogenesis, and TH-302, a hypoxia-activated prodrug, in clinical trials for the treatment of pancreatic cancer¹⁰. Future directions to further develop this work have been suggested following results in Chapters 3, 4, 5 and 6.

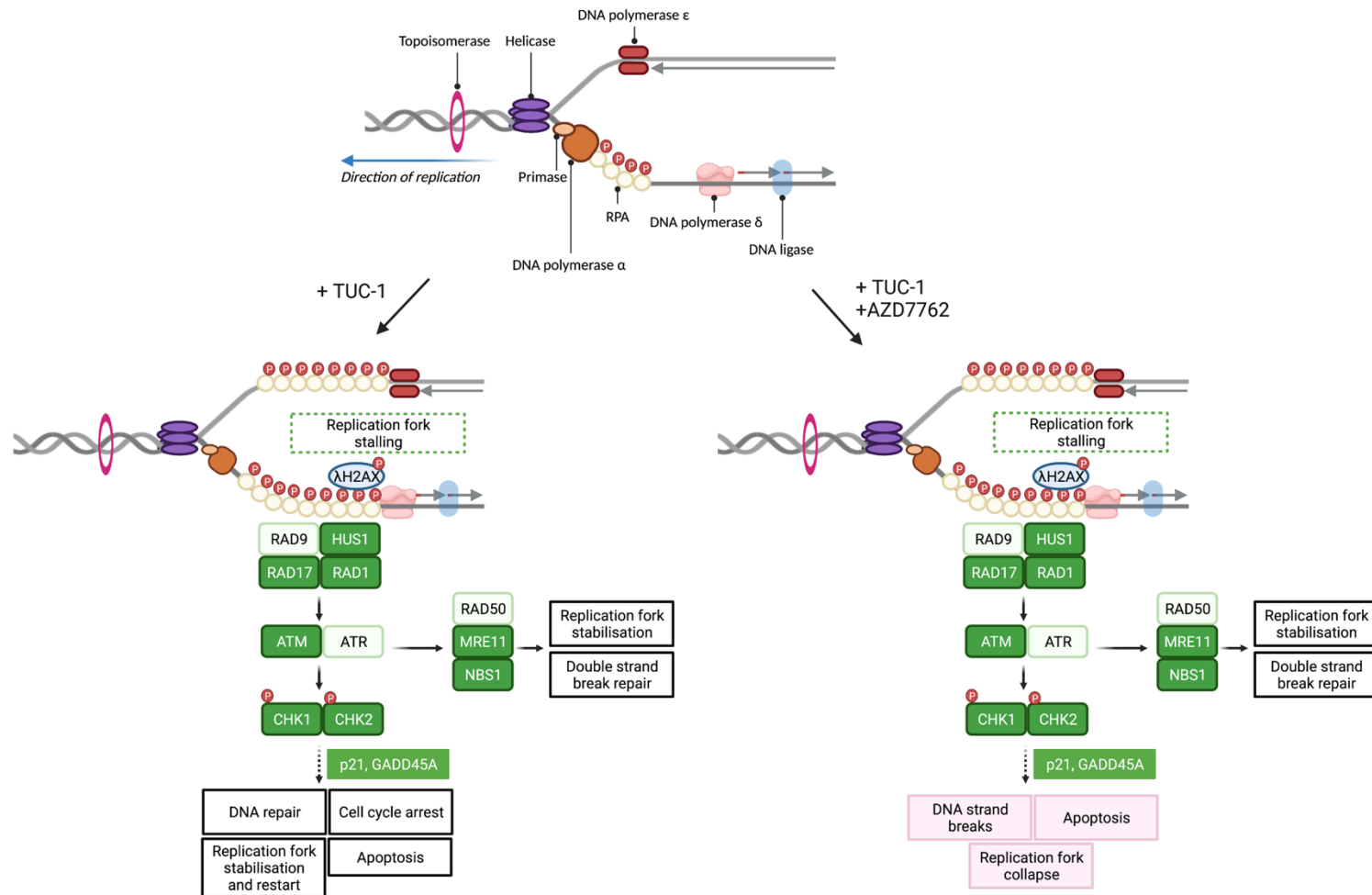


Figure 7.1. TUC-1 stalls DNA replication in pancreatic ductal adenocarcinoma leading to DNA strand breaks and Chk1 mediated intra-S checkpoint response. Cotreatment with Chk1/2 inhibitor AZD7762 potentiates the activity of TUC-1 by inhibiting Chk mediated DNA repair and fork stabilisation. Uncoupled helicase at stalled replication forks results in ssDNA coated with phosphorylated Replication Protein A (RPA), detected experimentally, inducing ATR-Chk1 axis via recruitment of the 9-1-1 complex of *RAD9*, *RAD1* and *HUS1* assisted by clamp loader *RAD17*. DNA double strand breaks, resulting from ssDNA at stalled forks, also activate ATM led response shown by the phosphorylation of Chk2 and activation of MRN complex comprising of *MRE11*, *RAD50* and *NBS1*. Highlighted in green are genes statistically significantly activated in transcriptional response to TUC-1. (Created in BioRender.com)

7.2 References

1. M. Patra and G. Gasser, 2017.
2. G. Jaouen, A. Vessi res and S. Top, *Chem. Soc. Rev.*, 2015, **44**, 8802-8817.
3. H. V. Nguyen, A. Sallustrau, J. Balzarini, M. R. Bedford, J. C. Eden, N. Georgousi, N. J. Hodges, J. Kedge, Y. Mehellou, C. Tselepis and J. H. Tucker, *J. Med. Chem.*, 2014, **57**, 5817-5822.
4. M. Orth, P. Metzger, S. Gerum, J. Mayerle, G. Schneider, C. Belka, M. Schnurr and K. Lauber, *Radiation Oncology*, 2019, **14**, 141.
5. A. K. Berger, G. M. Haag, M. Ehmann, A. Byl, D. J ger and C. Springfeld, *BMC Gastroenterology*, 2017, **17**, 143.
6. M. K. Ismail, Z. Khan, M. Rana, S. L. Horswell, L. Male, H. V. Nguyen, A. Perotti, I. Romero-Canel n, E. A. Wilkinson, N. J. Hodges and J. H. R. Tucker, *ChemBioChem*, 2020, **21**, 2487-2494.
7. P. James, J. Neud rfl, M. Eissmann, P. Jesse, A. Prokop and H.-G. Schmalz, *Org. Lett.*, 2006, **8**, 2763-2766.
8. A. A. Simenel, E. A. Morozova, L. V. Snegur, S. I. Zykova, V. V. Kachala, L. A. Ostrovskaya, N. V. Bluchterova and M. M. Fomina, *Appl. Organomet. Chem.*, 2009, **23**, 219-224.
9. J. Skiba, Q. Yuan, A. Hildebrandt, H. Lang, D. Trzybi ski, K. Wo niak, R. K. Balogh, B. Gyurcsik, V. Vr ek and K. Kowalski, *ChemPlusChem*, 2018, **83**, 77-86.
10. P. E. Oberstein and K. P. Olive, *Therapeutic advances in gastroenterology*, 2013, **6**, 321-337.
11. M. K. Ismail, K. A. Armstrong, S. L. Hodder, S. L. Horswell, L. Male, H. V.

- Nguyen, E. A. Wilkinson, N. J. Hodges and J. H. R. Tucker, *Dalton Trans.*, 2020, **49**, 1181-1190.
12. J. L. Kedge, H. V. Nguyen, Z. Khan, L. Male, M. K. I. Hodges, Holly V. Roberts, Nikolas J., S. L. Horswell, Y. Mehellou and J. H. R. Tucker, *Eur. J. Inorg. Chem.*, 2017, **2017**, 466-476.
 13. J. Ramirez-Vick, C. Acevedo, E. Melendez and S. Singh, *Journal of Cancer Science and Therapy*, 2012, **4**, 271-275.
 14. M. Görmén, P. Pigeon, S. Top, A. Vessièrès, M.-A. Plamont, E. A. Hillard and G. Jaouen, *MedChemComm*, 2010, **1**, 149-151.
 15. M. Gormén, D. Plažuk, P. Pigeon, E. Hillard, M.-A. Plamont, S. Top, A. Vessièrès and G. Jaouen, *Tetrahedron Lett.*, 2010, **51**, 118-120.
 16. A. Mooney, R. Tiedt, T. Maghoub, N. O'Donovan, J. Crown, B. White and P. T. Kenny, *J. Med. Chem.*, 2012, **55**, 5455-5466.
 17. D. Plažuk, A. Vessièrès, E. A. Hillard, O. Buriez, E. Labbé, P. Pigeon, M.-A. Plamont, C. Amatore, J. Zakrzewski and G. Jaouen, *J. Med. Chem.*, 2009, **52**, 4964-4967.
 18. G. Tabbì, C. Cassino, G. Cavigiolio, D. Colangelo, A. Ghiglia, I. Viano and D. Osella, *J. Med. Chem.*, 2002, **45**, 5786-5796.
 19. D. Hamels, P. M. Dansette, E. A. Hillard, S. Top, A. Vessièrès, P. Herson, G. Jaouen and D. Mansuy, *Angew. Chem. Int. Ed. Engl.*, 2009, **48**, 9124-9126.
 20. A. G. Baranovskiy, H. M. Siebler, Y. I. Pavlov and T. H. Tahirov, *Methods Enzymol.*, 2018, **599**, 1-20.
 21. S. Bailey, *Nat. Chem. Biol.*, 2012, **8**, 24-25.
 22. J. K. Barton, R. M. B. Silva and E. O'Brien, *Annual review of biochemistry*,

- 2019, **88**, 163-190.
23. J. Boyer, E. G. McLean, S. Aroori, P. Wilson, A. McCulla, P. D. Carey, D. B. Longley and P. G. Johnston, *Clin. Cancer Res.*, 2004, **10**, 2158.
 24. D. A. Anthoney, A. J. McIlwrath, W. M. Gallagher, A. R. M. Edlin and R. Brown, *Cancer Res.*, 1996, **56**, 1374.
 25. Y. Dabiri, M. A. Abu el Maaty, H. Y. Chan, J. Wölker, I. Ott, S. Wölfl and X. Cheng, *Frontiers in Oncology*, 2019, **9**.
 26. M. J. Chow, M. V. Babak, D. Y. Wong, G. Pastorin, C. Gaiddon and W. H. Ang, *Mol. Pharm.*, 2016, **13**, 2543-2554.
 27. M. Isono, M. J. Hoffmann, M. Pinkerneil, A. Sato, M. Michaelis, J. Cinatl, Jr., G. Niegisch and W. A. Schulz, *J. Exp. Clin. Cancer Res.*, 2017, **36**, 1-1.
 28. J. Zhu, H. Zou, W. Yu, Y. Huang, B. Liu, T. Li, C. Liang and H. Tao, *Cancer Cell Int.*, 2019, **19**, 195.
 29. D. D. Von Hoff, T. Ervin, F. P. Arena, E. G. Chiorean, J. Infante, M. Moore, T. Seay, S. A. Tjulandin, W. W. Ma, M. N. Saleh, M. Harris, M. Reni, S. Dowden, D. Laheru, N. Bahary, R. K. Ramanathan, J. Tabernero, M. Hidalgo, D. Goldstein, E. Van Cutsem, X. Wei, J. Iglesias and M. F. Renschler, *N Engl J Med*, 2013, **369**, 1691-1703.
 30. A. Farinde, Drug–Receptor Interactions, <https://www.msdmanuals.com/en-gb/professional/clinical-pharmacology/pharmacodynamics/drug-receptor-interactions>, 2021).
 31. X. Liu, M. Wright and C. E. C. A. Hop, *J. Med. Chem.*, 2014, **57**, 8238-8248.

Chapter 8 – Appendices

8.1 Supporting Information for Chapter 2

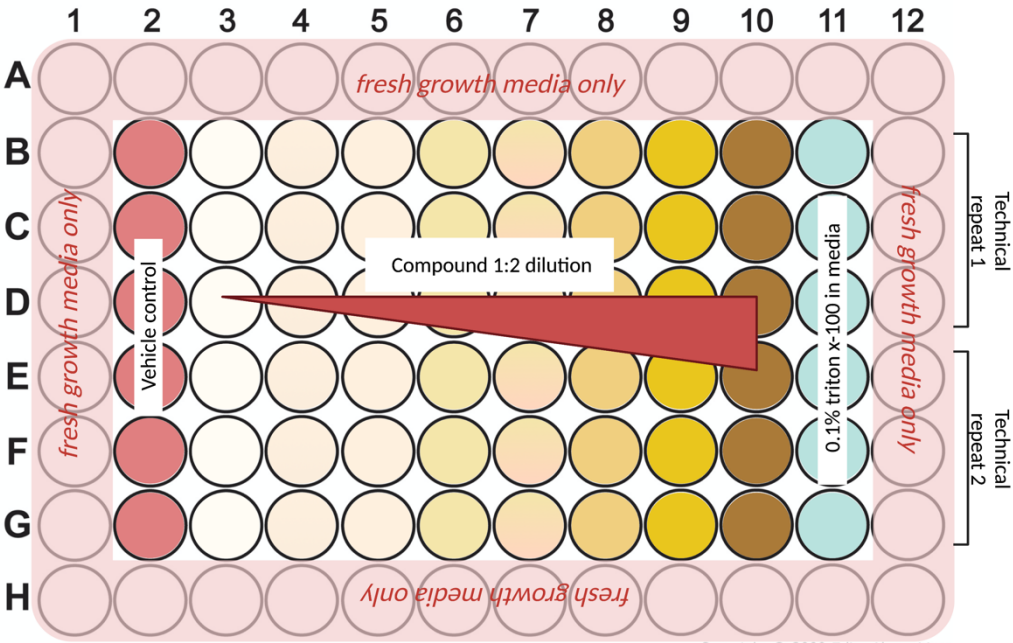


Figure S1. Experimental 96-well plate setup used for MTT cytotoxicity studies of compounds with typical concentration range 0-200 μ M (Created in Biorender.com)

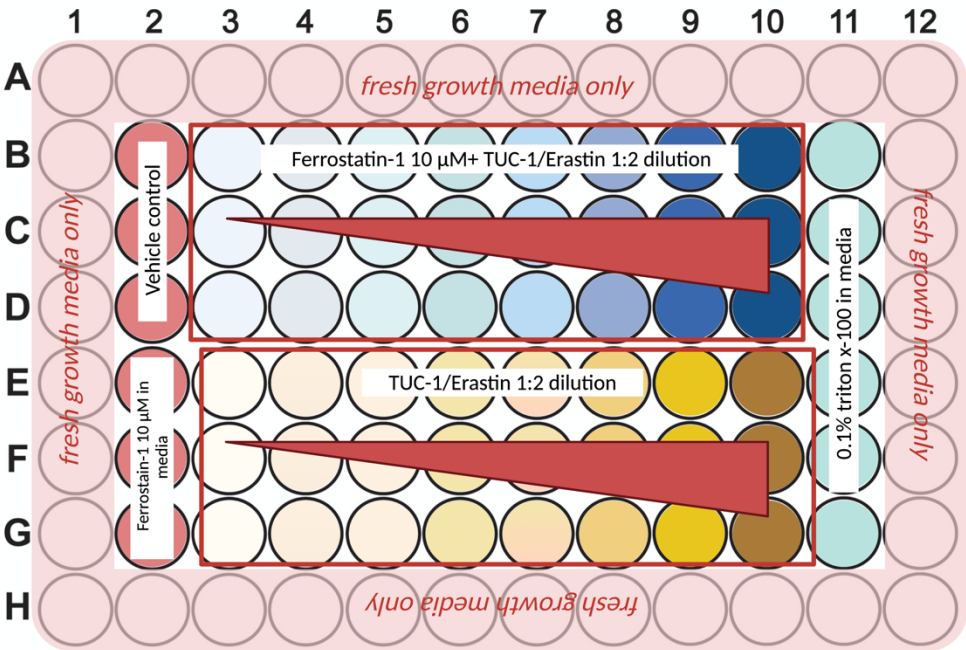


Figure S2. Experimental 96-well plate setup used to investigate ferroptosis by of TUC-1 or Erastin (0-200 μ M) in the presence and absence of Ferrostatin-1 10 μ M (Created in Biorender.com)

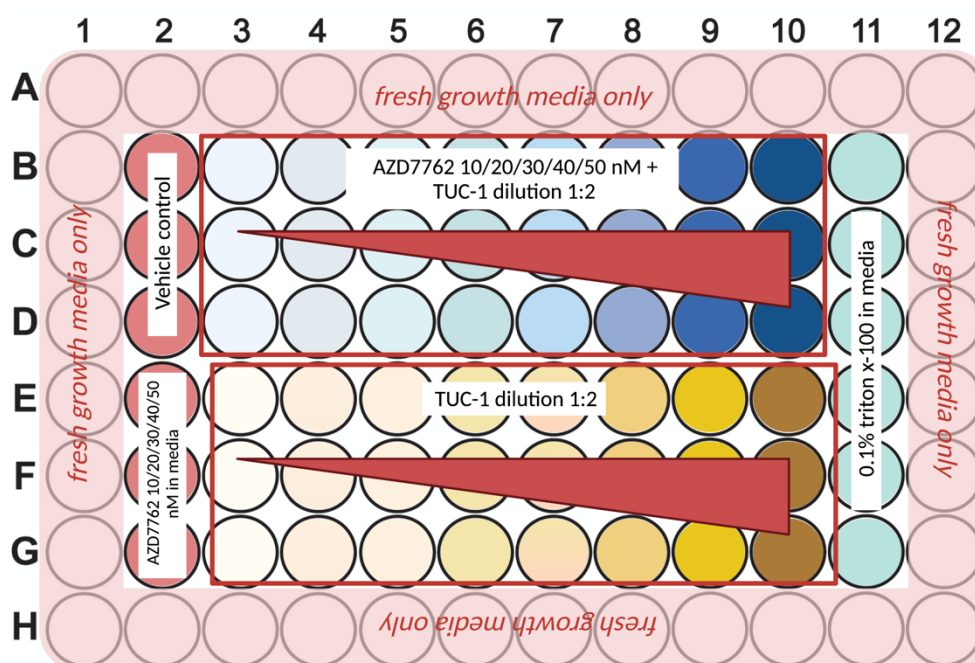


Figure S3. Experimental 96-well plate setup used for TUC-1 (0-200 μ M) cotreatment with fixed concentrations of AZD7762 (Created in Biorender.com)

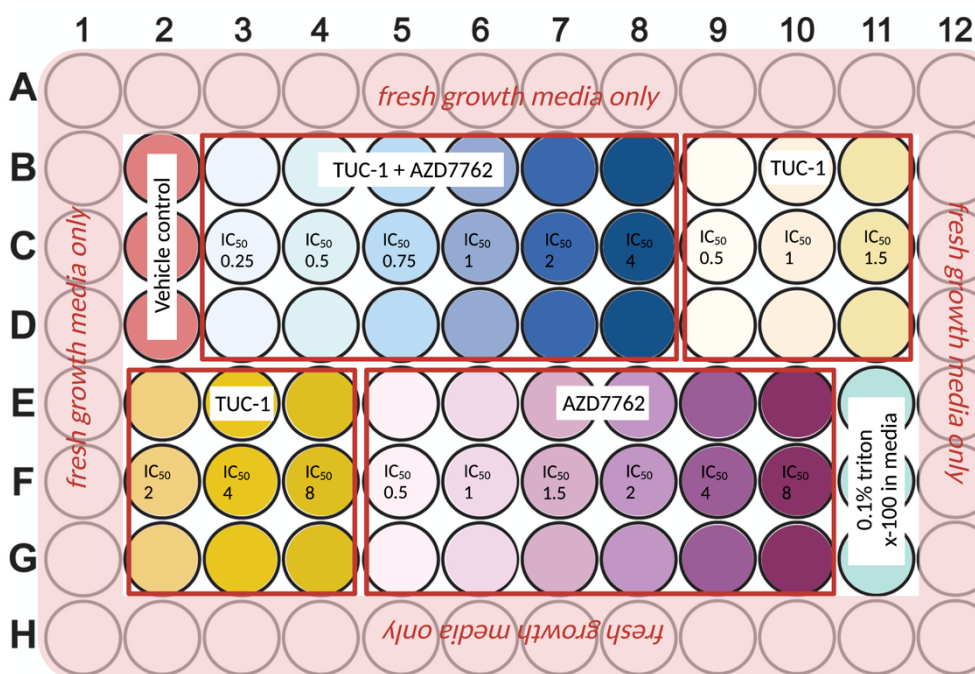


Figure S4. Experimental 96-well plate setup used for TUC-1 and AZD7762 co-treatment at fixed IC_{50} ratios (Created in Biorender.com)

Supporting Information for Chapter 3

Human	B:P ratio	Plasma MS response					
Male		blood incubations			plasma incubations		
Compound ID		n=1	n=2	mean	n=1	n=2	mean
TUC-1	0.82	2.74	2.70	2.72	2.07	2.37	2.22
Chloroquine*	4.33	0.14	0.10	0.12	0.47	0.57	0.52
Diclofenac*	0.66	0.33	0.23	0.28	0.17	0.20	0.18
Verapamil*	0.77	7.15	4.98	6.06	4.19	5.14	4.66

Mouse/C57Bl/6	B:P ratio	Plasma MS response					
Male		blood incubations			plasma incubations		
Compound ID		n=1	n=2	mean	n=1	n=2	mean
TUC-1	0.98	1.90	2.80	2.35	2.34	2.24	2.29
Chloroquine*	5.76	0.08	0.12	0.10	0.53	0.64	0.59
Diclofenac	0.80	0.23	0.32	0.27	0.21	0.23	0.22
Verapamil	1.22	3.74	4.88	4.31	4.96	5.58	5.27

Rat/SD	B:P ratio	Plasma MS response					
Male		blood incubations			plasma incubations		
Compound ID		n=1	n=2	mean	n=1	n=2	mean
TUC-1	0.79	2.99	3.00	2.99	2.15	2.57	2.36
Chloroquine*	5.32	0.12	0.11	0.12	0.58	0.65	0.62
Diclofenac*	0.63	0.36	0.35	0.36	0.22	0.23	0.22
Verapamil*	0.73	7.26	6.99	7.13	4.95	5.42	5.19

Figure S5. Raw data for blood to plasma ratio analysis with TUC-1 and control compounds evaluated in (A) human, (B) mouse and (C) rat models

Mixed Gender Human (Lithium Heparin) Plasma Protein Binding

Compound	Batch	Fraction Unbound			% Bound			Recovery		
		R1	R2	Mean	R1	R2	Mean	R1	R2	Mean
TUC-1	1	0.050	0.057	0.053	95.0	94.3	94.7	89	105	97
Verapamil	-	0.061	0.063	0.062	93.9	93.7	93.8	95	88	92
Warfarin	-	<0.010	<0.010	<0.010	>99.0	>99.0	>99.0	107	104	106

Male Mouse/C57Bl6 (Lithium Heparin) Plasma Protein Binding

Compound	Batch	Fraction Unbound			% Bound			Recovery		
		R1	R2	Mean	R1	R2	Mean	R1	R2	Mean
TUC-1	1	0.084	0.085	0.085	91.6	91.5	91.5	88	92	90
Verapamil	-	0.087	0.078	0.083	91.3	92.2	91.7	98	100	99
Warfarin	-	0.057	0.064	0.060	94.3	93.6	94.0	103	103	103

Male Rat/Sprague-Dawley (Lithium Heparin) Plasma Protein Binding

Compound	Batch	Fraction Unbound			% Bound			Recovery		
		R1	R2	Mean	R1	R2	Mean	R1	R2	Mean
TUC-1	1	0.111	0.109	0.110	88.9	89.1	89.0	95	108	102
Verapamil	-	0.088	0.094	0.091	91.2	90.6	90.9	100	103	102
Warfarin	-	<0.010	<0.010	<0.010	>99.0	>99.0	>99.0	85	86	86

Figure S6. Raw data for plasma protein binding of TUC-1 and control compounds evaluated in (A) human (male), (B) mouse (C57Bl6) and (C) rat (Sprague-Dawley) models

Compound Name	Species	Replicate	Time Point	RT	MS Response	% Remaining *	LN(MS)
TUC-1	Human	R1	60	0.69	0.73	69.7	-0.32
			45	0.69	0.54	52.0	-0.61
			30	0.69	0.95	91.2	-0.05
			15	0.69	0.90	86.7	-0.10
			5	0.69	0.78	74.5	-0.25
			2	0.69	1.04	100.0	0.04
		R2	60	0.69	0.76	89.1	-0.28
			45	0.69	0.82	96.4	-0.20
			30	0.69	0.94	110.3	-0.06
			15	0.69	0.88	103.5	-0.13
			5	0.69	0.75	88.4	-0.28
			2	0.69	0.85	100.0	-0.16
Propantheline	Human	R1	60	1.37	0.98	54.0	-0.02
			45	1.37	1.11	60.9	0.10
			30	1.37	1.35	74.0	0.30
			15	1.37	1.57	86.3	0.45
			5	1.37	1.68	92.3	0.52
			2	1.37	1.82	100.0	0.60
		R2	60	1.37	0.90	53.4	-0.11
			45	1.37	0.95	56.2	-0.06
			30	1.38	1.31	77.9	0.27
			15	1.37	1.48	87.9	0.39
			5	1.37	1.43	85.2	0.36
			2	1.37	1.68	100.0	0.52
TUC-1	Rat Sprague Dawley	R1	60	0.69	0.85	96.1	-0.16
			45	0.69	0.89	101.0	-0.11
			30	0.69	0.79	89.5	-0.23
			15	0.69	0.84	94.9	-0.18

				5	0.70	0.72	81.1	-0.33
				2	0.69	0.88	100.0	-0.12
			R2	60	0.70	0.77	78.9	-0.27
				45	0.69	0.78	80.1	-0.25
				30	0.70	0.79	81.2	-0.24
				15	0.69	0.90	92.4	-0.11
				5	0.69	0.68	70.2	-0.38
				2	0.70	0.97	100.0	-0.03
	Imidapril	Rat Sprague Dawley	R1	60	1.29	0.00	0.7	-5.63
				45	1.27	0.01	1.1	-5.21
				30	1.27	0.02	3.2	-4.16
				15	1.27	0.12	24.2	-2.13
				5	1.29	0.41	83.7	-0.89
				2	1.28	0.49	100.0	-0.71
			R2	60	1.29	0.00	0.6	-5.98
				45	1.26	0.01	1.2	-5.24
				30	1.27	0.02	3.3	-4.20
				15	1.27	0.11	24.4	-2.20
				5	1.28	0.35	76.3	-1.06
				2	1.28	0.46	100.0	-0.78
TUC-1	Mouse C57Bl6		R1	60	0.69	0.96	101.1	-0.05
				45	0.69	0.93	98.0	-0.08
				30	0.69	0.92	96.9	-0.09
				15	0.69	1.00	105.8	0.00
				5	0.69	0.74	78.4	-0.30
				2	0.69	0.94	100.0	-0.06
			R2	60	0.69	0.87	110.1	-0.14
				45	0.69	1.08	136.9	0.08
				30	0.69	0.95	120.9	-0.05

Propantheline	Mouse C57Bl6	R1	15	0.69	1.01	128.5	0.01
			5	0.69	0.54	67.9	-0.62
			2	0.69	0.79	100.0	-0.24
			60	1.38	0.22	17.1	-1.53
			45	1.37	0.39	31.1	-0.93
			30	1.37	0.54	42.2	-0.62
			15	1.38	1.09	86.1	0.09
			5	1.37	1.07	84.5	0.07
			2	1.37	1.27	100.0	0.24
		R2	60	1.38	0.23	16.7	-1.49
			45	1.37	0.39	29.4	-0.93
			30	1.37	0.57	42.6	-0.56
			15	1.37	1.12	83.4	0.11
			5	1.37	1.10	81.9	0.10
			2	1.37	1.34	100.0	0.30

Table S1. Raw data showing blood stability of TUC-1 and control compounds following incubation in blood samples from human (male), mouse (C57Bl6) and rat (Sprague-Dawley) species

*Percentage remaining calculated with 2-minute sample as 100%

Compound Name	Species	Replicate	Time Point (min)	RT	MS Height/Area/Response	% Remaining	LN(MS)
TUC-1	Human	R1	60	NF	-	-	-
1			45	NF	-	-	-
			30	NF	-	-	-
			15	0.70	0.10	11	-2.26
Height, Area or Response?			5	0.69	0.61	62	-0.50
Response			2	0.69	0.97	100	-0.03
TUC-1	Human	R2	60	NF	-	-	-
1			45	NF	-	-	-
			30	NF	-	-	-
			15	0.69	0.14	15	-2.00
Height, Area or Response?			5	0.69	0.60	68	-0.51
Response			2	0.69	0.88	100	-0.13
Diclofenac (A)	Human	R1	60	1.06	0.02	16	-4.17
			45	1.07	0.02	19	-4.02
			30	1.05	0.03	30	-3.56
			15	1.06	0.04	42	-3.23
Height, Area or Response?			5	1.06	0.07	75	-2.65
Response			2	1.05	0.09	100	-2.36
Diclofenac (A)	Human	R2	60	1.06	0.02	16	-4.06
			45	1.06	0.02	22	-3.74
			30	1.06	0.03	27	-3.57
			15	1.07	0.04	40	-3.16
Height, Area or Response?			5	1.06	0.08	77	-2.51
Response			2	1.06	0.11	100	-2.25

Diclofenac (B)	Human	R1	60	0.714	0.04	16	-3.17
			45	0.715	0.05	20	-2.96
			30	0.717	0.07	27	-2.67
			15	0.715	0.11	43	-2.19
			Height, Area or Response?		5	0.712	0.21
Response		2	0.714	0.26	100	-1.35	
Diclofenac (B)	Human	R2	60	0.715	0.05	16	-3.08
			45	0.714	0.05	19	-2.90
			30	0.717	0.08	27	-2.56
			15	0.714	0.12	43	-2.10
			Height, Area or Response?		5	0.714	0.21
Response		2	0.712	0.29	100	-1.24	
Diclofenac (C)	Human	R1	60	0.715	0.05	17	-3.00
			45	0.714	0.06	21	-2.83
			30	0.717	0.08	27	-2.58
			15	0.714	0.14	49	-1.96
			Height, Area or Response?		5	0.715	0.24
Response		2	0.712	0.29	100	-1.25	
Diclofenac (C)	Human	R2	60	0.714	0.06	19	-2.76
			45	0.714	0.07	20	-2.72
			30	0.715	0.10	29	-2.32
			15	0.715	0.15	43	-1.93
			Height, Area or Response?		5	0.714	0.27
Response		2	0.717	0.34	100	-1.08	
Diltiazem (A)	Human	R1	60	0.90	1.21	46	0.19
			45	0.87	1.31	50	0.27
			30	0.89	1.69	64	0.53
			15	0.90	1.99	75	0.69
			Height, Area or Response?		5	0.87	2.53

	Response		2	0.89	2.64	100	0.97
Diltiazem (A)	Human	R2	60	0.87	1.34	43	0.29
			45	0.89	1.51	49	0.41
			30	0.90	1.90	62	0.64
			15	0.88	2.23	72	0.80
	Height, Area or Response?		5	0.89	2.69	87	0.99
	Response		2	0.90	3.09	100	1.13
Diltiazem (B)	Human	R1	60	0.562	22.64	49	3.12
			45	0.562	27.32	59	3.31
			30	0.562	31.03	67	3.44
			15	0.562	42.33	91	3.75
	Height, Area or Response?		5	0.562	49.86	107	3.91
	Response		2	0.559	46.43	100	3.84
Diltiazem (B)	Human	R2	60	0.559	23.76	46	3.17
			45	0.562	28.08	54	3.34
			30	0.564	33.46	65	3.51
			15	0.559	43.02	83	3.76
	Height, Area or Response?		5	0.562	46.65	90	3.84
	Response		2	0.562	51.58	100	3.94
Diltiazem (C)	Human	R1	60	0.562	25.34	51	3.23
			45	0.559	31.01	63	3.43
			30	0.564	34.14	69	3.53
			15	0.562	46.99	95	3.85
	Height, Area or Response?		5	0.562	54.26	110	3.99
	Response		2	0.562	49.32	100	3.90
Diltiazem (C)	Human	R2	60	0.559	28.12	48	3.34
			45	0.562	30.74	52	3.43
			30	0.559	38.94	66	3.66
			15	0.559	46.13	78	3.83

Height, Area or Response?			5	0.559	59.69	101	4.09
Response			2	0.562	59.05	100	4.08
TUC-1	Mouse C57Bl6	R1	60	0.70	0.02	2	-3.95
1			45	0.70	0.05	6	-2.99
			30	0.69	0.12	14	-2.11
			15	0.69	0.34	41	-1.08
Height, Area or Response?			5	0.69	0.72	86	-0.33
Response			2	0.70	0.84	100	-0.18
TUC-1	Mouse C57Bl6	R2	60	0.70	0.02	2	-4.10
1			45	0.69	0.03	4	-3.36
			30	0.70	0.09	9	-2.44
			15	0.70	0.31	33	-1.16
Height, Area or Response?			5	0.69	0.65	69	-0.44
Response			2	0.69	0.94	100	-0.06
Diclofenac (A)	Mouse C57Bl6	R1	60	1.06	0.03	35	-3.37
			45	1.05	0.05	46	-3.10
			30	1.06	0.05	48	-3.05
			15	1.07	0.06	57	-2.87
Height, Area or Response?			5	1.06	0.08	79	-2.55
Response			2	1.06	0.10	100	-2.32
Diclofenac (A)	Mouse C57Bl6	R2	60	1.06	0.03	39	-3.42
			45	1.06	0.03	40	-3.38
			30	1.06	0.04	44	-3.29
			15	1.06	0.05	60	-2.99
Height, Area or Response?			5	1.06	0.07	82	-2.67
Response			2	1.06	0.08	100	-2.47
Diclofenac (B)	Mouse C57Bl6	R1	60	0.715	0.11	42	-2.21
			45	0.714	0.11	41	-2.23
			30	0.715	0.12	47	-2.11

			15	0.714	0.15	59	-1.87
			5	0.715	0.21	82	-1.54
			2	0.714	0.26	100	-1.34
Diclofenac (B)	Mouse C57Bl6	R2	60	0.714	0.11	40	-2.17
			45	0.715	0.12	42	-2.11
			30	0.715	0.13	47	-2.01
			15	0.714	0.17	59	-1.78
			5	0.714	0.23	80	-1.47
			2	0.714	0.29	100	-1.25
Diclofenac (C)	Mouse C57Bl6	R1	60	0.715	0.12	35	-2.08
			45	0.714	0.14	38	-1.98
			30	0.717	0.16	44	-1.84
			15	0.714	0.19	54	-1.64
			5	0.714	0.26	73	-1.34
			2	0.712	0.36	100	-1.02
Diclofenac (C)	Mouse C57Bl6	R2	60	0.714	0.13	39	-2.06
			45	0.717	0.12	37	-2.10
			30	0.715	0.17	53	-1.76
			15	0.714	0.21	64	-1.57
			5	0.714	0.27	83	-1.31
			2	0.717	0.33	100	-1.12
Diltiazem (A)	Mouse C57Bl6	R1	60	NF	-	-	-
			45	NF	-	-	-
			30	0.89	0.01	0	-5.27
			15	0.87	0.09	5	-2.41
			5	0.89	0.74	41	-0.30
			2	0.89	1.81	100	0.59
Diltiazem (A)	Mouse C57Bl6	R2	60	NF	-	-	-
			45	NF	-	-	-

			30	0.87	0.00	0	-6.75
			15	0.89	0.06	3	-2.90
		Height, Area or Response?	5	0.89	0.67	42	-0.39
		Response	2	0.87	1.60	100	0.47
Diltiazem (B)	Mouse C57Bl6	R1	60	0.57	0.05	0	-3.06
			45	0.566	0.06	0	-2.79
			30	0.564	0.24	1	-1.44
			15	0.564	2.75	7	1.01
		Height, Area or Response?	5	0.564	19.70	50	2.98
		Response	2	0.564	39.04	100	3.66
Diltiazem (B)	Mouse C57Bl6	R2	60	0.568	0.04	0	-3.25
			45	0.566	0.06	0	-2.90
			30	0.564	0.20	1	-1.60
			15	0.564	2.47	6	0.90
		Height, Area or Response?	5	0.564	19.21	48	2.96
		Response	2	0.564	39.67	100	3.68
Diltiazem (C)	Mouse C57Bl6	R1	60	0.564	0.06	0	-2.76
			45	0.562	0.11	0	-2.23
			30	0.564	0.45	1	-0.79
			15	0.562	3.82	9	1.34
		Height, Area or Response?	5	0.562	22.59	51	3.12
		Response	2	0.562	44.35	100	3.79
Diltiazem (C)	Mouse C57Bl6	R2	60	0.564	0.04	0	-3.11
			45	0.566	0.07	0	-2.66
			30	0.562	0.35	1	-1.04
			15	0.562	3.29	8	1.19
		Height, Area or Response?	5	0.562	21.95	56	3.09
		Response	2	0.564	39.25	100	3.67
TUC-1	Rat Sprague Dawley	R1	60	NF	-	-	-

			45	NF	-	-	-
			30	NF	-	-	-
			15	NF	-	-	-
		Height, Area or Response?	5	0.73	0.04	14	-3.31
		Response	2	0.73	0.26	100	-1.34
TUC-1	Rat Sprague Dawley	R2	60	NF	-	-	-
			45	NF	-	-	-
			30	NF	-	-	-
			15	NF	-	-	-
		Height, Area or Response?	5	0.73	0.04	14	-3.29
		Response	2	0.73	0.26	100	-1.35
Diclofenac (A)	Rat Sprague Dawley	R1	60	1.06	0.01	11	-4.61
			45	1.06	0.01	11	-4.61
			30	1.07	0.02	22	-3.91
			15	1.06	0.03	33	-3.51
		Height, Area or Response?	5	1.06	0.06	67	-2.81
		Response	2	1.06	0.09	100	-2.41
Diclofenac (A)	Rat Sprague Dawley	R2	60	1.06	0.02	20	-3.91
			45	1.06	0.02	20	-3.91
			30	1.06	0.02	20	-3.91
			15	1.06	0.04	40	-3.22
		Height, Area or Response?	5	1.06	0.07	70	-2.66
		Response	2	1.06	0.10	100	-2.30
Diclofenac (B)	Rat Sprague Dawley	R1	60	1.07	0.01	11	-4.61
			45	1.06	0.02	22	-3.91
			30	1.06	0.02	22	-3.91
			15	1.06	0.03	33	-3.51
		Height, Area or Response?	5	1.06	0.07	78	-2.66
		Response	2	1.07	0.09	100	-2.41

Diclofenac (B)	Rat Sprague Dawley	R2	60	1.06	0.01	11	-4.61	
			45	1.06	0.01	11	-4.61	
			30	1.06	0.02	22	-3.91	
			15	1.06	0.03	33	-3.51	
			Height, Area or Response?	5	1.06	0.07	78	-2.66
			Response	2	1.06	0.09	100	-2.41
Diclofenac (C)	Rat Sprague Dawley	R1	60	1.06	0.01	11	-4.61	
			45	1.07	0.01	11	-4.61	
			30	1.06	0.01	11	-4.61	
			15	1.06	0.03	33	-3.51	
			Height, Area or Response?	5	1.06	0.06	67	-2.81
			Response	2	1.07	0.09	100	-2.41
Diclofenac (C)	Rat Sprague Dawley	R2	60	1.06	0.01	10	-4.61	
			45	1.06	0.01	10	-4.61	
			30	1.06	0.02	20	-3.91	
			15	1.06	0.03	30	-3.51	
			Height, Area or Response?	5	1.06	0.06	60	-2.81
			Response	2	1.06	0.10	100	-2.30
Diltiazem (A)	Rat Sprague Dawley	R1	60	NF	-	-	-	
			45	NF	-	-	-	
			30	NF	-	-	-	
			15	NF	-	-	-	
			Height, Area or Response?	5	0.89	0.12	10	-2.12
			Response	2	0.87	1.15	100	0.14
Diltiazem (A)	Rat Sprague Dawley	R2	60	NF	-	-	-	
			45	NF	-	-	-	
			30	NF	-	-	-	
			15	NF	-	-	-	
			Height, Area or Response?	5	0.89	0.26	18	-1.35

			Response	2	0.86	1.43	100	0.36
Diltiazem (B)	Rat Sprague Dawley	R1		60	NF	-	-	-
				45	NF	-	-	-
				30	NF	-	-	-
				15	NF	-	-	-
			Height, Area or Response?	5	0.89	0.18	15	-1.71
			Response	2	0.87	1.24	100	0.22
Diltiazem (B)	Rat Sprague Dawley	R2		60	NF	-	-	-
				45	NF	-	-	-
				30	NF	-	-	-
				15	NF	-	-	-
			Height, Area or Response?	5	0.89	0.18	15	-1.71
			Response	2	0.86	1.24	100	0.22
Diltiazem (C)	Rat Sprague Dawley	R1		60	NF	-	-	-
				45	NF	-	-	-
				30	NF	-	-	-
				15	NF	-	-	-
			Height, Area or Response?	5	0.87	0.07	8	-2.66
			Response	2	0.87	0.93	100	-0.07
Diltiazem (C)	Rat Sprague Dawley	R2		60	NF	-	-	-
				45	NF	-	-	-
				30	NF	-	-	-
				15	NF	-	-	-
			Height, Area or Response?	5	0.87	0.13	11	-2.04
			Response	2	0.90	1.17	100	0.16

Table S2. Raw data for hepatocyte stability of TUC-1 and control compounds following incubation in hepatocytes from human (male), mouse (C57Bl6) and rat (Sprague-Dawley) species

8.2 Supporting Information for Chapter 4

Table S3: *TP53* mutational status of cell lines identified as most sensitive to TUC-1 in the NCI-60 panel. Gene mutation data reported by Leroy *et al.* (2014)¹

Cell line	TUC-1 GI ₅₀ (μM)	<i>TP53</i> status
UACC-62	2.6	Wild type
HL-60(TB)	2.8	ND
OVCAR-8	2.8	c.376-1G>A
SR	3.0	Wild type
BT-549	3.2	747G>C
SNB-75	3.2	c.772G>A
M14	3.2	c.797G>A
NCI-H23	3.2	c.738G>C
786-0	3.4	c.832C>G
CAKI-1	3.4	Wild type
U251	3.5	c.818G>A
RXF 393	3.5	c.524G>A
A549/ATCC	3.6	Wild type
NCI-H460	3.8	Wild type
NCI/ADR-RES	3.8	c.376-1G>A
SF-295	4.3	c.743G>A
LOX IMVI	4.3	Wild type
UO-31	4.3	Wild type

8.3 Supporting Information for Chapter 5

Table S4: List of all 53 genes with more than a 2-fold increase in expression in MIA PaCa2 cells treated with TUC-1 (10 μ M, 24 hours) compared to untreated controls. The results represent three independent biological repeats repeated in technical triplicates (n=3). Where statistically significant (t-test on 2^{-dCq} values) *P* values are shown.

Also highlighted are genes that were also more than 1.5-fold upregulated in either BxPC3 (green), CFPAC-1 (blue) or both (red) PDAC cell lines under the same experimental conditions in a single qPCR array experiment with the same set of primers (3 technical triplicates, 1 biological repeat)

GENE	Fold Change	P value
NM_001759 CCND2 Cyclin D2	3.4	0.006
NM_000389 CDKN1A Cyclin-dependent kinase inhibitor 1A	7.8	0.009
NM_001240 CCNT1 Cyclin T1	2.0	0.009
NM_000321 RB1 Retinoblastoma	2.5	0.009
NM_004354 CCNG2 Cyclin G2	4.7	0.011
NM_002894 RBBP8 Retinoblastoma binding protein 8	2.6	0.019
NM_001924 GADD45A Growth arrest and DNA-damage-inducible alpha	2.9	0.020
NM_005983 SKP2 S-phase kinase-associated protein 2 (p45)	2.0	0.022
NM_013376 SERTAD1 SERTA domain containing 1	3.0	0.023
NM_001238 CCNE1 Cyclin E1	2.7	0.025
NM_004507 HUS1 HUS1 checkpoint homolog (S. pombe)	2.3	0.026
NM_001799 CDK7 Cyclin-dependent kinase 7	2.6	0.027
NM_006286 TFDP2 Transcription factor Dp-2 (E2F dimerization partner 2)	2.3	0.028
NM_000051 ATM Ataxia telangiectasia mutated	3.5	0.028
NM_005590 MRE11A MRE11 meiotic recombination 11 homolog A (S. cerevisiae)	2.7	0.028
NM_002388 MCM3 Minichromosome maintenance complex component 3	2.0	0.030
NM_001254 CDC6 Cell division cycle 6 homolog (S. cerevisiae)	2.2	0.031
NM_001786 CDK1 Cyclin-dependent kinase 1	2.5	0.033
NM_002392 MDM2 Mdm2 p53 binding protein homolog (mouse)	2.0	0.033
NM_002417 MKI67 Antigen identified by antibody Ki-67	2.2	0.040
NM_016426 GTSE1 G-2 and S-phase expressed 1	2.0	0.040
NM_002873 RAD17 RAD17 homolog (S. pombe)	2.3	0.041
NM_005563 STMN1 Stathmin 1	2.0	0.041
NM_002485 NBN Nibrin	2.3	0.041
NM_007194 CHEK2 CHK2 checkpoint homolog (S. pombe)	2.0	0.041
NM_004060 CCNG1 Cyclin G1	2.3	0.041
NM_002853 RAD1 RAD1 homolog (S. pombe)	2.5	0.042
NM_006341 MAD2L2 MAD2 mitotic arrest deficient-like 2 (yeast)	2.0	0.042
NM_004346 CASP3 Caspase 3 apoptosis-related cysteine peptidase	2.5	0.042
NM_005611 RBL2 Retinoblastoma-like 2 (p130)	2.0	0.043
NM_000059 BRCA2 Breast cancer 2 early onset	2.5	0.043
NM_002875 RAD51 RAD51 homolog (S. cerevisiae)	2.1	0.044
NM_003903 CDC16 Cell division cycle 16 homolog (S. cerevisiae)	2.2	0.044
NM_007294 BRCA1 Breast cancer 1 early onset	2.4	0.044
NM_001274 CHEK1 CHK1 checkpoint homolog (S. pombe)	2.1	0.048
NM_003591 CUL2 Cullin 2	2.1	0.048
NM_014708 KNTC1 Kinetochore associated 1	2.3	0.049
NM_001798 CDK2 Cyclin-dependent kinase 2	2.2	0.049

NM_007111 TFDPI Transcription factor Dp-1	2.0	0.050
NM_001168 BIRC5 Baculoviral IAP repeat containing 5	2.4	NS
NM_001826 CKS1B CDC28 protein kinase regulatory subunit 1B	2.3	NS
NM_001827 CKS2 CDC28 protein kinase regulatory subunit 2	2.2	NS
ABL1 C-abl oncogene 1 non-receptor tyrosine kinase	2.2	NS
NM_013366 ANAPC2 Anaphase promoting complex subunit 2	2.1	NS
NM_001184 ATR Ataxia telangiectasia and Rad3 related	2.1	NS
NM_004217 AURKB Aurora kinase B	2.1	NS
NM_000633 BCL2 B-cell CLL/lymphoma 2	2.4	NS
NM_005190 CCNC Cyclin C	2.3	NS
NM_001239 CCNH Cyclin H	2.1	NS
NM_001790 CDC25C Cell division cycle 25 homolog C (S. pombe)	2.2	NS
NM_003885 CDK5R1 Cyclin-dependent kinase 5, regulatory subunit 1 (p35)	2.1	NS
NM_003590 CUL3 Cullin 3	2.1	NS
NM_002358 MAD2L1 MAD2 mitotic arrest deficient-like 1 (yeast)	2.1	NS
NM_004526 MCM2 Minichromosome maintenance complex component 2	2.1	NS



Figure S7. p53 genotyping by sequencing in PDAC cell lines (A) MIA PaCa-2, (B) CFPAC-1 and (C) BxPC3 analysed in SnapGene (<https://www.snapgene.com/snapgene-viewer/>). Annotations in red confirm the missense mutations comparing wild type (Query) to sequenced samples (Subject)

8.4 References

1. B. Leroy, L. Girard, A. Hollestelle, J. D. Minna, A. F. Gazdar and T. Soussi,
Hum. Mutat., 2014, **35**, 756-765.